



TECHNISCHE
UNIVERSITÄT
WIEN
Vienna University of Technology

DISSERTATION

Generation and Detection of Neutron Orbital Angular Momentum

ausgeführt zum Zwecke der Erlangung des akademischen Grades eines Doktors der
technischen Wissenschaften unter der Leitung von

Privatdoz. Dipl.-Ing. Dr. Stephan Sponar

by

Niels Geerits

A black rectangular redaction box covering the author's affiliation and contact information.

Wien
January 30, 2025

Who has performed these deeds?
Who has called forth the generations from the beginning?
Isaiah 41:4

AMDG

Acknowledgments

I wish to extend my gratitude towards Stephan Sponar, for the supervision and creation of this project, in addition to the thoughtful discussion and providing significant freedom in pursuing my scientific interests. Additional thanks go to Yuji Hasegawa who acted as supervisor in the beginning stages of this project and provided much useful insight.

I am also indebted to my colleagues at the Atominstitut, in particular Armin Danner, Richard Wagner, Andreas Dvorak, Ismaele Vincent and Kazuma Obigane for all the enlightening discussion, help with experiments, writing publications and creating a generally nice and fun atmosphere in the office.

At this point I must also mention and thank the mechanical workshop of the Atominstitut and the tireless efforts of Roman Gergen, who designed and constructed components for almost every single experiment mentioned in this thesis.

A special thanks must also be extended to all the instrument responsables at neutron sources around the world who helped conduct the experiments described in this thesis. I thank them not only for lending their instrument and expertise, but also for their direct involvement in making each experiment a success. Thank you Hartmut Lemmel, Robert Dalglish, Steven Parnell, Gregory Smith, Dirk Honecker, Fankang Li and Andrea Piovano.

At this point I would be amiss not to mention the Reactor Institute Delft, who allowed us to carry out a four month long diffraction experiment at their reactor. A particular thanks goes to Jeroen Plomp who not only organized this, but also set up the initial meeting that led to this thesis project.

As can be gauged by the publication lists at the end of this thesis, many of our collaborators hail from Indiana University. They were not only kind enough to involve me in interesting discussions and experiments, but also facilitated and contributed to experiments discussed in this thesis. I wish to highlight in particular Steve Kuhn, Sam McKay, Kyle Steffen and Roger Pynn not only for their aid and companionship on various experiments but also for helpful discussion/insight, openness and intriguing ideas.

On this note I also thank Mike Snow, from IU, who introduced me to the idea of spin to OAM transfer in the context of the neutron nucleus weak interaction and who has also involved me in a DOE grant, which partly funded this research.

I am particularly grateful to Victor de Haan, who, among many fascinating ideas, first posited that we could measure the Sagnac effect on Larmor and later helped conduct the experiment and independently analyzed the data in parallel to myself. In addition to Victor, Ad van Well also contributed, or I should say spearheaded, the coherence measurements, presented in part in this thesis. For this I am also thankful.

I am also indebted to Lars Bannenberg and Markus Arndt who graciously agreed to write the reviews for this thesis.

Finally I must thank my parents and Katalin, for their support and interest.

The work presented in this thesis was funded by the Austrian Science Fund (FWF), project numbers P34239 and P30677, and the United States Department of Energy, DE-SC0023695, for which I extend my gratitude.

Abstract

In quantum mechanics Orbital Angular Momentum (OAM) can be seen as an azimuthal phase structure imprinted on a wavefunction. As it turns out any azimuthal structure can be described using superpositions of the OAM basis functions, $e^{i\ell\phi}$, where ℓ , an integer, representing the OAM divided by \hbar . OAM is therefore a discrete quantum mechanical (QM) degree of freedom. Since these basis functions are also solutions of the cylindrical Schrödinger equation it follows that even free particles can possess QM OAM around the flight axis. In neutrons so far three other QM degrees of freedom have been identified: energy, position/momentum and spin. The addition of a fourth degree of freedom such as OAM would open up new avenues for experiments exploring quantum information and contextuality. In addition, various theoretical literature points out that neutrons carrying OAM should interact differently with some types of matter. However, generation of neutron OAM remains difficult, due to the low flux and coherence of typical neutron beams.

The aim of this thesis is to identify, develop and test new neutron optical equipment for the generation of OAM in neutrons. In particular I explore the neutron-spin electric field coupling (Schwinger effect), the neutron-nucleus weak interaction and space coherent averaging methods. Using some of the devices detailed in this thesis the first measurements towards the search for OAM dependent neutron absorption cross sections in polarized Helium-3 have been conducted. In addition, we look at an experiment measuring the Sagnac effect arising due to the coupling between a neutrons OAM and the rotation of the earth. Finally we propose that these exotic measurements may serve as useful OAM detectors, as they provide direct insight into the OAM of the particles.

Zusammenfassung

In der Quantenmechanik kann ein Bahndrehimpuls (OAM) als eine azimutale Phasenstruktur, die auf eine Wellenfunktion aufgedruckt ist, verstanden werden. Wie sich herausstellt, kann jede azimutale Struktur durch Überlagerungen der OAM-Basisfunktionen $e^{i\ell\phi}$ beschrieben werden, wobei ℓ eine ganze Zahl ist. Der Bahndrehimpuls ist dann gleich $\ell\hbar$. Daher kann OAM als ein diskreter quantenmechanischer Freiheitsgrad verstanden werden. Da diese Basisfunktionen auch Lösungen der zylindrischen Schrödinger-Gleichung sind, folgt daraus, dass sogar freie Teilchen einen quantenmechanischen Bahndrehimpuls um die Flugachse besitzen können. Bei Neutronen wurden bisher drei weitere QM-Freiheitsgrade identifiziert: Energie, Position/Impuls und Spin. Die Hinzufügung eines vierten Freiheitsgrades wie OAM würde neue Möglichkeiten für Experimente zur Erforschung von Quanteninformation und Kontextualität eröffnen. Darüber hinaus weist verschiedene theoretische Literatur darauf hin, dass Neutronen, die OAM tragen, unterschiedlich mit Materie interagieren könnten. Die Erzeugung von Neutronen-OAM bleibt jedoch schwierig, aufgrund des niedrigen Flusses und der Kohärenz typischer Neutronenstrahlen.

Ziel dieser Dissertation ist es, neue neutronenoptische Elemente für die Erzeugung von OAM in Neutronen zu identifizieren, zu entwickeln und zu testen. Insbesondere untersuche ich die Kopplung von Neutronen-Spins mit dem elektrischen Feld (Schwinger-Effekt), die schwache Wechselwirkung zwischen Neutron und Kern sowie Methoden zur räumlichen Kohärenzmittlung. Mit einigen der in dieser Dissertation beschriebenen Geräte wurden erste Messungen zur Suche nach OAM-abhängigen Absorptionsquerschnitten in polarisiertem Helium-3 durchgeführt. Außerdem betrachten wir ein Experiment, das den Sagnac-Effekt misst, der aufgrund der Kopplung zwischen dem OAM der Neutronen und der Erdrotation entsteht. Schließlich schlagen wir vor, dass diese exotischen Messungen als nützliche OAM-Detektoren dienen könnten, da sie direkte Einblicke in das OAM der Teilchen bieten.

Contents

1	Introduction	15
2	General Theory	21
2.1	The Orbital Angular Momentum Operator and its Eigenstates	21
2.2	Orbital Angular Momentum in Free Space	23
2.3	Useful Integral Transforms	25
2.3.1	Azimuthal Fourier Transform	26
2.3.2	Hankel Transform	27
2.3.3	Effects of Transforms on the OAM Operator	28
2.4	Intrinsic and Extrinsic Orbital Angular Momentum	30
2.5	Transverse and Longitudinal Orbital Angular Momentum	36
3	Electric Fields as OAM Generators	45
3.1	Neutrons in Electric Fields	45
3.1.1	Longitudinal OAM Generation in Transmission Geometry	48
3.1.2	OAM Generation in Reflection Geometry	51
3.1.3	Transverse OAM Generation in Transmission Geometry	52
3.2	Theory of Dynamical Diffraction	54
3.2.1	Basic Dynamical Diffraction	55
3.2.2	Adding Electric Fields to Dynamical Diffraction	64
3.3	OAM Generation in Bragg Reflection from Perfect Quartz	75
3.3.1	Linear OAM States in Bragg Geometry	77
3.3.2	Null Result in Laue Geometry	80
3.4	Conclusion	81
4	OAM Generation in the Neutron Nucleus Weak Interaction	83
4.1	Theoretical Framework	84
4.2	Experimental Evidence for Angular Momentum Conservation in the Neutron- Nucleus Weak Interaction	87
4.3	Conclusion	93
5	Coherent Averaging	95
5.1	Generation of Phase Vortices in Neutron Interferometry	96
5.1.1	Qualitative Description	96
5.1.2	Theoretical Description	98
5.1.3	Experimental Results and Applications	103

5.1.4	Generalizations of Coherent Averaging	107
5.2	OAM in Spin Echo Small Angle Neutron Scattering	111
5.2.1	SESANS: An Overview	111
5.2.2	CANISIUS the Austrian Spin Echo Interferometer	115
5.2.3	Two Dimensional SESANS as a Generator of OAM	123
5.3	Conclusion	127
6	OAM Detection in Interferometry	129
6.1	Theoretical Overview	129
6.2	Measurement of the Autocorrelation of a Neutron Wavefunction on a Spin Echo Interferometer	132
7	OAM Dependent Cross Sections	135
7.1	Theory and Motivation	136
7.2	Measurement of the Helium-3 Capture Cross Section with $ \ell = 1$ Neutrons	137
7.3	Conclusion and Outlook	142
8	Rotation Angular Momentum Coupling	145
8.1	The Sagnac Effect	146
8.1.1	Theoretical Framework	147
8.1.2	Experimental Setup and Results	149
8.1.3	Conclusion and Outlook	155
8.2	Rotary Drag: The Fizeau Effect	157
8.3	Conclusion	158
9	Conclusion	159
	Bibliography	161
A	Appendix 1	177
A.1	Note 1: Calculation of the Moments of $\langle \hat{\mathbf{L}} \rangle$ for Section 5.1.2	177
A.2	Note 2: Image Processing and Data Reduction of Phase Vortices Produced in Interferometry	181
A.2.1	Data Processing	181
A.2.2	Fitting Procedure	181
B	Curriculum Vitae	185
C	Related Publications	191

1 Introduction

Angular momentum is ubiquitous in nature, being found on the largest length and time scales, such as galactic clusters, all the way down to the shortest scales, for example the spins of fundamental particles. Our classical understanding of angular momentum is captured by our intuition, formed by every day experiences. When thinking about angular momentum we are likely to imagine a spinning object or a mass moving on a circular trajectory. We may think of the centripetal force required to keep a spinning object on a circular path. Most of our classical intuition and images break down when we consider the angular momentum of waves. As will also be shown in this thesis, wave angular momentum [1, 2] does not need a centripetal force to persist and does not require mass or some circular motion. Yet when absorbed waves with angular momentum can exert torque on a massive macroscopic object [3, 4, 5]. To complicate things further quantum mechanics has demonstrated that at the fundamental level matter behaves like waves. So if all of our intuitive pictures breakdown at the fundamental level, what is angular momentum really?

Angular momentum is one of nature's conserved quantities. In classical physics it is simply the cross product between position \mathbf{r} and momentum \mathbf{p}

$$\mathbf{L} = \mathbf{r} \times \mathbf{p} \quad (1.1)$$

This mathematical structure, derived from our intuitive picture, contains within itself a broader definition than what our intuitive image usually encompasses. It is quite clear from this equation that for a particle to possess some angular momentum, it need not be moving on a circular or even a closed trajectory. In fact a particle moving in a straight line at some distance from the origin will possess angular momentum with respect to the frame of reference. According to Newton's third axiom, such motion does not require a restoring force, hence angular momentum may also persist in classical physics without a central force. A simple example of this is a particle striking a wheel off axis, thereby causing the wheel to spin. Since the spinning wheel possesses angular momentum and angular momentum is conserved, it follows that the initial particle had the same amount of angular momentum. Wave angular momentum not requiring a restoring force therefore need not be counter-intuitive if we do not think of it as something requiring rotational velocity. Instead we can think of wave angular momentum as a type of spatial wave structure. It is thus a vortex or helical wave structure which carries angular momentum (see figure 1.1).

In quantum mechanics equation 1.1 does not tell the complete story. Particles have an

1 Introduction

additional intrinsic angular momentum, called spin, which in our current understanding is not necessarily related to motion. Nonetheless quantum mechanical spin can be transferred to macroscopic objects and induce rotation [3]. The total angular momentum of a particle is made up of this intrinsic spin component and an extrinsic component called orbital angular momentum (OAM). Quantum mechanical OAM is analogous to the classical quantity described in equation 1.1, however the vectors are promoted to operators

$$\hat{\mathbf{L}} = \hat{\mathbf{r}} \times \hat{\mathbf{p}} \quad (1.2)$$

it will be shown that the eigenvalues of $\hat{\mathbf{L}}$ are quantized/discrete. This property makes OAM a useful tool for quantum information [6, 7, 8], contextuality [9, 10, 11] and as a quantum probe for example in the quantum Cheshire cat [12]. In addition this degree of freedom can be used to sense rotation [13, 14, 15, 16], as will be further explored in this thesis. Quantum mechanical OAM has various expressions. In atomic physics bound electrons carry OAM with respect to the nucleus they orbit [17]. In interferometry split wavefunctions carry OAM with respect to the center of the interferometer [18, 13]. Roughly three decades ago twisted or helical waves, that carry OAM, were realized for the first time. The phase fronts of these waves appear to twist around the axis of propagation (see figure 1.1). Despite this apparent rotation around the momentum axis

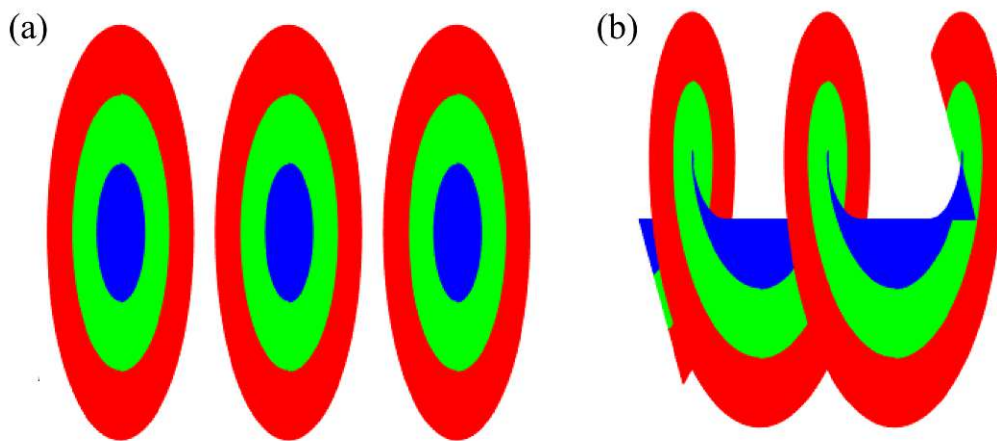


Figure 1.1: Depiction of the areas of equal phase/wavefronts for planewaves (a) and helical waves (b). The helical wave appears to twist as it propagates across the page. Hence when it is absorbed it can exert a torque around the propagation axis on a macroscopic object

these states can exist in free space in the absence of a restoring force, since no rotational velocity is associated with this twisting. These states have been realized in photons [1, 2], electrons [19], free atoms [20] and cold neutrons [21].

Neutron OAM has a wide range of applications, beyond the general uses of OAM

recorded above. Various calculations suggest that neutrons carrying OAM scatter differently from nuclei than neutrons without OAM [22, 23, 24], allowing one, for example, to observe independently the real and imaginary parts of the nuclear scattering amplitude. Furthermore it has been predicted that twisted neutrons may be invaluable for probing microscopic chiral structures [25, 26]. Finally vortex particles may be used to stimulate giant multipole resonances [27] and since giant resonances are nuclear excitations, twisted neutrons may be particularly suited to excite these transitions, since they interact primarily via the strong nuclear interaction. This may ultimately be utilized to investigate the possibility of a nuclear battery, where energy is stored in the nucleus instead of the electrons.

Due to these promising applications the aim of this dissertation is to investigate and develop instrumentation for the generation and detection of neutron OAM. Development of neutron OAM began in 2015 with the advent of the aluminium spiral phase plate for neutrons [28]. This device imprints a vortex phase structure on the neutron beam, however the method was criticized [29], since the imprinted structure was much larger ($\propto cm$) than the coherence length of an individual neutron ($\propto nm - \mu m$). As a result critics concluded that the neutrons making up the beam all possessed different OAM with respect to their axis of propagation, thereby making the composite state a mixed state. In 2016 a method using a quadrupole was introduced [30], which attempts to create a spin-orbit (spin-OAM) entangled state, by exchanging spin angular momentum to OAM. This technique suffers from the same complications as the spiral phase plate. Hence, a similar technique was proposed in 2018 [31, 32], which uses coherent averaging. Coherent averaging is the process of separating an input wavefunction into many partial wavefunctions and arranging these in a way such that the composite wavefunction (i.e. the coherent sum of all partial wavefunctions) exhibits the desired phase structure. The method introduced in 2018 uses at least two perpendicular linear magnetic gradients to implement a coherent averaging protocol. The end result is a lattice of vortices across the beam cross section. With a strong enough magnetic field the vortices could be tuned down to the transverse coherence length of individual neutrons. The technique was demonstrated experimentally in 2019 [33], where the authors were able to create vortices with a diameter on the order of 6 mm. In practice it is exceedingly difficult to produce magnetic potentials strong enough such that vortices on the order of the neutron coherence length could be observed. To remedy this, in 2023, the coherent averaging technique for neutrons was generalized in interferometry, such that the the strong nuclear potential can be exploited, which is 1000 times stronger than the magnetic potentials used in the 2019 experiment [34]. In 2021 it was demonstrated that a strong electric field polarized along the flight path of a neutron beam can generate OAM in spin polarized neutrons, by exchanging spin angular momentum for OAM [35]. While the electric fields required are too large to be produced in the lab, the natural electric field present inside of atoms, between the nucleus and the electron shell is very large ($\propto 10^{10} V \cdot m^{-1}$) and can be exploited in diffraction from perfect crystals [36]. Later in this thesis it will be demonstrated that the experiment detailed in [36], constituted an observation of a spin-orbit entangled state. The neutron nucleus weak interaction also produces spin-orbit

1 Introduction

entangled states, by exchanging neutron spin for OAM in a spin polarized beam, the effect may be enhanced in p-wave resonances such as those found in Lanthanum 139 [37]. This may be useful for the production of spin-orbit entangled states in hot ($E \propto eV$) neutrons. Vortex states in neutrons with a diameter on the order of the transverse coherence length were produced in cold neutrons in 2022 [21] using forked phase gratings. These gratings imprint a spiral phase pattern multiplied by a planewave phase pattern on the neutron wavefunction, thereby producing the desired states. However the efficiency of these gratings is very low and as a result can only be used for neutrons on the tail of the cold spectrum. To increase the available flux of twisted neutrons, methods must be developed for producing vortex states on the thermal and cold peaks. To this end electric fields and coherent averaging are the most promising techniques. The coherent averaging proposals from 2018 [31, 32] and 2019 [33], which was expanded on in 2023 [34], are reciprocal space coherent averaging schemes, that is to say, the partial wavefunctions are separated and arranged into a spiral pattern in reciprocal space. The 2023 paper proposes a real space coherent averaging scheme, where partial wavefunctions are arranged in a spiral pattern in real space. As it turns out the latter is more feasible for neutrons, such that even the smaller potentials found in magnetic prisms can be exploited. In 2024 a real space coherent averaging interferometer was reported on [38]. The technique is based on Spin Echo Small Angle Neutron Scattering (SESANS) [39, 40], a spin echo type interferometry technique which uses real space coherent averaging [41] to produce a composite wavefunction with a larger coherence, thus able to probe larger structures not accessible with regular neutron scattering techniques.

Detection of neutron OAM has been limited to interferometric techniques, where the vortex neutron is superposed with a reference wavefunction, thereby resolving the relative phase structure between the two. Such techniques place constraints on instruments, requiring an interferometer to assess the quality of the OAM states. In addition these techniques are time consuming as they must resolve the phase structure of a 2D wavefunction. This requires a sufficient level of statistics, which take a long time to achieve since neutron beams have relatively low flux. Additional techniques have been proposed to detect neutron OAM, relying on the different scattering and absorption properties of vortex neutrons [22, 23, 24], however these rely on unknown matrix elements, which have failed to be detected to date. In 2024 a new technique was proposed, which uses the Sagnac effect, a coupling between the rotation rate of the reference frame and the OAM of the particles [14], thereby definitively detecting the OAM of the beam.

After a theoretical introduction describing general concepts and properties of quantum OAM possessed by free particles the following methods of neutron OAM production will be detailed:

- Static electric fields
 - Theoretical overview
 - Generalization of the dynamical theory of diffraction to accommodate the potential generated by the intra-atomic electric field

- Neutron diffraction experiment from a perfect quartz crystal demonstrating the generation of a neutron vortex state
- The neutron nucleus weak interaction
 - Theoretical overview
 - Neutron optical experiment demonstrating angular momentum conservation
- Coherent averaging
 - Reciprocal space coherent averaging applied to neutron interferometry
 - Real space coherent averaging
 - Development of CANISIUS the real space coherent averaging interferometer
 - * The white beam SESANS technique

Next a few detection methods are explored

- Interferometry
- Absorption cross-sections
 - Neutron optical experiment measuring the neutron nucleus absorption cross section of ^3He for twisted neutrons
- OAM Rotation Coupling
 - Theoretical overview
 - SESANS experiment demonstrating a coupling between the transverse OAM of a neutron and the rotation of the earth
 - Future development

Finally a general summary and outlook on the future of neutron OAM, looking both at production and detection techniques, as well as possible applications, will be provided.

2 General Theory

In this chapter we introduce the general concepts and methods used to discuss quantum mechanical OAM. First we will derive the Eigenstates and Eigenvalues of the OAM operator (eq. 1.2) and demonstrate that these are also Eigenstates of the free space Schroedinger equation, thereby proving that vortex states can exist in the absence of a restoring potential. At this point it is useful to introduce two integral transforms, the azimuthal Fourier transform, which allows one to extract the OAM mode distribution from any wavefunction and the Hankel transform [42], which allows us to examine the radial wavevector distribution of a wavefunction. Next We will introduce the distinction between intrinsic and extrinsic OAM and derive the conditions necessary to produce the former. Finally We will demonstrate that quantum mechanical OAM can be both parallel to propagation (longitudinal) or transverse to it and go over various properties of both types of OAM.

2.1 The Orbital Angular Momentum Operator and its Eigenstates

The quantum mechanical OAM operator is given by the cross product between the position and momentum operators

$$\hat{\mathbf{L}} = \hat{\mathbf{r}} \times \hat{\mathbf{p}} \quad (2.1)$$

In Cartesian coordinates the k^{th} component of the OAM operator is given by

$$\hat{L}_k = -i\hbar \left[x_i \frac{\partial}{\partial x_j} - x_j \frac{\partial}{\partial x_i} \right] \quad (2.2)$$

The Eigenfunctions can easily be determined by transforming to a polar coordinate system $x_i = r \cos(\phi)$ and $x_j = r \sin(\phi)$, with $0 < r < \infty$ and $0 < \phi < 2\pi$. The OAM operator then becomes

$$\hat{L}_k = -i\hbar \frac{\partial}{\partial \phi} \quad (2.3)$$

In this form Eigenfunctions can easily be determined

$$\hat{L}_k f_\ell = \ell \hbar f_\ell \rightarrow f_\ell = e^{i\ell\phi} \quad (2.4)$$

2 General Theory

where ℓ must be integer to satisfy the continuity conditions: $f_\ell(\phi = 0) = f_\ell(\phi = 2\pi)$. The Eigenfunctions of the OAM operator are therefore simply phase vortices, the phase being proportional to the azimuthal coordinate, varying from 0 to $\ell\phi$. Since we often associate rotational motion with angular momentum it is useful to determine the azimuthal contribution of the velocity of these Eigenfunctions.

$$\langle v_\phi \rangle = \int d\mathbf{r}^2 f_\ell^* \hat{v}_\phi f_\ell = - \int d\mathbf{r}^2 e^{-i\ell\phi} \frac{i\hbar}{mr} \frac{\partial}{\partial\phi} e^{i\ell\phi} \hat{\phi} = \int d\mathbf{r}^2 \frac{\ell\hbar}{mr} \hat{\phi} \quad (2.5)$$

which we will solve by converting to Cartesian coordinates

$$\langle v_\phi \rangle = \int dx dy \frac{\ell\hbar}{m(x^2 + y^2)} [-y\hat{x} + x\hat{y}] = 0 \quad (2.6)$$

which is zero since the integrands are odd functions: $\frac{1}{x^2+y^2}$ is even while the x and y are odd. As a result the quantum mechanical OAM is not associated with any kind of rotational velocity [43]. It follows that quantum OAM does not require any kind of restoring potential to persist. In the next section we will show that the OAM eigenfunctions are also eigenfunctions of the free space Schroedinger equation. Before moving on it is useful to explore the OAM carried by planewaves. Starting from a planewave propagating in the x_j direction

$$\psi = e^{ik_j x_j} \quad (2.7)$$

we can determine the OAM density of a planewave

$$\psi^* \hat{L}_k \psi = \hbar k_j x_i \quad (2.8)$$

it follows that planewaves carry OAM locally in the directions perpendicular to propagation. This is analogous to the classical angular momentum carried by a particle traveling in a straight line. When averaged over all space the mean OAM of such a planewave is zero.

$$\langle \hat{L}_k \rangle = \int d\mathbf{r}^2 \psi^* \hat{L}_k \psi = 0 \quad (2.9)$$

However if the planwave has some spatial envelope (i.e. localization), the expectation value of the OAM operator is no longer necessarily zero and some net OAM is carried with respect to the chosen reference frame. Finally we define the OAM raising and lowering operators

$$\hat{\ell}_\pm = e^{\pm i\phi} \quad (2.10)$$

By the product rule it can easily be seen that these operators raise/lower the OAM expectation value by one unit of \hbar for any wavefunction

$$\langle \hat{\ell}_\pm | \hat{L}_k \rangle = \langle \hat{L}_k \rangle_\pm = -i\hbar \int d\mathbf{r}^2 e^{\mp i\phi} \psi^* \frac{\partial}{\partial\phi} e^{\pm i\phi} \psi = \langle \hat{L}_k \rangle \pm \hbar \quad (2.11)$$

Later we will see that these operators appear in OAM generating potentials, such as the potential seen by a neutron in an electric field [35] or a quadrupole magnetic field [30].

2.2 Orbital Angular Momentum in Free Space

In the previous section it was demonstrated that the Eigenfunctions of the OAM operator do not carry any rotational velocity. This makes intuitive that quantum mechanical OAM can persist without a restoring force. In this section we shall show that the OAM Eigenfunctions are also Eigenfunctions of the cylindrical free space Schroedinger equation:

$$-\frac{\hbar^2}{2m}\left[\frac{1}{r}\frac{\partial}{\partial r}\left(r\frac{\partial}{\partial r}\right) + \frac{1}{r^2}\frac{\partial^2}{\partial\phi^2} + \frac{\partial^2}{\partial z^2}\right]\psi = E\psi \quad (2.12)$$

We can see that the second derivative in the azimuthal coordinate is simply \hat{L}_z^2/\hbar^2 , which obviously has the same Eigenfunctions as \hat{L}_z and Eigenvalues $-\ell^2$. In addition the second derivative in z is the cartesian kinetic energy operator, which has planewave solutions. Hence under the assumption that ψ is separable such that $\psi(r, \phi, z) = R(r)\Phi(\phi)Z(z)$ we can easily see that

$$\Phi(\phi) = e^{i\ell\phi} \quad Z(z) = e^{ik_z z} \quad (2.13)$$

Filling these solutions into the cylindrical Schroedinger equation we are left with a differential equation in r .

$$\left[r^2\frac{\partial^2}{\partial r^2} + r\frac{\partial}{\partial r} - \ell^2 + \left(\frac{2mE}{\hbar^2} - k_z^2\right)r^2\right]R = 0 \quad (2.14)$$

which is the Bessel equation and has the Bessel functions of the first kind as solution. We exclude Bessel functions of the second kind since these are singular at $r = 0$ and therefore not physical as free space solutions to the Schroedinger equation. Hence the eigenfunctions of the Schroedinger equation in cylindrical coordinates are

$$\psi = J_\ell(k_r r)e^{i\ell\phi}e^{ik_z z} \quad (2.15)$$

with $k_r = \sqrt{\frac{2mE}{\hbar^2} - k_z^2}$. It therefore follows that the kinetic energy of these Bessel waves is given by

$$E = \frac{\hbar^2}{2m}[k_z^2 + k_r^2] \quad (2.16)$$

once again confirming that quantum mechanical OAM does not correspond to any sort of rotational velocity, since the OAM does not contribute to the energy of the particle. While all realistic wavefunctions spread as they propagate it should now be clear that OAM does not cause wavefunctions to spread by some quantum mechanical equivalent of the centrifugal force. Since the intensity of a Bessel beam $|\psi|^2$ has the same profile for all z the wave is non-diffracting [44]. For visualization the transverse profile of a Bessel beam with $\ell = 50$ and $k_r = 1$ is shown in figure 2.1. Note that the cylinder wave of mode ℓ passes through ℓ light and dark fringes over a circle of radius roughly equal to ℓ . Although Bessel beams cannot be produced in the lab since they are not localized, approximations have been generated, which demonstrate interesting properties including non-diffraction [45].

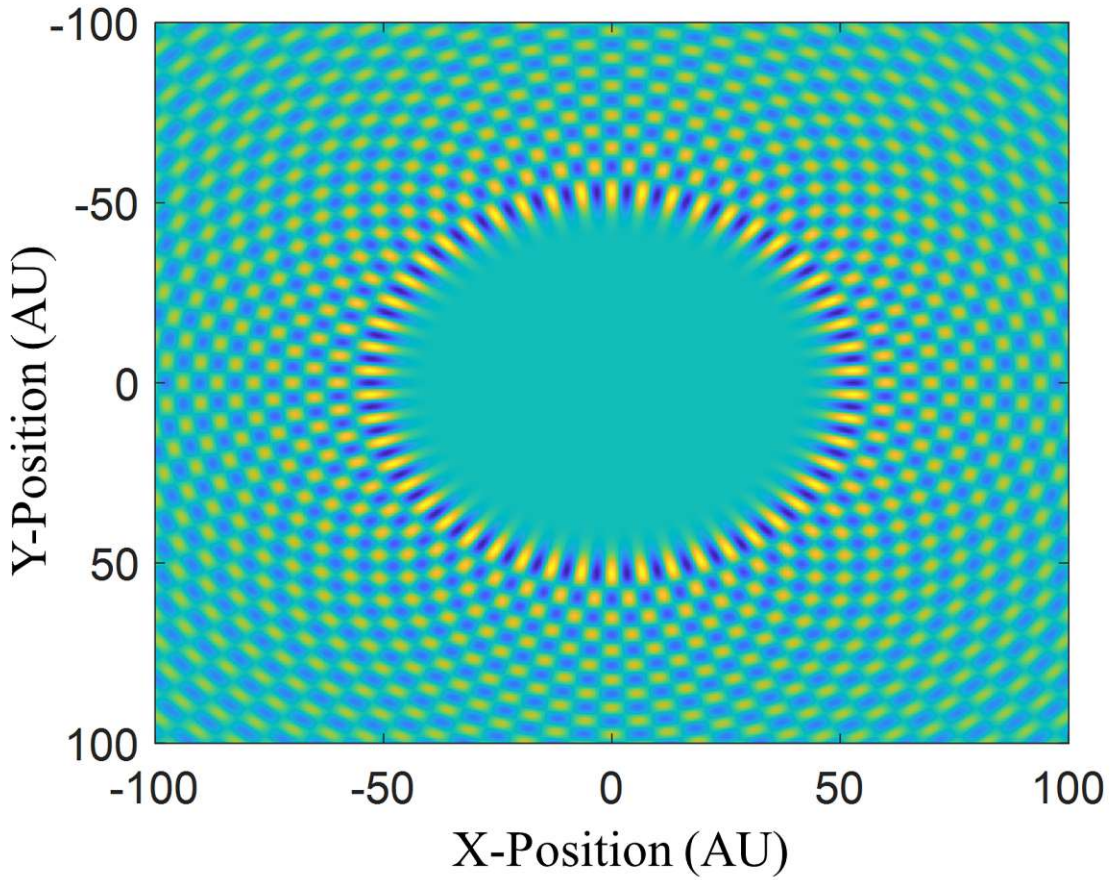


Figure 2.1: Real part of a cylindrical Eigenfunction of the free space Schrodinger equation (eq. 2.15) with $\ell = 50$ and $k_r = 1$. Note that the ring at $r = \sqrt{x^2 + y^2} = 50$ consists of 50 dark and 50 light fringes equal to the mode number of the Bessel beam.

As in the previous section we will now look at the angular velocity, OAM density and OAM expectation value carried by these Bessel waves. The angular velocity

$$\langle v_\phi \rangle = \int d\mathbf{r}^3 \psi^* \hat{v}_\phi \psi = \int d\mathbf{r}^3 \frac{\hbar \ell}{mr} J_\ell^2(k_r r) \hat{\phi} = 0 \quad (2.17)$$

is once again zero. This is most easily seen by transforming to Cartesian coordinates

$$\langle v_\phi \rangle = \int d\mathbf{r}^3 \frac{\hbar \ell}{m(x^2 + y^2)} J_\ell^2(k_r \sqrt{x^2 + y^2}) [-y\hat{x} + x\hat{y}] = 0 \quad (2.18)$$

since as in the previous section the integrand is an odd function: $\frac{1}{x^2 + y^2}$ is even and the squared Bessel function is even for all ℓ . They are multiplied by the odd functions x and y , making the whole integrand odd. This confirms the above result that no centrifugal force acts on a Bessel beam even if it carries OAM.

Moving on to determining OAM density we start by writing the OAM operator (eq. 2.1) using cylindrical coordinates

$$\hat{\mathbf{L}} = \hat{\mathbf{r}} \times \hat{\mathbf{p}} = -i\hbar \begin{bmatrix} y \frac{\partial}{\partial z} - z \frac{\partial}{\partial y} \\ z \frac{\partial}{\partial x} - x \frac{\partial}{\partial z} \\ x \frac{\partial}{\partial y} - y \frac{\partial}{\partial x} \end{bmatrix} = -i\hbar \begin{bmatrix} r \sin(\phi) \frac{\partial}{\partial z} - z(\sin(\phi) \frac{\partial}{\partial r} + \frac{\cos(\phi)}{r} \frac{\partial}{\partial \phi}) \\ z(\cos(\phi) \frac{\partial}{\partial r} - \frac{\sin(\phi)}{r} \frac{\partial}{\partial \phi}) - r \cos(\phi) \frac{\partial}{\partial z} \\ \frac{\partial}{\partial \phi} \end{bmatrix} \quad (2.19)$$

next we convert the Cartesian vector to a cylindrical one with $[\hat{\rho} \ \hat{\phi} \ \hat{z}]^T$

$$\hat{\mathbf{L}} = -i\hbar \begin{bmatrix} -\frac{z}{r} \frac{\partial}{\partial \phi} \\ z \frac{\partial}{\partial r} - r \frac{\partial}{\partial z} \\ \frac{\partial}{\partial \phi} \end{bmatrix} \quad (2.20)$$

We now apply this operator to equation 2.15 to determine the cylindrical OAM density of Bessel beams.

$$\psi^* \hat{\mathbf{L}} \psi = -i\hbar \begin{bmatrix} -\frac{i\ell z}{r} |\psi|^2 \\ k_r z J_\ell(k_r r) [J_{\ell-1}(k_r r) - \frac{\ell}{k_r r} J_\ell(k_r r)] - ik_z r |\psi|^2 \\ i\ell |\psi|^2 \end{bmatrix} \quad (2.21)$$

Since both the \hat{r} and $\hat{\phi}$ components are odd functions it can easily be understood that \hat{z} is the only non-zero component of the OAM expectation value

$$\langle \hat{\mathbf{L}} \rangle = \begin{bmatrix} 0 \\ 0 \\ \ell\hbar \end{bmatrix} \quad (2.22)$$

Pure Bessel beams therefore only carry OAM along the z-axis, the axis of propagation. Superpositions of Bessel beams may propagate along a different axis, since they form a complete basis and one can therefore expand a wavefunction propagating in any direction using cylindrical Bessel waves. Later we will explore how such superpositions can generate states where OAM and propagation are not parallel. However first in the next section I introduce the azimuthal Fourier transform and the Hankel transform, which are useful tools to extract the cylinder wave components of any wavefunction.

2.3 Useful Integral Transforms

In this section starting from the two dimensional Fourier transform we will derive the azimuthal Fourier transform (also known as the multipole expansion) and the Hankel transform [46]. The former will be especially useful for us, since it will allow us to determine the OAM mode distribution of any wavefunction.

In Cartesian coordinates the unitary two dimensional Fourier transform is well known

$$F(k_x, k_y) = \frac{1}{2\pi} \int dx dy f(x, y) e^{-i(k_x x + k_y y)} \quad (2.23)$$

2 General Theory

We start by applying a coordinate transformation to cylindrical coordinates. Here we define θ as the reciprocal azimuthal angle and ϕ as the real space angle.

$$F(k_r, \theta) = \frac{1}{2\pi} \int_0^\infty \int_0^{2\pi} dr d\phi r f(r, \phi) e^{-ik_r r \cos(\theta - \phi)} \quad (2.24)$$

Inserting the Jacobi Anger expansion [47]

$$e^{iz \cos(\phi)} = \sum_{\ell=-\infty}^{\ell=\infty} i^\ell J_\ell(z) e^{i\ell\phi} \quad (2.25)$$

the cylindrical Fourier transform becomes

$$F(k_r, \theta) = \frac{1}{2\pi} \sum_\ell \int_0^\infty \int_0^{2\pi} dr d\phi r f(r, \phi) i^\ell J_\ell(k_r r) e^{-i\ell\phi} e^{i\ell\theta} \quad (2.26)$$

from this follow the definitions of the Azimuthal Fourier and Hankel transforms, further explored in the next subsections.

2.3.1 Azimuthal Fourier Transform

While the cylindrical Fourier transform $F(k_r, \theta)$ described in equation 2.26 has its utility, for this work it would be more useful to obtain a result which expresses the OAM mode number distribution. To this end we focus on the integration over ϕ in equation 2.26 and for the time being separate out the ϕ independent terms. This leads us to the azimuthal Fourier transform

$$f^\ell(r) = \frac{1}{2\pi} \int_0^{2\pi} d\phi f(r, \phi) e^{-i\ell\phi} \quad (2.27)$$

henceforth abbreviated as AFT. We can easily verify that the inverse transform is

$$f(r, \phi) = \sum_\ell f^\ell(r) e^{i\ell\phi} \quad (2.28)$$

which we also refer to as the multipole expansion. The AFT and multipole expansion allow us to express any wavefunction in terms of the OAM Eigenfunctions. One of the most important such expansions is the Jacobi Anger expansion (equation 2.25), which expresses a planewave in cylindrical coordinates. In addition these transforms allow us to derive the OAM mode number distribution of any wavefunction. This can most easily be derived by examining the OAM expectation value. As previously shown in cylinder coordinates we need only look at the z -component

$$\langle \hat{L}_z \rangle = -i\hbar \int dr r d\phi f^*(r, \phi) \frac{\partial}{\partial \phi} f(r, \phi) \quad (2.29)$$

the multipole expansion of $f(r, \phi)$ is applied leading to

$$\langle \hat{L}_z \rangle = \sum_{l,m} \int dr r d\phi \hbar l f^{m*}(r) f^\ell(r) e^{i(\ell-m)\phi} \quad (2.30)$$

Then we recognize that the integral $\int_0^{2\pi} d\phi e^{i(\ell-m)\phi}$ is zero for $\ell \neq m$ and 2π for $\ell = m$. Using this our expectation value becomes

$$\langle \hat{L}_z \rangle = 2\pi \sum_l \int dr r \hbar \ell |f^\ell(r)|^2 \quad (2.31)$$

If we now omit averaging over the mode number ℓ we obtain the OAM distribution function

$$p[\ell] = 2\pi \int dr r |f^\ell(r)|^2 \quad (2.32)$$

it obviously follows

$$\langle \hat{L}_z \rangle = \sum_l \ell \hbar p[\ell] \quad (2.33)$$

We will use the OAM distribution function mainly to determine the relative amplitude of each OAM mode that make up the wavefunction.

2.3.2 Hankel Transform

When we substitute the multipole expansion (eq. 2.28) into the cylindrical Fourier transform (eq. 2.26) and execute the trivial integration over ϕ we obtain

$$F(k_r, \theta) = \sum_\ell i^\ell \int_0^\infty dr r f^\ell(r) J_\ell(k_r r) e^{i\ell\theta} \quad (2.34)$$

applying the AFT to $F(k_r, \theta)$ we find that the multipole components $F^\ell(k_r)$ are related to the multipole components $f^\ell(r)$ by a Hankel transform

$$F^\ell(k_r) = i^\ell \int_0^\infty dr f^\ell(r) J_\ell(k_r r) r \quad (2.35)$$

The inverse is given by

$$f^\ell(r) = -i^\ell \int_0^\infty dk_r F^\ell(k_r) J_\ell(k_r r) k_r \quad (2.36)$$

Using this result we will try to express the probability amplitude of the ℓ th mode (eq. 2.32) in both reciprocal and real space. To do this we multiply equation 2.36 by its conjugate and integrate over all space

$$\int_0^\infty dr r |f^\ell(r)|^2 = \int_0^\infty dr r \left([-i^\ell \int_0^\infty dk_r F^\ell(k_r) J_\ell(k_r r) k_r] [i^\ell \int_0^\infty dk'_r F^{\ell,*}(k'_r) J_\ell(k'_r r) k'_r] \right) \quad (2.37)$$

switching the order of integration leads to

$$\int_0^\infty dr r |f^\ell(r)|^2 = \int_0^\infty \int_0^\infty dk_r dk'_r k_r k'_r F^\ell(k_r) F^{\ell,*}(k'_r) \int_0^\infty dr r J_\ell(k_r r) J_\ell(k'_r r) \quad (2.38)$$

2 General Theory

We note that the Bessel functions $J_\ell(k_r r)$ and $J_\ell(k'_r r)$ are orthogonal functions, such that $\int dr r J_\ell(k_r r) J_\ell(k'_r r) = \frac{\delta(k_r - k'_r)}{k_r}$. Using this the above reduces to

$$\int_0^\infty dr r |f^\ell(r)|^2 = \int_0^\infty dk_r k_r |F^\ell(k_r)|^2 = \frac{1}{2\pi} p[\ell] \quad (2.39)$$

which is Parseval's theorem for Hankel transforms [48]. This demonstrates not only that the OAM expectation value is conserved upon transformation to and from reciprocal space, but also that the probability amplitude of each individual mode is unchanged upon transformation.

In this thesis we often make use of the table of integrals by Bateman [42], where the following more elegant Hankel transform is used

$$F(k_r) = \int dr f(r) J_\ell(k_r r) \sqrt{k_r r} \quad (2.40)$$

which is its own inverse.

2.3.3 Effects of Transforms on the OAM Operator

Finally it should be noted that under the two dimensional Fourier transform the z -component of the OAM operator retains its mathematical form

$$\hat{L}_z = -i\hbar \left(x \frac{\partial}{\partial y} - y \frac{\partial}{\partial x} \right) \xrightarrow{\mathcal{F}} -i\hbar \left(k_x \frac{\partial}{\partial k_y} - k_y \frac{\partial}{\partial k_x} \right) \quad (2.41)$$

Hence if any kind of wavefunction structure in real space produces OAM an identical structure in reciprocal space will also produce OAM. This fact is further emphasized by equations 2.35 and 2.36, which shows that the ℓ th order multipole component in reciprocal space depends only on the ℓ th order component in real space. In fact equation 2.39 demonstrates that the probability amplitude of the ℓ th is the same in both reciprocal and real space. This means angular structure is conserved by the Fourier transform.

A final interesting question remains: what happens to the real space wavefunction if the reciprocal wavefunction has its OAM raised or lowered? This question was in part answered above, when we showed that the OAM operator retains its form under transformation, hence raising or lowering the OAM by one unit of \hbar in reciprocal space has the exact same effect in real space. The question remains, however, if multiplying the reciprocal wavefunction with the OAM raising/lowering operator (eq. 2.10) is identical to multiplying the real space wavefunction by the raising or lowering operator and vice versa. To investigate this we start from equation 2.26 and multiply the function under investigation by the raising/lowering operator

$$F(k_r, \theta) = \frac{1}{2\pi} \sum_\ell \int_0^\infty \int_0^{2\pi} dr d\phi r f(r, \phi) i^\ell J_\ell(k_r r) e^{-i(\ell \mp 1)\phi} e^{i\ell\theta} \quad (2.42)$$

and we substitute the multipole expansion (eq. 2.28) for $f(r, \phi)$

$$F(k_r, \theta) = \sum_{\ell} i^{\ell} \int_0^{\infty} dr r f^{\ell \mp 1}(r) J_{\ell}(k_r r) e^{i\ell\theta} \quad (2.43)$$

We can substitute $n = \ell \mp 1$ and rewrite the equation in terms of the reciprocal raising and lowering operator. When applying the AFT we can see explicitly that the ℓ^{th} mode in reciprocal space becomes related to the $(\ell \mp 1)^{\text{th}}$ mode in real space by a Hankel transform of order ℓ

$$F^{\ell}(k_r) = i^{\ell} \int_0^{\infty} dr f^{\ell \mp 1}(r) J_{\ell}(k_r r) r \quad (2.44)$$

In this form it is quite clear that applying the OAM raising or lowering operator in real space is not equivalent to applying the reciprocal space variant. We can check this by lowering/raising the index of eq. 2.44 by one (i.e. the opposite of the operation we applied in real space), if the two operations were equivalent the result should reduce to eq. 2.35. This is obviously not the case. Though if it were not for the Hankel transform the two operations would be the same. In summary when we apply the raising operator in real space the index of the Bessel function is shifted with respect to the index of f . Conversely raising the index of F results in all indices on the right hand side of the transform being raised.

Exploring this question has led us to unknowingly use the convolution theorem for AFTs. The only step taken between eq. 2.42 and eq. 2.44 through eq. 2.43, was to execute the AFT (eq. 2.27). Since the AFT is identical to the standard Fourier transform, with the exception that the transform variable is discrete, we can apply the convolution theorem

$$\int_0^{2\pi} d\phi f(r, \phi) g(r, \phi) e^{-i\ell\phi} = \sum_n f^n(r) g^{\ell-n}(r) \quad (2.45)$$

where the convolution is of course discrete. In the case of the raising/lowering operator $g(r, \phi) = e^{\pm i\phi}$ and $g^{\ell} = \delta_{\ell, \pm 1}$, with δ the Kronecker delta. So the convolution would reduce to $f^{\ell \mp 1}$, consistent with our result above.

2.4 Intrinsic and Extrinsic Orbital Angular Momentum

In discussions of OAM in free quantum particles one distinguishes between intrinsic and extrinsic OAM [49, 50, 43, 34]. That is OAM that depends on the choice of the coordinate system (extrinsic) and OAM that is to a degree independent of the coordinate system (intrinsic). In the intrinsic case OAM emerges from the non-locality of the wavefunction, the fact that wavefunctions can have structure. In the case of localized point particles, the OAM they carry must be a consequence of the coordinate system and hence must be extrinsic. These points can be demonstrated and explored by looking at what happens to the OAM operator (eq. 2.1) and its expectation value under translation $\hat{\mathbf{r}}' \rightarrow \hat{\mathbf{r}} + \hat{\mathbf{r}}_0$

$$\hat{\mathbf{L}}' = (\hat{\mathbf{r}} + \hat{\mathbf{r}}_0) \times \hat{\mathbf{p}} = \hat{\mathbf{L}} + \hat{\mathbf{r}}_0 \times \hat{\mathbf{p}} \quad (2.46)$$

Previously we showed that in cylindrical coordinates the only non-zero component of $\hat{\mathbf{L}}$ is the z -component (equation 2.20). For a localized particle $\frac{\partial}{\partial \phi}$ is zero. It follows that all of its OAM is a consequence of the choice of coordinate system. Hence classical particles can only carry extrinsic OAM.

Intrinsic OAM must be translation invariant. In our previous examination of the OAM of Bessel beams only the z component of this expectation value is non-zero. This examination used an "on-axis" coordinate system. If OAM in the radial or azimuthal direction were to arise in another coordinate system it would by definition be extrinsic. Hence, in determining what properties a wavefunction must have to possess intrinsic OAM, we need only examine which properties ensure that $\langle \hat{L}_z \rangle$ is translation invariant. To this end let us examine the difference between the z component of the translated OAM operator (eq. 2.46) and the untranslated operator (eq. 2.1)

$$\Delta \hat{L}_z = -i\hbar(x_0 \frac{\partial}{\partial y} - y_0 \frac{\partial}{\partial x}) \quad (2.47)$$

and determine its expectation value

$$\langle \Delta \hat{L}_z \rangle = -i\hbar \int dx dy \psi^* (x_0 \frac{\partial}{\partial y} - y_0 \frac{\partial}{\partial x}) \psi \quad (2.48)$$

Since this must be zero for all combinations of x_0 and y_0 it follows that each integral must be zero. This leads to the following two conditions for intrinsic OAM

$$\int dx dy \psi^* \frac{\partial}{\partial x} \psi = 0 \rightarrow \langle k_x \rangle = 0 \quad (2.49a)$$

$$\int dx dy \psi^* \frac{\partial}{\partial y} \psi = 0 \rightarrow \langle k_y \rangle = 0 \quad (2.49b)$$

hence, if the momentum components perpendicular to the OAM are zero, the OAM can be considered translation invariant and therefore purely intrinsic.

2.4 Intrinsic and Extrinsic Orbital Angular Momentum

Let us now examine whether or not the OAM Eigenfunctions $e^{i\ell\phi}$ satisfy this condition, by substituting them for ψ and transforming the integrals to cylindrical coordinates:

$$-\int dr d\phi e^{-i\ell\phi} \sin(\phi) \frac{\partial}{\partial\phi} e^{i\ell\phi} = -i \int dr d\phi \ell \sin(\phi) = 0 \quad (2.50a)$$

$$\int dr d\phi e^{-i\ell\phi} \cos(\phi) \frac{\partial}{\partial\phi} e^{i\ell\phi} = i \int dr d\phi \ell \cos(\phi) = 0 \quad (2.50b)$$

which are zero since $\int_0^{2\pi} d\phi \cos(\phi + \theta)$ is zero for all θ . It follows that the OAM Eigenfunctions carry intrinsic OAM. Let us now consider an arbitrary superposition of OAM Eigenfunctions $\psi = \sum_{\ell} A^{\ell}(r) e^{i\ell\phi}$

$$\langle k_x \rangle \propto \int dr d\phi \sum_{\ell,n} A^{\ell,*}(r) e^{-i\ell\phi} \left[r \cos(\phi) \frac{\partial}{\partial r} - \sin(\phi) \frac{\partial}{\partial\phi} \right] A^n(r) e^{in\phi} \quad (2.51a)$$

$$\langle k_y \rangle \propto \int dr d\phi \sum_{\ell,n} A^{\ell,*}(r) e^{-i\ell\phi} \left[r \sin(\phi) \frac{\partial}{\partial r} + \cos(\phi) \frac{\partial}{\partial\phi} \right] A^n(r) e^{in\phi} \quad (2.51b)$$

which are only zero if

$$\int d\phi \cos(\phi) \sum_{\ell,n} A^{\ell,*}(r) A^n(r) e^{-i(\ell-n)\phi} = 0 \quad (2.52a)$$

$$\int d\phi \sin(\phi) \sum_{\ell,n} A^{\ell,*}(r) A^n(r) e^{-i(\ell-n)\phi} = 0 \quad (2.52b)$$

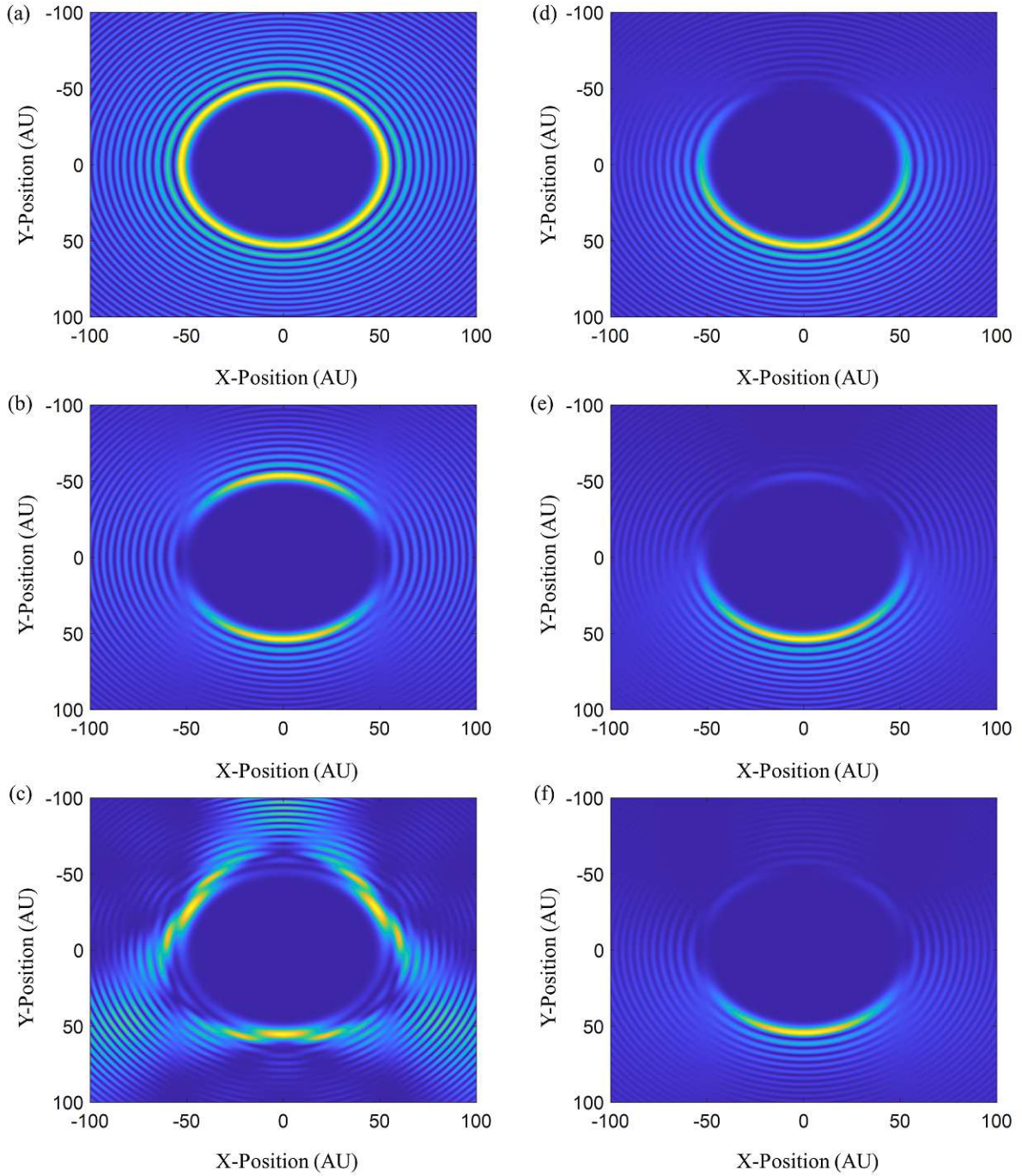


Figure 2.2: Transverse intensity distribution $|\psi|^2$ for various superpositions of different Bessel modes. k_r is always equal to 1. Insets (a)-(c) contain non-neighboring superpositions (a) $\ell = 50$, (b) $\ell = 50; \ell = 52$, (c) $\ell = 50; \ell = 53; \ell = 56; \ell = 59$, while (d)-(f) show superpositions of different numbers of neighboring modes: (d) $\ell = 50; \ell = 51$ (e) $\ell = 50; \ell = 51; \ell = 52$ (f) $\ell = 50; \ell = 51; \ell = 52; \ell = 53$. In case of neighboring superpositions of OAM the intensity distribution localizes to one side of the plane, indicating a preferred propagation direction. When the superposition does not contain neighboring mode there is no localization to one side of the plane, hence there is no preferred propagation in the x or y direction.

We may begin by recognizing that this is the case for all $\ell - n \neq \pm 1$. Using this the above conditions reduce to

$$\sum_{n-\ell=1} A^{\ell,*}(r)A^n(r) + \sum_{\ell-n=1} A^{\ell,*}(r)A^n(r) = 0 \quad (2.53a)$$

$$\sum_{n-\ell=1} A^{\ell,*}(r)A^n(r) - \sum_{\ell-n=1} A^{\ell,*}(r)A^n(r) = 0 \quad (2.53b)$$

which is only ever the case if

$$A^{\ell,*}(r)A^{\ell\pm 1}(r) = 0 \quad (2.54)$$

which leads to the curious conclusion that superpositions of OAM Eigenfunctions can only carry purely intrinsic OAM if the superposition does not consist of any spatially overlapping neighboring modes. If the superposition on the other hand contains neighboring and spatially overlapping modes it follows that at least a part of the carried OAM is extrinsic, depending on the choice of coordinate system. The implication is that the existence of overlapping neighboring modes mean propagation, since our condition of $\langle k_x \rangle = \langle k_y \rangle = 0$ is not met in this case. This phenomenon of neighboring modes inducing propagation is illustrated in figure 2.2. This figure demonstrates that superpositions of neighboring modes localize to one side of the plane, indicating a preferred Cartesian propagation direction. As the number of neighboring modes in the superposition increases the intensity distribution begins to localize to a point.

To separate the intrinsic and extrinsic contributions to the OAM, for example in the case of a superposition of neighboring cylindrical modes, we need a method of calculating either the intrinsic or extrinsic component independently. Since the extrinsic OAM component arises solely from coordinate translation it follows that it can be calculated using the cross product of the position and momentum expectation values [43]:

$$\langle \hat{\mathbf{L}}_{ext} \rangle = \langle \hat{\mathbf{r}} \rangle \times \langle \hat{\mathbf{p}} \rangle \quad (2.55)$$

and the intrinsic component can then easily be determined using the total OAM

$$\langle \hat{\mathbf{L}}_{int} \rangle = \langle \hat{\mathbf{L}} \rangle - \langle \hat{\mathbf{L}}_{ext} \rangle \quad (2.56)$$

As an example we will determine the intrinsic and extrinsic OAM components of a superposition of two neighboring cylindrical modes $\frac{1}{\sqrt{4\pi}}(e^{i\ell\phi} + e^{i(\ell+1)\phi})$. We start by calculating the total OAM

$$\langle \hat{L}_z \rangle = \frac{\hbar}{4\pi} \int d\phi (e^{-i\ell\phi} + e^{-i(\ell+1)\phi})(\ell e^{i\ell\phi} + (\ell+1)e^{i(\ell+1)\phi}) = \frac{\hbar(2\ell+1)}{2} \quad (2.57)$$

Next we must determine the extrinsic OAM component which we do by first determining the transverse position expectation value

$$\langle \hat{\mathbf{r}}_{\perp} \rangle = \frac{1}{2\pi} \int d\phi \begin{bmatrix} r \cos(\phi) \\ r \sin(\phi) \end{bmatrix} \cos(\phi) = \begin{bmatrix} r/2 \\ 0 \end{bmatrix} \quad (2.58)$$

2 General Theory

followed by the transverse momentum expectation value

$$\langle \hat{\mathbf{p}}_{\perp} \rangle = -\frac{i\hbar}{4\pi} \int d\phi (e^{-i\ell\phi} + e^{-i(\ell+1)\phi}) \left[\frac{\partial/\partial x}{\partial/\partial y} \right] (e^{i\ell\phi} + e^{i(\ell+1)\phi}) \quad (2.59)$$

which when completely rewritten in cylindrical coordinates becomes

$$\langle \hat{\mathbf{p}}_{\perp} \rangle = \frac{\hbar}{4\pi r} \int d\phi (e^{-i\ell\phi} + e^{-i(\ell+1)\phi}) \left[\frac{-\sin(\phi)}{\cos(\phi)} \right] (\ell e^{i\ell\phi} + (\ell+1)e^{i(\ell+1)\phi}) \quad (2.60)$$

this can be further simplified by eliminating all terms that integrated become zero

$$\langle \hat{\mathbf{p}}_{\perp} \rangle = \frac{\hbar}{4\pi r} \int d\phi \left[\frac{-\sin(\phi)}{\cos(\phi)} \right] (2\ell \cos(\phi) + e^{i\phi}) = \frac{\hbar}{4r} \left[\frac{-i}{2\ell+1} \right] \quad (2.61)$$

Leading to an extrinsic and intrinsic OAM of

$$\langle \hat{L}_{z,ext} \rangle = \frac{\hbar(2\ell+1)}{8} \quad (2.62a)$$

$$\langle \hat{L}_{z,int} \rangle = \frac{3\hbar(2\ell+1)}{8} \quad (2.62b)$$

Perhaps a counter-intuitive result, since the calculated intrinsic OAM is slightly lower than the averaged intrinsic OAM of the constituent states that make up our superposition: $\ell\hbar$ and $(\ell+1)\hbar$ respectively. In fact later we will see that as the number of neighboring modes is increased, the intrinsic component of the OAM decreases.

We have learned that pure OAM states (i.e. $J_{\ell}(k_r r)e^{i\ell\phi}$) carry purely intrinsic OAM, that is the expectation value $\langle \hat{L}_z \rangle$ is translation invariant. In addition we have seen that this expectation value remains invariant under translation for superpositions of any number non-neighboring cylinder modes. However, if a wavefunction carries pure intrinsic OAM in one reference frame, that OAM is no longer pure in a translated frame of reference. That is to say the OAM distribution function (eq. 2.32) is not translation invariant. We can demonstrate this by examining the second moment of the OAM operator

$$\hat{L}_z^2 = -\hbar^2 \frac{\partial^2}{\partial \phi^2} = -\hbar^2 (x^2 \frac{\partial^2}{\partial y^2} + y^2 \frac{\partial^2}{\partial x^2} - 2xy \frac{\partial}{\partial x} \frac{\partial}{\partial y} - y \frac{\partial}{\partial y} - x \frac{\partial}{\partial x}) \quad (2.63)$$

the difference between this operator and its translation is then given by

$$\Delta \hat{L}_z^2 = -\hbar^2 ((x_0^2 - 2xx_0) \frac{\partial^2}{\partial y^2} + (y_0^2 - 2yy_0) \frac{\partial^2}{\partial x^2} + 2(xy_0 + yx_0) \frac{\partial}{\partial x} \frac{\partial}{\partial y} + y_0 \frac{\partial}{\partial y} + x_0 \frac{\partial}{\partial x}) \quad (2.64)$$

while the last two terms have an expectation value of zero for wavefunctions with intrinsic OAM, all other terms must also have an expectation value of zero if we want $\langle \hat{L}_z^2 \rangle$ to

be translation invariant. This is not the case. Take for example the momentum spread operator $\hat{p}_x^2 = -\frac{\partial^2}{\partial x^2}$, which for a pure OAM state has a non-zero expectation value

$$\langle \hat{p}_x^2 \rangle = - \int d\phi e^{-i\ell\phi} \frac{\partial^2}{\partial x^2} e^{i\ell\phi} = - \int d\phi e^{-i\ell\phi} (\cos(\phi) \sin(\phi) \frac{\partial}{\partial \phi} + \sin^2(\phi) \frac{\partial^2}{\partial \phi^2}) e^{i\ell\phi} = \pi \ell^2 \quad (2.65)$$

except in the case where $\ell = 0$. So we can expect the expectation values of pure OAM states to be translation invariant, however which Eigenstates and their amplitudes that compose the wavefunction will always change under translation except if no OAM is carried at all. For many observable phenomenon and interactions it is not $\langle \hat{L}_z \rangle$ that is of great importance, but rather the amplitude of each individual OAM mode (i.e. eq. 2.32) [22, 23, 24, 51]. In some literature it is argued or implied that for OAM to be "quantum" it must be intrinsic or that extrinsic OAM always mimics classical angular momentum and is not related to wave structure [43, 29]. Both of these claims are untrue as demonstrated by the analysis above. The states $e^{i\ell\phi}$ and $e^{i(\ell+1)\phi}$, both individually carry intrinsic and quantized/integer OAM, however as previously shown the superposition of the two does not produce a purely intrinsic OAM state. Yet why would the superposition of two quantum states produce a non-quantum state? It follows that intrinsicity is not a deciding factor when it comes to the quantumness of OAM. Our example also demonstrates that extrinsic OAM can still be related to wave structure, as in this example it arises from the superposition of two vortex structures. In fact all waves that carry OAM, carry it due to their wave structure, as will be shown in the next section on transverse and longitudinal OAM, it is simply a matter of perspective. Finally an extrinsic OAM state can often be transformed into an intrinsic one (and vice versa) by transforming to a moving frame, such that $\langle k_y \rangle = \langle k_x \rangle = 0$. Note that such a transformation is a translation in reciprocal space.

While intrinsic OAM is robust to translations in real space, in reciprocal space this property is not given. There are also states such as $e^{i\ell\theta}$ (with θ the reciprocal azimuthal coordinate), which have an OAM expectation which is translation invariant in reciprocal space. Finally it should be obvious that no wavefunction can have a translation invariant OAM expectation value in both real and reciprocal space. If we translate the OAM operator (eq. 2.1) in both momentum and space we get

$$\hat{\mathbf{L}}' = (\hat{\mathbf{r}} + \hat{\mathbf{r}}_0) \times (\hat{\mathbf{p}} + \hat{\mathbf{p}}_0) = \hat{\mathbf{L}} + (\hat{\mathbf{r}} \times \hat{\mathbf{p}}_0) + (\hat{\mathbf{r}}_0 \times \hat{\mathbf{p}}) + (\hat{\mathbf{r}}_0 \times \hat{\mathbf{p}}_0) \quad (2.66)$$

the difference between this and the untranslated OAM operator is then

$$\Delta \hat{\mathbf{L}} = (\hat{\mathbf{r}} \times \hat{\mathbf{p}}_0) + (\hat{\mathbf{r}}_0 \times \hat{\mathbf{p}}) + (\hat{\mathbf{r}}_0 \times \hat{\mathbf{p}}_0) \quad (2.67)$$

The expectation value of the first two terms could be zero as previously shown if the wavefunctions fulfills the properties $\langle k_x \rangle = \langle k_y \rangle = \langle x \rangle = \langle y \rangle = 0$, however the final term $(\hat{\mathbf{r}}_0 \times \hat{\mathbf{p}}_0)$ does not produce a zero expectation value for all possible translations. It follows that there are no wavefunctions which have a translation invariant OAM expectation value in both real and reciprocal space. That is not to say that there isn't a component to a particles total OAM, that is robust to translations in both space and momentum, as will be demonstrated in the next section.

2.5 Transverse and Longitudinal Orbital Angular Momentum

In this section we explore the effect of orientation on the properties of quantum mechanical OAM. The OAM orientation is defined by the propagation axis. Hence we can define longitudinal OAM, where the OAM is parallel to the propagation direction and transverse OAM, which is perpendicular to propagation [52]. Mainly, the difference between intrinsic longitudinal and transverse OAM is simply a matter of perspective. As shown in [52] transforming the frame of reference may change a longitudinal state into a transverse one and vice versa. In the section on OAM in free space it was shown that the intrinsic OAM expectation value of a free particle can be fully defined in cylindrical coordinates by a single axis, the cylinder axis, henceforth called the z -axis. Intuition may lead us to believe that this is the propagation direction, since the preferred propagation direction of the Eigenstates of the free space Schroedinger equation is obviously along the z -axis. However as shown in the last section a superposition of two neighboring cylinder modes (i.e. $e^{i\ell\phi} + e^{i(\ell+1)\phi}$) has a preferred propagation in the x - y plane. A more extreme example was used in the section on useful integral transforms: the Jacobi Anger expansion (eq. 2.25), rewrites a planewave propagating in the x - y plane in terms of an infinite number of cylindrical modes. The OAM of each mode in this case is very obviously transverse to the propagation direction. However as shown in equation 2.9, planewaves carry on average no OAM. Nonetheless we can multiply a planewave by the OAM raising operator (eq. 2.10) to generate a wavefunction carrying on average one unit of quantum mechanical OAM transverse to the propagation direction

$$\hat{\ell}_+ e^{ik_x x} = \sum_{\ell=-\infty}^{\ell=\infty} i^\ell J_\ell(z) e^{i(\ell+1)\phi} \quad (2.68)$$

We can easily understand that the transverse OAM carried by this wavefunction is intrinsic. This follows from the fact that the extrinsic OAM, $\langle \hat{\mathbf{r}} \rangle \times \langle \hat{\mathbf{p}} \rangle$ is zero, since $\langle \hat{\mathbf{r}} \rangle = 0$ for planewaves. This OAM carrying planewave is shown contrasted with the regular planewave in figure 2.3 The planewave carrying transverse OAM has a forked structure. This is particularly interesting, since this phase profile is often imprinted on waves, by means of forked gratings [53, 54, 19, 21], to produce particles carrying longitudinal OAM. However since such a grating also imprints a small transverse planewave component on the incoming beam, the OAM is strictly speaking quasi-longitudinal with respect to the incoming beams momentum.

Sometimes extrinsic transverse OAM is compared to classical angular momentum, since it can be calculated in the same way (eq. 2.55) and it therefore has no "quantum" nature. In addition, it is sometimes said that this type of OAM is not related to wave structure. In the following we will examine these claims with an example wavefunction, a planewave with Gaussian envelope moving offset from the axis of propagation by some distance δ :

$$\psi_t = A e^{-\frac{(x-\delta)^2}{\sigma_x^2} - \frac{y^2}{\sigma_y^2}} e^{ik_y y} \quad (2.69)$$

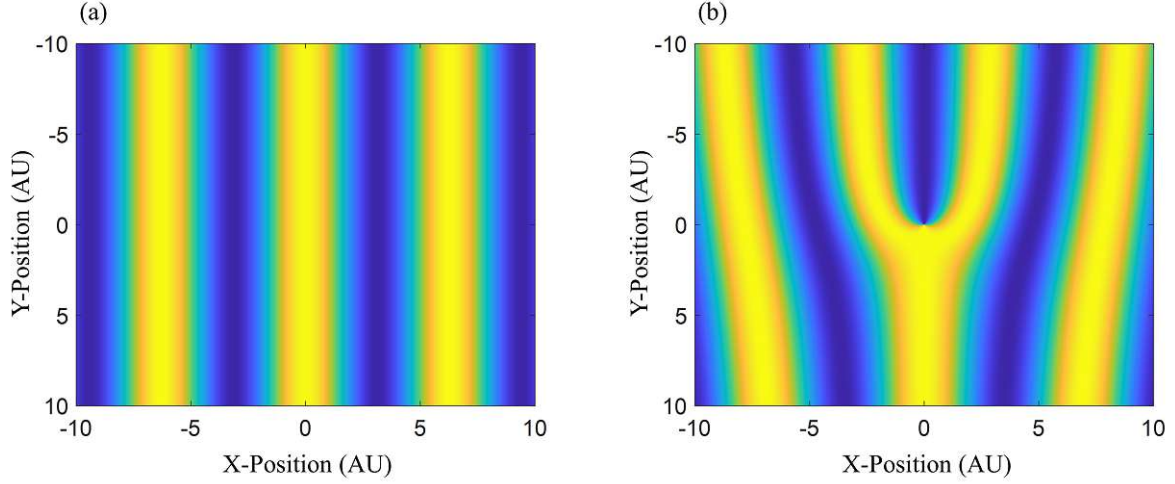


Figure 2.3: Real parts of (a) a planewave traveling along the x-direction with $k = 1$, contrasted against (b) the same planewave multiplied by the OAM raising operator. As a result this forked planewave carries one unit of \hbar of transverse OAM

σ_x and σ_y denote the coherence lengths in x and y direction respectively and A is a normalization constant. It is apparent that the classical or extrinsic transverse OAM is then given by

$$\langle \psi_t | \hat{L}_{z,ext} | \psi_t \rangle = \hbar \delta k_y \quad (2.70)$$

We can calculate the total OAM quite simply as well

$$\langle \psi_t | \hat{L}_z | \psi_t \rangle = -iA^2 \hbar \int dx dy e^{-\frac{(x-\delta)^2}{\sigma_x^2} - \frac{y^2}{\sigma_y^2}} e^{-ik_y y} \left(x \frac{\partial}{\partial y} - y \frac{\partial}{\partial x} \right) e^{-\frac{(x-\delta)^2}{\sigma_x^2} - \frac{y^2}{\sigma_y^2}} e^{ik_y y} \quad (2.71)$$

The partial derivatives in x and y of the Gaussian yield anti-symmetric functions which when integrated over all space yield zero, hence we may drop these terms.

$$\langle \psi_t | \hat{L}_z | \psi_t \rangle = A^2 \hbar k_y \int dx dy e^{-2\frac{(x-\delta)^2}{\sigma_x^2} - 2\frac{y^2}{\sigma_y^2}} x \quad (2.72)$$

the integral is nothing more than the x position expectation value of the Gaussian. Therefore the total OAM of our wavefunction is fully determined by its extrinsic OAM

$$\langle \psi_t | \hat{L}_z | \psi_t \rangle = \langle \psi_t | \hat{L}_{z,ext} | \psi_t \rangle = \hbar \delta k_y \quad (2.73)$$

So the first claim, that extrinsic transverse OAM mimics classical OAM is correct. To investigate the second and third claims we will use two approaches. The first approach is quantitative. We will expand ψ_t in terms of its cylinder modes using the integral transforms derived earlier. In particular we will derive the OAM distribution function (eq. 2.32). In the second approach we will qualitatively compare the main vortex/cylinder

2 General Theory

mode which makes up ψ_t with ψ_t . We will start our derivation of the OAM distribution function by writing ψ_t in cylindrical coordinates

$$\psi_t = Ae^{-\frac{(r \cos(\phi) - \delta)^2}{\sigma_x^2} - \frac{r^2 \sin(\phi)^2}{\sigma_y^2}} e^{ik_y r \sin(\phi)} = Ae^{-\frac{r^2 + 2\delta^2}{2\sigma_x^2} - \frac{r^2}{2\sigma_y^2}} e^{-\frac{r^2 \cos(2\phi)(\sigma_y^2 - \sigma_x^2)}{2\sigma_x^2 \sigma_y^2}} e^{\frac{2\delta r \cos(\phi)}{\sigma_x^2}} e^{ik_y r \sin(\phi)} \quad (2.74)$$

After the second equality the ϕ independent terms are grouped together, while each ϕ dependent exponential is written in a way such that the Jacobi Anger expansion (eq. 2.25) can be applied to each exponential.

$$\psi_t = Ae^{-\frac{r^2 + 2\delta^2}{2\sigma_x^2} - \frac{r^2}{2\sigma_y^2}} \sum_{j,m,n} i^{j+m} J_j\left(i \frac{r^2(\sigma_y^2 - \sigma_x^2)}{2\sigma_x^2 \sigma_y^2}\right) J_m\left(-2i \frac{\delta r}{\sigma_x^2}\right) J_n(k_y r) e^{i(2j+m+n)\phi} \quad (2.75)$$

In this form the azimuthal Fourier transform is trivial

$$\psi_t^\ell(r) = Ae^{-\frac{r^2 + 2\delta^2}{2\sigma_x^2} - \frac{r^2}{2\sigma_y^2}} \sum_{2j+m+n=\ell} i^{j+m} J_j\left(i \frac{r^2(\sigma_y^2 - \sigma_x^2)}{2\sigma_x^2 \sigma_y^2}\right) J_m\left(-2i \frac{\delta r}{\sigma_x^2}\right) J_n(k_y r) \quad (2.76)$$

this expression will become important later on for numerically calculating the OAM distribution function of planewaves with Gaussian envelopes. For now we will simplify our analysis by assuming $\sigma_x = \sigma_y = \sigma$

$$\psi_t^\ell(r) = Ae^{-\frac{r^2 + \delta^2}{\sigma^2}} \sum_m i^m J_m\left(-2i \frac{\delta r}{\sigma^2}\right) J_{\ell-m}(k_y r) \quad (2.77)$$

Using Graf's addition theorem [55] the summation over m can be explicitly calculated

$$\psi_t^\ell(r) = Ae^{-\frac{r^2 + \delta^2}{\sigma^2}} e^{i\ell\alpha} J_\ell(k' r) \quad (2.78)$$

with $k' = \sqrt{k_y^2 - 4\frac{\delta^2}{\sigma^4}}$ and $\alpha = \sin^{-1}(-2i\delta/\sigma^2 k') = \cos^{-1}(k_y/k')$. Finally the OAM distribution function can be determined according to equation 2.32.

$$p[\ell] = \frac{A^2 e^{-\frac{2\delta^2}{\sigma^2}}}{\sqrt{k'}} e^{i\ell(\alpha - \alpha^*)} \int dr \sqrt{r} e^{-\frac{2r^2}{\sigma^2}} J_\ell(k'^* r) J_\ell(k' r) \sqrt{k' r} \quad (2.79)$$

which is a standard Hankel transform given in [42]

$$p[\ell] = \frac{A^2 \sigma^2}{4} e^{i\ell(\alpha - \alpha^*)} e^{-\frac{\sigma^2 k'^2}{4} - \frac{2\delta^2}{\sigma^2}} I_\ell\left(\frac{\sigma^2 |k'|^2}{4}\right) \quad (2.80)$$

Figure 2.4 shows this OAM distribution function for various combinations of σ and δ . It demonstrates quite clearly a central point of this chapter any wavefunction can be seen as a superposition of vortex waves. This is useful to know, since these vortices will each individually interact with matter and fields as vortex states, as we will see in later chapters where it is shown that planewaves interact in an unintuitive or unexpected way with rotating media/frames of reference. A particularly interesting example of this is

the rotary drag effect, in which an image imprinted on a beam appears to rotate or drag along as it passes through a rotating medium [56]. This is the cylindrical equivalent of the Fizeau effect. In the rotating frame of reference $\phi' \rightarrow \phi + \Omega t$ each OAM mode becomes doppler shifted $E' \rightarrow E + \ell\hbar\Omega$, causing each mode to experience a different refractive index in the medium. This can ultimately lead to spatial separation of the different modes that make up the total wavefield.

In addition figure 2.4 shows that the central vortex mode of a planewave with a Gaussian

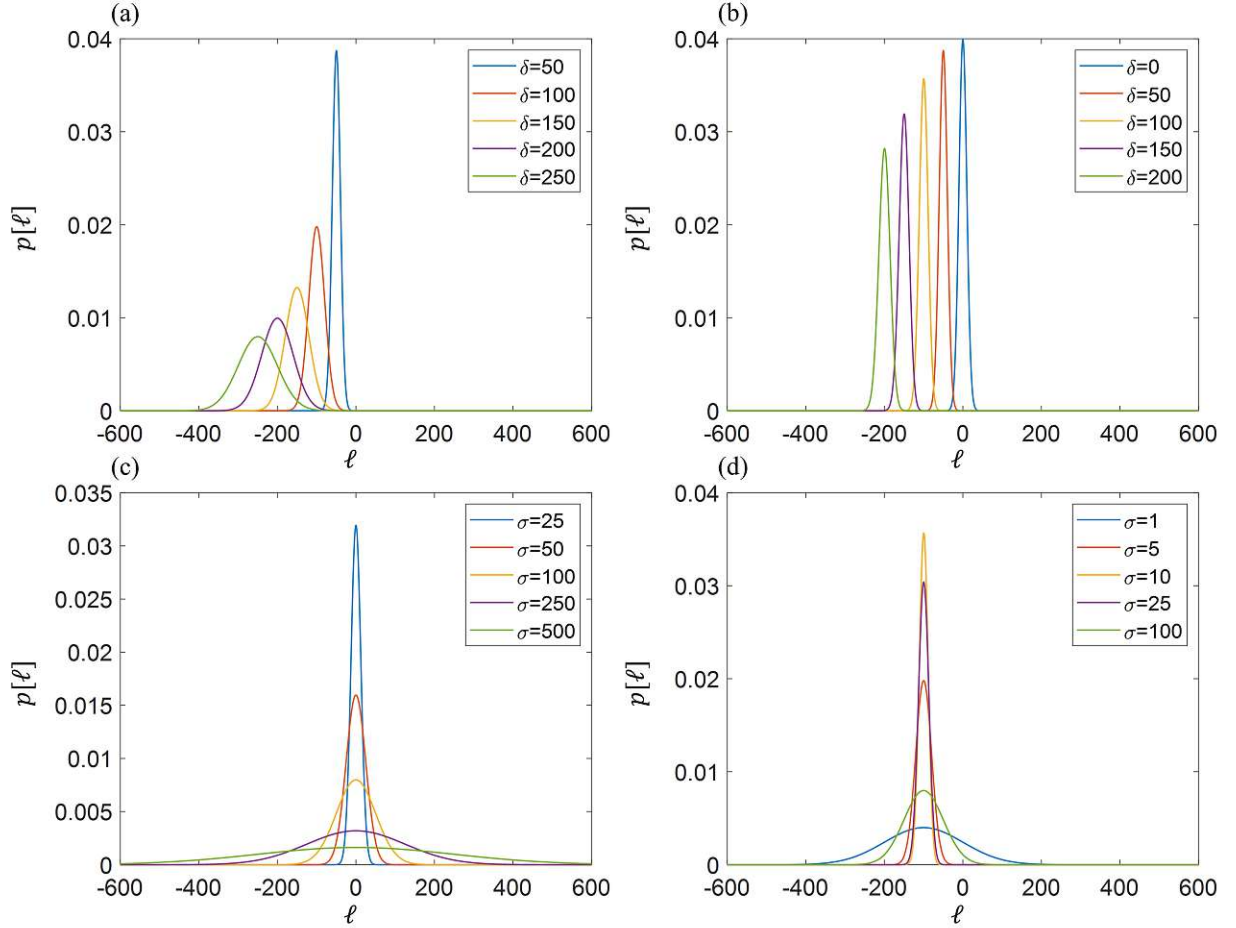


Figure 2.4: OAM distribution function of a planewave with a Gaussian envelope according to equation 2.80 for various different coherence lengths, σ and offsets from the cylinder axis δ . In insets (a) and (b) the coherence length is fixed to 5 and 20 respectively, while in (c) and (d) δ has been fixed to 0 and 100 respectively. The momentum k_y is -1 in all cases.

envelope has a mode number equal to the OAM expectation value of the wave. In fact we will now qualitatively show that this Gaussian planewave can also be seen as a part of the vortex state. In figure 2.5 the real part of the Gaussian planewave (eq. 2.69) and

2 General Theory

its dominant cylinder mode (eq. 2.78) are compared for two different momenta $k_y = 2$ and $k_y = 4$. One can see that the Gaussian planewave makes up a fragment of the

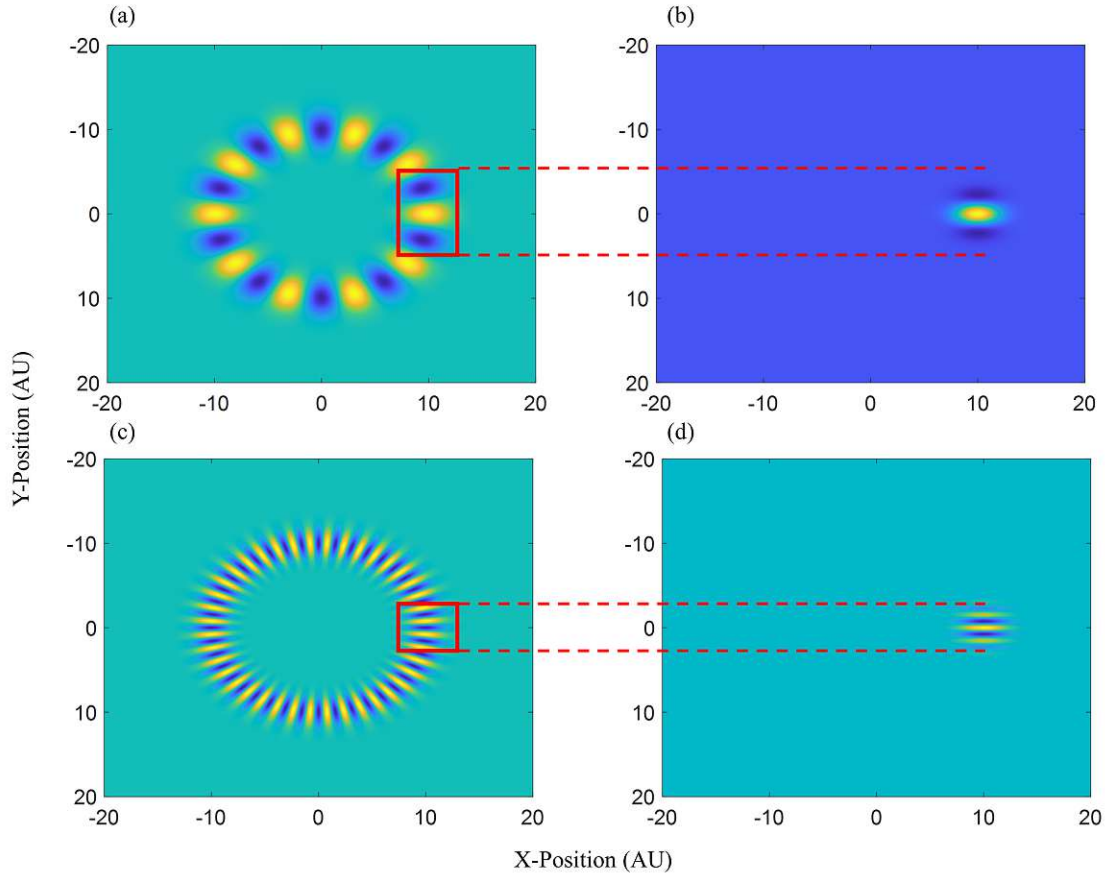


Figure 2.5: Comparison between the real part of a vortex state with $\ell = 20$ (a) and a planewave with Gaussian envelope and a momentum $k_y = 2$ (b). In addition a vortex state with $\ell = 40$ (c) is compared to a Gaussian planewave with $k_y = 4$ (d). The planewaves are calculated using equation 2.69, while the cylinder waves are determined using 2.78. The coherence length is chosen to be $\sigma = 2$ and the offset from the cylinder axis is $\delta = 10$

vortex wave. In fact one can imagine that one could construct the entire vortex ring using a superposition of such planewaves. This should come as no surprise given our knowledge on Fourier analysis. It will be the basic principle behind producing vortex states using the coherent averaging method. This demonstrates that the claims that extrinsic (transverse) OAM has nothing to do with wave structure and is therefore not quantum are therefore false. We have seen that it is simply a matter of perspective. Extrinsic OAM can just as well be seen as a type of wave structure. In addition these states can be seen as a superposition of many vortex states, each with its own quantized OAM.

A particularly useful Gaussian planewave superposition to look at and construct is a

pair of wavepackets propagating on opposite sides of the cylinder with some phase shift β between them

$$\psi_{t,2} = \frac{A}{\sqrt{2}} \left(e^{i\beta/2} e^{-\frac{(x-\delta)^2 - y^2}{\sigma^2}} + e^{-i\beta/2} e^{-\frac{(x+\delta)^2 - y^2}{\sigma^2}} \right) e^{ik_y y} \quad (2.81)$$

Analogous to the analysis from before the azimuthal Fourier transform of this wavefunction is

$$\psi_{t,2}^\ell(r) = \sqrt{2} A e^{-\frac{r^2 + \delta^2}{\sigma^2}} J_\ell(k' r) \cos(\ell\alpha + \beta/2) \quad (2.82)$$

and therefore the OAM distribution function is given by

$$p[\ell] = \frac{A^2 \sigma^2}{2} e^{-\frac{\sigma^2 k'^2}{4} - \frac{2\delta^2}{\sigma^2}} I_\ell\left(\frac{\sigma^2 |k'|^2}{4}\right) |\cos|^2(\ell\alpha + \beta/2) \quad (2.83)$$

This OAM distribution function is shown in figure 2.6, for $\beta = 0$, $\beta = \pi$ and various values of σ . The OAM of this particular wavefunction is intrinsic, albeit zero on average,

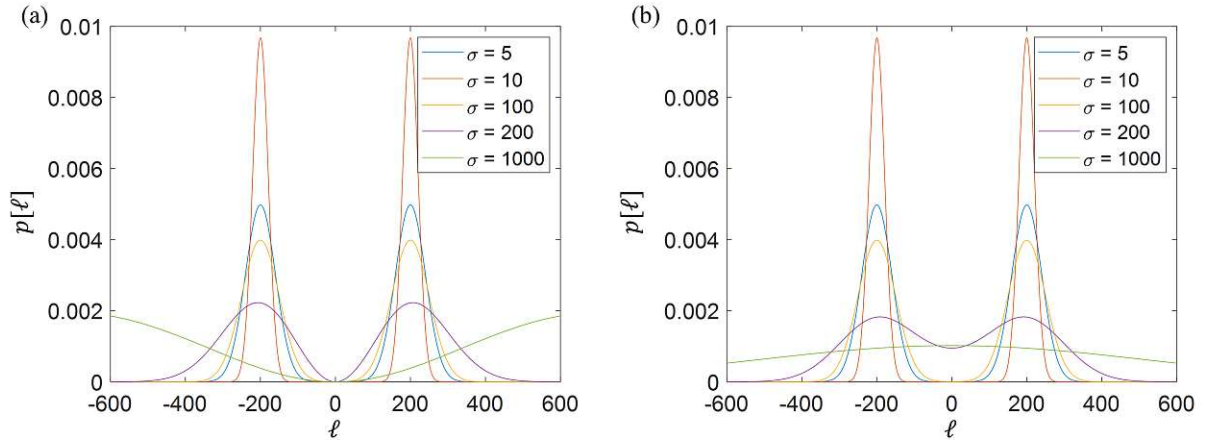


Figure 2.6: OAM distribution function for a superposition of two Gaussian planewaves propagating on opposite in the same direction on opposite sides of the cylinder axis (eq. 2.83), for various coherence lengths σ . δ is fixed to 100 and $k_y = 1$. In inset (a) there is a phase shift of $\beta = \pi$ between the two wavepackets while in (b) the phase shift is zero.

$\langle \hat{L}_z \rangle = 0$. However, as seen in the figure, when $\delta > \sigma$ equation 2.83 always exhibits a double peak structure ($\ell = \pm k_y \delta$), which remain equidistant for all translations of the frame of reference. So the OAM difference is always $\Delta\ell = 2k_y \delta$, regardless of the observer. Hence such a wavefunction can be useful for experiments that probe large amounts of OAM. The double peak structure remains for all σ in case $\beta = \pi$, however when σ is much larger than δ , the peaks move to larger $|\ell|$. Due to the \sin^2 function, when $\beta = \pi$, the $\ell = 0$ mode is always eliminated for all combinations of k_y , σ and δ .

Finally we will explore the longitudinal case, i.e. the special case where $k_y = 0$. k_z can take on any value as it doesn't affect \hat{L}_z . Figure 2.7, shows the OAM distribution

2 General Theory

function 2.83 for $k_y = 0$, in the cases $\beta = 0$ and $\beta = \pi$, for various coherence lengths. One can see that for $\beta = 0$ and short coherence lengths compared to the separation

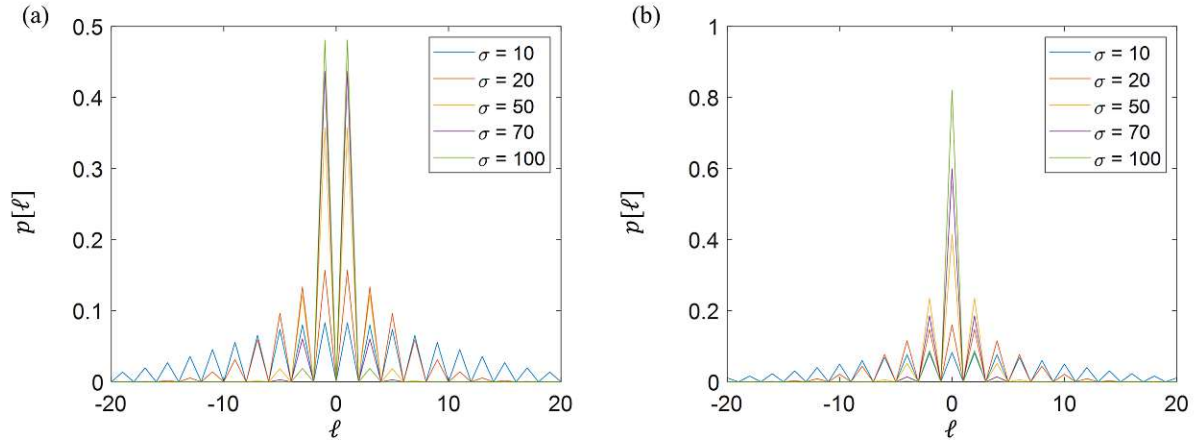


Figure 2.7: OAM distribution function eq. 2.83, in the special case where $k_y = 0$, $\delta = 100$ (a) $\beta = 0$ and (b) $\beta = \pi$ for various coherence lengths σ . Since $k_y = 0$ the OAM is longitudinal as long as k_z is not also zero. For both β the OAM amplitude is non-zero only for every other mode, as derived in the previous section where it was shown that $k_x = k_y = 0$ implies that no neighboring modes are present. In (a) only odd modes contribute, while in (b) only even modes make up the wavefunction.

parameter δ , many modes contribute to the wavefunction, while as the coherence length increases the number of modes decrease. The state becomes purer. We note that all non-zero modes have an even mode number. As was shown in the previous section neighboring modes are not allowed since this would imply transverse propagation. In the case of $\beta = \pi$ only odd modes contribute to the wavefunction.

A particularly interesting wavefunction which will find much use later on is found in the case $\beta = \pi$ and $\delta < \sigma$, such a wavefunction may be approximated by an equal superposition of $\ell = 1$ and $\ell = -1$. In other words a superposition of a right and left twisting state. Analogous to polarization optics, this can be seen as the OAM equivalent of a linearly polarized state, which is quite distinct from the $\ell = 0$ state, despite having the same OAM expectation value. The principle behind such linear OAM state is shown in the figure 2.8 Here a left rotating state is subtracted from a right rotating state to produce a linearly polarized (sine oscillation) state. Such a linearly polarized state can be approximated by a superposition of two Gaussian wavepackets with opposite amplitudes on opposite sides of the cylinder axis (eq. 2.81). If σ is chosen much larger than δ , figure 2.7 and equation 2.83 demonstrate that this very closely approximates a linearly polarized OAM state with $|\ell| = 1$. As will be shown later, such states are remarkably simple to produce using existing neutron optics and are therefore a good starting point to study OAM dependent interactions.

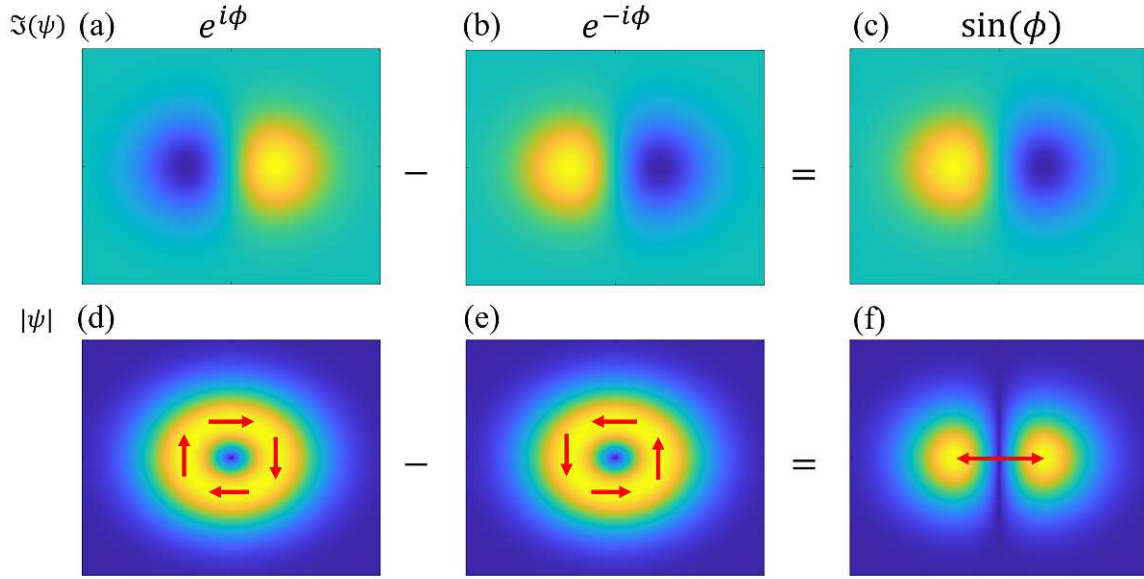


Figure 2.8: Illustration of the construction of a linearly polarized OAM state. A clockwise rotating state (a)/(d) has a counter clockwise rotating state (b)/(e) subtracted from it, producing a linearly polarized state (c)/(f). The top insets (a)-(c), show the imaginary parts of the respective transverse wavefunction, while the bottom insets (d)-(f) show the absolute values, which is directly related to the expected intensity pattern.

We have shown that transverse and longitudinal OAM can both have extrinsic and intrinsic components. Moreover, it has been demonstrated that while extrinsic transverse OAM mimics classical angular momentum it can still be seen as related to wave structure and is "built" using quantum states, since in fact all wavefunctions can be described using superpositions of quantum vortex states. Finally we introduced a few useful wavefunctions which to an extent exhibit tuneable OAM. In addition in this chapter we explored the basic properties of the OAM operator and its close relatives. It was shown that the Eigenfunctions of the OAM operator are also Eigenfunctions of the Schroedinger equation in free space. The Fourier transform and its properties in cylindrical coordinates were explored. This led us to define the very useful OAM distribution function 2.32. Finally we found that in some cases the OAM expectation value is invariant under spatial translations. In these cases we speak about intrinsic OAM. However it was also argued that this is not a necessary condition for the "quantumness" of OAM. After this general introduction to OAM we will now move on to the OAM generation and detection methods that were explored, during this project.

3 Electric Fields as OAM Generators

This chapter describes the interaction between neutrons and external static electric fields, known as the Schwinger interaction [57]. In particular we will find that this coupling produces spin flips in the neutron, while also preserving the total angular momentum of the neutron, thereby generating OAM [58, 35]. We will find that the electric field strength required to generate large amplitudes of longitudinal OAM states is prohibitively large. As a result we will dive into the theory of dynamical diffraction [59, 60, 61], which describes the propagation of waves in periodic potentials such as in perfect crystals. In particular we will look into integrating the electric potential produced by the positively charged nuclei into the formalism of dynamical diffraction [62]. This is because in non-centrosymmetric crystals the nuclear electric field, which is several orders of magnitude larger than that which can be produced in the lab, can be exploited, leading to easily measurable changes in neutron spin and even spin flips [63, 64, 65]. We will demonstrate that previous experiments with perfect quartz, which predate the concept of neutron vortex states, produced linear OAM states, defined in the last chapter as an equal superposition of $\ell = 1$ and $\ell = -1$ [66, 36]. Finally we report on our own measurement carried out at a test beamline of the reactor institute of the Technical University Delft, looking at OAM generation in Bragg and Laue diffraction from perfect crystal quartz.

3.1 Neutrons in Electric Fields

Despite being electrically neutral, the magnetic moment of a moving neutron can still couple to an external electric field. This is due to the relativistic relationship between electric and magnetic fields. An observer moving through a lab frame, with static charges producing electric fields, will see moving charges (i.e. currents) producing magnetic fields [67]. If the observer is moving much slower than the speed of light $v \ll c$, the magnetic field seen by the observer \mathbf{B}' can be expressed in terms of the electric field in the lab frame \mathbf{E} as follows

$$\mathbf{B}' = \frac{\mathbf{v} \times \mathbf{E}}{c^2} \quad (3.1)$$

Hence neutrons which possess a magnetic moment $\hat{\mu}$ experience a potential equal to

$$\hat{V} = -\frac{\hat{\mu} \cdot (\hat{\mathbf{p}} \times \mathbf{E})}{mc^2} \quad (3.2)$$

3 Electric Fields as OAM Generators

conversely in the lab frame a moving magnetic dipole appears to exhibit an electric dipole moment

$$\hat{\mathbf{d}}' = \frac{\mathbf{v} \times \hat{\boldsymbol{\mu}}}{c^2} \quad (3.3)$$

which leads to the exact same potential in the lab frame as in the moving frame of the neutron (eq. 3.2). Using this potential we can write down the Schroedinger equation

$$\left(-\frac{\hbar^2}{2m}\nabla^2 - \frac{\hbar\gamma}{2mc^2}\hat{\sigma} \cdot (\hat{\mathbf{p}} \times \mathbf{E})\right)\psi = E\psi \quad (3.4)$$

we have used that $\mu = \frac{\hbar\gamma}{2}\sigma$, with γ the gyromagnetic ratio of the neutron and $\hat{\sigma}$ the Pauli spin matrices. We will simplify our analysis by setting $\hbar = 1$ and assuming a static electric field $\mathbf{E} = E_z\hat{z}$. Then we can rewrite the differential equation as

$$\left(-\nabla^2 - \frac{\gamma E_z}{c^2}\hat{\sigma} \cdot (\hat{\mathbf{p}} \times \hat{z})\right)\psi = \epsilon\psi \quad (3.5)$$

with $\epsilon = 2mE$. We will now follow the solution given in [35].

We start by explicitly writing out the dot and cross products in the above differential equation. This leads to

$$-\nabla^2\hat{\psi}_{\pm} + iC\left(\frac{\partial}{\partial y} \pm i\frac{\partial}{\partial x}\right)\psi_{\mp} = \epsilon\psi_{\pm} \quad (3.6)$$

Here the wavefunction ψ is described by a two dimensional spinor $\psi = \begin{pmatrix} \psi_+(x, y, z) \\ \psi_-(x, y, z) \end{pmatrix}$, where the basis has been chosen such that the index \pm refers to the spin state parallel or anti-parallel to the z-axis respectively. The coupling constant C is given by $C = \gamma E_z/c^2$. Next the Fourier transform in the $x - y$ plane is taken which reduces the coupled second order partial differential equation to an ordinary coupled differential equation

$$-\left(\frac{\partial^2}{\partial z^2} - k_x^2 - k_y^2\right)\hat{\psi}_{\pm} + iC(ik_y \mp k_x)\hat{\psi}_{\mp} = \epsilon\hat{\psi}_{\pm} \quad (3.7)$$

which when transformed to cylindrical coordinates becomes

$$-\left(\frac{\partial^2}{\partial z^2} - k_r^2\right)\hat{\psi}_{\pm} \mp iCk_r e^{\mp i\theta}\hat{\psi}_{\mp} = \epsilon\hat{\psi}_{\pm} \quad (3.8)$$

At this point we note that in reciprocal cylindrical coordinates the potential term of the Schroedinger equation appears to contain the OAM raising and lowering operator $e^{\pm i\theta}$ (eq. 2.10). In this way the reciprocal space potential offered by a static electric field mimics that of a quadrupole in real space [30].

We can diagonalize equation 3.8, by transforming the wavefunction spinor $\hat{\psi} = T\hat{\psi}'$ and multiplying eq. 3.8 by T^{-1} from the left.

$$\left[-\left(\frac{\partial^2}{\partial z^2} - k_r^2 + \epsilon\right) \mp Ck_r\right]\hat{\psi}'_{\pm} = 0 \quad (3.9)$$

For this particular diagonalization T is given by $\begin{pmatrix} ie^{-i\theta} & -ie^{-i\theta} \\ 1 & 1 \end{pmatrix}$. The general solution to Eq. 3.9 is simply a superposition of a forward and backward propagating plane wave for each spin state

$$\hat{\psi}' = \begin{pmatrix} \hat{t}_1 e^{ik_+z} + \hat{t}_2 e^{-ik_+z} \\ \hat{t}_3 e^{ik_-z} + \hat{t}_4 e^{-ik_-z} \end{pmatrix} \quad (3.10)$$

with $k_{\pm} = \sqrt{\epsilon - k_r^2 \pm Ck_r}$. The amplitudes can be deduced from the boundary conditions. If we assume that the spatial extent of the electric field is semi infinite i.e. constant on the domain $0 < z < \infty$, we can set the amplitudes of the backward propagating waves, \hat{t}_1 and \hat{t}_3 , to zero. The general solution of the untransformed wavefunction $\hat{\psi}$ is simply found by applying the transformation $T\hat{\psi}'$.

$$\hat{\psi} = \begin{pmatrix} ie^{-i\theta} [\hat{t}_2 e^{-ik_+z} - \hat{t}_4 e^{-ik_-z}] \\ \hat{t}_2 e^{-ik_+z} + \hat{t}_4 e^{-ik_-z} \end{pmatrix}; z > 0 \quad (3.11)$$

To solve for the values of \hat{t}_2 and \hat{t}_4 we must specify the incident wavefunction impinging on the electric field boundary. For this we use a planewave of arbitrary amplitude, such that later we can produce any type of wavefunction using as superposition of our solutions. Hence in real space the incident wavefunction is given by

$$\psi_{\pm}^I = f_{\pm}(r, \phi) e^{-ik_z z}; z < 0 \quad (3.12)$$

and therefore in reciprocal space we can write

$$\hat{\psi}_{\pm}^I = \hat{f}_{\pm}(k_r, \theta) e^{-ik_z z}; z < 0 \quad (3.13)$$

using these we may express the boundary conditions used to solve for \hat{t}_2 and \hat{t}_4

$$\begin{aligned} \hat{\psi}_{\pm}(k_r, \theta, z = 0) &= \hat{f}_{\pm} + \hat{r}_{\pm} \\ \hat{\psi}_{\pm,z}(k_r, \theta, z = 0) &= ik_z(\hat{r}_{\pm} - \hat{f}_{\pm}) \end{aligned} \quad (3.14)$$

The subscript z here denotes the first partial derivative in z , while \hat{r}_{\pm} denotes the transverse wavefunction amplitude of the wave reflected at the boundary:

$$\psi_{\pm}^R = r_{\pm}(r, \phi) e^{ik_z z}; z < 0 \quad (3.15)$$

To determine the transmitted and reflected amplitudes we rewrite the boundary value problem as a simple linear algebra problem

$$\begin{pmatrix} 1 & -1 & 1 & 0 \\ 1 & 1 & 0 & -1 \\ k_+ & -k_- & -k_z & 0 \\ k_+ & k_- & 0 & k_z \end{pmatrix} \begin{pmatrix} \hat{t}_2 \\ \hat{t}_4 \\ i\hat{r}_+ e^{i\theta} \\ \hat{r}_- \end{pmatrix} = \begin{pmatrix} -i\hat{f}_+ e^{i\theta} \\ \hat{f}_- \\ -ik_z \hat{f}_+ e^{i\theta} \\ k_z \hat{f}_- \end{pmatrix} \quad (3.16)$$

By inverting the matrix we can find the transmission and reflection amplitudes

$$\begin{aligned}\hat{t}_{(2)} &= \frac{\mp ik_z \hat{f}_+ e^{i\theta} + k_z \hat{f}_-}{(k_z + k_{\pm})} \\ \hat{r}_{\pm} &= \pm \frac{(k_z^2 - k_+ k_-) \hat{f}_{\pm} \mp ik_z (k_+ - k_-) e^{\mp i\theta} \hat{f}_{\mp}}{(k_+ + k_z)(k_- + k_z)}\end{aligned}\quad (3.17)$$

which leads us to the following solution for the transmitted waves

$$\hat{\psi}_{\pm} = \frac{k_z \hat{f}_{\pm} \pm ik_z \hat{f}_{\mp} e^{\mp i\theta}}{(k_z + k_+)} e^{-ik_+ z} + \frac{k_z \hat{f}_{\pm} \mp ik_z \hat{f}_{\mp} e^{\mp i\theta}}{(k_z + k_-)} e^{-ik_- z}\quad (3.18)$$

Here one can see that the spin flipped component of the wavefunction also has its OAM raised/lowered, confirming the assertion that the total angular momentum $\mathbf{J} = \mathbf{L} + \mathbf{S}$ of the neutron is conserved. In section 2.3.3 we demonstrated that this raising/lowering operation being carried out in reciprocal space increases/decreases the OAM expectation value in real space by one unit of \hbar , however it is not equivalent to applying the same raising/lowering operator in real space. So it is important to properly invert the two dimensional Fourier transform to obtain the real space wavefunction. Applying the conjugated version of eq. 2.26 to eq. 3.18 leads to

$$\psi_{\pm} = \sum_{\ell} i^{-\ell} k_z e^{i\ell\phi} \int_0^{\infty} \left[\frac{\hat{f}_{\pm}^{\ell} \pm i \hat{f}_{\mp}^{\ell\pm 1}}{(k_z + k_+)} e^{-ik_+ z} + \frac{\hat{f}_{\pm}^{\ell} \mp i \hat{f}_{\mp}^{\ell\pm 1}}{(k_z + k_-)} e^{-ik_- z} \right] J_{\ell}(k_r r) k_r dk_r \quad (3.19)$$

3.1.1 Longitudinal OAM Generation in Transmission Geometry

We begin by looking at a special case where the transmitted beam acquires OAM in the longitudinal direction. The simplest case to explore would be an incident wave described by a Bessel beam with definite OAM (i.e. $\hat{f}_{\pm} = b_{\pm} \delta(k_r - k_{\rho}) / k_r e^{i\ell\theta}$ with b_{\pm} a complex spinor describing the initial spin state and $\epsilon = k_z^2 + k_{\rho}^2$). In section 2.2 we showed that Bessel functions are Eigenfunctions of the Schroedinger equation, making them a sensible option to explore. We start by looking at the case where the incident Bessel beam carries no OAM. In this case the $\ell = 0$ and $|\ell| = 1$ components of the real space wavefunction in the electric field are given by

$$\begin{aligned}\psi_{\pm}^0 &= k_z b_{\pm} J_0(k_{\rho} r) \left(\frac{e^{-i\sqrt{k_z^2 + Ck_{\rho}} z}}{(k_z + \sqrt{k_z^2 + Ck_{\rho}})} + \frac{e^{-i\sqrt{k_z^2 - Ck_{\rho}} z}}{(k_z + \sqrt{k_z^2 - Ck_{\rho}})} \right) \\ \psi_{\pm}^1 &= \pm k_z b_{\mp} J_1(k_{\rho} r) \left(\frac{e^{-i\sqrt{k_z^2 + Ck_{\rho}} z}}{(k_z + \sqrt{k_z^2 + Ck_{\rho}})} - \frac{e^{-i\sqrt{k_z^2 - Ck_{\rho}} z}}{(k_z + \sqrt{k_z^2 - Ck_{\rho}})} \right)\end{aligned}\quad (3.20)$$

where ψ_{\pm}^0 and ψ_{\pm}^1 are the components without and with OAM respectively, such that $\psi_{\pm} = \psi_{\pm}^0 + e^{\mp i\phi} \psi_{\pm}^1$. For a collimated beam geometry we may use $k_{\rho} = k_z \tan(\alpha) \approx k_z \alpha$,

where α is the beam divergence. Furthermore if Ck_ρ is sufficiently small we may linearize the square root terms in equation 3.20 and obtain a much simpler expression for the transmitted wavefunction.

$$\psi_\pm = [b_\pm \cos(\frac{\gamma E_z \alpha}{2c^2} z) J_0(k_\rho r) \pm b_\mp \sin(\frac{\gamma E_z \alpha}{2c^2} z) e^{\mp i\phi} J_1(k_\rho r)] e^{-ik_z z} \quad (3.21)$$

Since in this case the OAM of each individual spin state can be described by a pure OAM state we can conclude that the OAM is intrinsic as shown in section 2.4. From this expression one can deduce that the beam enters a fully "twisted" state (i.e. $\ell = \pm 1$) once the voltage drop $V = E_z z$ experienced by the neutron is

$$V = \frac{\pi c^2}{\gamma \alpha} \quad (3.22)$$

Hence an electric longitudinal OAM generator could consist simply of a parallel plate capacitor, with the surfaces of the plates normal to the beam. As indicated by eq. 3.22 the efficiency of such a device would be wavelength independent, making it a broad-band OAM generator. The only free parameter is the beam divergence α . Realistically if the beam divergence is one degree this results in a required voltage drop of 88 GV, which cannot be produced in the lab.

The solution explored so far is valid for a single Bessel beam. However Bessel functions are not normalizable [68] and therefore have infinite coherence, making them unphysical. In a realistic setup the incident wave can always be expressed as a normalizable superposition of Bessel beams, which has finite coherence. This superposition interferes and results in damping of OAM production, due to dephasing. Using eq. 3.18 we can calculate the OAM distribution function (eq. 2.32) of the transmitted wave for any transverse momentum distribution $|\hat{f}_\pm|^2$ and extract the probability of finding the neutron in the $\ell = \pm 1$ state

$$A_\pm^{\mp 1} = 2\pi \int dr k_r |\hat{\psi}_\pm^{\mp 1}(k_r)|^2 \quad (3.23)$$

These probabilities are shown in figure 3.1 for the most common divergence profiles, assuming that the incident wave is polarized along the + direction (i.e. $b_+ = 1$ and $b_- = 0$) and carries no OAM. Here we see dephasing effects which cause the contrast of the oscillations to wash out as the wave penetrates deeper into the electric field. As the transverse wavelength spread is decreased the dephasing effects are also reduced. This is analogous to dephasing seen in magnetic spin echo instruments, due to the longitudinal wavelength spread [69]. Also in this case, where we consider incident waves that can be described as superpositions of Bessel beams in the $\ell = 0$ mode, the OAM can be considered intrinsic since once again if the incident wave is purely in the $\ell = 0$ state, then the spin flipped state will be purely in the $\ell = 1$ state, hence the OAM is pure and therefore intrinsic.

The voltage constraints, however, demonstrate that intrinsic longitudinal OAM states will not be produced using standard lab equipment. Hence we will continue to explore other geometries in which OAM could be generated using electric fields.

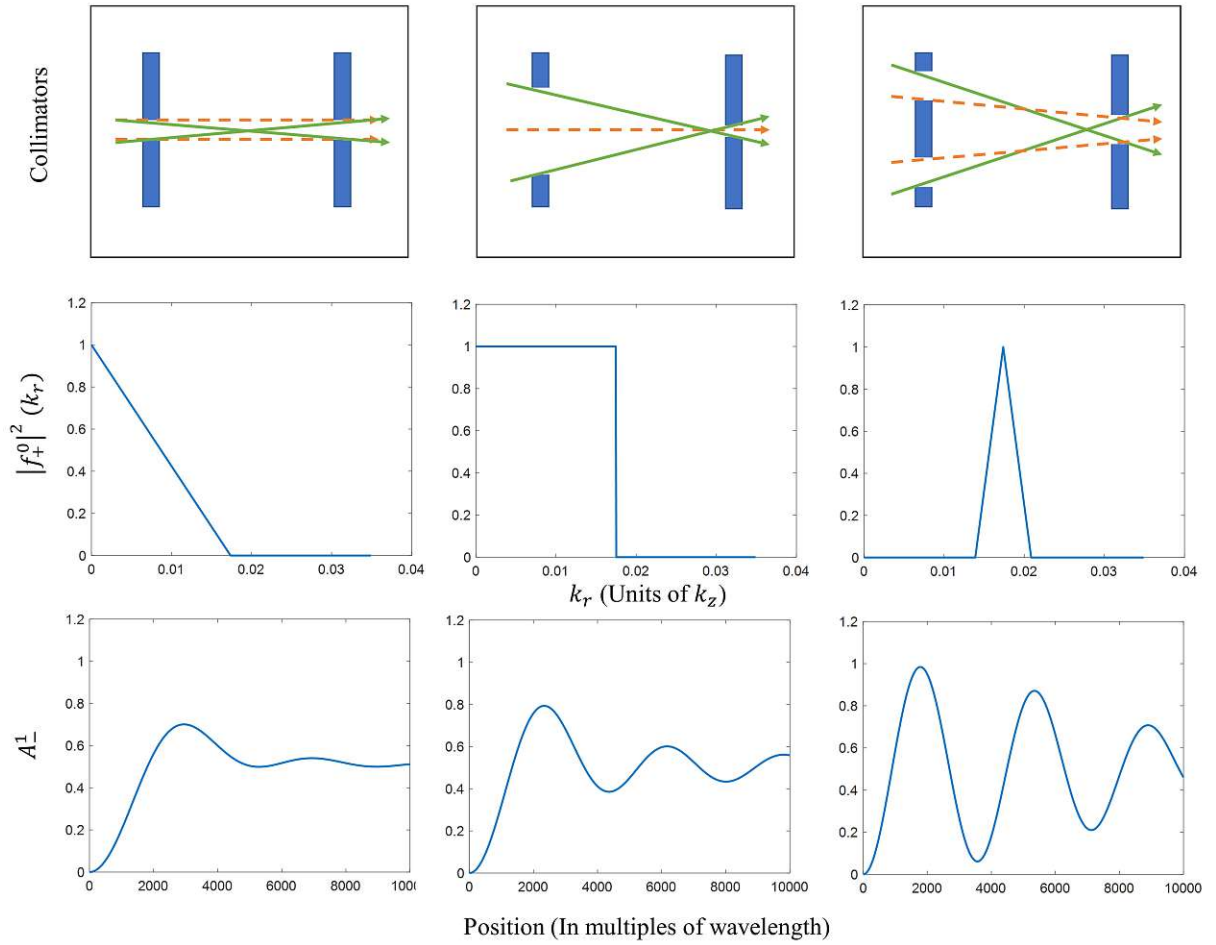


Figure 3.1: For various common collimator types such as two identical pinholes (left), a large exit and a comparatively small pinhole (middle) and an annulus with pinhole (right), we show the possible beam paths through a hypothetical instrument (top) and the respective divergence profiles (middle). The paths with the lowest divergence are drawn as dashed orange arrows, while the maximum divergence paths are shown in solid green. The divergence profiles are used as $|f_+^{01}|^2(k_r)$ in equation 3.23 to determine the probability of finding the particle in the $l = 1$ OAM state as a function of the z position in an electric field (bottom). The parameters are chosen such that $k_z = 1$, $\epsilon \approx k_z^2$ and $C = 0.1$. We note that that in a real instrument these divergence profiles might represent the incoherent average of all possible incident wavefields and not the actual transverse incident wavefield of a single neutron.

3.1.2 OAM Generation in Reflection Geometry

Next we consider waves interacting with an electric field interface at grazing incident angles. This results in a more pronounced coupling, due to a larger k_r and a smaller value for k_z . The OAM carried by the transmitted and reflected waves in this case is quasi-transverse to the wavevector \vec{k} . Since the quantization axis of the OAM is normal to interface, parallel to the electric field, the incident wave must be described by an infinite superposition of OAM modes. Nonetheless the mean OAM of the transmitted and reflected waves can be raised or lowered by one unit of \hbar with respect to the incident OAM. The reflection probability $|R_{\pm}|^2$ can be calculated using eq. 3.17

$$|R_{\pm}|^2 = \int dk_y dk_x |r_{\pm}|^2 \quad (3.24)$$

This reflectivity, normalized to the total flux (Reflection + Transmission) is shown as a function of incident angle in Fig. 3.2 for an electric field of $10^{10}V/m$ (found in electric double layers [70, 71]), a neutron wavelength of 2 \AA and an initial spin aligned along the $-z$ direction. As demonstrated previously OAM generation occurs in the flipped spin

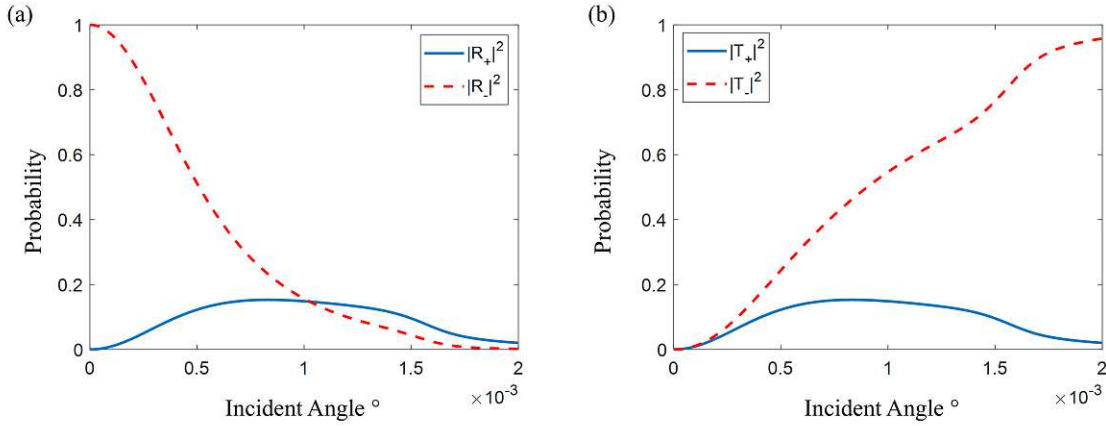


Figure 3.2: Reflection (a) and transmission probabilities according to equation 3.24 assuming $\hat{f}_+ = 0$ and $\hat{f}_- = 1$. A wavelength of 2 \AA and an electric field of $10^{10}V/m$ are assumed. The blue solid curve corresponds to a spin flip reflection/transmission which generates OAM, while the red dashed curve shows the non spin flip reflection/transmission probability.

state ($+z$) to conserve the total angular momentum of the neutron. From the figure, we can deduce the maximal reflectivity of the spin flipped state occurs between 0.0005 and 0.0015 degrees incident angle. Though at these angles there is still a strong mixing with the non-spin flip state $|R_-|^2$ which does not carry OAM. This can be filtered out either by spin filtering or by choosing a higher angle of reflection. The combination of the relatively low spin flip probability and the small angular acceptance, likely make this OAM generation technique unfeasible.

3.1.3 Transverse OAM Generation in Transmission Geometry

In this subsection we explore in more detail transverse OAM generation in a transmission geometry. In this geometry the flux limitation encountered in the last subsections can be overcome. We consider transmission through a transversely polarized electric field which leads to the generation of transverse spin-OAM coupled states. To demonstrate this we consider the time dependent Schroedinger equation for a neutral spin 1/2 particle in an electric field

$$[-\nabla^2 - \frac{\gamma}{c^2} \vec{\sigma} \cdot (\vec{p} \times \vec{E})] \psi = -i \frac{\partial}{\partial t} \psi \quad (3.25)$$

Again we will assume that the electric field is polarized along the z-direction. However this time we will consider a field which extends infinitely in space. To reduce the problem to an ordinary differential equation we apply an unbounded Fourier transform to the spatial coordinates. In cylindrical coordinates this leads to

$$\epsilon \hat{\psi}_{\pm} \mp i C k_r e^{\mp i \theta} \hat{\psi}_{\mp} = -i \frac{\partial}{\partial t} \hat{\psi}_{\pm} \quad (3.26)$$

ϵ now denotes the kinetic energy parameter $k_r^2 + k_z^2$. Once again we diagonalize this set of equations using the transform $\hat{\psi} = T \hat{\psi}'$

$$[\epsilon \mp C k_r] \hat{\psi}'_{\pm} = -i \frac{\partial}{\partial t} \hat{\psi}'_{\pm} \quad (3.27)$$

Applying the initial conditions $\hat{\psi}_{\pm}(t=0) = \hat{a}_{\pm}(k_r, \theta, k_z)$ we can determine the homogeneous solution of equation 3.26.

$$\hat{\psi}_{\pm} = e^{i \epsilon t} [\hat{a}_{\pm} \cos(C k_r t) \pm \hat{a}_{\mp} \sin(C k_r t) e^{\mp i \theta}] \quad (3.28)$$

which appears almost equivalent to equation 3.21. If the wave propagates along the y-direction the value of k_r , which may be approximated by k_y is a factor $10^2 - 10^3$ larger than in the longitudinal case (equation 3.21). Hence the required electric field integral to raise or lower the mean OAM is reduced to a more practical level. The incident wave in this case must be described by an infinite superposition of transverse OAM modes. Upon being transmitted through an ideal beam twister device the mean ℓ value of this superposition will be raised or lowered by one. Here we will assume that \hat{a}_{\pm} can be approximated by a Gaussian. The standard deviation in k_x direction is expressed as σ_x , while the standard deviation in k_y is σ_y . The reciprocal space amplitudes can then be written as

$$\hat{a}_{\pm} = e^{-\frac{(k_y - k'_y)^2}{\sigma_y^2}} e^{-\frac{k_x^2}{\sigma_x^2}} \quad (3.29)$$

, with k'_y , the mean momentum in the y-direction. In Fig. 3.3 we show one such Gaussian wavepacket multiplied by the OAM raising operator transformed to real space. The wavepacket with transverse OAM appears to be displaced along the transverse axis, while along the longitudinal axis the wavepacket is shifted by $\pi/2$. From fig. 3.3 it is clear that the transverse OAM generated by the Schwinger interaction is extrinsic,

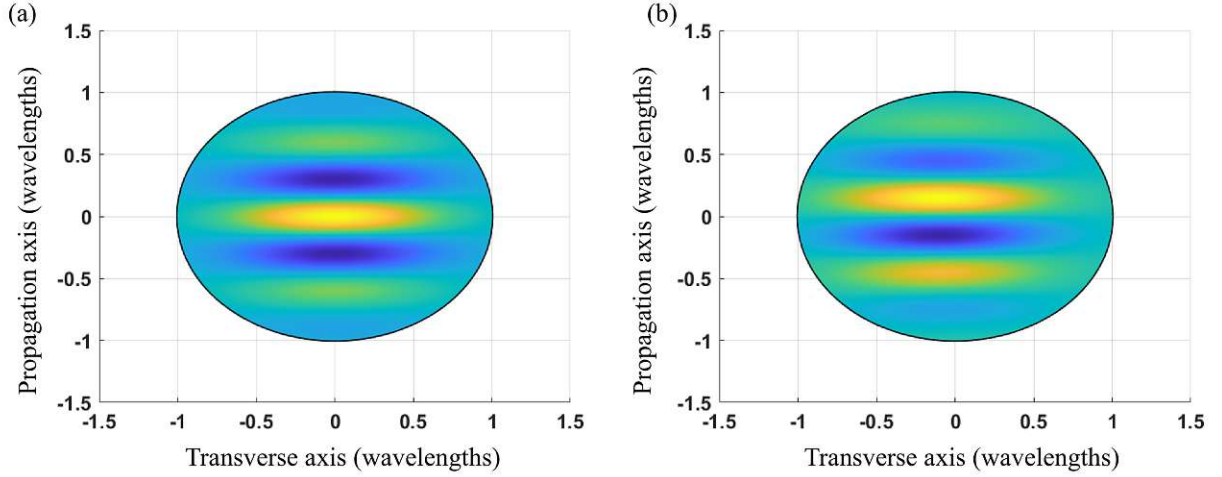


Figure 3.3: Surface plots of the real parts of Gaussian wavepackets in real space, with $k'_y = 1$ and $\sigma_x^2 = \sigma_y^2 = 0.1$ carrying (a) no orbital angular momentum and (b) one unit of transverse orbital angular momentum.

since it can be understood simply as a displacement of the wavepacket. To be precise the displacement is such that one unit of OAM is generated i.e. $p\Delta x = \pm\hbar$. Intrinsic transverse OAM can be produced if the electric field is co-moved with the neutron. In this case k'_y goes to zero in the frame of the applied field:

$$\hat{a}'_{\pm} = e^{-\frac{k_y \cdot 2}{\sigma_y^2}} e^{-\frac{k_x^2}{\sigma_x^2}} \quad (3.30)$$

and the raising/lowering operator is applied to this amplitude. After the field induces a π flip the reciprocal wavefunction can then be described in the lab frame as

$$\hat{\psi}_{\pm} = \pm \hat{a}'_{\mp} e^{\mp i\theta} e^{i\epsilon t} * \delta(k_y - k'_y) \quad (3.31)$$

and hence the real space wavefunction is simply

$$\psi_{\pm} = \pm e^{i\epsilon t} \int dk_x dk_y \hat{a}'_{\mp} e^{\mp i\theta} e^{ik_x x} e^{i(k_y - k'_y)y} \quad (3.32)$$

The convolution with the delta function has been taken into the kernel of Fourier transform. An example real space wavefunction with raised OAM, assuming a Gaussian reciprocal amplitude \hat{a}'_{\pm} , is shown in figure 3.4 (b). In this case the transverse OAM is intrinsic and mimics the characteristic forked structure we saw previously in figure 2.3 (section 2.5). The main problem with this approach of using a co-moving electric field to produce intrinsic transverse OAM, is that in this case the electric field cannot couple to a large momentum k'_y but must, like in the longitudinal case, couple to the momentum spread in x and y direction. This means that the coupling strength is reduced to a level comparable to the longitudinal case. The only advantage that remains in the transverse case is that a relatively low voltage, which can correspond to a large electric field, can be

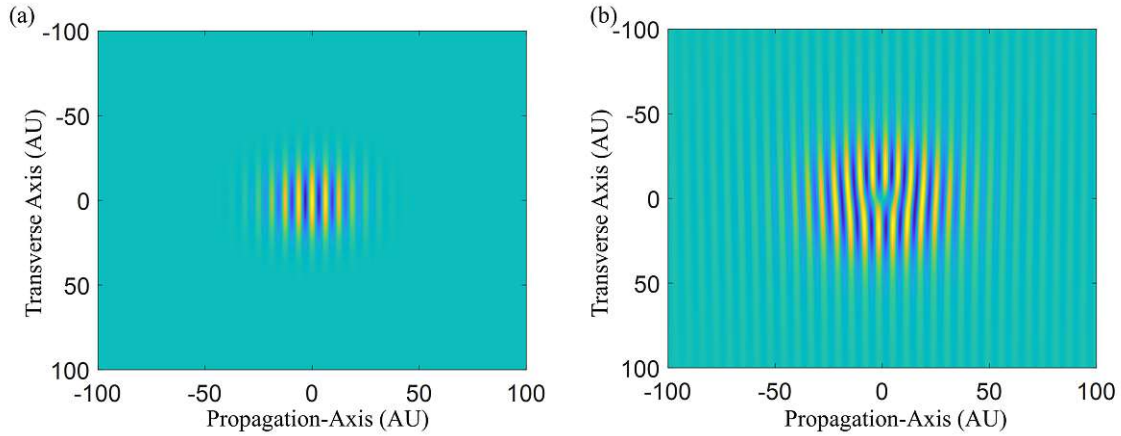


Figure 3.4: Real parts of (a) a Gaussian wavepacket without OAM according to the Fourier transform of the reciprocal wavefunction eq. 3.29, compared to (b) the same reciprocal wavefunction with raised OAM, produced using a co-moving electric field. The wavefunction is calculate using 3.32. In both cases $k'_y = 1$ and $\sigma_x = \sigma_y = 0.1$

applied over a larger distance, leading to a higher field integral. Even then, however, it is technically impossible to produce a field integral with a co-moving source corresponding to the required 10 – 100 GV. Instead we need to find a method which either amplifies the electric field, the transverse momentum spread and/or slows down the neutron. In the next section we explore dynamical diffraction, where all of these conditions can be fulfilled. For now the most important take-away from this section on OAM generation in electric fields is that the Schwinger interaction generates OAM in the spin flipped state by angular momentum conservation.

3.2 Theory of Dynamical Diffraction

The theory of dynamical diffraction describes interactions with perfectly periodic potentials, such as those found in perfect crystals [59, 60, 61]. This description is necessary to make accurate predictions of wave propagation if a momentum component of the particle matches the lattice spacing. As a result, dynamical diffraction has been an indispensable tool for describing neutron and x-ray perfect crystal interferometers [72, 73, 74]. Our interest derives from the large electric fields present in crystals. In particular the electric field between a nucleus and the electron shell. The electromagnetic potential seen by a bound Hydrogen electron is -13.6 eV, while the diameter of the electron shell is about 1\AA . As a result the electric field between the nucleus and the electron corresponds to $\propto 10^{11} \text{ V} \cdot \text{m}^{-1}$. If this nuclear field can be exploited it would easily be sufficient to produce a highly efficient "beam twister" as shown in the previous section. In most crystals the average electric field seen by neutrons is zero, due to symmetry. However, in crys-

tals which lack a center of symmetry (non-centrosymmetric crystals) this is no longer the case and neutrons see a net non-zero field which can be exploited. Furthermore, we will see that according to the theory of dynamical diffraction, neutrons diffracted from a perfect crystal in Laue geometry slow down as they propagate through the crystal [75]. The most extreme case occurs at a Bragg angle of 90 degrees, where the particle completely stops propagating in the crystal. Thus by choosing a Bragg angle close to 90 degrees we can produce large amplitudes of the $\ell = \pm 1$ state as it exploits both the large electric field present in the crystal and the long interaction time that follows from the low propagation velocity.

In the following subsections we will begin by introducing a bare bones version of the dynamical theory of diffraction, following mostly [72], sufficient for calculating reflected and transmitted wavefunctions in Laue and Bragg geometry. Then following [61] and [62] we will add the Schwinger potential and spin to the formalism. Finally using our model we will explicitly calculate the wavefunctions produced from diffraction from perfect quartz in reflection and transmission in both Bragg and Laue geometry and determine the OAM carried by these wavefunctions.

3.2.1 Basic Dynamical Diffraction

The simplest theory of diffraction, the kinematic theory, is quite accurate when it comes to determining diffraction angles and the derivation is quite didactic. It leads to the famous Bragg condition [76]

$$n\lambda_B = 2d \sin(\theta_B) \quad (3.33)$$

where d is the crystal lattice spacing and θ_B is the Bragg angle. However since the kinematic theory does not properly model multiple scattering from every atom within the lattice it fails to accurately describe more subtle effects. Examples include refraction and specular reflection due to the crystal potential and anomalous absorption effects, where an otherwise absorbing crystal becomes more transparent close to a Bragg angle in Laue geometry, since the wavefield can slip through the lattice planes without encountering any atoms [77, 78]. Furthermore the effect of the nuclear electric field which we wish to study cannot be properly accounted for. Hence we turn to the dynamical theory of diffraction, which properly describes these phenomena. We will for the first part just take into account nuclear scattering, mainly follow the approach described in [72].

We start by describing the strong nuclear interaction of thermal and cold neutrons with nuclei via the Fermi pseudo potential [79]

$$\hat{V} = \frac{2\pi\hbar^2 b}{m} \delta(\mathbf{r}) \quad (3.34)$$

Generally a complex number, b , is the coherent neutron scattering length. The real part represents coherent scattering, while the imaginary part can be understood as the

3 Electric Fields as OAM Generators

absorption part of the scattering length. In a macroscopic target the total potential one simply sums over all atoms

$$\hat{V} = \frac{2\pi\hbar^2}{m} \sum_j b_j \delta(\mathbf{r} - \mathbf{r}_j) \quad (3.35)$$

with \mathbf{r}_j the position of the j^{th} atom. If the target is a perfect crystal, that is the atoms are ordered in a periodic lattice, the position is separable $\mathbf{r}_j = \mathbf{R}_j + \mathbf{r}_i$, with \mathbf{R}_j the position of the j^{th} unit cell

$$\mathbf{R}_j = H\mathbf{a}_1 + K\mathbf{a}_2 + L\mathbf{a}_3 \quad (3.36)$$

with \mathbf{a}_n the basis vectors of the unit cell shown in figure 3.5 and H K and L integers. \mathbf{r}_i is the position of the i^{th} atom within the unit cell, which is the same for all unit cells. These vectors are all visualized in figure 3.5. Taking the Fourier transform of eq. 3.35 over the crystal volume, $\frac{1}{\mathcal{V}} \int_{\mathcal{V}} d\mathbf{r} V e^{-i\mathbf{k}\cdot\mathbf{r}}$, allows us to view the potential in momentum space

$$\hat{V} = \frac{2\pi\hbar^2}{m\mathcal{V}} \sum_j e^{-i\mathbf{k}\cdot\mathbf{R}_j} \sum_i b_i e^{-i\mathbf{k}\cdot\mathbf{r}_i} \quad (3.37)$$

with \mathcal{V} the total crystal volume, which can be expressed in terms of the lattice volume \mathcal{V}_l and the number of cells N_l : $\mathcal{V} = N_l\mathcal{V}_l$. In the case of a macroscopic crystal where we must sum over a very large number of cells, we note that the first summation in eq. 3.37 (known as the lattice factor) is only non zero if $\mathbf{k} \cdot \mathbf{R}_j$ is a multiple of 2π , this is by definition the case if \mathbf{k} is equal to the reciprocal lattice vector

$$\mathbf{G} = h\mathbf{g}_1 + k\mathbf{g}_2 + l\mathbf{g}_3 \quad (3.38)$$

with h , k and l integer, and \mathbf{g}_i are related to the basis/lattice vectors \mathbf{a}_i by

$$\mathbf{g}_1 = \frac{2\pi}{\mathcal{V}_l} \mathbf{a}_2 \times \mathbf{a}_3; \quad \mathbf{g}_2 = \frac{2\pi}{\mathcal{V}_l} \mathbf{a}_3 \times \mathbf{a}_1; \quad \mathbf{g}_3 = \frac{2\pi}{\mathcal{V}_l} \mathbf{a}_1 \times \mathbf{a}_2 \quad (3.39)$$

Using the fact that the lattice factor is zero for macroscopic crystals if $\mathbf{k} \neq \mathbf{G}$ we can rewrite the potential eq. 3.37

$$V = \frac{2\pi\hbar^2}{m\mathcal{V}_l} \sum_{\mathbf{G}} \delta(\mathbf{k} - \mathbf{G}) \sum_i b_i e^{-i\mathbf{k}\cdot\mathbf{r}_i} \quad (3.40)$$

We will now invert the Fourier transform

$$V(r) = \int d\mathbf{k} e^{i\mathbf{k}\cdot\mathbf{r}} \frac{2\pi\hbar^2}{m\mathcal{V}_l} \sum_{\mathbf{G}} \delta(\mathbf{k} - \mathbf{G}) \sum_i b_i e^{-i\mathbf{k}\cdot\mathbf{r}_i} = \sum_{\mathbf{G}} e^{i\mathbf{G}\cdot\mathbf{r}} \frac{2\pi\hbar^2}{m\mathcal{V}_l} F_{hkl} \quad (3.41)$$

Here we have defined the structure factor

$$F_{hkl} = \sum_i b_i e^{-i\mathbf{G}\cdot\mathbf{r}_i} \quad (3.42)$$

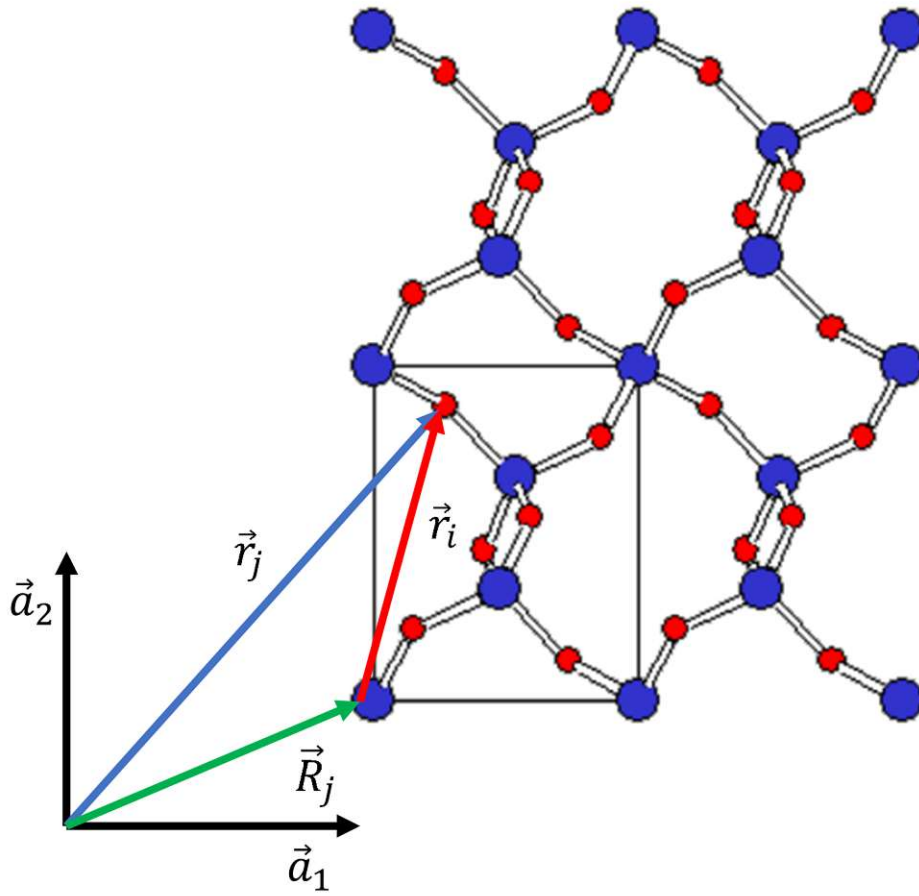


Figure 3.5: Schematic representation of the structure of a quartz crystal [80]. \mathbf{r}_j denotes the position of the j^{th} atom, which can be separated into $\mathbf{R}_j + \mathbf{r}_i$, with \mathbf{R}_j the position of the j^{th} unit cell (drawn as a black rectangle) and \mathbf{r}_i the position of the i^{th} atom in a cell. \mathbf{a}_1 and \mathbf{a}_2 are the basis vectors of the unit cell.

Finally defining the crystal or lattice potential

$$V(\mathbf{G}) = \frac{2\pi\hbar^2}{m\mathcal{V}_l} F_{hkl} \quad (3.43)$$

we can express the real space potential quite compactly

$$V(r) = \sum_{\mathbf{G}} e^{i\mathbf{G}\cdot\mathbf{r}} V(\mathbf{G}) \quad (3.44)$$

With the potential in this form we can begin to solve for the wavefunction. The Bloch Ansatz

$$\psi = e^{i\mathbf{k}\cdot\mathbf{r}} u(r) = e^{i\mathbf{k}\cdot\mathbf{r}} \sum_{\mathbf{G}} u(\mathbf{G}) e^{i\mathbf{G}\cdot\mathbf{r}} = \sum_{\mathbf{G}} u(\mathbf{G}) e^{i(\mathbf{G}+\mathbf{k})\cdot\mathbf{r}} \quad (3.45)$$

is an established approach to finding solutions to the Schroedinger equation with a periodic potential [81]. Before inserting our Ansatz into the Schroedinger equation it is

3 Electric Fields as OAM Generators

useful to simplify the expression $V(r)\psi$

$$V\psi = \sum_{\mathbf{G}''} e^{i\mathbf{G}'' \cdot \mathbf{r}} V(\mathbf{G}'') \sum_{\mathbf{G}'} u(\mathbf{G}') e^{i(\mathbf{G}'+\mathbf{k}) \cdot \mathbf{r}} = \sum_{\mathbf{G}\mathbf{G}'} V(\mathbf{G} - \mathbf{G}') u(\mathbf{G}') e^{i(\mathbf{k}+\mathbf{G}) \cdot \mathbf{r}} \quad (3.46)$$

where we have defined $G = G'' + G'$. Now we can insert our Ansatz into the Schroedinger equation to determine the amplitude terms $u(\mathbf{G})$

$$\sum_{\mathbf{G}} \frac{\hbar^2}{2m} (\mathbf{k}+\mathbf{G})^2 u(\mathbf{G}) e^{i(\mathbf{k}+\mathbf{G}) \cdot \mathbf{r}} + \sum_{\mathbf{G}\mathbf{G}'} V(\mathbf{G}-\mathbf{G}') u(\mathbf{G}') e^{i(\mathbf{k}+\mathbf{G}) \cdot \mathbf{r}} = E \sum_{\mathbf{G}} u(\mathbf{G}) e^{i(\mathbf{k}+\mathbf{G}) \cdot \mathbf{r}} \quad (3.47)$$

we then group the terms with the same summation index together

$$\sum_{\mathbf{G}} \left[\frac{\hbar^2}{2m} (\mathbf{k} + \mathbf{G})^2 - E \right] u(\mathbf{G}) e^{i(\mathbf{k}+\mathbf{G}) \cdot \mathbf{r}} = - \sum_{\mathbf{G}\mathbf{G}'} V(\mathbf{G} - \mathbf{G}') u(\mathbf{G}') e^{i(\mathbf{k}+\mathbf{G}) \cdot \mathbf{r}} \quad (3.48)$$

since each planewave component must be equal we can drop the summation over \mathbf{G} , this is equivalent to the Fourier transform rule

$$\int dx f(x) e^{ikx} = \int dx g(x) e^{ikx} \rightarrow f(x) = g(x) \quad (3.49)$$

Hence it follows

$$\left[\frac{\hbar^2}{2m} (\mathbf{k} + \mathbf{G})^2 - E \right] u(\mathbf{G}) = - \sum_{\mathbf{G}'} V(\mathbf{G} - \mathbf{G}') u(\mathbf{G}') \quad (3.50)$$

From here on out we will follow the two beam approximation in which we assume only the forward (transmitted) beam ($\mathbf{G} = \mathbf{0}$) and the diffracted (reflected) beam ($\mathbf{G} = \mathbf{H}$, with \mathbf{H} the specific reciprocal lattice vector under consideration) have a non-zero amplitude. In this case we can rewrite 3.50 as a simple matrix vector problem

$$\begin{bmatrix} \frac{\hbar^2}{2m} \mathbf{k}^2 - E + V(\mathbf{0}) & V(-\mathbf{H}) \\ V(\mathbf{H}) & \frac{\hbar^2}{2m} (\mathbf{k} + \mathbf{H})^2 - E + V(\mathbf{0}) \end{bmatrix} \begin{bmatrix} u(\mathbf{0}) \\ u(\mathbf{H}) \end{bmatrix} = 0 \quad (3.51)$$

The solutions of \mathbf{u} are only non trivial if the determinant of the matrix is zero. From this determinant

$$\left(\frac{\hbar^2}{2m} \mathbf{k}^2 - E + V(\mathbf{0}) \right) \left(\frac{\hbar^2}{2m} (\mathbf{k} + \mathbf{H})^2 - E + V(\mathbf{0}) \right) = V(\mathbf{H})V(-\mathbf{H}) \quad (3.52)$$

we can derive the dispersion relation via a perturbation approach where we allow \mathbf{k} to vary by a small amount normal to the crystal boundary around the incident wavevector \mathbf{k}_0 :

$$\mathbf{k} = \mathbf{k}_0 + \frac{|\mathbf{k}_0|}{\cos(\gamma)} \epsilon \mathbf{n} \rightarrow |\mathbf{k}|^2 \approx |\mathbf{k}_0|^2 (1 + 2\epsilon) \quad (3.53)$$

with \mathbf{n} the unit vector normal to the crystal surface and γ the angle between \mathbf{n} and \mathbf{k}_0 . We may then solve eq. 3.52 for the perturbation parameter ϵ

$$\left(2\epsilon + \frac{V(\mathbf{0})}{E} \right) \left(\frac{2}{b} \epsilon + a + \frac{V(\mathbf{0})}{E} \right) = \frac{V(\mathbf{H})V(-\mathbf{H})}{E^2} \quad (3.54)$$

with $a = \frac{\mathbf{H}^2}{\mathbf{k}_0^2} + \frac{2\mathbf{k}_0 \cdot \mathbf{H}}{\mathbf{k}_0^2}$ and $\frac{1}{b} = 1 + \frac{\mathbf{n} \cdot \mathbf{H}}{|\mathbf{k}_0| \cos(\gamma)}$. The solutions to this quadratic equation in ϵ are given by

$$\epsilon_{1,2} = \frac{1}{4} \left[-ab - \frac{V(\mathbf{0})}{E}(1+b) \pm \sqrt{\left(ab + \frac{V(\mathbf{0})}{E}[1+b] \right)^2 - 4b \left(\left[\frac{V(\mathbf{0})}{E} \right]^2 + a \frac{V(\mathbf{0})}{E} - \frac{V(\mathbf{H})V(-\mathbf{H})}{E^2} \right)} \right] \quad (3.55)$$

It follows that within the crystal there are two transmitted

$$\psi_T = e^{i\mathbf{k}_0 \cdot \mathbf{r}} \left[e^{i \frac{\mathbf{k}_0 \epsilon_1}{\cos(\gamma)} \mathbf{n} \cdot \mathbf{r}} u_1(\mathbf{0}) + e^{i \frac{\mathbf{k}_0 \epsilon_2}{\cos(\gamma)} \mathbf{n} \cdot \mathbf{r}} u_2(\mathbf{0}) \right] \quad (3.56)$$

and two reflected waves

$$\psi_R = e^{i(\mathbf{k}_0 + \mathbf{H}) \cdot \mathbf{r}} \left[e^{i \frac{\mathbf{k}_0 \epsilon_1}{\cos(\gamma)} \mathbf{n} \cdot \mathbf{r}} u_1(\mathbf{H}) + e^{i \frac{\mathbf{k}_0 \epsilon_2}{\cos(\gamma)} \mathbf{n} \cdot \mathbf{r}} u_2(\mathbf{H}) \right] \quad (3.57)$$

Next we can determine the relation between the reflected and transmitted amplitudes:

$$\frac{u_{1,2}(\mathbf{H})}{u_{1,2}(\mathbf{0})} = -\frac{\frac{\hbar^2}{2m} \mathbf{k}^2 - E + V(\mathbf{0})}{V(-\mathbf{H})} = -\frac{2\epsilon_{1,2} + \frac{V(\mathbf{0})}{E}}{\frac{V(-\mathbf{H})}{E}} = X_{1,2} \quad (3.58)$$

The coefficients $u_{1,2}(\mathbf{0})$ follow from the boundary conditions, which depend on the geometry and the incident wavefield. For now we will assume that the incoming wave is simply a planewave with arbitrary amplitude and momentum

$$\psi_I = u_0 e^{i\mathbf{k} \cdot \mathbf{r}} \quad (3.59)$$

Later we will then be able to determine the solution for any incident wave if we expand our incident wave in terms of planewaves. As for geometry we will examine both Bragg and Laue diffraction. For both geometries at the crystal surface $\mathbf{r} \cdot \mathbf{n} = \mathbf{0}$, the sum of the transmitted amplitudes must be equal to the incident wave amplitude

$$u_1(\mathbf{0}) + u_2(\mathbf{0}) = u_0 \quad (3.60)$$

Bragg Geometry

We start by determining the boundary condition given by Bragg geometry. Here the lattice planes are roughly parallel to the crystal surface on which the external wave is incident. This particular geometry is shown below in figure 3.6 It is quite clear that at the back of the crystal there is no reflected wave. Hence it follows that the reflected wavefield (eq. 3.57) at the end of the crystal $\mathbf{r} \cdot \mathbf{n} = D$ is zero. From this we can derive our second boundary condition

$$X_1 u_1(\mathbf{0}) e^{i \frac{\mathbf{k}_0 \epsilon_1}{\cos(\gamma)} D} + X_2 u_2(\mathbf{0}) e^{i \frac{\mathbf{k}_0 \epsilon_2}{\cos(\gamma)} D} = 0 \quad (3.61)$$

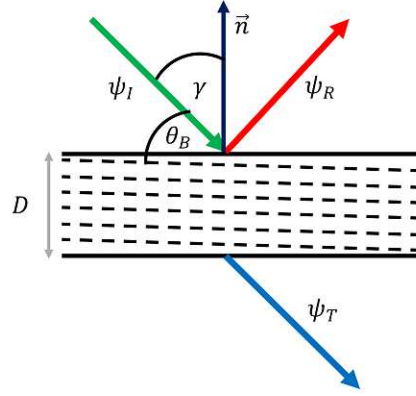


Figure 3.6: Schematic representation of Bragg diffraction. The solid black lines denote the crystal borders, while the dashed lines indicate lattice planes. The incident, reflected and transmitted waves are colored green, red and blue respectively. The Bragg angle θ_B is shown as the angle between the incident wavevector and the lattice planes, while the angle γ indicates the angle between the surface normal, \mathbf{n} , and the incident wavevector.

Using this and our universal boundary condition eq. 3.60 we can solve for u_1 and u_2

$$u_1(\mathbf{0}) = \frac{X_2 e^{\frac{ik_0 \epsilon_2 D}{\cos(\gamma)}}}{X_2 e^{\frac{ik_0 \epsilon_2 D}{\cos(\gamma)}} - X_1 e^{\frac{ik_0 \epsilon_1 D}{\cos(\gamma)}}} u_0 \quad (3.62a)$$

$$u_2(\mathbf{0}) = -\frac{X_1 e^{\frac{ik_0 \epsilon_1 D}{\cos(\gamma)}}}{X_2 e^{\frac{ik_0 \epsilon_2 D}{\cos(\gamma)}} - X_1 e^{\frac{ik_0 \epsilon_1 D}{\cos(\gamma)}}} u_0 \quad (3.62b)$$

With all the amplitudes determined we can calculate the reflectivity R and transmission T

$$R = |\psi_R(\mathbf{r} \cdot \mathbf{n} = 0)|^2 \quad (3.63a)$$

$$T = |\psi_T(\mathbf{r} \cdot \mathbf{n} = D)|^2 \quad (3.63b)$$

Figure 3.7 shows the reflection and transmission probabilities experienced by a planewave neutron under various incident angles close to the Bragg angle. These are called rocking curves, since they are usually obtained by rocking a crystal through a neutron beam with fixed momentum. The probabilities are calculated for quartz crystals of 100 and 200 micron thickness. In each case the (110) reflection (i.e. $h = 1$, $k = 1$ and $l = 0$) is considered. Absorption is taken into account and amplified to show the effects of absorption on diffraction. Both reflectivity and transmission are characterized by a plateau, known as the Darwin Plateau, very close to the Bragg condition and oscillations, known as Pendellösung oscillations, slightly further away from the Bragg condition. Once sufficiently far from the Bragg condition these oscillations dampen out completely and both transmission and reflectivity become constant. Absorption skews the rocking curves. The width of the Darwin plateau for this particular reflection corresponds to

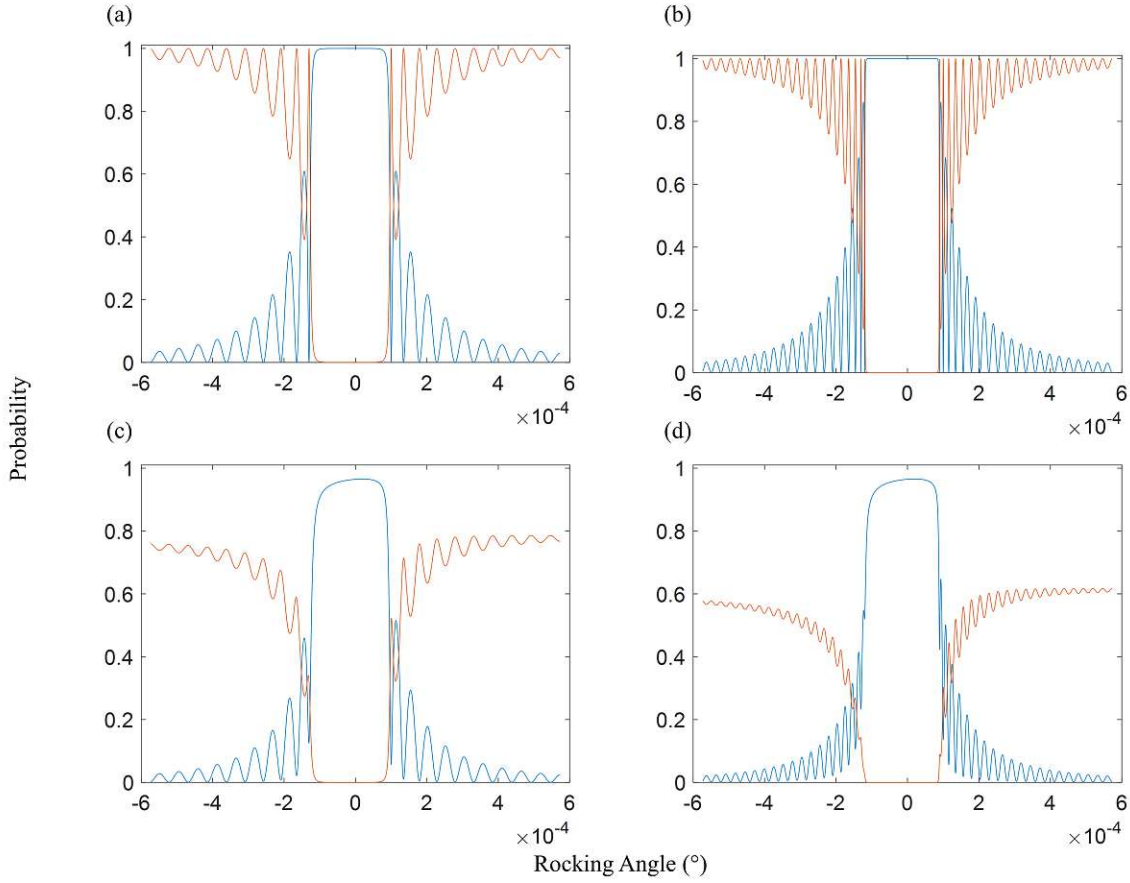


Figure 3.7: Bragg geometry reflection (blue) and transmission (red) probabilities against rocking angle for a 2 Å neutron incident on the (110) plane of alpha quartz. The crystal thickness is varied between 100 μm (a) and (c) and 200 μm (b) and (d). Furthermore in figure (c) and (d) absorption is amplified by setting the imaginary part of the scattering length of the oxygen atoms to -0.05 fm .

roughly 0.8° , a typical number for thermal neutrons diffracted from perfect crystals. In general the Darwin width may be approximated with the following formula [82]

$$\Delta\theta = \frac{2\lambda_B^2 F_{hkl}}{\pi\mathcal{V} \sin(2\theta_B)} \quad (3.64)$$

which can be understood intuitively. We see that the Darwin width is proportional to the structure factor F_{hkl} which is in turn proportional to the lattice potential. One can imagine for small lattice potential, more lattice planes must contribute to the reflection, due to the larger penetration depth into the crystal. As a result the angular range over which constructive interference can be produced in the far field is reduced, resulting in a smaller Darwin width. In a similar way the Bragg wavelength λ_B^2 is inversely proportional to the neutrons kinetic energy. Low energies typically correspond to a stronger

interaction with the crystal, resulting in a lower penetration depth. High energies therefore correspond to a larger penetration depth in the crystal, resulting in more lattice planes becoming excited and contributing to the reflection. As explained before a large number of excited point sources contributing to the reflection results in a more narrow Darwin width.

Laue Geometry

We now move on to Laue geometry, where the lattice planes are roughly perpendicular to the crystal surface on which the incoming wavefield impinges. The geometry is shown in figure 3.8 Interestingly in Laue geometry when on Bragg condition, the crystal acts

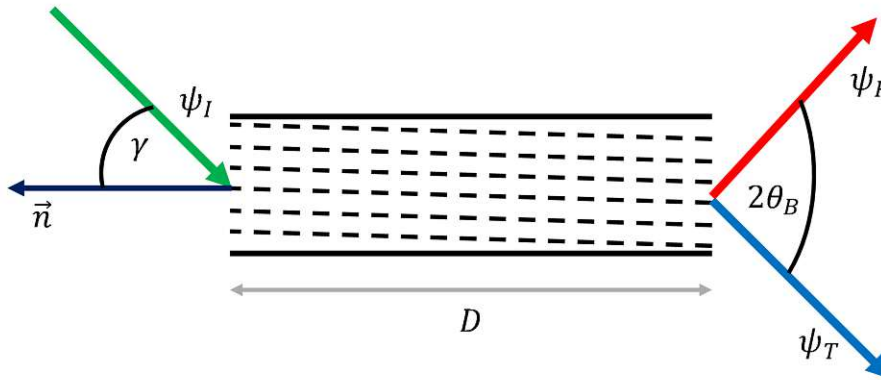


Figure 3.8: Schematic representation of Laue diffraction. The solid black lines denote the crystal borders, while the dashed lines indicate lattice planes. The incident, reflected and transmitted waves are colored green, red and blue respectively. The Bragg angle θ_B is shown as half the angle between the transmitted and reflected wavevectors, while the angle γ indicates the angle between the surface normal, \mathbf{n} , and the incident wavevector.

as a waveguide for the incident wave, which propagates through the crystal along the lattice planes by many reflections. In this geometry we note that contrary to the Bragg case there is no reflected wave at the entry surface. This leads to the second boundary condition in the Laue case

$$X_1 u_1(\mathbf{0}) + X_2 u(\mathbf{0}) = 0 \quad (3.65)$$

Combined with our universal boundary condition 3.60 we can derive the wave amplitudes in the crystal for this geometry by elimination

$$u_1(\mathbf{0}) = \frac{X_2}{X_2 - X_1} u_0 \quad (3.66a)$$

$$u_2(\mathbf{0}) = -\frac{X_1}{X_2 - X_1} u_0 \quad (3.66b)$$

and also the transmission and reflection probabilities

$$R = |\psi_R(\mathbf{r} \cdot \mathbf{n} = D)|^2 \quad (3.67a)$$

$$T = |\psi_T(\mathbf{r} \cdot \mathbf{n} = D)|^2 \quad (3.67b)$$

Figure 3.9 shows various rocking curves containing the reflection and transmission probabilities experienced by a planewave neutron impinging on a crystal in Laue geometry under various incident angles close to the Bragg condition. We see that in Laue diffrac-

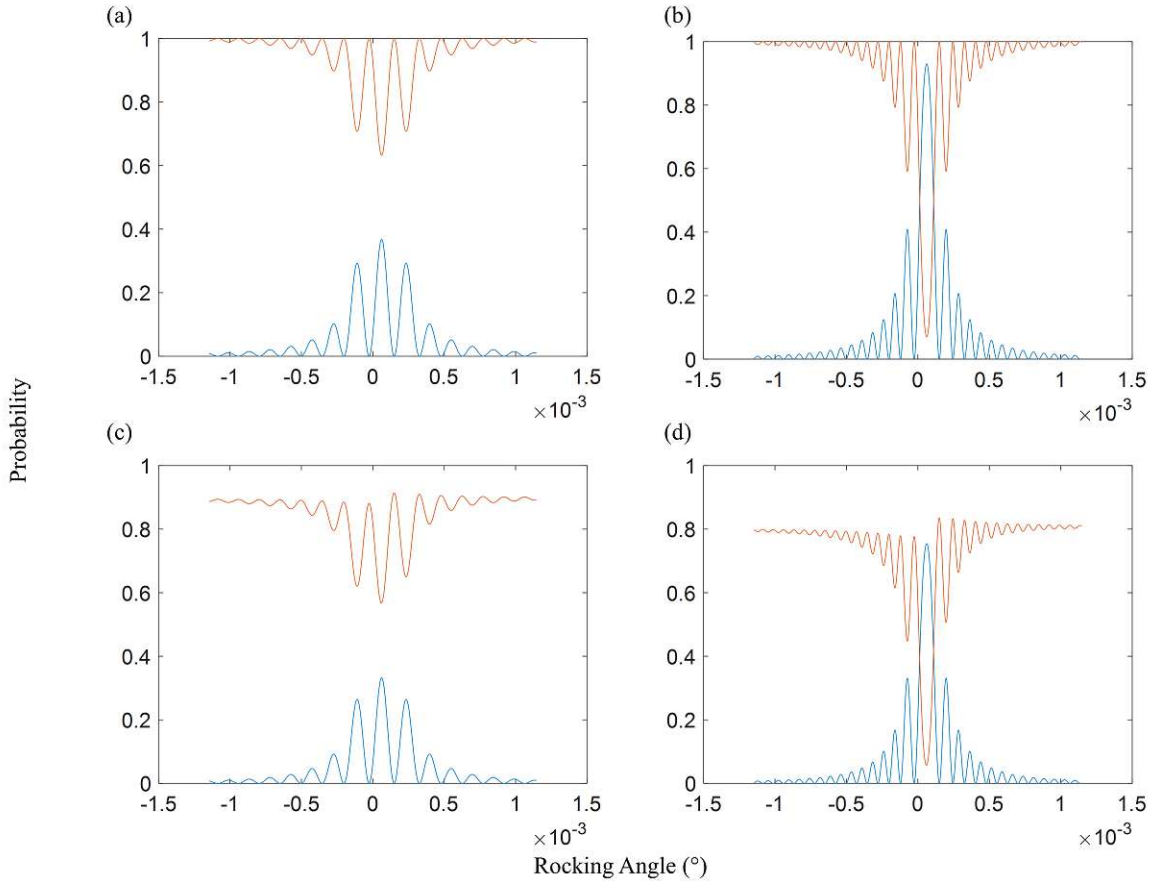


Figure 3.9: Laue reflection (blue) and transmission (red) probabilities against rocking angle for a 2 Å neutron incident on the (110) plane of alpha quartz. The crystal thickness is varied between 100 μm (a) and (c) and 200 μm (b) and (d). Furthermore in figure (c) and (d) absorption is amplified by setting the imaginary part of the scattering length of the oxygen atoms to $-0.05 fm$.

tion close to the Bragg condition intensity is shuffled back and forth between the reflected and transmitted beam. As the crystal thickness is increased these oscillations become more dense as in the Bragg case. As a result for a realistic beam with non-zero divergence about half of the incident intensity is reflected while the other half is transmitted. When absorbing nuclei are present we find that the transmission probability may become

larger, close to the Bragg condition (in our figure to the right of the Bragg condition), compared to far from the Bragg condition when the beam isn't diffracted. One way to understand this is by recognizing that the forward and reflected waves in the crystal interfere to produce two standing waves. One of the standing waves has its anti-nodes on the lattices planes (i.e. on the nuclei), while the other has anti-nodes between the planes [83, 74]. The first standing wave therefore has a higher probability of being absorbed, while the other standing wave can "slip" through the lattice without being absorbed. This leads to anomalous transmission. Since in Laue geometry the wave must pass through the entire crystal, the neutron ends up interacting with far more nuclei. Intuitively, Laue geometry is therefore ideal to search for weak neutron/nuclear interactions. In addition neutrons slow down in the crystal coming to a complete halt for Bragg angles of 90 degrees, as is shown by the perturbation parameter $\epsilon_{1,2}$, eq. 3.56 and eq. 3.57 [75]. This allows for longer interaction times, amplifying weak interactions.

3.2.2 Adding Electric Fields to Dynamical Diffraction

To study OAM generation in dynamical diffraction we need to add the Schwinger term to the potential 3.35. Since the Schwinger term is SU(2), we need to analyze our work from the previous subsection, to verify that the steps taken to determine the perturbation parameter $\epsilon_{1,2}$ and the wavefunction amplitudes u_1 and u_2 , which now become spinors, are valid for lattice potentials that can only be described using matrices. We will follow the approaches given by [62] and [61], while sticking with the perturbation approach used in the previous section where we assume that the momentum in the crystal can be described by the incident wave momentum plus some perturbation, ϵ , parallel to the surface normal. We will begin by examining the total potential in the crystal which corresponds to the sum of the strong nuclear potential and the Schwinger term

$$V = \frac{2\pi\hbar^2}{m} \sum_j b_j \delta(\mathbf{r} - \mathbf{r}_j) + \frac{\mu}{mc^2} \boldsymbol{\sigma} \cdot [\mathbf{p} \times \mathbf{E}(\mathbf{r})] \quad (3.68)$$

The electric field is given by

$$\mathbf{E} = -\nabla \left[\sum_j \frac{Z_j e}{|\mathbf{r} - \mathbf{r}_j|} - \sum_k \frac{e}{|\mathbf{r} - \mathbf{r}_k|} \right] \quad (3.69)$$

with e , the electron charge, Z_j the atomic number of the j^{th} nucleus and \mathbf{r}_k the position of the k^{th} electron. The Fourier components of the potential $V(\mathbf{G})$ are then given by

$$V(\mathbf{G}) = \frac{2\pi\hbar^2}{m\mathcal{V}_l} \left[F_{hkl} + \sum_i (-2i\gamma_i \boldsymbol{\sigma} \cdot \frac{\mathbf{K} \times \mathbf{G}}{|\mathbf{G}|^2}) e^{-i\mathbf{G} \cdot \mathbf{r}_i} \right] \quad (3.70)$$

with

$$\gamma_i = \frac{\gamma e^2}{2mc^2} Z_i [1 - f_i(\mathbf{G})] \quad (3.71)$$

where the index i refers to the i^{th} atom in the unit cell, $f(\mathbf{G})$ the electronic structure factor of the relevant atom and \mathbf{K} the momentum operator in reciprocal space which we will approximate with the incident moment \mathbf{k}_0 . We note that then $V(\mathbf{G} = 0)$ is practically a scalar and commutes with all operators. In the previous section we did not use the commutation property or the inversion of V for the perturbation parameter $\epsilon_{1,2}$, hence we may safely assume that it can be calculated according to eq. 3.55 using the potential 3.70. Afterwards when it comes to calculating the amplitudes $u_{1,2}(\mathbf{G})$ we need to be more careful, since when we take neutron spin into consideration, which is necessary when looking at the Schwinger interaction, these amplitudes must be described using spinors. As a result we can no longer divide amplitudes by each other like we did in eq. 3.58. In addition since the perturbation parameter is now a matrix, the exponentials, $e^{i \frac{\mathbf{k}_0 \epsilon_{1,2}}{\cos(\gamma)} \mathbf{n} \cdot \mathbf{r}}$, in eq. 3.56 and 3.57 are also matrices. We can begin by rewriting the equations 3.51 using matrices

$$M_{1,2}u_{1,2}(\mathbf{0}) + V(\mathbf{H})u_{1,2}(\mathbf{H}) = 0 \quad (3.72a)$$

$$V(-\mathbf{H})u_{1,2}(\mathbf{0}) + M'_{1,2}u_{1,2}(\mathbf{H}) = 0 \quad (3.72b)$$

with $M_{1,2} = [2E\epsilon_{1,2} + V(\mathbf{0})]I$ and I the identity matrix. It follows that the forward and backward amplitudes are therefore related by

$$u_{1,2}(\mathbf{H}) = -V^{-1}(\mathbf{H})M_{1,2}u_{1,2}(\mathbf{0}) = X_{1,2}u_{1,2}(\mathbf{0}) \quad (3.73)$$

To determine the amplitudes $u_{1,2}(\mathbf{0})$ we need to apply the boundary conditions. The universal boundary condition 3.60 is unchanged. Bragg and Laue geometries need to be examined individually. At this point we note that to obtain a large non-zero Schwinger effect in the dynamical theory of diffraction we require that $V(\mathbf{H}) \neq V^*(-\mathbf{H})$, since otherwise the Schwinger term would not produce a polarization dependent change in the perturbation parameter $\epsilon_{1,2}$. As a result the crystals we investigate must violate Friedels law and therefore be non-centrosymmetric [84, 85]. For this reason we specifically look at the [110] planes of quartz which lacks a center of symmetry. In addition large perfect crystals of quartz are produced commercially. Finally before deriving the spinor amplitudes of the reflected and transmitted waves in Bragg and Laue geometry it is useful to define and visualize the relevant axes. For this we refer to figure 3.10 which shows our definition of the spin axes, as well as the so called ρ axis, which will be used later when deriving the OAM produced in diffraction.

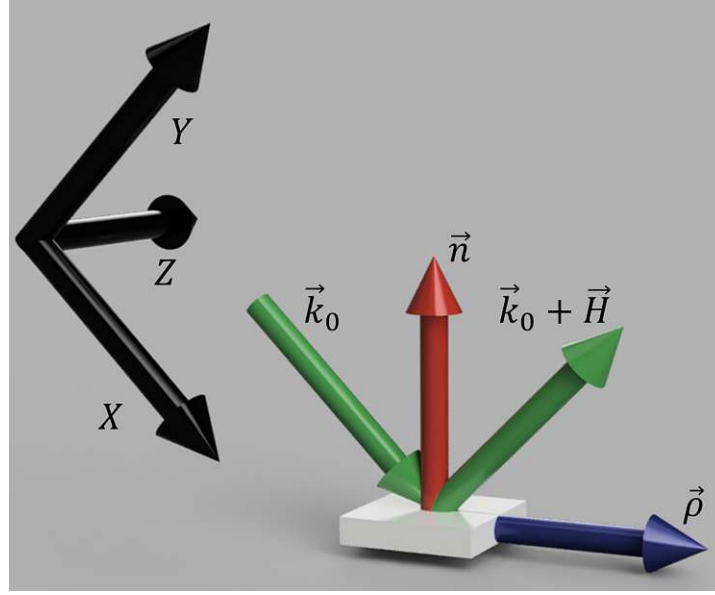


Figure 3.10: Three dimensional render depicting Bragg diffraction of a neutron (green) by a crystal (white). The axes that define the spin operators σ are shown in black, the surface normal in red and the so called ρ axis in blue. Rocking represents a rotation of the surface normal towards or away from ρ , while a rotation around the ρ axis is defined as tilting.

Bragg Geometry

We begin determining the transmitted and reflected wave amplitudes in the Bragg case. In this geometry the second boundary condition stating that there is no reflected wave at the back part of the crystal, eq. 3.61, can be expressed with SU(2) operators as

$$E_1 X_1 u_1(\mathbf{0}) + E_2 X_2 u_2(\mathbf{0}) = 0 \quad (3.74)$$

with $E_{1,2} = e^{\frac{ik_0 \epsilon_{1,2} D}{\cos(\gamma)}}$. Together with the universal boundary condition we can derive the amplitudes for the Bragg case.

$$u_1(\mathbf{0}) = -(E_1 X_1 - E_2 X_2)^{-1} E_2 X_2 u_0 \quad (3.75a)$$

$$u_2(\mathbf{0}) = -(E_2 X_2 - E_1 X_1)^{-1} E_1 X_1 u_0 \quad (3.75b)$$

The reflectivity is practically unchanged compared to the case which ignores the Schwinger effect. However the electric fields do influence the neutron polarization, \mathbf{P} which can be calculated for the transmitted and reflected beams using the spin operator σ

$$\mathbf{P}_R = \frac{\langle \psi_R(\mathbf{r} \cdot \mathbf{n} = 0) | \sigma | \psi_R(\mathbf{r} \cdot \mathbf{n} = 0) \rangle}{R} \quad (3.76a)$$

$$\mathbf{P}_T = \frac{\langle \psi_T(\mathbf{r} \cdot \mathbf{n} = D) | \sigma | \psi_T(\mathbf{r} \cdot \mathbf{n} = D) \rangle}{T} \quad (3.76b)$$

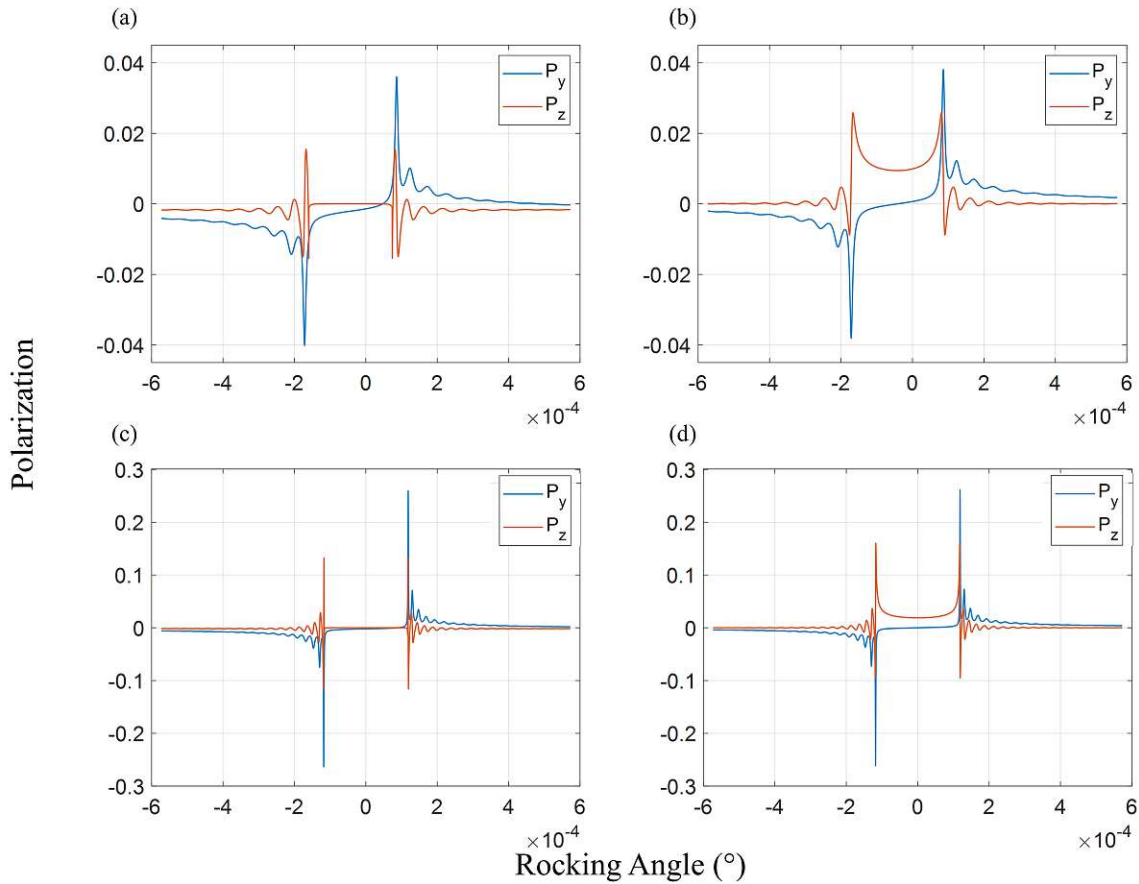


Figure 3.11: Plots of the y (blue) z (red) components of the neutron polarization against rocking angle after being Bragg reflected from a (a) $100 \mu\text{m}$ and (b) $200 \mu\text{m}$ thick piece of quartz ([110] plane). Insets (c) and (d) show the polarization components of the transmitted waves for both thickness respectively. The incident wave is initially polarized along the x direction which is chosen to be parallel to the incident wavevector. The incident wave has a wavelength of 2 \AA

In figure 3.11 these polarizations are shown for the case where neutrons are reflected from the [110] planes of quartz. From these figures it is quite clear that the y component of the polarization appears to rotate by 180 degrees when the sign of the rocking angle is inverted. Inverting the rocking angle is equivalent to inverting the neutron momentum component parallel to the lattice planes. Hence after diffraction from the [110] planes of quartz neutron momentum and polarization are coupled/entangled. Since a 180 degree rotation of the momentum leads to a 180 degree rotation of the spinor amplitude, the nature of the momentum coupling is such that one can speak of spin-orbit (i.e. spin-OAM) coupling/entanglement. In short Bragg diffraction from quartz produces OAM in neutrons. To investigate OAM generation in more detail we will calculate the reciprocal two dimensional wavefunctions produced by diffraction from the [110] planes of quartz.

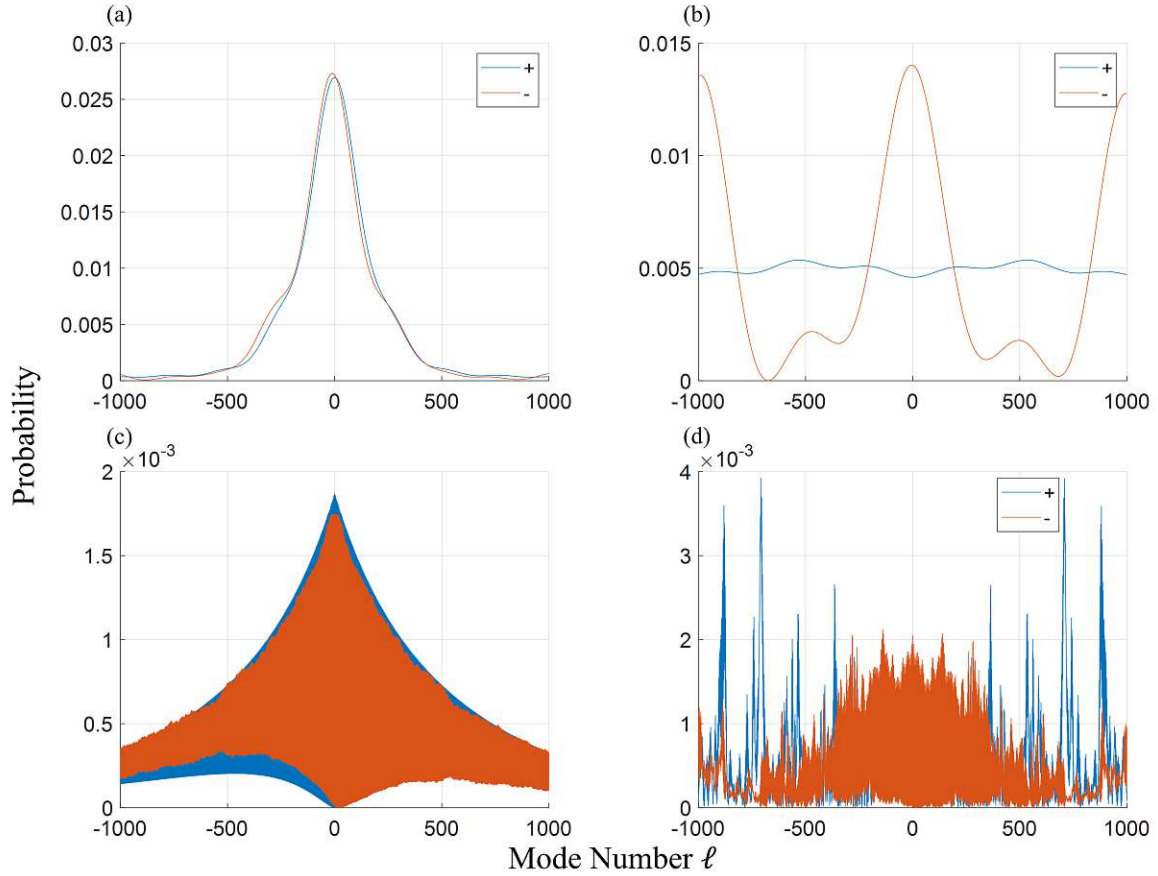


Figure 3.12: OAM distribution functions 2.32 calculated for a 2 Å neutron diffracted from a 300 micron thick piece of [110] quartz. Inset (a) shows the distribution functions of the reflected wave, while inset (b) treats the transmitted waves. Both insets assume that ϕ is defined around the reciprocal lattice vector \mathbf{H} . Inset (c) and (d) also show the distribution functions of the reflected and transmitted waves respectively, however here the OAM is longitudinal (i.e. ϕ is defined around the momentum vector) The blue curve shows the non-spin flipped distribution while the red curve refers to the spin flipped distribution function. Finally we note the fast oscillations visible in (c) and (d) indicating strong suppression of neighboring modes, indicating an intrinsic OAM component.

To do this we need to consider not only the rocking angle as we have before, but also the perpendicular angle, commonly referred to as the rho angle, or tilt. This tilting is visualized in figure 3.10. We will calculate numerically the reflected and transmitted wave amplitudes in the case where the [110] planes of a quartz crystal are illuminated by an incident wavefunction with a wide and homogeneous angular/momentum distribution i.e. $\psi_I(k_x, k_y) = 1$, where we approximate k_x via the incident momentum $|k_0|$ and the rocking angle, θ i.e. $k_x = |k_0|(\pi - \theta)$ and the momentum component k_y is approximated

	$\mathbf{H}, +$	$\mathbf{H}, -$	$\mathbf{k}_0, +$	$\mathbf{k}_0, -$
R	0	-11.1	0	-34.5
T	-0.1	-22.2	0.1	-18.8

Table 3.1: Mean mode numbers of the (non) spin flipped transmitted and reflected wavefunctions. The distribution functions are shown in figure 3.12. The index + indicates non-spin flip, while - indicates a spin flip. The vectors \mathbf{H} and \mathbf{k}_0 define the axes around which the azimuthal coordinate ϕ is defined.

in a similar way using the tilt angle $k_y = |k_0|\rho$. After calculating the wavefunctions we will apply a numeric version of the AFT (2.27) to determine the OAM distribution functions (2.32) of the (non) spin flipped reflected/transmitted wavefunctions. We note that the azimuthal coordinate of ϕ is in this case defined around the reciprocal lattice vector \mathbf{H} . We may also calculate the longitudinal OAM by defining ϕ around \mathbf{k}_0 , which results in k_x be defined by $k_x = |k_0|\Delta\theta$ with $\Delta\theta$ the deviation from the Bragg angle. OAM distribution functions for both definitions of ϕ are shown in figure 3.12, for a 2 Å neutron diffracted from 300 micron thick [110] quartz.

Examining the figure closely one can observe a shift/translation along the mode number ℓ between the spin flipped and non-spin flipped distributions. Indicating a change in the OAM expectation value $\langle L_z \rangle$. The table 3.1 indicates the calculated expectation value for each distribution function. The oscillating nature of the OAM distribution

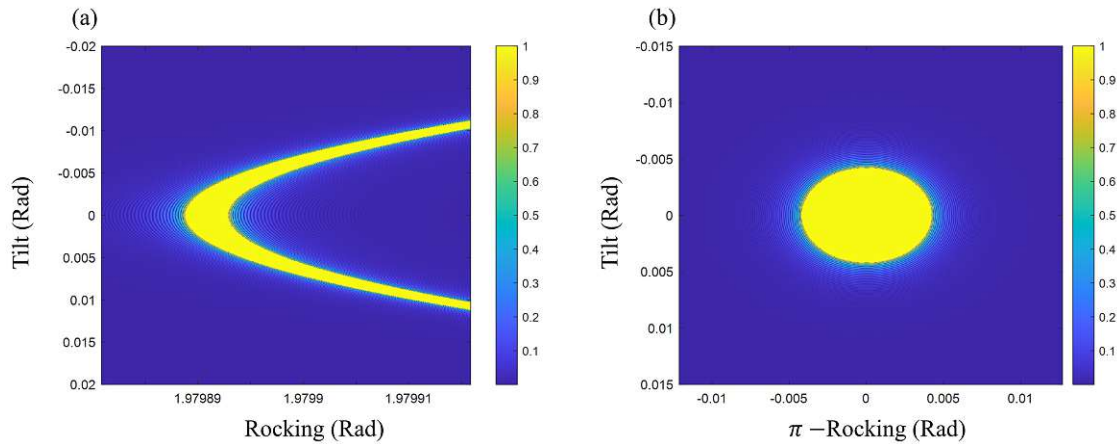


Figure 3.13: Reflectivity of a [110] quartz for neutrons with (a) 2 Å and (b) 5.0279 Å wavelength. The latter corresponds to backscattering (i.e. a Bragg angle of 90 degrees). In the latter case we can see that the momentum distribution of the reflected wavefunction is symmetric and that tilt and rocking angle become virtually identical.

functions indicates that neighboring modes are suppressed in the longitudinal OAM case. As a result it is likely that the OAM can be considered partially intrinsic. The suppression is only partial since the angular acceptance of a crystal is usually much

larger in the tilt direction than in the rocking direction. This results in reflected and transmitted waves with ellipsoidal transverse momentum distribution and therefore a distortion of the phase imprinted on the wavefunction. To circumvent this and obtain pure OAM states one must go into a backscattering geometry where the Bragg angle is close to 90 degrees. In this case the acceptance in ρ and θ are identical as shown in figure 3.13 Such a symmetric momentum distribution is practically a prerequisite for

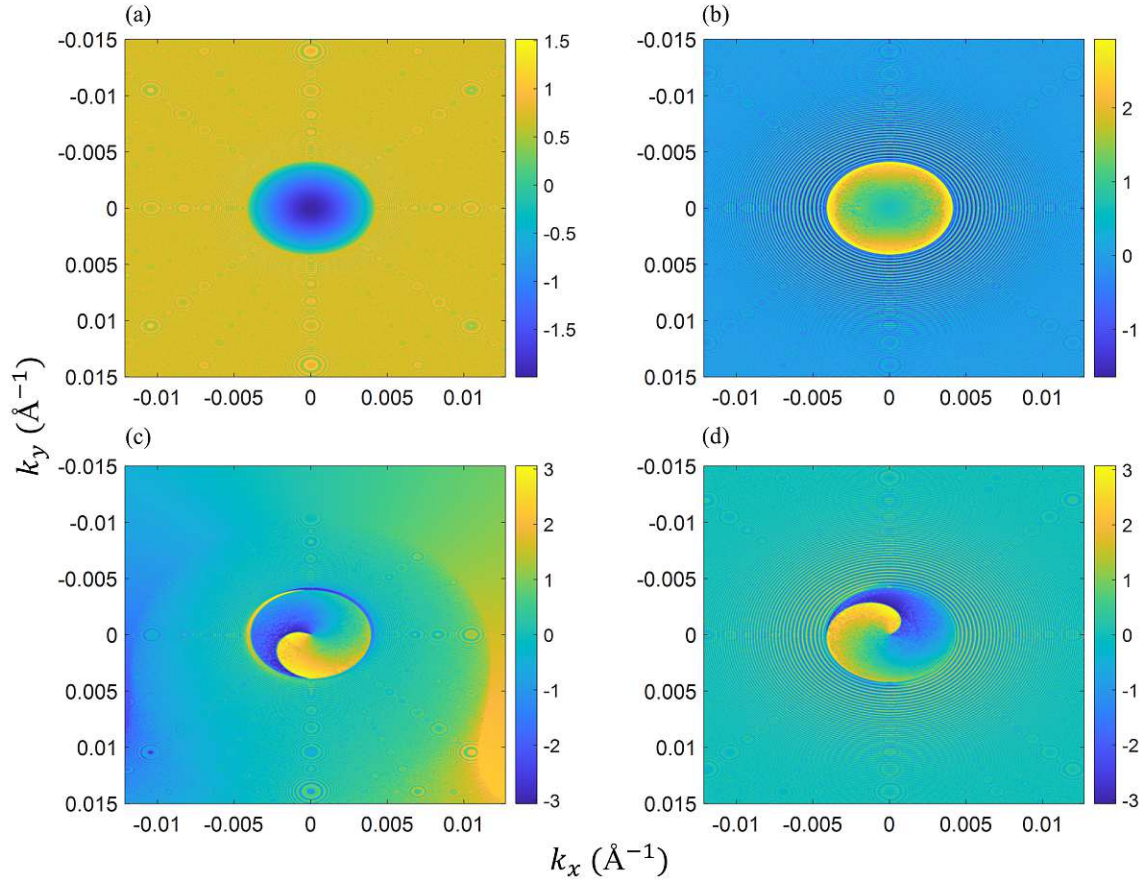


Figure 3.14: Phase of the (a) reflected and (b) transmitted non spin flipped wavefunctions and the (c) reflected and (d) transmitted spin flipped wavefunctions. The latter show a clear vortex structure "spinning" in opposite directions. The vortex line is the line on which the phase flips from $+\pi$ to $-\pi$. Since there is only one vortex line (or curve) in this case we can conclude that the mode number is equal to $\ell = \pm 1$. The incident wave has a wavelength of 5.0279 \AA with a spin polarized along the momentum direction.

producing pure vortex states. To prove this statement we will numerically calculate the transverse wavefunctions of the reflected and transmitted waves as before, now assuming an incident wavelength of 5.0279 \AA , which corresponds to a Bragg angle of 90 degrees. In figure 3.14 the results of these numerical calculations are shown. Specifically the phase of the wavefunctions is pictured, showing clearly the vortex structure of the spin flipped

wavefunctions in both reflection and transmission. There is only one vortex line, which signifies the phase transition from $+\pi$ to $-\pi$, indicating that the mode number of the spin flipped wavefunction corresponds to unity. This is confirmed by applying an AFT and calculating the OAM distribution function, which is non-zero only at $\ell = -1$ for the reflected spin flipped wavefunction and $\ell = 1$ for the transmitted wavefunction. We conclude that backscattering from a non-centrosymmetric crystal in Bragg geometry acts as an OAM raising/lowering operator coupled to a spin flip operator, thereby entangling the spin and OAM degrees of freedom. The additional detail that the OAM carrying part of the wavefunction is also spin flipped, makes it exceptionally easy to detect as a spin filter could be used to separate the spin flipped beam from the non-scattered beam, even in a backscattering geometry. The limiting factor with this method is the low efficiency. For a 10 mm thick quartz crystal the ratio between the integrated spin flipped reflectivity and the non spin flipped reflectivity is on the order of 10^{-6} . The same is true for the transmitted wave. Note that these ratios improve for shorter wavelengths (6% at 2 Å), however as shown above the spin-orbit states produced with thermal neutrons are not pure. We will find in Laue geometry the efficiency is much higher, even in backscattering, since the neutrons must propagate through the whole crystal.

Laue Geometry

We now proceed to look at vortex state generation by diffraction from [110] quartz in Laue geometry. We will start by deriving the transmission and reflection amplitudes, so that we may once again numerically determine the reflected and transmitted wavefunctions. To begin we must write down the second boundary condition which is unique to Laue geometry. Again this condition states that there is no reflected wavefield at the crystal entrance. This condition previously written as eq. 3.65 can be expressed using matrices and spinors as follows

$$X_1 u_1(0) + X_2 u_2(0) = 0 \quad (3.77)$$

which leads to the following spinor amplitudes

$$u_1(\mathbf{0}) = (X_2 - X_1)^{-1} X_2 u_0 \quad (3.78a)$$

$$u_2(\mathbf{0}) = -(X_2 - X_1)^{-1} X_1 u_0 \quad (3.78b)$$

As in the Bragg case we will first look at the polarization of the reflected and transmitted waves

$$\mathbf{P}_R = \frac{\langle \psi_R(\mathbf{r} \cdot \mathbf{n} = D) | \sigma | \psi_R(\mathbf{r} \cdot \mathbf{n} = D) \rangle}{R} \quad (3.79a)$$

$$\mathbf{P}_T = \frac{\langle \psi_T(\mathbf{r} \cdot \mathbf{n} = D) | \sigma | \psi_T(\mathbf{r} \cdot \mathbf{n} = D) \rangle}{T} \quad (3.79b)$$

The orthogonal polarization components, assuming a thermal incident wave polarized along the momentum direction x , are shown in figure 3.15 for two different crystal thicknesses. As in the Bragg case, spin-orbit entanglement is evident in the y component of

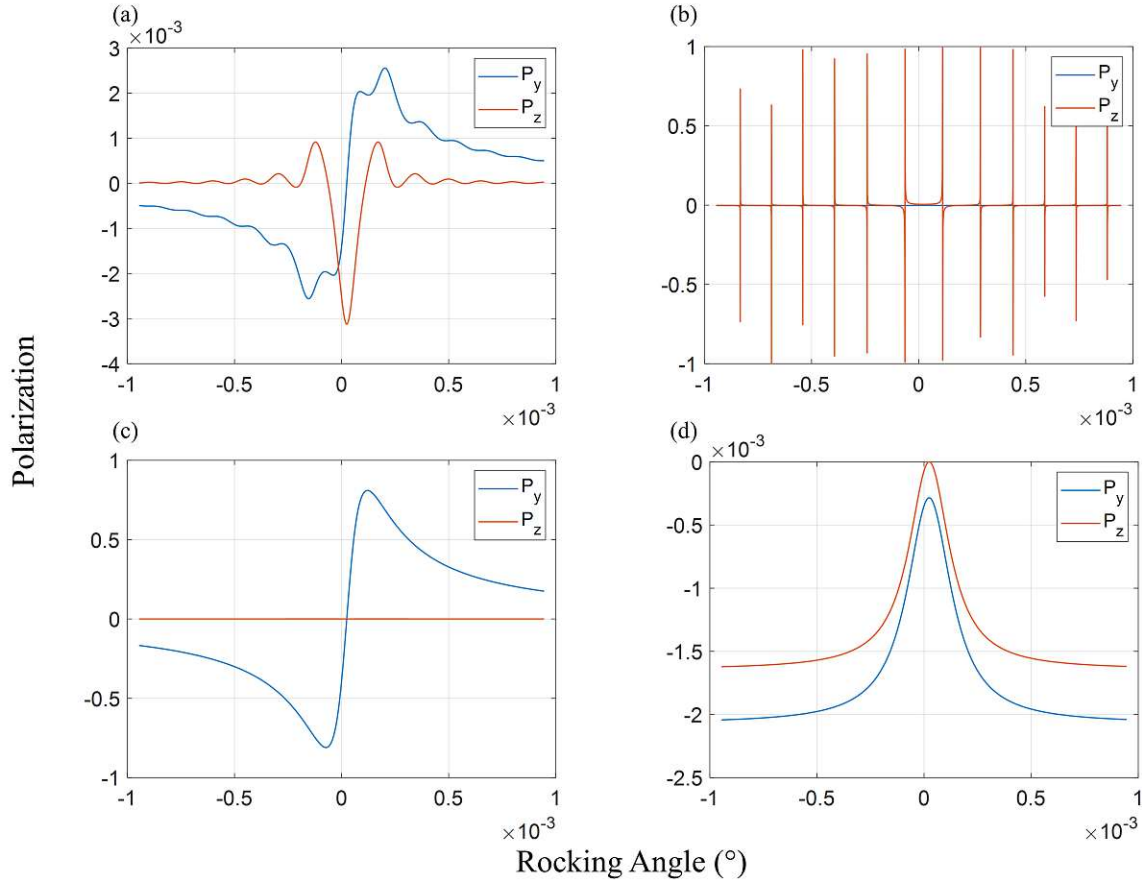


Figure 3.15: Plots of the y (blue) z (red) components of the neutron polarization against rocking angle after being Laue reflected from a (a) 100 μm and (b) 35 mm thick piece of quartz ([110] plane). Insets (c) and (d) show the polarization components of the transmitted waves for both thickness respectively. The incident wave is initially polarized along the x direction which is chosen to be parallel to the incident wavevector. The incident wave has a wavelength of 2 \AA . For the thicker crystal an approximation is used which averages over the Pendelösung oscillations (visible in the top insets), this aids in visibility of the polarization.

the neutron polarization. A few differences are however apparent. First the coupling can be much stronger in the Laue case, since neutrons can propagate through the full length of large crystals. In addition the polarization of the reflected and transmitted waves are qualitatively quite different. When we investigate further, however, we find that the OAM states produced in Laue diffraction aren't as "clean" as those produced in Bragg diffraction. We will numerically calculate the transmitted wavefunction produced in back diffraction, assuming that the initial spin is polarized along the flight direction. While real Laue back diffraction is not possible, since the angle between \mathbf{n} and \mathbf{k}_0 would be 90 degrees and the incoming wave wouldn't impact the crystal surface, we can tilt

the surface slightly to allow for a Bragg angle close to 90 degrees. In the following calculations we will however assume a flat surface and look at Bragg angles close to 90 degrees. Below in figure 3.16 one can see the orthogonal polarization components calculated using the exact wavefunction of a neutron initially polarized along the momentum direction, diffracted from [110] planes of quartz in Laue configuration. The figures indi-

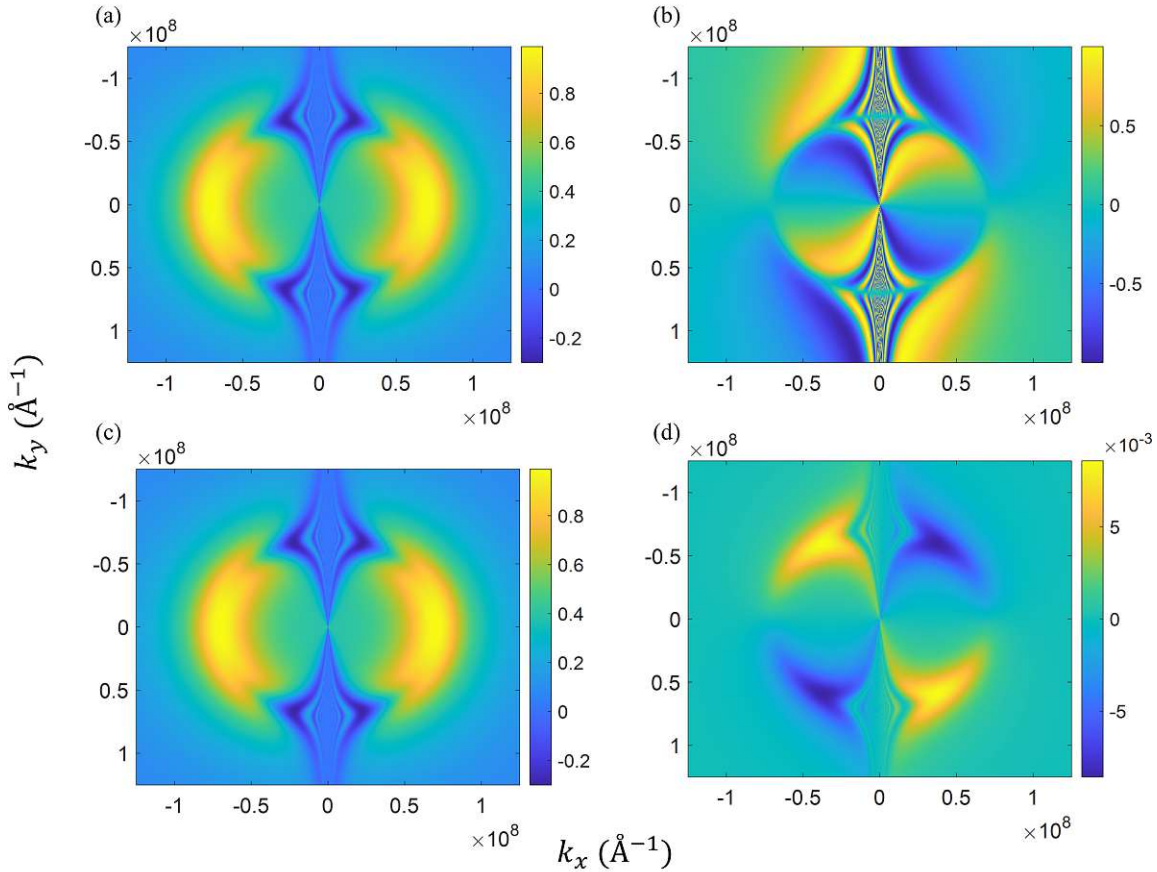


Figure 3.16: Orthogonal polarization components of a neutron diffracted from a 35 mm thick piece of [110] quartz. The initial polarization is chosen along the momentum direction x . The insets each show a different polarization component (a) P_y and (b) P_z of the transmitted beam and (c) P_y and (d) P_z of the reflected beam. Since the wavelength of the incident beam is chosen such that we are in a Backscattering configuration, $\lambda = 5.0279\text{\AA}$, k_x going through 0 represents the rocking angle surpassing 90 degrees which cannot technically be accomplished in a true Laue geometry, unless the entry surface of the crystal is tilted. Note the colorbar to the left of each figure, indicating that P_y of the transmitted and reflected waves are almost identical, however P_z of the reflected wave is a few orders of magnitude weaker than that of the transmitted wave.

cate that the polarization is separated over two lobes, the left lobe represents the side

of the rocking curve below the 90 degree Bragg angle which can be physically reached, while the right lobe goes beyond 90 degrees. In both lobes we see that the transverse polarization components of the transmitted wave follow very closely the azimuthal coordinate vector $\hat{\phi}$, indicating a coupling between polarization and orbit (i.e. spin-orbit entanglement). For the reflected beam it is evident that this coupling is much weaker. Orthogonal polarization components such as those seen in figure 3.16 are basically the interference between the non spin flipped ψ_+ and spin flipped ψ_- states. Hence a polarization vortex indicates that the OAM of the up and down spin states are different. To further explore this we can calculate the OAM distribution function of $\psi_+^* \psi_-$. By using this product common phase factors between the up and down wavefunctions can be eliminated. These distribution functions are shown in figure 3.17. Note that from this point forward all analysis focuses on the left lobe of the wavefunctions indicated in figure 3.16. Both figures in 3.17 show clearly that the average OAM of the flipped and

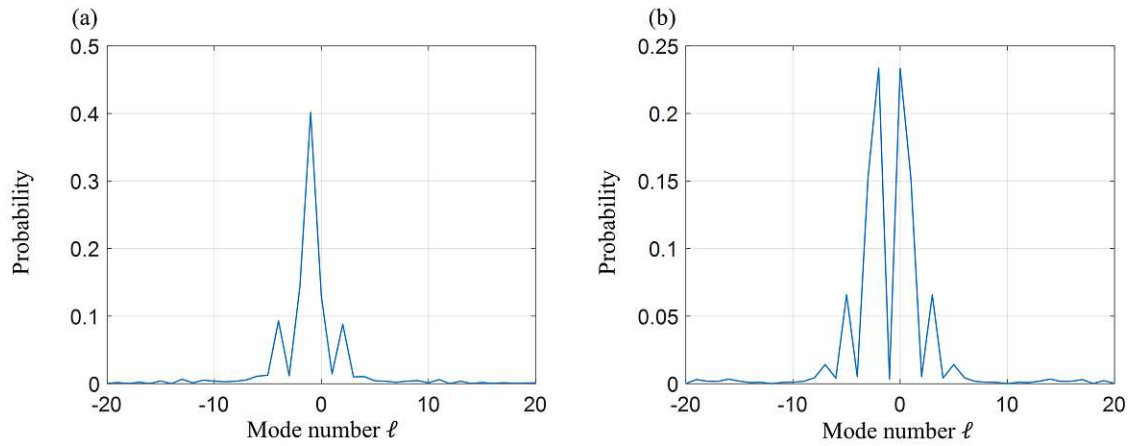


Figure 3.17: OAM distribution functions of the product between the conjugate of the up spin wavefunction with the down spin wavefunction, $\psi_+^* \psi_-$. Inset (a) shows the transmitted wave case, while inset (b) looks at the reflected wave. Both waves OAM distributions have an average mode number of $\bar{\ell} = -1$.

non flipped wavefunctions differ by one unit of \hbar , indicating that the electric field in quartz can lower/raise the OAM of an incident wave. Interestingly in the transmitted beam case the most prominent mode number is $\ell = -1$, while in the reflected case $\ell = 0$ and $\ell = -2$ are the most prominent modes. Indicating that the transmitted beam might be more useful for studying OAM dependent interactions (as we will see later), since the state is purer. We can finally look at the OAM distribution functions calculated using the pure wavefunctions ψ_+ and ψ_- . These are shown in figure 3.18. Note that these distributions feature many more symmetric sidebands, which emerge from the very fast Pendellösung oscillations induced by the nuclear potential in the crystal. Recall from section 2.5 that symmetric bands (i.e. equal amplitudes at $\ell = n$ and $\ell = -n$), which when calculating the OAM distribution functions of transverse standing waves, also indicate what we have termed linear OAM states. It is clear that both the reflected and transmitted spin flipped waves have had their OAM lowered as the central mode appears

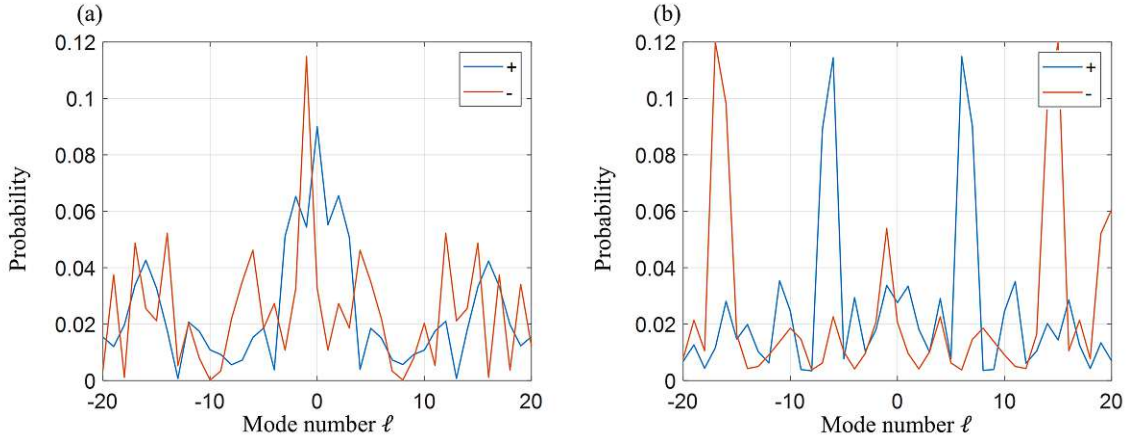


Figure 3.18: OAM distribution functions of the (a) transmitted and (b) reflected spin flipped (red) and non spin flipped (blue) wavefunctions. The average mode number of the spin flipped wavefunctions is $\bar{\ell} = -1$, while the non spin flipped wavefunctions have an average mode number of zero.

on $\ell = -1$ and the symmetric sidebands emerging from transverse standing waves have also been lowered by one unit of \hbar . The non spin flipped wavefunctions however appear to have an average OAM of zero, nonetheless, Laue diffraction appears to induce a great number of linear OAM modes.

We may conclude that both Bragg and Laue diffraction can be used to produce linear OAM states in thermal neutrons. In back diffraction the average intrinsic OAM produced in the Bragg and Laue case are the same. OAM produced by Bragg diffraction is cleaner and has a higher purity, however only in the Laue case can a sufficient intensity of OAM carrying neutrons be produced. A 35 mm thick crystal is sufficient to produce a maximally entangled spin-orbit state (i.e. a $\pi/2$ pulse). This observation leads us to conclude that experiments such as those described in [66] and [36], unknowingly produced twisted spin-orbit neutron waves before the field of twisted neutrons was even established.

3.3 OAM Generation in Bragg Reflection from Perfect Quartz

The previous sections of this chapter treated the theoretical arguments for OAM generation in neutrons by the Schwinger effect, specifically in dynamical diffraction from perfect crystals. In this section experiments testing the generation of spin-orbit states in thermal neutrons by dynamical diffraction are described. The example crystal used in all calculations was quartz, specifically the [110] planes. This was not a randomly chosen example, since quartz not only fulfills the theoretical conditions necessary to produce

large effective electric fields, such as non-centrosymmetry, but also can technically be produced to a high degree of perfection at a low cost. Hence also the crystals used in these experiments consist of perfect quartz, cut with surface parallel to the [110] planes.

Experiments described here were carried out at a thermal test beamline of the 2.3 MW reactor of the Reactor Institute Delft as a collaboration between TU Wien and TU Delft. A schematic of the setup is shown in figure 3.19. Neutrons are polarized vertically (i.e.

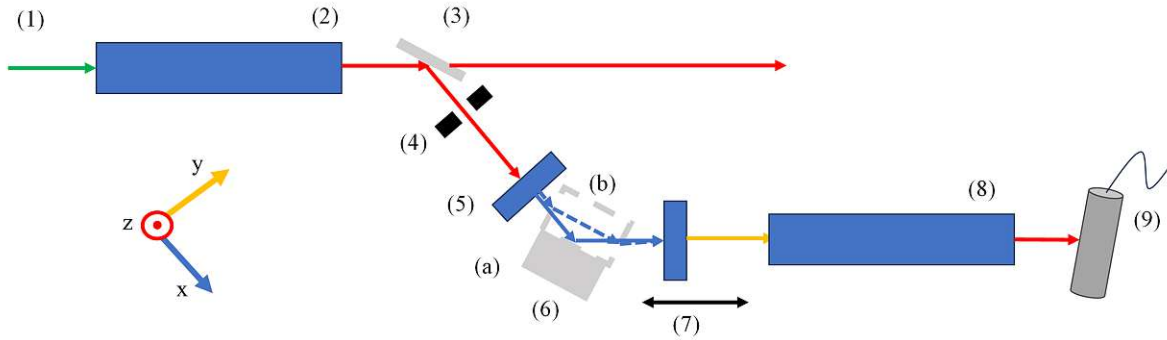


Figure 3.19: Schematic of the setup used to test spin-orbit state generation in neutrons by dynamical diffraction. A broad-band unpolarized (green) neutron beam comes from the guide (1) and enters a bender mirror (2) where the beam is polarized along z (red). A perfect crystal quartz monochromator (3) reflects a small portion of the beam into the setup. The crystal is cut such that the [110] planes are parallel to the crystal surface. The Bragg angle is chosen to be 22.5 degrees which results in a wavelength of 1.8 Å, corresponding to the peak of the spectrum. Neutrons continue from the monochromator through a slit collimator (4) to a $\pi/2$ flipper, which prepares the neutron spin along the x direction (blue). After this the neutron is Bragg (a) or Laue (b) reflected from a second "test" quartz crystal (6), cut in the same orientation as the monochromator. A movable $\pi/2$ flipper (7) paired with a polarization analyzer (8) project the neutron spin on the y direction (yellow). Finally the neutrons are detected using a He3 counter. A 1 mT guide field surrounds the entire setup. The test crystal is attached to a pair of rotation stages, enabling rotations around the z -axis (rocking) and the x -axis (tilt).

along z) by a polarizer mounted in the guide, after which they are Bragg reflected by a $25 \times 25 \times 5 \text{ mm}^3$ [110] quartz crystal into the setup. The first coil in the setup rotates the neutron spin such that it is parallel to the momentum (x -) direction. After this the neutrons are Bragg or Laue reflected from a $25 \times 25 \times 35 \text{ mm}^3$ [110] test quartz crystal. By combining a movable $\pi/2$ flipper and a polarization analyzer the y -projector can be measured. The advantage of using a quartz monochromator is that it removes minimal intensity from the guide, while at the same time providing a dispersion which fits the test crystal perfectly, hence minimizing unusable background in the setup. The Bragg angle was selected to use the peak of the spectrum offered by the guide 1.8Å. While the transmitted beam demonstrates unique polarization effects in Laue geometry, it was not

possible to measure these since the background in transmission direction was too high. Hence we will look at the polarization states produced first in Bragg geometry and then in Laue geometry.

3.3.1 Linear OAM States in Bragg Geometry

We begin by looking at the generation of linear OAM states in Bragg geometry. An unpolarized rocking curve compared to the theoretical expectation is shown in figure 3.20. The theoretical expectation is calculated by convolving two Bragg reflection curves,

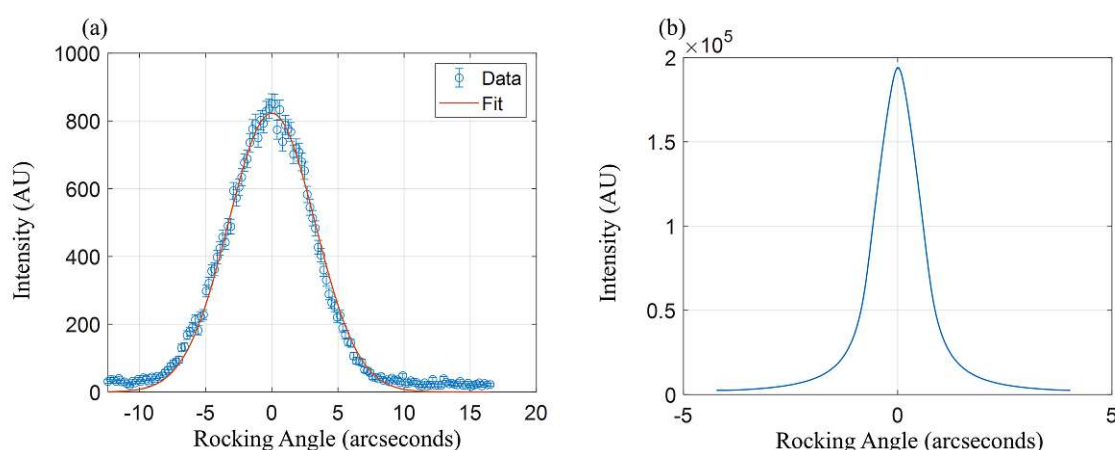


Figure 3.20: (a) Intensity measured against rocking angle in seconds of arc, the blue points show the data, while the red curve represents a Gaussian fit. (b) Theoretical expectation for the rocking curve according to the dynamical theory of diffraction.

comparable to figure 3.7, one for each crystal. One can see that the experimental rocking curve is significantly wider than the curve calculated using dynamical diffraction. The standard deviation of the two distributions differ by a factor of 4 – 6. Numerous explanations exist, ranging from imperfections in the test crystals leading to mosaicity to stress and strain within the test crystals leading to a gradient in the lattice spacing [86]. Regardless of the cause, a washing out of the rocking curve will also lead to a washing out of the spin-orbit coupling. This spin-orbit coupling observed in a Bragg reflection geometry is shown in figure 3.21 together with a simple model which convolves the calculated polarization (i.e. figure 3.11) with the estimated resolution function of the monochromator, a Gaussian with half the width of that shown in figure 3.20 (a). Qualitatively the two agree in terms of form. Quantitatively, slight differences can be seen in terms of amplitude and width, likely due to the fact that the resolution function of the monochromator is not exactly known, in addition to possible defects in the test crystal (described above), which perturb the polarization.

Nonetheless the data shows evidence for neutron spin neutron orbit coupling as the

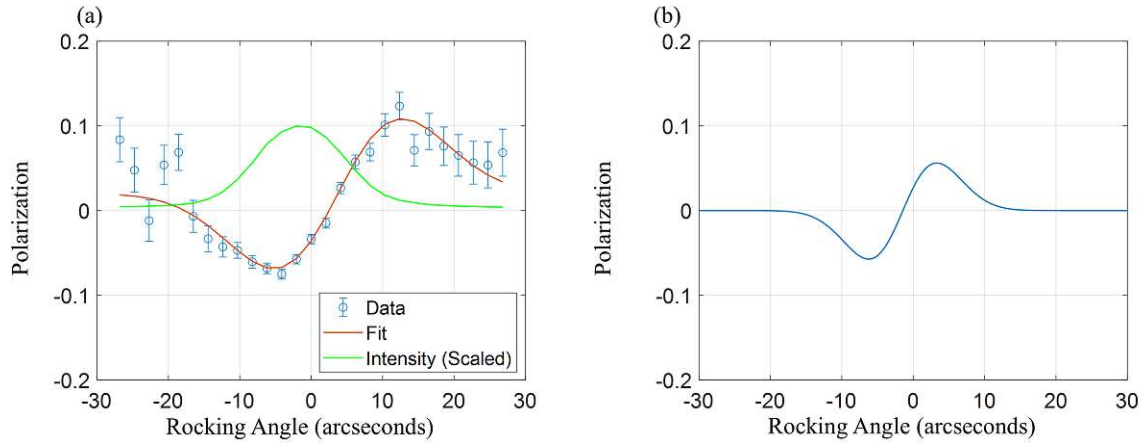


Figure 3.21: (a) The y polarization component measured against rocking angle in arcseconds. The data is shown in blue, while a fit, based on the first derivative of a Gaussian is shown in red. The rocking curve is shown scaled in green. This measurement is compared to (b) a model which convolves the expected polarization calculated using dynamical theory of diffraction with a Gaussian resolution function, to account for the momentum spread of the monochromator.

polarization rotates by 180 degrees for a 180 degree rotation of the transverse momentum. Since we do not expect a coupling between the any other momentum component with any other polarization component we may wish to conclude that we are dealing with a linearly polarized OAM state (i.e. a superposition of $\ell = \pm m$). To examine this in more detail we attempted to further characterize the spin-orbit state. To this end the z-polarization was also measured against divergence in z-direction. This is similar to tilting the crystal (i.e. changing the ρ angle). Recall in the case of an $\ell = -1$ or $\ell = +1$ state this polarization component ought to mimic the shape of the y-polarization against rocking angle (i.e. a flip in the divergence angle should flip the polarization component). Again the dynamical theory of diffraction predicts no such coupling for thermal neutrons in quartz, however other spin-optical components in the setup may introduce such a spin-momentum dependence. Our measurement was implemented by vertically scanning a thin horizontal cadmium slit between the analyzer and detector and measuring the z-polarization against the position of the slit. The analyzer coil (nr. 7 in figure 3.19) was disabled for this measurement. The polarization against the estimated vertical divergence angle is shown in figure 3.22. Despite the large error, the data shows a clear linear dependence of the z-polarization on the vertical divergence angle. Our model using dynamical diffraction predicts a spin rotation on the order of 10^{-3} radians, smaller than the measurement error. Hence a different mechanism is necessary to explain this coupling. Such a mechanism is proposed in figure 3.22 (b). If the preparation coil is tilted even by a small amount, neutrons traversing through the coil with a divergence in direction of the coil tilt experience a shorter path length and therefore less spin rotation than neutrons traveling straight through the coil. In addition neutrons diverging under

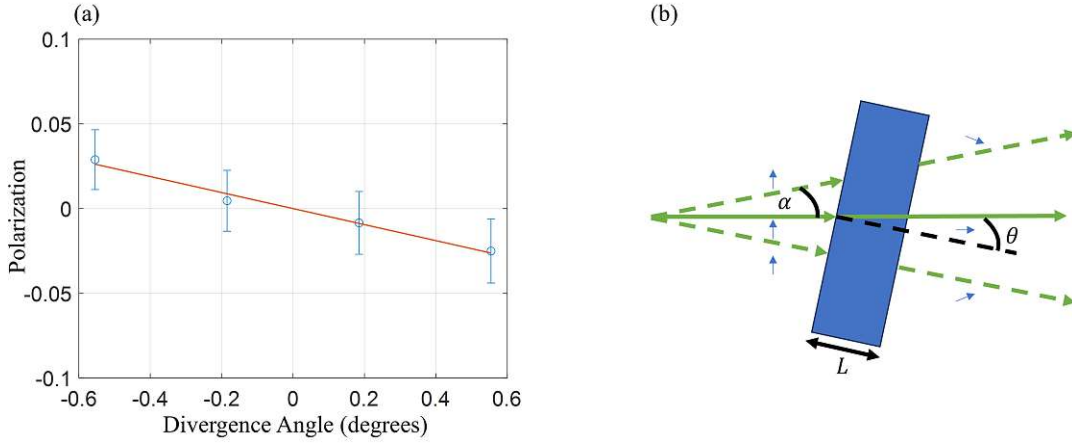


Figure 3.22: (a) z (vertical) polarization component measured as a function of vertical divergence in degrees. A linear fit is shown in red. (b) Hypothetical mechanism by which this momentum-spin coupling is produced. A divergent neutron beam (green) passes through a slightly tilted coil (blue square). Due to the different path lengths taken through the coil, the spin (blue arrows) rotation angle becomes coupled to the divergence angle.

an angle opposite the tilt angle of the coil experience an even larger path length causing the spin to be over-rotated. This divergence dependent phase can be expressed as

$$\delta\phi = \gamma B \frac{\Delta L}{v} = \gamma B \frac{L}{v} \left[\frac{1}{\cos(\theta)} - \frac{1}{\cos(\theta - \alpha)} \right] = \frac{\pi}{2} \left[\frac{1}{\cos(\theta)} - \frac{1}{\cos(\theta - \alpha)} \right] \quad (3.80)$$

θ is the tilt angle of the coil and α the divergence angle of the beam. In the last step we assume that B is chosen such that for $\alpha = 0$ the coil provides a $\pi/2$ flip. For small θ this equation is second order in α . In the case of a 5 degree coil tilt the spin phase would change by $5 \cdot 10^{-4}$ radians over a 1 degree divergence change. However, if an external guide field is present a larger B field is required to produce the $\pi/2$ leading to a larger divergent dependent phase. For a 1 mT guide field and a 5 degree coil tilt the spin phase as a function of divergence increases significantly to $1.5 \cdot 10^{-2}$. The effect can be further amplified in the case of an open coil design as in our experiment, since the field bulge results in a higher effective θ . This method of tilting a magnetic field region to generate spin-momentum coupling, here used unintentionally, is the basic principle behind Spin Echo Small Angle Neutron Scattering (SESANS) [39, 40] and the coherent averaging method for producing OAM states [31, 32, 33, 38] discussed in chapter 5.

However figure 3.22 demonstrates that P_z is rather small compared to P_y shown in figure 3.21, hence on the momentum scale of the rocking width the OAM state of the wavefunction can be understood as a linearly polarized state. Adding a sufficiently strong vertical magnetic gradient however, could produce an $\ell = 1$ or $\ell = -1$ state on the same length/momentum scale. Note that this length/momentum scale is quite important, as for thermal neutrons diffracted from quartz the vertical momentum spread is much wider than in rocking direction, hence when calculating the expectation value integral $\langle L_z \rangle$

the OAM washes out when integrated over the whole space. If one however constrains integration to a length/momentum scale similar to that of the rocking width one would find a non-zero value, even in the thermal neutron case.

3.3.2 Null Result in Laue Geometry

We now move on to Laue geometry where the polarization of the reflected beam was measured as a function of rocking angle. Recall that the theory of dynamical diffraction predicts no visible coupling between momentum and polarization in this case. In this measurement the crystal was moved into Laue geometry ((b) in figure 3.19). Again the preparation coil was used to prepare the neutron spin along the momentum direction, while the analysis coil together with the polarization analyser measured the orthogonal, y component of the polarization. This y component is measured against rocking angle and shown in figure 3.23. Our measurement confirms the lack of polarization rotation

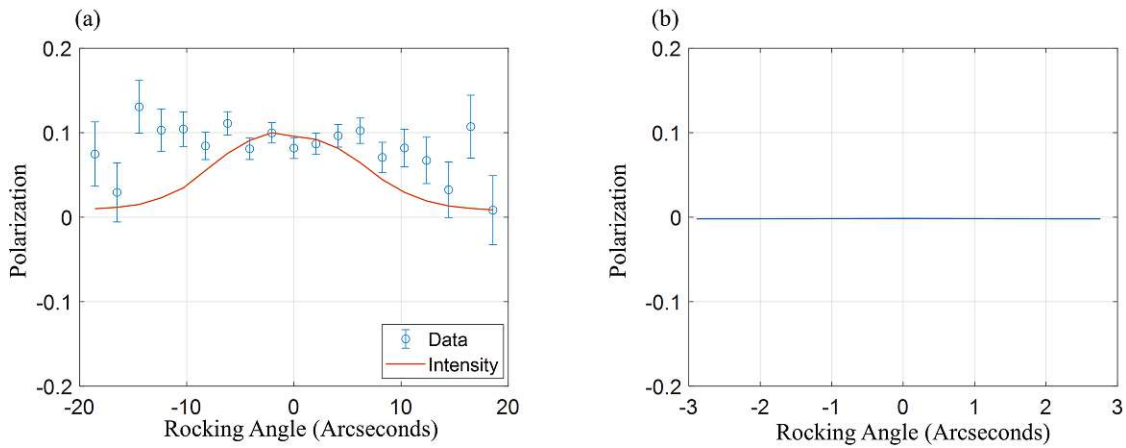


Figure 3.23: (a) y-component of the neutron polarization against rocking angle in Laue reflection geometry. The data is shown in blue, while the intensity/rocking curve is shown in red. (b) Predicted y polarization of the Laue reflected beam according to the dynamical theory of diffraction.

predicted by the dynamical theory of diffraction, shown in figure 3.23 (b). However we may observe that the measured rocking width is much wider than the predicted width according to the dynamical theory, hence any Schwinger effect would also be weakened.

Recall that our theory does predict that the spin flipped wavefunction carries OAM, however the observable evidence for this isn't as obvious as in the transmission or Bragg case, where we can observe a coupling between polarization and momentum. These other OAM dependent observables, such as the change in absorption cross sections were not measured in this experiment but are discussed in more detail in the chapters on OAM detection.

3.4 Conclusion

In this chapter we have seen that static electric fields act as a sort of catalyst enabling coupling between neutron spin and neutron momentum. The exchange of spin angular momentum to the neutron momentum generates OAM by the principle of angular momentum conservation. The nature of this mechanism also ensures that the spin and OAM degree of freedom become coupled or entangled, thereby generating so called spin-orbit states. While the electric fields produced in the lab are too low to create significant OAM, the nuclear electric field found between nuclei and electrons is about the right order of magnitude to produce large amplitudes of non-zero OAM states. These fields can be exploited in diffraction from perfect non-centrosymmetric crystals. We investigated OAM generation in neutrons in dynamical diffraction from quartz, both theoretically and experimentally. We found a backscattering configuration to be ideal for producing twisted wavefronts. In Bragg geometry we found that the spin-flipped transmission and reflection wavefunctions carry a classic spiral phase pattern, however the amplitude of this state is relatively small. In Laue geometry we found that the OAM of the spin-flipped wavefunction is raised or lowered compared to the non-spin-flipped wavefunction and the amplitude of the spin-flipped wavefunction can be significant, however many sidebands are produced in the OAM spectrum. Hence, the state is not pure. Finally an experiment was presented which looked at spin-orbit coupling in thermal neutron reflected from perfect quartz. In Bragg geometry we found a positive result and argued that the OAM state can be interpreted as a linearly polarized state and could be transformed into an $\ell = 1$ or $\ell = -1$ state with an appropriate magnetic gradient. In Laue reflection we found no such coupling between momentum and polarization, confirming our theoretical predictions.

4 OAM Generation in the Neutron Nucleus Weak Interaction

In the previous chapter we exploited that electric fields act as a mediator effectively coupling neutron momentum to neutron spin, allowing for angular momentum exchange between the two. We found that if spin angular momentum is transferred to the neutron momentum by a spin flip, OAM is generated to conserve total angular momentum. Hence we can imagine that any interaction that couples neutron momentum to neutron spin can produce OAM states. The weak interaction is another such example. This, including the neutron nucleus weak interaction is explored in great theoretical detail in [87], which already includes angular momentum considerations. While the weak interaction can be observed in a variety of ways, purely using neutrons this interaction can be observed through the slight neutron spin rotation induced by the interaction. However, since the interaction strength is so low, this spin rotation can only be observed, to date, in materials that exhibit a strong p-wave resonance, which amplifies the weak interaction [88]. Some of these resonances are broad enough such that the spin rotation can even be observed in cold and thermal neutrons. Hence in 1980 this spin rotation was observed for the first time after passing cold neutrons through specific tin isotopes, which exhibit a broad p-wave resonance [89]. Only four years later the spin rotation effect was observed from the strongest known amplifier of the neutron nucleus weak interaction: Lanthanum 139 [37]. Despite being the strongest amplifier of the neutron nucleus weak interaction the total effect still only amounts to a spin rotation of $2.2 \cdot 10^{-4} \text{rad} \cdot \text{cm}^{-1}$. Furthermore, due to strong absorption in these materials the neutron nucleus weak interaction is not likely to be a primary method by which OAM is produced in thermal and cold neutrons. Nonetheless it may represent an interesting avenue for analyzing neutron OAM.

In addition to Tin and Lanthanum a few other nuclei have been found to exhibit a strong p-wave resonance, such as Xenon-131 [90], Bromine-81 and Cadmium-111 [91]. Since then spin-optics adapted to epithermal ($\propto \text{eV}$) neutrons, such as the polarized Helium-3 based neutron spin filter [92, 93], have been developed, which help to explore these spin rotations closer to the resonance energy [94, 95]. At these energies the effect is much more pronounced. In Lanthanum the spin rotation is about ten times stronger than for thermal and cold neutrons. This in addition to the lack of a large arsenal of neutron optical devices for these energies, may make Lanthanum not only a good spin polarizer/analyzer, but also ideal for OAM generation/detection.

Similar to the last chapter we will begin by exploring the theoretical basis for OAM

generation in the neutron nucleus interaction weak interaction, starting from the weak potential in the Schroedinger equation. Finally we report on an experiment demonstrating angular momentum conservation in the neutron nucleus weak interaction.

4.1 Theoretical Framework

Our starting point for analyzing OAM generation in the neutron nucleus weak interaction will be the Hamiltonian derived from the lowest order approximation of the weak interaction [87].

$$\hat{H} = -\frac{\hbar^2}{2m}\nabla^2 + b\hat{\sigma} \cdot \hat{p} \quad (4.1)$$

with b effectively a coupling constant for the weak interaction. We note that there exists also a so called spin dichromism term proportional to $ib'\sigma \cdot \hat{r}$, which can be used to polarize neutrons with energies close to the p-wave resonance. Given that the form of this term is similar to that of a magnetic quadrupole [30], which is known to generate OAM, one may intuit, that this term also promotes OAM generation. However as b' drops off quickly away from the resonance this term is no longer relevant for cold and thermal neutrons and hence we ignore it in our analysis of OAM generation in the neutron nucleus weak interaction in cold and thermal neutrons.

Our Hamiltonian 4.1 is quite close to that of a neutron in an electric field experiencing the Schwinger interaction 3.2. The main difference being that the weak potential couples spin and momentum directly via the dot product. Hence, the subsequent derivation of the neutron wavefunction will follow closely the derivation detailed in the previous chapter. The analysis of this Hamiltonian begins by taking the Fourier transform and examining its form in reciprocal cylindrical coordinates.

$$\hat{H} = k_r^2 + k_z^2 - b' \begin{pmatrix} k_z & k_r e^{-i\phi} \\ k_r e^{i\phi} & -k_z \end{pmatrix} \quad (4.2)$$

Note that $\frac{\hbar^2}{2m}$ has been set to one. We observe the OAM raising/lowering operator on the off-diagonal components of the potential matrix, indicating that angular momentum changes that occur due to spin flips can be conserved by OAM generation. Applying a parity ($\mathbf{r}' \rightarrow -\mathbf{r}$) or mirror ($r'_i \rightarrow -r_i$) operation to this Hamiltonian, leads to a flip of the sign of the potential. Hence, our interaction does not conserve parity, it is *parity odd*.

The Eigenvalues of our Hamiltonian are given by $E_{\pm} = k_r^2 + k_z^2 \mp b'\sqrt{k_r^2 + k_z^2}$, where the \pm subscript denotes the up and down spin state respectively. We can diagonalize the Hamiltonian such that $\hat{H}' = T^{-1}\hat{H}T$, with

$$T = \begin{pmatrix} e^{-i\phi} \frac{[k_z + \sqrt{k_r^2 + k_z^2}]}{k_r} & e^{-i\phi} \frac{[k_z - \sqrt{k_r^2 + k_z^2}]}{k_r} \\ 1 & 1 \end{pmatrix} \quad (4.3)$$

In this transformed frame we can solve the time dependent Schroedinger equation:

$$\hat{H}'\hat{\psi}' = \frac{\partial}{\partial t}\hat{\psi}' \quad (4.4)$$

The solution for the reciprocal wavefunction $\hat{\psi}'$ is then given by

$$\hat{\psi}'_{\pm} = a_{\pm}e^{iE_{\pm}t} \quad (4.5)$$

Finally we determine $\hat{\psi}$ by inverting the transform: $\hat{\psi} = T\hat{\psi}'$. Furthermore we find the integration constants a_{\pm} using the initial conditions $\hat{\psi}_{\pm}(t=0) = c_{\pm}(k_r, \phi, k_z)$.

$$\hat{\psi} = \begin{pmatrix} c_+ \cos(b'\sqrt{\epsilon}t) - i\left[\frac{c_+k_z}{\sqrt{\epsilon}} - \frac{c_-k_r}{\sqrt{\epsilon}}e^{-i\phi}\right] \sin(b'\sqrt{\epsilon}t) \\ c_- \cos(b'\sqrt{\epsilon}t) + i\left[\frac{c_-k_z}{\sqrt{\epsilon}} - \frac{c_+k_r}{\sqrt{\epsilon}}e^{i\phi}\right] \sin(b'\sqrt{\epsilon}t) \end{pmatrix} \quad (4.6)$$

with $\epsilon = k_r^2 + k_z^2$ the kinetic energy parameter. Up to now we haven't defined a flight direction or initial spin orientation. Both can be freely chosen. Defining the direction of propagation along z (i.e. $k_z \gg k_r$), we can choose to have the initial spin aligned in this direction too. If the initial spin is prepared along the flight axis (z -direction) with $c_- = 0$, we find that over time the spin rotates to point anti-parallel to the flight axis. During this process the wavefunction obtains one unit of \hbar of longitudinal orbital angular momentum parallel to the propagation direction. Hence the total angular momentum of the neutron is conserved. This mechanism is proportional to $\frac{k_r}{\epsilon}$, which is equal to the beam divergence for small angles, hence this type of parity odd spin rotation is roughly a factor of 100 to 1000 weaker than previously observed parity odd spin rotation, where the spin is prepared perpendicular to the flight direction. When we look at the case where the initial spin is prepared perpendicular to the flight path (i.e. the classical parity non-conserving spin rotation experiments [37]), we find that transverse OAM is generated. In this case we place the propagation direction in the k_r plane, while we take the initial spin perpendicular to the flight path (for example $c_- = 0$). k_r is now the dominating factor, while $c_{\pm} \frac{k_z}{\sqrt{\epsilon}} \approx 0$. Under this approximation and $\sqrt{\epsilon} \approx k_r$ the expression 4.6 becomes identical to the expression found for twisted neutrons in electric fields eq. 3.28.

$$\hat{\psi}_{\pm} = c_{\pm} \cos(b'k_r t) \pm ic_{\mp} e^{\mp i\phi} \sin(b'k_r t) \quad (4.7)$$

Thus all parity odd spin rotations induced by the neutron nuclear weak interaction are compensated by an equal amount of orbital angular momentum generation thereby preserving total angular momentum.

As with electric fields in the transverse case the generated OAM is extrinsic and consists simply as a displacement of the spin flipped wavefunction with respect to the incident and non spin flipped wavefunction, such that $p\Delta x = \pm\hbar$. For a single unit of OAM this displacement corresponds to about one sixth of a wavelength. Resolving such a small displacement would be difficult. In general doing so would require a potential which presents a gradient in the direction of the displacement. This can be realized for example by refraction or reflection from a curved mirror. An additional difficulty

arises from the weak interaction strength, as stated in the introduction thermal neutrons experience a spin rotation of $2.2 \cdot 10^{-4} \text{ rad} \cdot \text{cm}^{-1}$ in Lanthanum-139, leading to a very weak signal.

In the longitudinal OAM case, where the initial spin is also longitudinal, the efficiency is modified by a factor k_{\perp}/k_{\parallel} . Hence it is particularly effective to use a conical beam with a large opening angle to detect the longitudinal OAM effect. This can be achieved by passing a neutron beam through a powdered crystal. Diffraction from the powder causes the beam to be reflected on to multiple cones, where the opening angle of the cone corresponds to four times the Bragg angle of the respective lattice plane. After scattering the conical beam can be passed through a weak field, where the spin couples to the transverse momentum component. Since this momentum component is coupled to the angular coordinate on the cone, the spin after passing through the weak field will be aligned to the azimuthal coordinate, thereby producing a spin-orbit entangled state. This setup is shown in figure 4.1 Such an experiment requires a spin analyzer

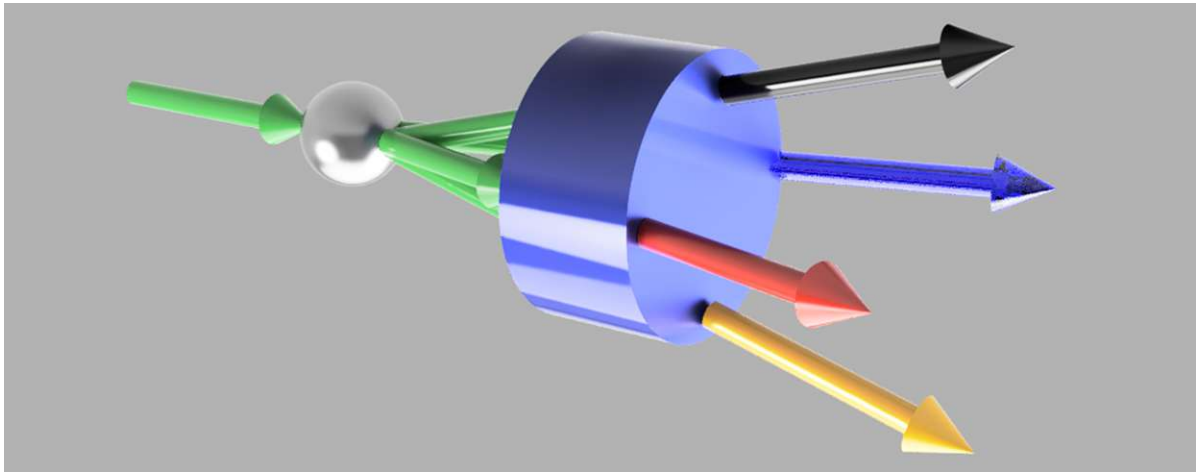


Figure 4.1: Schematic representation of a proposed setup to measure the longitudinal OAM generating mechanism in the weak interaction. An incident neutron (green arrow) with longitudinal polarization is scattered by a powder sample (metallic sphere) into a conical beam. This beam traverses through cylindrical Lanthanum-139 sample (blue), where the initially longitudinal spin couples to the transverse momentum component, thereby coupling the spin to the azimuthal coordinate. This spin-orbit coupling is visualized by the colors of the exiting beams, black and yellow represent spin right and spin left, while blue and red indicate spin up and spin down.

with a wide angular and spatial acceptance to resolve the spin structure of the conical beam. In addition an appropriate powder sample is required to produce a beam with an appropriate opening angle and significant intensity. While these technical challenges can be overcome, in a demonstration experiment they can be circumvented by realizing that the proposed experiment relies simply on the dot product between spin and momentum. In figure 4.1 the momentum structure is conical and the spin longitudinal, however this

can just as well be reversed, such that one uses a par-axial beam with a conical spin distribution across the beam. This leads to the exact same dot product $\sigma \cdot \mathbf{p}$ as the case shown in the figure. Doing so removes the need for a wide angle spin analyzer as well as an appropriate powder sample. These requirements are replaced by the need for a spin optical device, which can produce the conical spin pattern. This can be accomplished using a magnetic quadrupole [30]. Note that this particular spin pattern corresponds to a spin orbit state. When passed through a weak field the spin-orbit pattern is rotated around the optical axis, despite this changing the spatial distribution of OAM and spin angular momentum, the total angular momentum of the neutron is conserved. Although this effect can be reproduced with a longitudinal magnetic field, the magnetic interaction does not generally conserve the total angular momentum of a neutron. In addition to demonstrating that the weak interaction conserves total angular momentum, it can be argued that the described experiment shows that the weak interaction generates OAM. In particular when one takes the difference between the spin-orbit pattern produced by the quadrupole and the pattern produced using the combination of quadrupole and weak field one obtains another spin-orbit pattern equivalent to that which would be produced in the conical beam experiment (figure 4.1).

4.2 Experimental Evidence for Angular Momentum Conservation in the Neutron-Nucleus Weak Interaction

In this section we explore an experiment, demonstrating OAM production and angular momentum conservation in the neutron nucleus weak interaction. Our experiment, arose from a collaboration between TU Wien and Indiana University and was conducted at the IN3 triple axis instrument of the Institute Laue Langevin, which hosts a 60 MW research reactor. Our setup, shown in figure 4.2, uses a magnetic quadrupole to produce a spin-orbit pattern, as described in the previous section. This spin-orbit pattern is past through a 5 cm long Lanthanum-139 sample, the strongest known amplifier of the neutron nucleus weak interaction. Since the interaction strength is weak ($2.2 \cdot 10^{-4} \text{ rad} \cdot \text{cm}^{-1}$), both the Lanthanum target and the quadrupole are contained within a zero field chamber. This zero field chamber, originally named Poly-Axis Neutron Depolarization Analyzer (PANDA) [96], kindly provided by the Reactor Institute Delft, consists of three shielding layers, two passive metal (steel and μ metal) and one internal active stage. This active shielding is realized by three pairs of orthogonal Helmholtz coils. The coils are driven using a feedback loop which is controlled using a fluxgate inside the zero field chamber. When activated the remnant field in the chamber can be suppressed to $\propto 100 \text{ nT}$. The Lanthanum target sits in an aluminium and μ metal housing, to further suppress the field and prevent oxidation. In addition to the magnetic shields PANDA has a pair of mezei and v-coils on the entrance and exit of the chamber, so that the neutron spin can be prepared and analyzed along any direction.

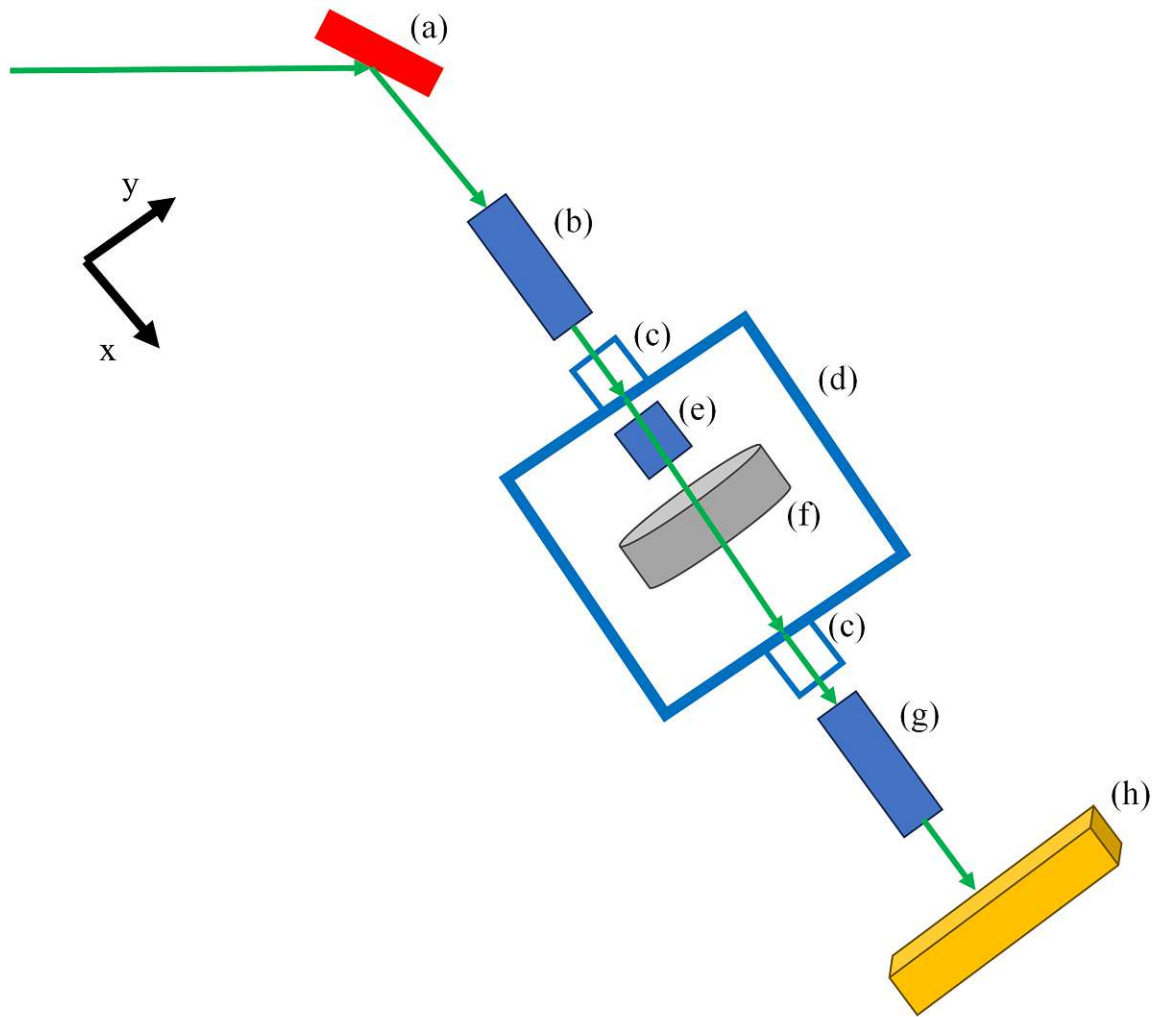


Figure 4.2: Schematic representation of a top down view of the setup at IN3 used to demonstrate OAM generation and angular momentum conservation in the weak interaction. Thermal neutrons coming from the guide are Bragg diffracted and monochromatized ($\propto 1.8\text{\AA}$) by a pyrolytic graphite crystal (a). After reflection neutrons are polarized by a bender polarizer (b). Next neutrons enter the zero field chamber (d) via the spin preparation/analysis coils (c). Inside the chamber a spin orbit state is prepared using a quadrupole (e), after which neutrons propagate through a Lanthanum target. Behind the zero field chamber a bender (g) analyzes the neutron spin. Finally a position sensitive detector (h) resolves the spin-orbit pattern. The x and y axes are shown in black, while the z-axis points out of the page.

The instrument uses a pyrolytic graphite monochromator in a thermal guide to reflect neutrons from the thermal peak into the setup. Neutrons are then polarized via a bender and enter into the PANDA chamber. While entering the chamber the neutron spin is rotated in the longitudinal (x) direction. Inside the chamber a quadrupole produces the

spin orbit pattern. To resolve the spin orbit pattern both transverse spin components need to be analyzed using the exit coils and the bender and the resulting intensity pattern must be imaged using a position sensitive detector. In our case the position sensitive detector consists of a Helium-3 wire chamber with $2 \times 2 \text{ mm}^2$ resolution [97, 98]. At thermal energies the efficiency is around 80%. When the Lanthanum is inserted in the beam the spin orbit pattern is rotated. By subtracting the spin pattern measured without Lanthanum from the pattern measured with Lanthanum one can obtain the OAM generation efficiency, as well as the change in spin. This allows us to determine whether or not angular momentum is conserved within the neutron.

The magnetic quadrupole is realized by a figure eight coil. Pictures of this quadrupole, the setup, PANDA and the packed Lanthanum target are shown in figure 4.3.

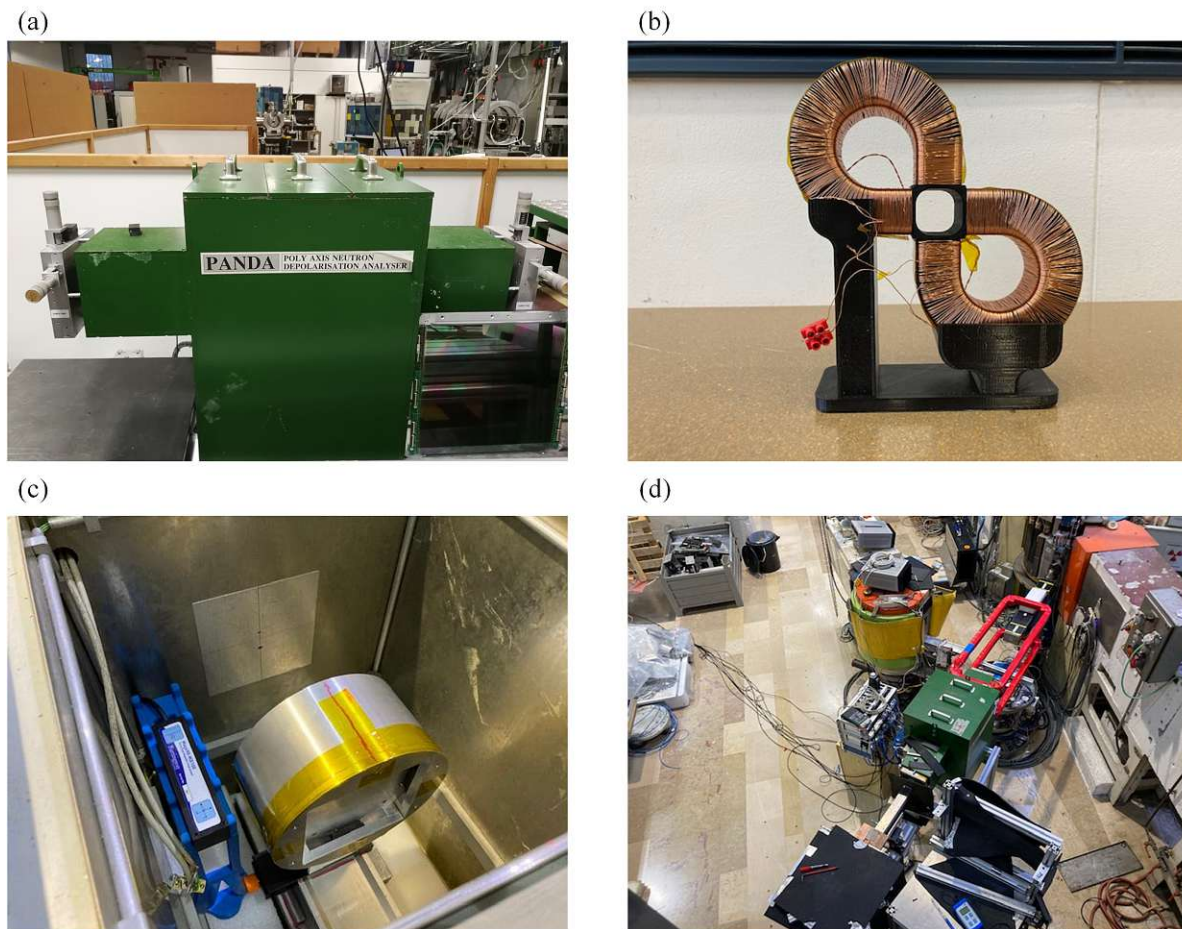


Figure 4.3: Pictures of the zero field chamber PANDA (a), the magnetic quadrupole used to produce spin-orbit patterns (b), the Lanthanum target inside of the zero field chamber (c) and the full setup at IN3 (d).

We note that this is the first neutron spin-optical experiment demonstrating twisted spin patterns using a magnetic quadrupole. The transverse polarization patterns produced

using the quadrupole are shown in the top insets of figure 4.4. These spin orbit patterns rotated by the weak interaction are shown in the bottom insets. This rotation is cannot be seen upon visual inspection, hence additional analysis is required, to determine the rotation angle. To this end we make circular cuts out of the y and z polarizations and

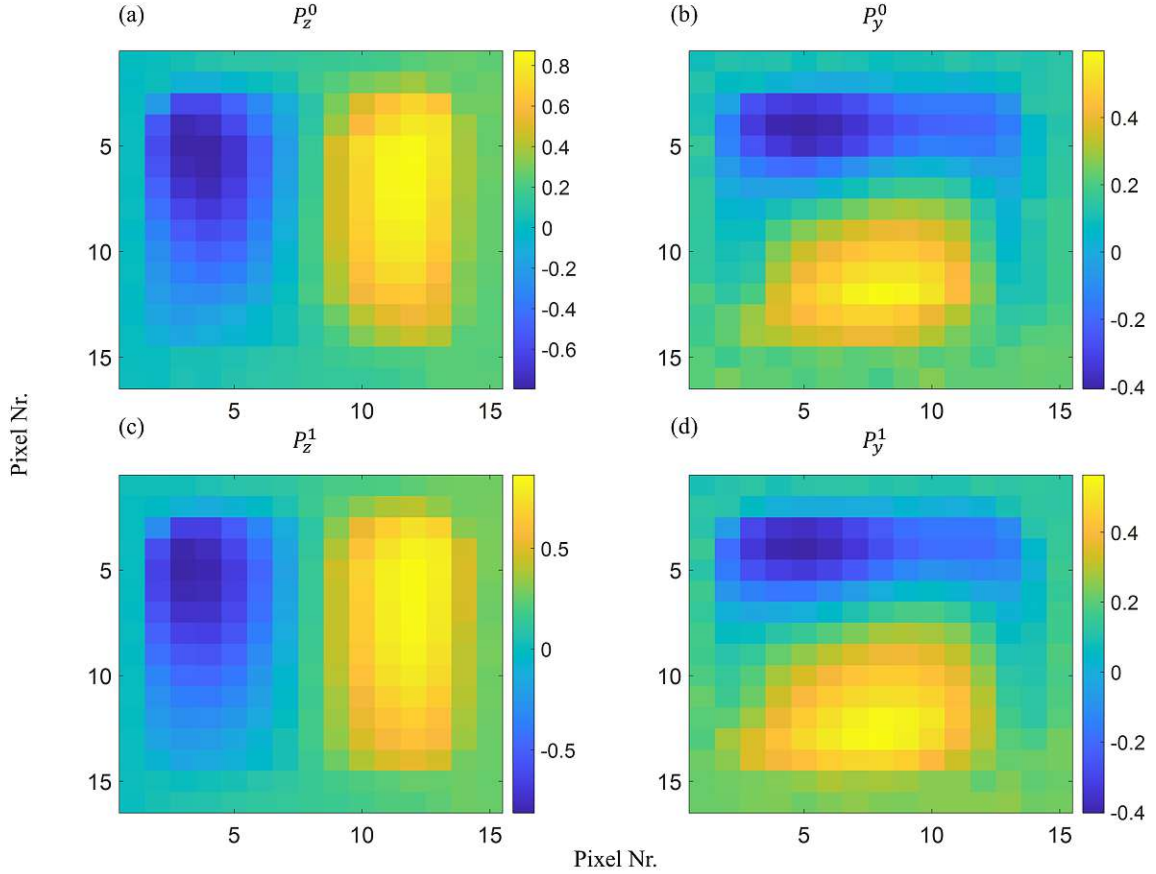


Figure 4.4: Transverse polarization patterns produced using the quadrupole magnet. The z component is shown in (a), while the y component can be seen in (b). The same components are shown rotated due to the weak interaction in (c) and (d) respectively.

perform AFTs on each cut. For illustration purposes we have plotted the polarization against the azimuthal angle ϕ for one such circular cut in figure 4.5. Here the y and z polarization are shown for a cut out of the spin-orbit pattern produced by the quadrupole without Lanthanum in the beam. After performing these cuts for various different radii, we apply the azimuthal Fourier transform for $\ell = 1$ to extract the phase of this particular OAM mode from $P_y + iP_z$. Finally the extracted phases are averaged over the different radii and the average phase determined without the Lanthanum sample is subtracted from the phase determined with the Lanthanum sample in the beam. The phase is shown as a function of the ring radius in figure 4.6. When calculating the weighted average over these phases we find an average image rotation of $(2.4 \pm 0.27) \cdot 10^{-3}$ radians.

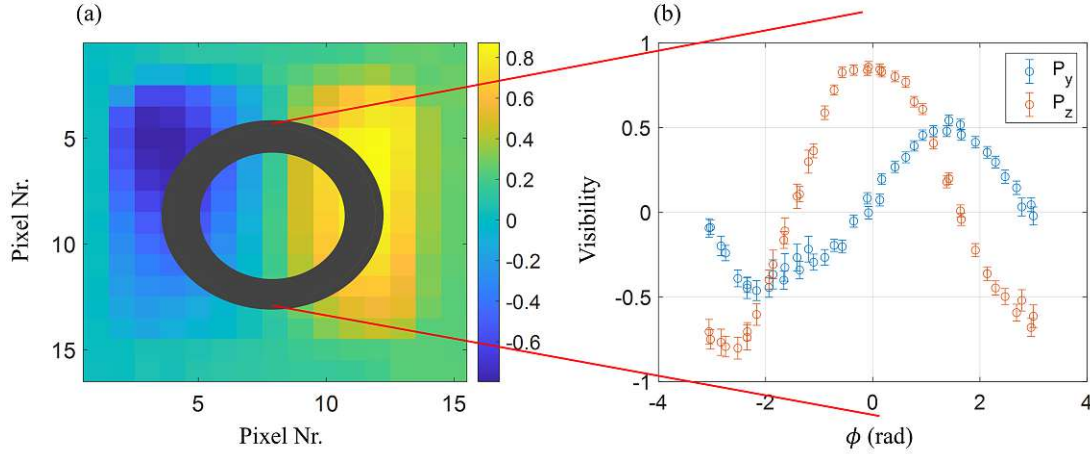


Figure 4.5: Polarization against azimuthal angle (b) for a certain circular cut out of the two dimensional polarization pattern (a). The circular cut taken is shown as a grey annulus. The pixels that lay inside of the ring are used to construct the polarization plots seen in (b).

This is about two times the rotation expected due to the weak interaction, hence it is reasonable to assume that the Lanthanum sample includes a magnetic component arising from ferromagnetic impurities in the sample. This can be isolated by rotating the Lanthanum sample by 180° such that the surface normal is inverted. This inverts the effective magnetic field due to impurities seen by the neutrons, while leaving the weak contribution unchanged. Doing so we find that the magnetic contribution to the spin rotation was $1.1 \cdot 10^{-3}$ radians. Hence we can conclude that the contribution coming from the weak interaction is within the expected range for Lanthanum. At this point we note that this is the first measurement of the parity non-conserving spin rotation produced by Lanthanum in thermal neutrons. We find, as expected, that this value does not differ from that found in cold neutrons [37]. At the start of this section we promised to demonstrate that the angular momentum of the neutron is conserved in the weak interaction. In figure 4.7 we show the orbital and spin angular momentum of the beam with and without the Lanthanum sample in the beam as a function of beam radius. The OAM is calculated simply via the expectation value of $-i\frac{\partial}{\partial\phi}$, while the Spin expectation value is approximated by the average magnitude of the measured 2D polarization vector.

The difference between the total angular momentum of the empty beam and the beam with Lanthanum in it is zero to within error ($\pm 4 \cdot 10^{-4}$).

Finally at the beginning of this section we argued that the difference between the spin patterns produced with and without Lanthanum in the beam is also twisted and carries one unit of OAM. Figure 4.8 shows the OAM distribution function calculated using this difference. It can be seen that the main mode number in this case is also $\ell = 1$. This demonstrates that a neutron which possesses a spin-momentum pattern such that $\sigma \cdot \mathbf{p}$ is conical in space will gain some OAM as it traverses through a weak field.

4 OAM Generation in the Neutron Nucleus Weak Interaction

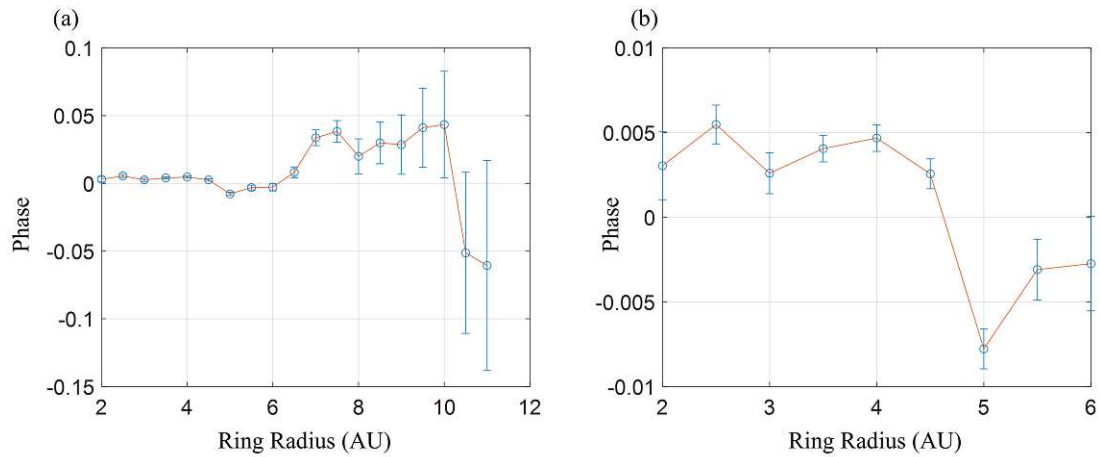


Figure 4.6: Image rotation phase plotted against the ring radius within which the image rotation is calculated. Inset (a) shows the entire dataset, while inset (b) shows a zoomed variant, localized to an area in which the statistical error was small.

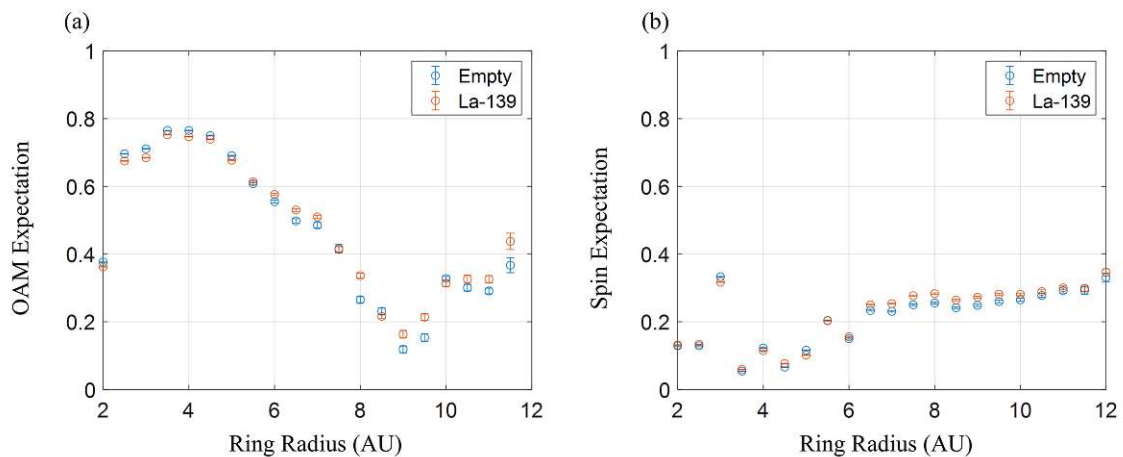


Figure 4.7: (a) Expectation value of the orbital angular momentum operator as function of beam radius for the empty beam (blue) and the case where Lanthanum is inserted into the beam (red) and (b) the expectation value of the spin angular momentum as a function of beam radius.

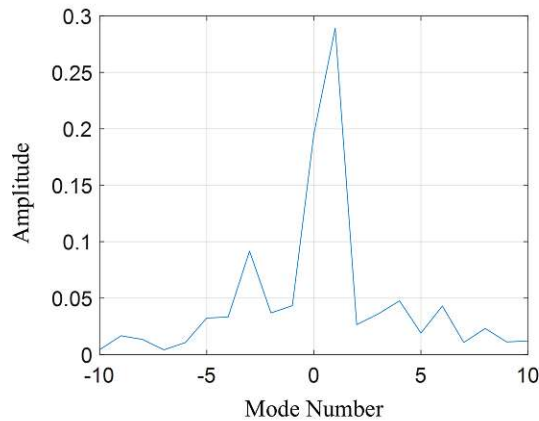


Figure 4.8: OAM distribution function of the difference between the spin pattern produced with and without Lanthanum in the beam.

4.3 Conclusion

We have demonstrate that the neutron nucleus weak interaction in a very similar way to the Schwinger interaction generates OAM in neutrons by spin flips and conservation of total angular momentum in the neutron. Furthermore using thermal neutrons we have experimentally confirmed previous experiments done with cold neutrons on Lanthanum-139 that the weak interaction in this sample, amplified by a p-wave resonance, induces a parity non conserved spin rotation of $(2.2 \pm 0.5) \cdot 10^{-4} \text{ rad} \cdot \text{cm}^{-1}$. By entangling spin and OAM this spin rotation is transferred to an image rotation which we have measured experimentally. Our experiment simulates a neutron beam with a conical momentum distribution by introducing a conical spin distribution using a magnetic quadrupole and demonstrates that in this case one unit of OAM is generated in the neutron. Finally we showed that in this experiment total angular momentum is conserved in the neutron to within statistical error.

5 Coherent Averaging

In this chapter we explore the application of coherent averaging, originally a technique to enhance measurement sensitivity [99, 100], to OAM generation [32]. In the context of this chapter we view coherent averaging as an interferometric technique, which takes a simple input wavefunction and splits this input wavefunction up into an arbitrary number of copies called partial wavefunctions. Simple neutron optical devices, such as prisms or magnetic coils are used to individually manipulate these partial wavefunctions (i.e. translations/phase shifts). Then, finally, these partial wavefunctions are recombined to generate the output wavefunction. Hence one can look at coherent averaging as exploiting the Huygens principle to generate any kind of structured wavefunction [101]. As a reminder, Huygens principle states that a wave of any structure can be seen as an infinite number of spherical point sources with a unique phase.

Generation of non-zero average OAM can occur with as few as three partial wavefunctions. Take the simple example of a Gaussian input wavefunction, split into three partial wavefunctions. These partial wavefunctions can be translated such that the composite output wavefunction has a spiral shape, with $\ell = 1$ or $\ell = -1$. With only two point sources of partial wavefunctions one can generate states that exist in an equal superposition of $\ell = 1$ and $\ell = -1$ or $\ell = 2$, $\ell = 0$ and $\ell = -2$ depending on the phase difference between the partial wavefunctions. This simple principle underlies all the methods described in this and all the following chapters.

Coherent averaging has been used to produce OAM states in photons [32] and neutrons [33, 34]. In [33], authors used a Mach-Zehnder interferometer, which used magnetic refraction to separate the input wavefunction into four partial wavefunctions by a small microscopic distance (0.01-10 μm). Due to this small separation the partial wavefunctions can not be individually manipulated, however due to the different spin associated with each path one can use appropriate magnetic coils to produce the phase differences between the partial wavefunctions required to produce a vortex. This type of interferometer mirrors the Spin Echo type instruments [102, 69] used to measure ultra small angle scattering [39, 40, 41]. This OAM view of Spin Echo Small Angle Neutron Scattering will be discussed in section 5.2. In addition we will look at a spin echo interferometer developed at the Atominstitut specifically to explore linear OAM states [38]. But first we will look at the generalized method described in [34] in section 5.1. Furthermore we will look at an experiment where three partial wavefunctions are produced using a nested loop perfect crystal neutron interferometer [103, 104]. Since in this case the separation is macroscopic ($\propto \text{cm}$), each partial wavefunction can be manipulated independently

using prisms and phase shifters to produce a twisted composite wavefunction. An added advantage of this setup comes from the fact that the strong nuclear interaction can be used, which couple more strongly to the neutron than the magnetic fields that can be produced in spin echo type interferometers. This stronger coupling results in a higher flexibility in terms of possible vortex sizes and shapes which can be generated. However, finally we will establish a coherent averaging method, which enable us to generate vortices of almost any size, while using relatively small potentials (magnetic or nuclear).

5.1 Generation of Phase Vortices in Neutron Interferometry

In this section we present and discuss the work presented in [34], which reports on a generalized method for producing phase vortices using the coherent averaging technique. Here we will begin by qualitatively describing the experiment. Next we move on to the theoretical description, followed by the experimental results and applications of our method. Finally we will look at a more generalized theoretical model for OAM production using coherent averaging.

5.1.1 Qualitative Description

Our experiment addresses the challenge of generating OAM in thermal neutrons by generalizing the magnetic coherent averaging method described in [33], such that the strong nuclear potential can be exploited, enabling production of smaller vortex diameters at thermal energies. This experiment demonstrates the generation of a vortex lattice using strongly interacting aluminium prisms in a nested loop neutron interferometer. In a two path, single loop, interferometer the combination of a phase shifter and a pair orthogonal prisms enables us to generate a composite wavefunction exhibiting azimuthal structure where the $\ell = \pm 1$ mode amplitude is significant (as demonstrated in Chapter 2, figure 2.7). To extract the phase structure of the composite wavefunction an additional reference beam is needed. For this purpose a three path nested loop interferometer was used.

In somewhat more qualitative detail, the purpose of the prisms is to translate transversely (either vertically or horizontally) the reciprocal partial wavefunctions with respect to each other, while the phase shifter effects the relative phase between the partial wavefunctions. The latter can also be seen as a longitudinal translation. Combining these different tools we can re-arrange the composite wavefunctions such that the composite wavefunction displays some helicity.

The experiment was carried out at a wavelength of 1.92 \AA on the thermal neutron interferometry station, S18, at the high-flux reactor of the Institute Laue Langevin (ILL) in

Grenoble, France [105]. Our setup is shown in figure 5.1. This interferometer generates three nested loops [103, 104, 106, 107], two small loops between the first and third plate and the second and fourth plate respectively, and a large loop between the first and fourth plate. Our prisms each have a 5 degree slope and are made from aluminium. To control the phase difference of each loop a minimum of two phase shifters are re-

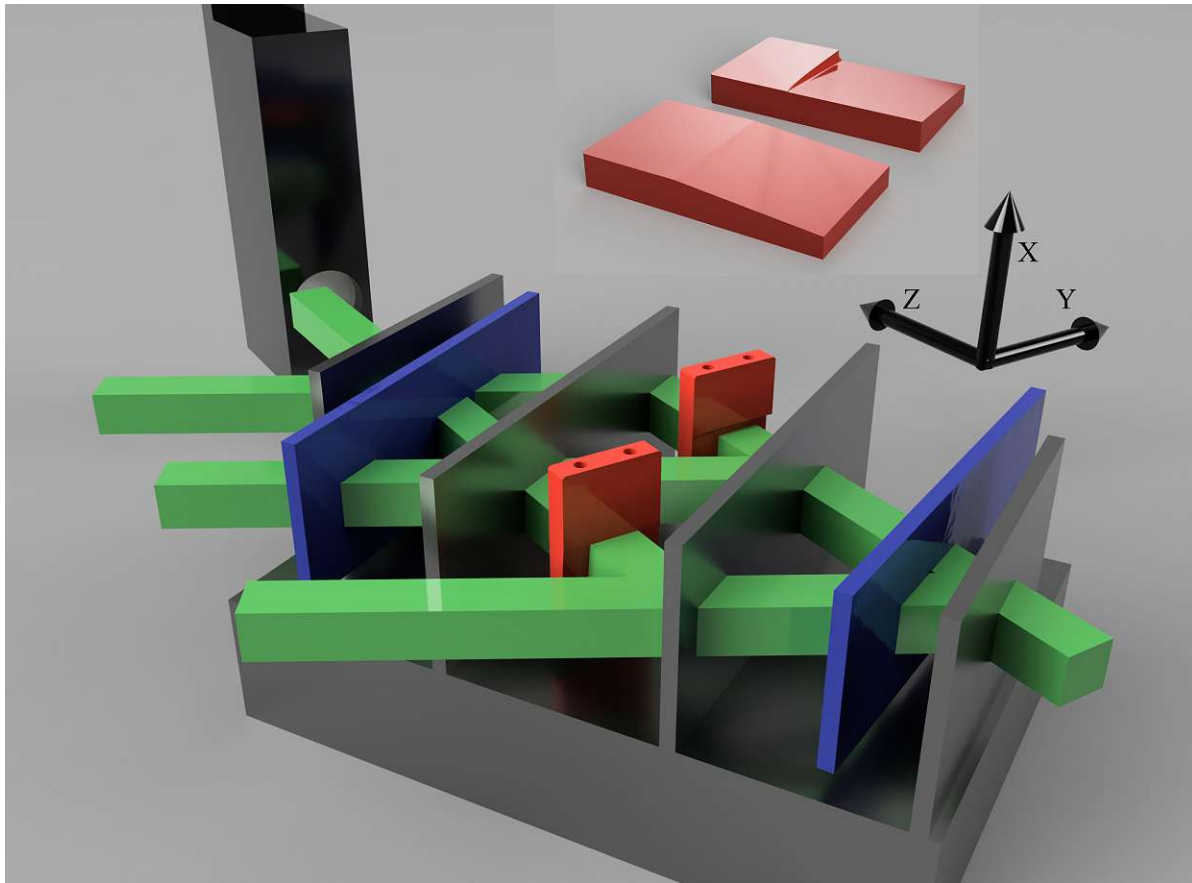


Figure 5.1: Sketch of the 4 plate interferometer (145 mm long), containing two (red) orthogonal prisms (blown up on the top portion) and two phase shifters (blue). The neutron beam, coming from the right, forms three loops, two small ones between the first and third and second and fourth plate respectively and a large loop between the first and last plate. The phase shifters can be rotated around the vertical to induce phase shifts between the paths in their respective loops. A position sensitive detector is shown in black. Additionally in black the coordinate convention is shown

quired. These phase shifters consist of flat silicon and sapphire slabs. To resolve the phase vortices produced by this setup we employed a scintillator based position sensitive detector.

5.1.2 Theoretical Description

We now move on to a theoretical description of the states produced in our interferometer. In the case of thermal neutrons where the nuclear potential is low compared to the kinetic energy, the action of a prism can be approximated by a translation of the reciprocal wavefunction (i.e. by convolving with a delta function) $\psi'(\mathbf{k}) = \psi_0(\mathbf{k}) * \delta(\mathbf{k} - \mathbf{k}')$, while phase shifters imprint a global phase on the wavefunction $\psi'(\mathbf{k}) = e^{i\alpha}\psi_0(\mathbf{k})$. In principle prisms also apply a global phase to the wavefunction, however for the sake of this model we choose to account for this phase in the action of the phase shifter. The input wavefunction (in k-space) is assumed to be Gaussian

$$\psi_0(\mathbf{k}) = \sqrt{\frac{1}{2\pi\zeta^2}} e^{-\frac{(k_x^2+k_y^2)}{4\zeta^2}} \Phi(k_z) \quad (5.1)$$

with k_x and k_y denoting the transverse wavenumbers and ζ the transverse momentum spread. Again this momentum spread is related to the average divergence of individual neutrons, θ , by $\zeta \approx k_z\theta$, for small θ . $\Phi(k_z)$ refers to the longitudinal part of the reciprocal wavefunction that is virtually unaffected by the action of the prisms. The composite wavefunction projected from the last interferometer plate to the detector can then be written as

$$\psi_1(\mathbf{k}) = \frac{1}{\sqrt{3}} [\psi_0(\mathbf{k}) + e^{i\alpha_1}\psi_0(\mathbf{k} - k_\perp\hat{y}) + e^{i\alpha_2}\psi_0(\mathbf{k} - k_\perp\hat{x})] \quad (5.2)$$

where the transverse momentum shift, k_\perp , is related to the angle of refraction, γ , induced by the prisms $k_\perp = k_z\gamma$. It can be instructive to look at equation (5.2) in real space cylindrical coordinates, (ρ, ϕ, z) , since the real space equation allows us to more easily deduce the orbital angular momentum properties of this wavefunction.

$$\psi_1(\mathbf{r}) = \frac{1}{\sqrt{3}} \psi_0(\mathbf{r}) [1 + e^{i\alpha_1} e^{ik_\perp\rho\sin(\phi)} + e^{i\alpha_2} e^{ik_\perp\rho\cos(\phi)}] \quad (5.3)$$

The expression $\psi_0(\mathbf{r}) = \sqrt{\frac{2}{\pi\sigma^2}} e^{-\frac{\rho^2}{\sigma^2}} \Phi(z)$ is the Fourier transform of (5.1). $\sigma = \frac{1}{\zeta}$ denotes the real space coherence length and $\Phi(z)$ is the real space component of the wavefunction along the z direction. We require that $\Phi(z)$ is normalized (i.e. $\int dz |\Phi(z)|^2 = 1$). From here on out it is important to distinguish between the constant reference wavefunction, $\psi_0(\mathbf{r})$, and the test wavefunction $\psi_t(\mathbf{r})$, which is postulated to carry OAM.

$$\begin{aligned} \psi_t(\mathbf{r}) &= \frac{1}{\sqrt{2}} \psi_0(\mathbf{r}) (e^{ik_\perp\rho\sin(\phi)} + e^{i\Delta\alpha} e^{ik_\perp\rho\cos(\phi)}) \\ \psi_1(\mathbf{r}) &= \frac{1}{\sqrt{3}} [\psi_0(\mathbf{r}) + \sqrt{2} e^{i\alpha_1} \psi_t(\mathbf{r})] \end{aligned} \quad (5.4)$$

with $\Delta\alpha = \alpha_2 - \alpha_1$. We note that the above wavefunctions are not properly normalized, since they do not represent the total neutron wavefunction emerging from the interferometer, but only the part of the wavefunction projected towards the detector. The test wavefunction is the wavefunction of which we are investigating the OAM properties. This is similar to the wavefunction we investigated at the end of chapter 2 (i.e. figure 2.7). However in section 5.1.4 we will also investigate the OAM of ψ_1 numerically.

Calculation of the OAM of the Test Wavefunction

We begin by calculating the OAM expectation value (eq. 2.9) using our test wavefunction (eq. 5.4). For a step by step derivation we refer to the appendix (A.1). For now let it suffice to say that it can be shown that the OAM expectation value of our test wavefunction can be written as

$$\langle L_z \rangle = \sqrt{2\pi} \sin(\Delta\alpha) \frac{\int d\rho k_\perp \rho^2 |\psi_0|^2 J_1(\sqrt{2}k_\perp \rho)}{\int d\mathbf{r} |\psi(\mathbf{r})|^2} \quad (5.5)$$

In our special case of where $\psi_0(\mathbf{r})$ is Gaussian this integral is a standard Hankel transform with the result

$$\langle L_z \rangle = \sin(\Delta\alpha) \frac{k_\perp^2 \sigma^2}{4N} e^{-\frac{k_\perp^2 \sigma^2}{4}} \quad (5.6)$$

with the normalization parameter $N = \int d\mathbf{r} |\psi(\mathbf{r})|^2 = 1 + \cos(\Delta\alpha) e^{-\frac{k_\perp^2 \sigma^2}{4}}$. For large k_\perp , the normalization parameter goes to unity. We can easily see in this limit that the OAM is maximal/minimal for $\Delta\alpha = \pm\pi/2$. In addition using $N \approx 1$ and the derivative of equation 5.6 we find the approximate value of k_\perp for which the OAM is maximized/minimized: $k_\perp = \pm\frac{2}{\sigma} = \pm 2\zeta$. That is to say that the refraction angle must be about one order of magnitude larger than the average momentum spread of an individual neutron for maximal OAM. Another interesting region of equation 5.6, is found for small k_\perp in the vicinity of $\Delta\alpha \approx \pi$. Here, around $\Delta\alpha = \pi$, the OAM may vary rapidly and even attain a significant value for a relatively small value of k_\perp .

Recall that OAM can always be considered entirely intrinsic if

$$\langle k_x \rangle = \langle k_y \rangle = 0 \quad (5.7)$$

Since for our setup $\langle k_x \rangle = \langle k_y \rangle = k_\perp$ and $k_\perp \sigma$ is at most 0.01 we can consider the OAM to be quasi intrinsic, since $k_\perp r_0 \approx 0$. As the interaction range of the neutron is proportional to its' coherence length it does not make sense to look at $r_0 \gg \sigma$ when examining the OAM of single neutrons. In section 5.1.4 we will look at the intrinsic nature of the OAM more rigorously.

In addition to the expectation value it is instructive to look at the OAM spread, defined as a standard deviation:

$$\chi = \sqrt{\langle L_z^2 \rangle - \langle L_z \rangle^2} \quad (5.8)$$

with the second moment given by (see the appendix A.1 for a complete derivation)

$$\langle L_z^2 \rangle = \frac{k_\perp^2 \sigma^2}{4N} - \cos(\Delta\alpha) \frac{k_\perp^4 \sigma^4}{16N} e^{-\frac{\sigma^2 k_\perp^2}{4}} \quad (5.9)$$

It can be seen that the OAM bandwidth is maximal for a phase shift $\Delta\alpha = \pm\pi$. Both the OAM bandwidth and the expectation value are shown for a variety of $\Delta\alpha$ and k_\perp (in units of ζ) in figure 5.2. At this point it should be remembered that perfect

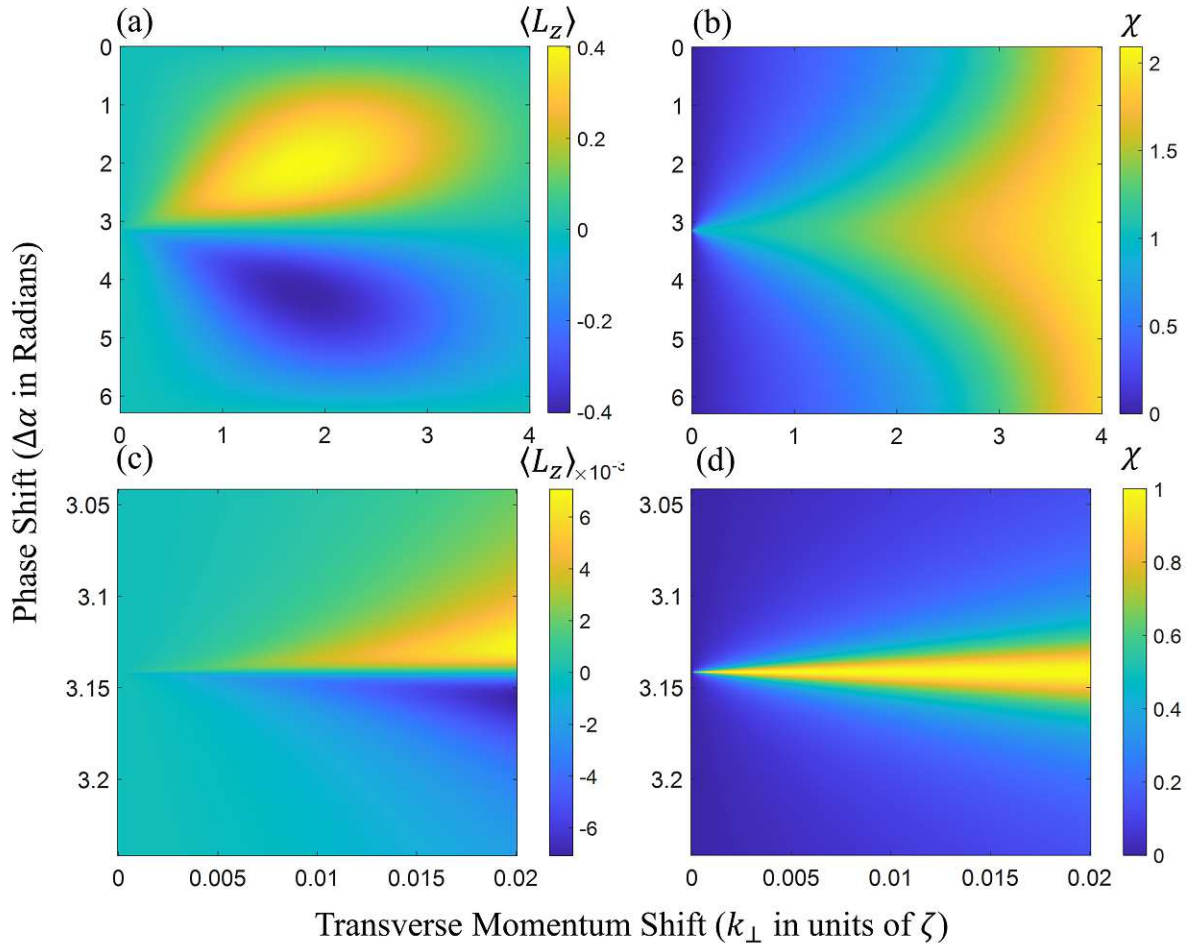


Figure 5.2: (a) Expectation value of the test wavefunction (eq. 5.4) as given by the analytical expression in equation 5.6 for various transverse momentum shifts k_{\perp} and phase shifts $\Delta\alpha$. Around $\Delta\alpha = \pm\alpha/2$ and $k_{\perp} = 4\pi$ the OAM attains a maximal/minimal value of ± 0.4 (b) The OAM bandwidth defined by equation 5.8 for ψ_t as a function of transverse momentum shift k_{\perp} and phase shift $\Delta\alpha$. Inserts (c) and (d) show the behavior of $\langle L_z \rangle$ and χ respectively for small k_{\perp} in the vicinity of $\Delta\alpha = \pi$. In all figures k_{\perp} is in units of ζ . In the case of the described experiment the normalized k_{\perp} ranges from 10^{-5} (vertical refraction) to 0.02 (horizontal refraction).

crystal neutron interferometry, the momentum spread ζ is direction dependent, due to dynamical diffraction, such that the input wavefunction should be written as

$$\psi_0(\mathbf{k}) = \sqrt{\frac{1}{2\pi\zeta_x\zeta_y}} e^{-\frac{(\zeta_y^2 k_x^2 + \zeta_x^2 k_y^2)}{4\zeta_x^2\zeta_y^2}} \Phi(k_z) \quad (5.10)$$

where ζ_x and ζ_y differ by three orders of magnitude. Nonetheless the above theory for isotropic momentum spread ($\zeta_x = \zeta_y = \zeta$) is still valid if the transverse momentum shifts induced by the prisms are adapted to the momentum spread in the respective direction. However, the experiment we are describing employed identical prisms, hence it is possible that figure 5.2 does not give an accurate representation of the quasi-intrinsic OAM of our wavefunction. Nonetheless, when we calculate the OAM expectation value analytically (the step-by-step calculation is shown in the appendix A.1), using the $\psi_0(\mathbf{r})$ implied by equation 5.10, it can be shown that

$$\langle L_z \rangle = \sin(\Delta\alpha) \frac{k_\perp^2 (\sigma_x^2 + \sigma_y^2)}{8N} e^{-\frac{k_\perp^2 (\sigma_x^2 + \sigma_y^2)}{8}} \quad (5.11)$$

which in form is identical to equation 5.6. This expression becomes completely identical to equation 5.6, if we define an effective transverse coherence $\sigma^2 = (\sigma_x^2 + \sigma_y^2)/2$, the normalization parameter N is then unchanged. So figure 5.2 can also be considered for anisotropic momentum spreads and the maximal amount of OAM generated by this type of setup is not affected by an anisotropic momentum distribution. It follows that in the experiment described here the effective $k_\perp\sigma$ is on the order of 0.015.

Given this effective $k_\perp\sigma$, we may regard the OAM as quasi intrinsic. However as can be seen in figure 5.2 the OAM production is small for this configuration. Nonetheless it is instructive to look at the amplitudes of the wavefunctions first OAM modes for small $k_\perp\sigma$. To this end we calculate the AFT of the test wavefunction which is given by the Jacobi-Anger expansion [47]

$$\psi_t^\ell(\rho) = (-1)^\ell \frac{2}{\sigma} e^{-\frac{\rho^2}{\sigma^2}} J_\ell(k_\perp\rho) (1 + i^{-\ell} e^{i\Delta\alpha}) \quad (5.12)$$

Note that we have dropped the longitudinal part of the wavefunction, $\Phi(z)$ for this analysis. Realistically the refraction angle induced by a neutron optical prism is much smaller than the beam divergence, therefore the width of the Gaussian envelope in (5.12) is much smaller than the period of the Bessel functions, $J_\ell(k_\perp\rho)$. This implies that linearizing the Bessel functions will yield a good approximation of the OAM amplitudes. We note that in the linear limit only Bessel functions of modes $\ell = -1$, $\ell = 0$ and $\ell = 1$ are non zero, therefore only these OAM modes play a non-vanishing role in our wavefunction. The approximation yields

$$\begin{aligned} \psi_t^{\ell=0}(\rho) &\approx \frac{2}{\sigma} e^{-\frac{\rho^2}{\sigma^2}} (1 + e^{i\Delta\alpha}) \\ \psi_t^{\ell=\pm 1}(\rho) &\approx \mp \frac{k_\perp\rho}{\sigma} e^{-\frac{\rho^2}{\sigma^2}} (1 \mp i e^{i\Delta\alpha}) \end{aligned} \quad (5.13)$$

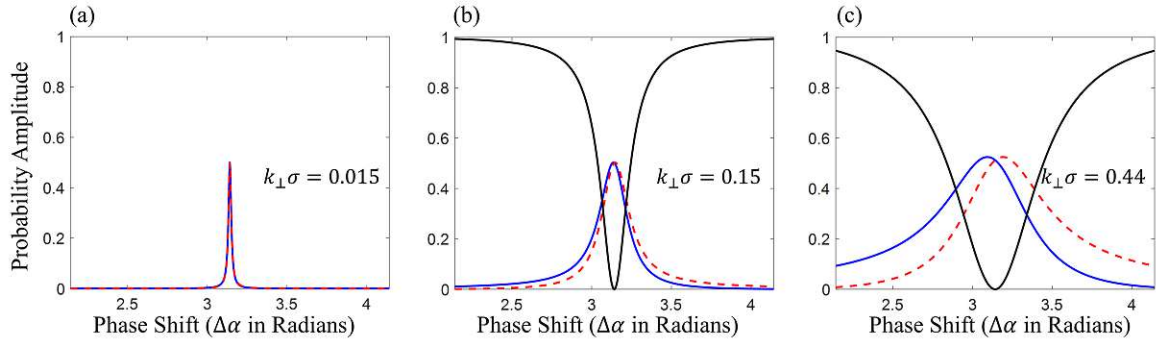


Figure 5.3: Probability amplitudes of the first and zeroth order OAM modes. The first order mode probabilities $\ell = 1$ (blue), $\ell = -1$ (red dashed) and the zeroth order mode probability $\ell = 0$ (black) are plotted against the phase shift $\Delta\alpha$ (centered on $\Delta\alpha = \pi$) for various transverse momentum shifts, (a) equal to the experimental case $k_{\perp}\sigma = 0.015$, (b) ten times larger and (c) thirty times larger than in the experimental case. In (a) the $\ell = 0$ amplitude is not plotted for improved visibility. It can be clearly discerned that $\ell = \pm 1$ probabilities widen for increasing refraction, k_{\perp} . In addition the $\ell = 1$ and $\ell = -1$ probabilities appear to be mirror images of one another (mirrored around $\Delta\alpha = \pi$).

As previously shown the average OAM $\langle L_z \rangle$ is zero for $\Delta\alpha = \pm\pi$. However this analysis using the AFT shows that, despite this, the intrinsic neutron OAM is dominated by an equal superposition of $\ell = \pm 1$ modes, while the $\ell = 0$ mode is totally suppressed. Hence in this case we have created a linear OAM state as described in the last section of chapter 2. We may calculate the probability amplitudes of the $\ell = 0$ and $\ell \pm 1$ modes, using the OAM distribution function (eq. 2.32) and our approximate expressions in equation 5.13. Figure 5.3 shows these probability amplitudes for various k_{\perp} around $\Delta\alpha = \pi$. It can be seen that for increasing k_{\perp} the $\ell = 1$ and $\ell = -1$ probabilities widen and begin to separate from one another. It can also be seen that the $\ell = 1$ and $\ell = -1$ amplitudes are asymmetric around $\Delta\alpha = \pi$, having a steeper slope to one side of the peak compared to the other side. This results in the OAM becoming net positive for $\Delta\alpha < \pi$ and negative for phase shifts above π .

Treatment of Beam OAM

Until now we have considered a microscopic treatment of OAM where a single wavefunction is centered on the optical axis. Now we turn to the macroscopic treatment where we consider an ensemble of quasi-paraxial wavefunctions which make up a beam. On this scale vortex lattices can appear, which carry macroscopic beam OAM. Since the individual neutrons that make up the beam can be far off-axis, compared to their coherence length, our theory predicts that most neutrons will have extrinsic OAM with respect to the axis around which (beam) OAM is defined.

It is well known that a prism inserted into a single loop interferometer generates a Moire fringe pattern along the refraction direction [32]. In our nested loop interferometer the Moire patterns generated by each loop are overlaid, thereby creating a lattice like structure. The spatial intensity profile can be calculated using the wavefunction projected to the detector (equation 5.3). The wave function impinging on the detector at position \mathbf{r}' is simply equation 5.3 with the input wavefunction $\psi_0(\mathbf{r})$ translated by \mathbf{r}'

$$\psi_1(\mathbf{r} - \mathbf{r}') = \frac{1}{\sqrt{3}}\psi_0(\mathbf{r} - \mathbf{r}')[1 + e^{i\alpha_1}e^{ik_{\perp}y} + e^{i\alpha_2}e^{ik_{\perp}x}] \quad (5.14)$$

The intensity profile which would be measured can be calculated by taking the absolute value squared of equation (5.14):

$$I(\mathbf{r}') = \int_{\mathcal{P}} d\mathbf{r} |\psi_1(\mathbf{r} - \mathbf{r}')|^2 \quad (5.15)$$

with \mathcal{P} a domain given by the pixel size of the detector, which is quasi infinite in size compared to the wavefunction. Assuming \mathbf{r}' falls within the domain \mathcal{P} , we may approximate this integral by

$$I(\mathbf{r}') = \frac{1}{3} \int_{\mathcal{P}} d\mathbf{r} \delta(\mathbf{r} - \mathbf{r}') [3 + 2 \cos(k_{\perp}y + \alpha_1) + 2 \cos(k_{\perp}x + \alpha_2) + 2 \cos(k_{\perp}(x - y) + \Delta\alpha)] \quad (5.16)$$

where we used that $|\psi_0(\mathbf{r} - \mathbf{r}')|^2$ may be approximated by a delta function since the coherence length is very small compared to the period of the cosines. Hence it follows

$$I(\mathbf{r}') = \frac{1}{3} [3 + 2 \cos(k_{\perp}y + \alpha_1) + 2 \cos(k_{\perp}x + \alpha_2) + 2 \cos(k_{\perp}(x - y) + \Delta\alpha)] \quad (5.17)$$

For the prisms used in this experiment we expect a value of k_{\perp} which corresponds to a lattice period of 1.75 mm.

5.1.3 Experimental Results and Applications

We now look at the experimental results and compare these with our theory. Afterwards we will look at the potential applications of our setup and explore possible improvements to increase vortex yield.

Experimental Results

The vortex lattice generated by our setup is shown in figure 5.4 (a). In addition, the figure contains a fit (fig. 5.4 (b)) based on equation (5.17). For more details on the fitting technique, image processing and data reduction the reader should refer to the appendix

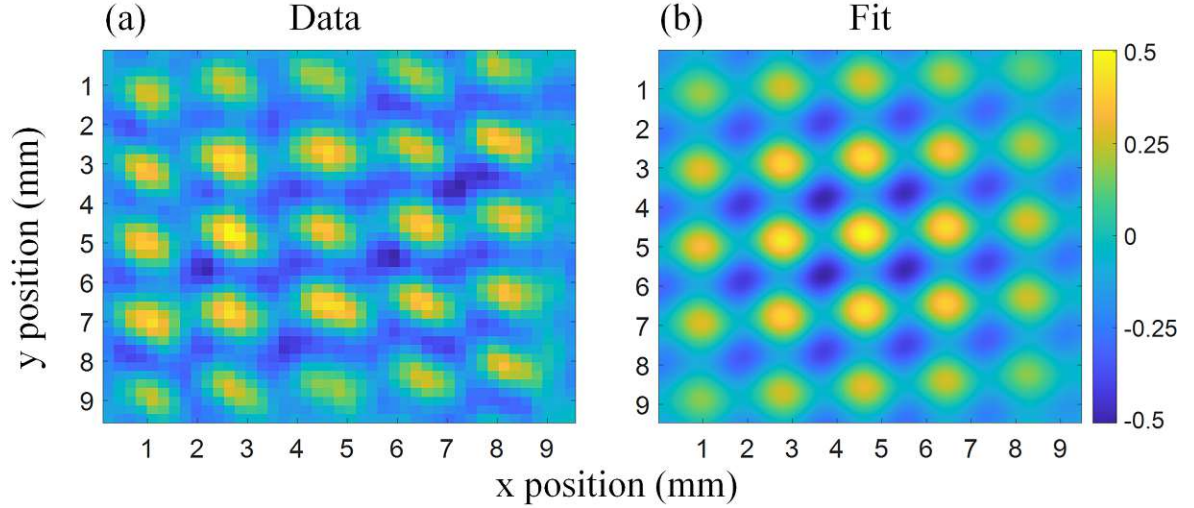


Figure 5.4: Measurement results and fit. (a) The processed, normalized and filtered image of the neutron vortex lattice, recorded using the position sensitive detector seen in figure 5.1. The contrast, according to the fit (b) based on (5.17), is 0.53. The lattice period is 1.83 mm.

A.2. The discrepancies between the fit and the data could be explained by different amplitudes of the three Cosine terms in equation 5.17. These amplitudes can differ depending on the amount of material each partial wavefunction in the interferometer goes through. If two paths "see" a similar amount of material, the amplitude of the Moire fringes from that loop will be large, while if there is a discrepancy in the amount of material, dephasing may occur, thereby lowering the amplitude of the respective loop.

Since the model used for our fit assumes that the intensity is given by $|\psi_1(\mathbf{r})|^2$, we may extract a part of the test wavefunction, $\psi_t(\mathbf{r})/\psi_0(\mathbf{r})$, from the data, using our model, yielding the phase data needed to compute the amplitude of each OAM mode and the average OAM normal to any domain. Note that since the reconstructed test wavefunction is given by $\psi_t(\mathbf{r})/\psi_0(\mathbf{r})$, we do not observe any coherence effects, as these are all contained within $\psi_0(\mathbf{r})$. Figure 5.5 (a), shows the real part of the reconstructed test wavefunction zoomed in on a single vortex. For numerical calculation purposes we introduce a spatially averaged AFT

$$\bar{\psi}_t^\ell = \int_{\mathcal{D}} e^{i\ell\phi(x,y)} \psi_t(x,y) d^2\mathbf{x} \quad (5.18)$$

with $\phi(x,y)$ defined by the argument between the x and y coordinate (i.e. $\phi = \text{Arg}(x + iy)$) and \mathcal{D} an arbitrary two dimensional domain, over which the average mode amplitude is to be determined. From the amplitudes calculated in equation (5.18) an approximate expectation value of the OAM orthogonal to the domain surface can be determined

$$\langle L_z \rangle = \frac{\sum_\ell \ell |\bar{\psi}_t^\ell|^2}{\sum_\ell |\bar{\psi}_t^\ell|^2} \quad (5.19)$$

To closely approximate an actual AFT a circular domain is chosen to calculate the amplitudes, $\bar{\psi}_t^\ell$, given by equation (5.18). To first order it was shown that the $\ell = \pm 1$ amplitudes increase linearly with ρ (equation (5.13)), hence a larger domain will see a larger maximal value of the OAM. We will, therefore, choose the maximal domain size on which the first order approximations of the test wavefunction are valid. The first order approximation can be used up to $k_\perp \rho = 0.75$ with a maximal relative error of less than 0.1. In our setup this corresponds to a domain size of 0.22 mm. Being much larger than the effective transverse coherence of the beam (roughly $5 \mu\text{m}$) it follows that the OAM must be considered to be extrinsic. The domain on which the spatially averaged AFT is calculated is indicated in figure 5.5 (a). It can be scanned across the reconstructed test wavefunction, $\psi_t(\mathbf{r})/\psi_0(\mathbf{r})$, to calculate $\langle L_z \rangle$ in each section of the image. This OAM expectation value is shown in figure 5.5 (b). Note the diagonal (45 degree) "lines" of constant OAM in figure 5.5 (b), confirming the predictions made in section 2.4.

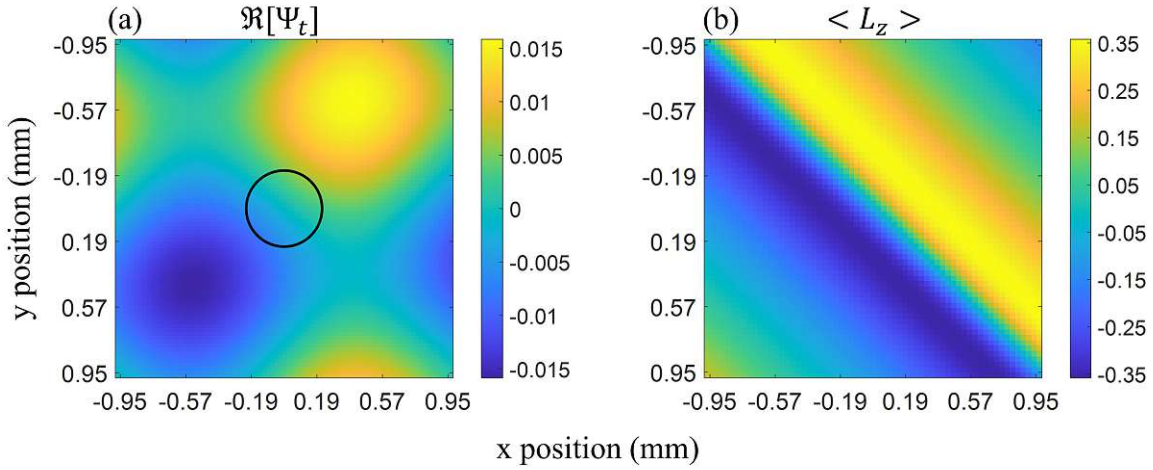


Figure 5.5: (a) Image of the real part of the test wavefunction of a single vortex carrying extrinsic OAM. This test wavefunction is reconstructed using the fit parameters generated by the model shown in figure 5.4. A circle is drawn in the center of the image indicating the domain on which the spatially averaged AFTs are applied and the first order approximations used throughout the paper are valid. The axis around which the OAM is defined is centered on and normal to this circular domain. (b) The average extrinsic OAM $\langle L_z \rangle$ over the image is shown. This is calculated using the spatially averaged AFT (equation 5.18) and equation (5.19).

Discussion and Applications

We see that our method using only two prisms generates extrinsic vortices with a significant $\ell = \pm 1$ component, such that the average beam OAM can reach up to $|\langle L_z \rangle| \approx 0.35$.

While the vortex diameter is still much larger than the calculated coherence length and therefore cannot be applied to experiments requiring intrinsic OAM [22, 23, 24]. However spatially modulated beams like the one generated in our setup can be applied to ultra small angle scattering. In numerous configurations it has been shown that one dimensional intensity modulation (such as Moire patterns) can be applied to ultra small angle scattering, for example in neutron dark field imaging/Talbot-Lau interferometry [108, 109] and spin echo modulated small angle neutron scattering [110, 111, 112]. With the exception of a recent development in Talbot-Lau interferometry [113] the latter methods can only measure the elastic scattering function $S(q)$ in one dimension. Two dimensional intensity modulation, as generated by our setup, could be used to measure two dimensional elastic scattering functions, allowing analysis of anisotropic samples in a single measurement. Such a measurement would employ the same instrument as described here. A sample could be placed between the interferometer and position sensitive detector. Small angle scattering from the sample would wash out the intensity modulation leading to contrast reduction. This contrast reduction is proportional to the Fourier transform of $S(q)$ analogous to spin-echo modulated small angle neutron scattering methods [110, 111]. By Fourier transforming the modulated intensity pattern it is possible to separate the contrasts of the vertical and horizontal modulation. This allows the instrument to distinguish between vertical and horizontal scattering. Hence, the instrument could simultaneously measure $S(q_x)$ and $S(q_y)$. This scheme could also be applied to the magnetic method for generating vortex lattices [33]. Both the latter method and our approach still lack the focusing prisms used for first order corrections to the divergence/coherence, which prevent dephasing and are available in the one dimensional method [110, 111, 112]. Though a recent analysis [114] has demonstrated how to implement first order divergence corrections in a setup analogous to the magnetic coherent averaging method [33] and the setup described in this paper. Focusing elements increase the modulation contrast and allow for larger beam sizes/divergences, thereby increasing the available intensity. These focusing prisms become a requirement when one looks towards generating intrinsic OAM using our method. Equation (5.6), shows that the refraction angle of the prisms or k_{\perp} must be on the same order of magnitude as the beam divergence or ζ , such that the amplitude of the $|\ell| = 1$ mode becomes significant. This may be achievable in the near future with recent developments in compound neutron optics [115] and micromachining [116]. In addition, steeper prisms made from more dense optical material can be employed in compound devices. The additional space required by obligatory focusing prisms call for larger perfect crystal interferometers. Ongoing developments in neutron interferometry with split crystals may make this possible in the near future [117]. However a fundamental limit is reached as k_{\perp} approaches the beam divergence ζ along the diffraction direction, as in this case beams are only poorly diffracted by interferometer plates. For diffraction to efficiently occur the momentum shifted wavefunction $\psi_0(\mathbf{k} - k_{\perp}\hat{j})$ must have significant overlap with the input wavefunction $\psi_0(\mathbf{k})$, which is defined by the angular acceptance of the interferometer. \hat{j} here refers to the direction normal to the crystal planes. As a result we can estimate that k_{\perp} can be on the order of ζ . Using equation 5.6 it can be shown that the OAM expectation value cannot exceed 0.1, due to the diffraction limit. Though as will

be discussed in the next subsection, if we adopt a real space coherent averaging scheme we can avoid the diffraction limit altogether.

5.1.4 Generalizations of Coherent Averaging

In this subsection we will further generalize the theory of coherent averaging presented in the previous subsections. we will begin by presenting and justifying the real space coherent averaging scheme, which was implicitly explored at the end of chapter 2. After that, following the work described in [101], we will explore the general case of coherent averaging where N sources or partial wavefunctions are used to create an output wavefunction with arbitrary OAM.

Real Space Coherent Averaging

In the experiment described thus far we have conducted our translation and phase shift operations on the reciprocal space wavefunctions. However as we already demonstrated in section 2.3.3 any kind of reciprocal space structure that produces OAM also produces OAM when constructed in real space, since the form of the OAM operator does not change under Fourier transformation. This offers enormous advantages, since as it will turn out optics for real space coherent averaging are simpler and much smaller vortices can be produced with comparatively low effort.

As an example one could use a composite wavefunction where the partial wavefunctions are shifted in real space relative to each other.

$$\psi(\mathbf{r}) = \frac{1}{\sqrt{2}}[\psi_0(\mathbf{r} - \delta\hat{y}) + e^{i\Delta\alpha}\psi_0(\mathbf{r} - \delta\hat{x})] \quad (5.20)$$

Where real space separations, δ , can be achieved using prism pairs or parallelogram shaped optical devices. Note that this is the real space equivalent of the reciprocal test wavefunction used previously. Since the OAM operator does not change form under a Fourier transform, it follows that the OAM of equation 5.20 can be derived identically to that of equation 5.4, detailed in the previous subsections. Therefore the form of the OAM expectation value is identical to that which is described in 5.6. Contrary to what one may intuitively think the wavefunction in equation 5.20 does not obey $\langle k_x \rangle = \langle k_y \rangle = 0$ it follows that, the OAM is therefore not invariant under translation. However as shown in figure 5.3, such a state is a linear OAM state, which can be seen as a superposition of the two intrinsic OAM states with $\ell = 1$ and $\ell = -1$. As stated before this method is much simpler than the reciprocal space method, since a pair of prisms can produce displacements, δ that are on the order of the coherence length σ , which is necessary to produce large amplitudes of OAM. It is even possible to produce displacements orders of magnitude larger than the coherence length [118, 119].

Moving forward it is therefore pertinent to focus on real space coherent averaging to produce a high yield OAM generator device for neutrons. For this reason in the following sections we will focus only on the real space variant of the technique.

Coherent Averaging with an Arbitrary Number of Discrete Sources

we now turn to what is basically a special application of Huygens principle. Specifically we will look at producing vortex states with mode number ℓ using N discrete sources or partial wavefunctions arranged in a circular pattern. This is explored in more detail in [101]. Here we will explore the idea in a more simple fashion. we will start by describing the composite wavefunction as a superposition of N partial wavefunctions

$$\psi_c(\mathbf{r}) = \sum_{i=0}^{N-1} e^{i\varphi_i} \psi_i(\mathbf{r} - \mathbf{r}_i) \quad (5.21)$$

where the partial wavefunctions are defined by a phase φ_i and a displacement \mathbf{r}_i . To generate the ℓ^{th} mode number we require that the phase is given by

$$\varphi_i = i\ell \frac{2\pi}{N} \quad (5.22)$$

since for the ℓ^{th} mode the phase of the composite wavefunction must go through ℓ oscillations. We will also require the position \mathbf{r}_i to be such that the partial wavefunctions sit on a circular domain of radius δ

$$\mathbf{r}_i = \delta \left[\cos\left(\frac{2\pi i}{N}\right) \hat{x} + \sin\left(\frac{2\pi i}{N}\right) \hat{y} \right] \quad (5.23)$$

It is useful then to look at the AFT of the composite wavefunction

$$\psi_c^n(r) = \sum_i e^{i\varphi_i} \int_0^{2\pi} d\phi \psi_i(\mathbf{r} - \mathbf{r}_i) e^{-in\phi} \quad (5.24)$$

if we assume ψ_i to be a symmetric Gaussian (i.e. $\sigma_x = \sigma_y = \sigma$) we can completely re-use our work from section 2.5, specifically equation 2.78, if we realize, that a simple coordinate rotation ($\phi' = \phi - \frac{2\pi i}{N}$) can reduce each Gaussian ψ_i to eq. 2.69 with $k_y = 0$. The solution to the above AFT is then

$$\psi_c^n(r) = A e^{-\frac{r^2 + \delta^2}{\sigma^2}} i^n J_n\left(2i \frac{\delta}{\sigma^2} r\right) \sum_i e^{i \frac{2\pi i}{N} (\ell - n)} \quad (5.25)$$

We can already intuitively see that for quasi-infinite N , the summation will go to zero for all terms $\ell \neq n$, hence for infinite sources/partial waves we can generate a perfect vortex state of any mode number. If we recognize the summation as a finite geometric series we may further simplify our expression

$$\psi_c^n(r) = A e^{-\frac{r^2 + \delta^2}{\sigma^2}} i^n J_n\left(2i \frac{\delta}{\sigma^2} r\right) \frac{1 - e^{i2\pi(\ell-n)}}{1 - e^{i \frac{2\pi}{N} (\ell-n)}} \quad (5.26)$$

From this expression it is trivial to derive the OAM distribution function, given that we have already done the heavy lifting in section 2.5

$$p[n] = \frac{A^2 \sigma^2}{4} e^{-\frac{\delta^2}{\sigma^2}} I_n\left(\frac{\delta^2}{\sigma^2}\right) \frac{1 - \cos(2\pi(\ell - n))}{1 - \cos\left(\frac{2\pi}{N}(\ell - n)\right)} \quad (5.27)$$

Now let us examine more closely the relationship between the number of sources N and the desired amount of OAM ℓ of the composite state. We can easily see that the distribution is maximal when $p[n = \ell]$. It is also trivial to recognize that for there to be some net OAM we require $p[n = \ell] \neq p[n = -\ell]$. Using this we can derive the minimal number of sources/partial waves required to generate a vortex state with mode number ℓ .

$$N > 2|\ell| \quad (5.28)$$

This is a minimal requirement. As it turns out if $x > 1$ we require more sources to produce the vortex state. To further investigate this we will numerically calculate the OAM expectation value. First however it is useful to recognize that for our wavefunction to be normalized the parameter A must contain a factor of $1/\sigma$. In addition we can reduce the number of variables in our OAM distribution function using $x = \frac{\delta}{\sigma}$. Thus we can use the following simplified distribution function

$$p[n] \propto e^{-x^2} I_n(x^2) \frac{1 - \cos(2\pi(\ell - n))}{1 - \cos\left(\frac{2\pi}{N}(\ell - n)\right)} \quad (5.29)$$

to calculate the OAM expectation value

$$\langle \hat{L}_z \rangle = \frac{\sum_n n p[n]}{\sum_n p[n]} \quad (5.30)$$

Numerical results are shown in figure 5.6 for the first few vortex modes. The figure confirms the rule we found regarding the minimal number of sources (eq. 5.28). In addition we find that the largest OAM generation efficiency occurs for small x (i.e. the displacement δ must be equal to or smaller than the coherence length σ). The downside of using small x , can be seen in the composite wavefunction. For small x the partial wavefunctions destructively interfere producing a low intensity output. To account for this we can define a figure of merit which weighs the OAM yield by the intensity.

$$F = \frac{|\langle \hat{L}_z \rangle|}{\ell} \quad (5.31)$$

with $I = \int d\mathbf{r} |\psi_c|^2$ the intensity. This figure of merit is shown for two case in figure 5.7. Here we find that the figure of merit is maximized for $x = 0.6$, as soon as the number of sources N exceeds the minimal number of required sources (eq. 5.28). This result shows why in the case of neutrons real space coherent averaging is superior to the reciprocal space analog when working with neutrons. It is incredibly difficult to displace the wavefunction in reciprocal space by such a large amount to produce a value of x

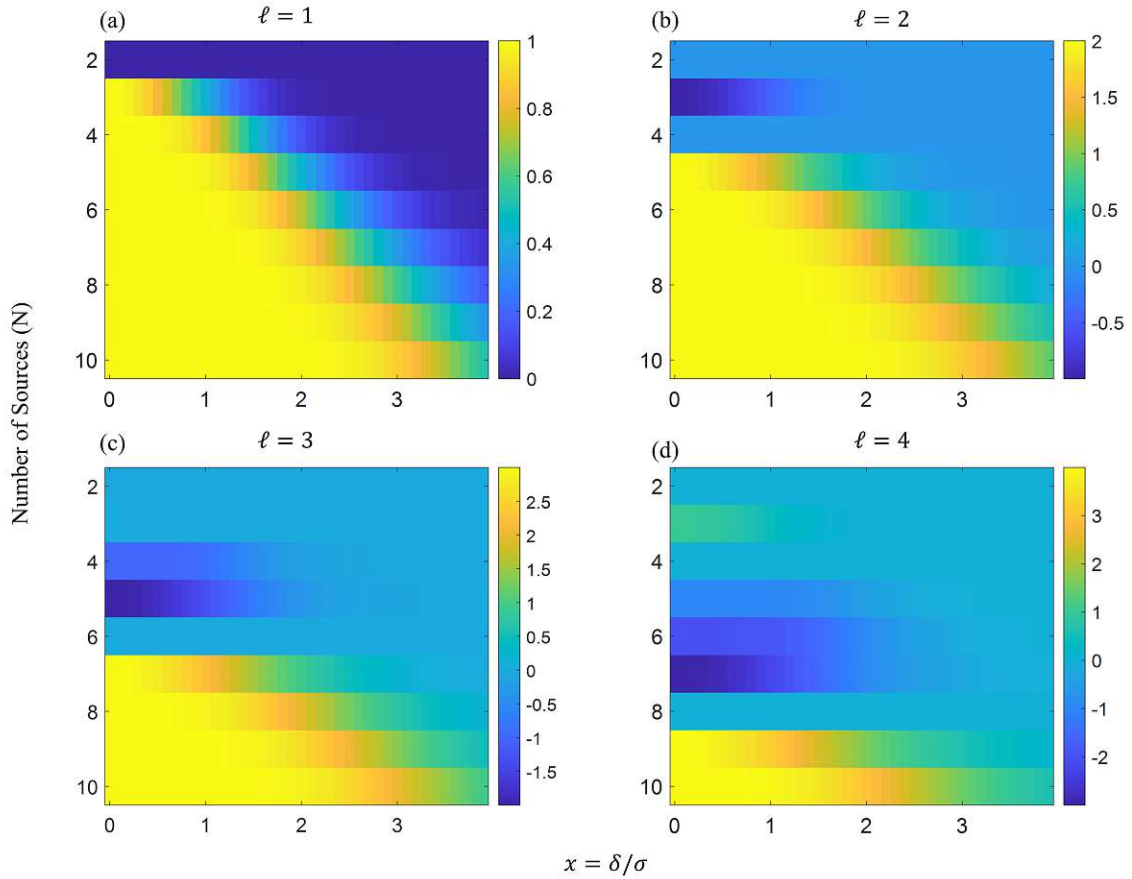


Figure 5.6: OAM expectation value of the composite wavefunction described in this section plotted against the number of partial wavefunctions that contribute to the total wavefield N and the ratio between the displacement parameter δ and the coherence length σ . Plots are shown for four different cases (a) $\ell = 1$, (b) $\ell = 2$, (c) $\ell = 3$ and (d) $\ell = 4$. We find that the highest yield occurs when the parameter x is below one and when equation 5.28 is satisfied.

large enough to maximize the figure of merit, while in real space these displacements can be produced with relative ease [118, 74].

In summary, the key takeaway from this subsection is to produce a vortex state of mode ℓ by coherent averaging with N Gaussian partial waves, one requires at least $N = 2\ell + 1$ partial waves. In addition for maximal efficiency the displacement parameter δ should equal 0.6 coherence lengths σ . Finally this implies that real space coherent averaging is more feasible for producing a high yield OAM generating device than reciprocal space coherent averaging.

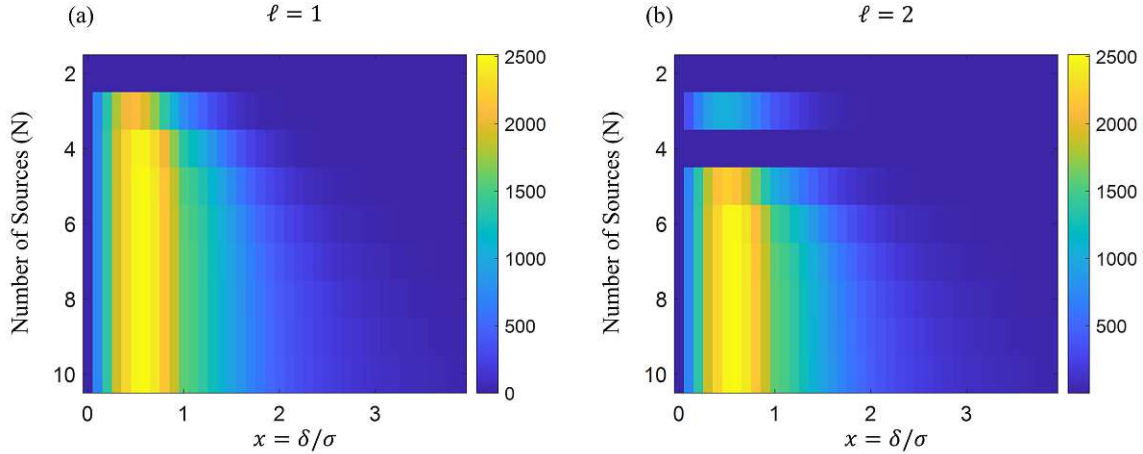


Figure 5.7: Plots of the figure of merit defined by equation 5.31 for two different cases (a) $\ell = 1$ and (b) $\ell = 2$. The figure of merit is plotted against the number of partial wavefunctions that contribute to the total wavefield N and the ratio between the displacement parameter δ and the coherence length σ .

5.2 OAM in Spin Echo Small Angle Neutron Scattering

In this section we will explore OAM generation in the Spin Echo Small Angle Neutron Scattering (SESANS) technique, which was first done theoretically in [31] and later experimentally [33], using a setup closely related to SESANS. We will begin by shortly presenting the SESANS technique and analyze the states generated by a SESANS device through the lens of OAM. After this we will look at the SESANS instrument CANISIUS built at the Atominstutut to investigate neutron OAM. Finally we will adapt SESANS to construct a coherent averaging device capable of producing $\ell = 1$ and $\ell = -1$ states. We will mainly follow the work described in [38].

5.2.1 SESANS: An Overview

Originally neutron spin echo (NSE) [102, 69], referred to an interferometric high resolution inelastic scattering technique used to resolve slow dynamics. The technique employs two rectangular shaped magnetic field regions, with opposite fields, but equal length. Neutrons entering the first region are split longitudinally according to their spin state (either aligned with the field or anti-aligned). The second region, being equal in length, but opposite in field recombines the two spin states. If no scattering takes place between the two field regions, the original polarization is recovered. If however there is some scattering between the two regions, the two spin states fail to fully recombine and we can measure a depolarization, proportional to the change in energy induced by the scattering event.

Now over 50 years later, there exist a whole host of different spin echo techniques. Some of these techniques serve the original purpose of measuring inelastic scattering, however spin echo has also been adapted to small angle scattering [39, 40] as will be discussed in this subsection. The main difference between this SESANS technique and NSE is the shape of the field regions. In SESANS we use field regions shaped as parallelograms which has as end result that the final polarization becomes sensitive to the scattering angle if scattering takes place between the two arms (see figure 5.8). Since this technique is not sensitive to divergence it was initially designed to measure small angle scattering smaller than the beam divergence, without sacrificing intensity. SESANS can also be seen as

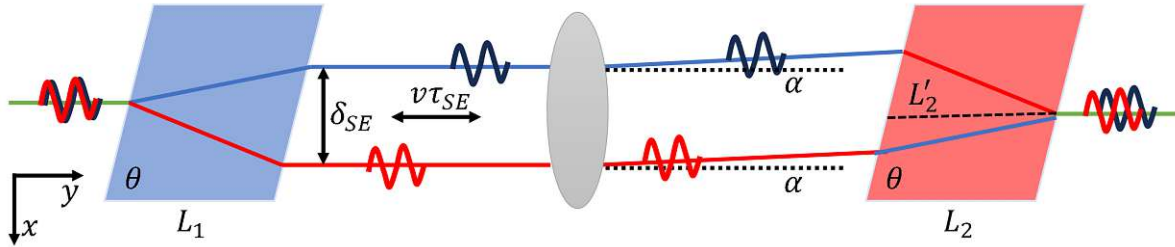


Figure 5.8: Schematic representation of Spin Echo Small Angle Neutron Scattering. Two inclined magnetic field regions of opposite polarization (represented in light blue and red) are used to induce a transverse separation between the two neutron spin states, also indicated in blue and red. The SESANS configuration shown here also induces a longitudinal separation between the wavepackets indicated by $v\tau_{SE}$. The sample indicated in gray causes the beam to be scattered by a small angle α . As a result the path length through the second field region is changed L'_2 , resulting in a net phase shift between the two spin states upon recombination.

an interferometric technique. Since the face of the magnetic field regions are inclined with respect to the momentum vector of the incident neutron spin dependent magnetic refraction takes place upon entering the field, thereby transversely separating the spin states [41]. In recent years the interferometric applications were further developed and applied to a variety of questions ranging from quantum contextuality [10, 11] to (exotic [120]) gravity [121] and to probe properties of the neutron itself, such as the intrinsic coherence of a single neutron [119].

As stated earlier regular Spin Echo, uses two oppositely polarized field regions, such that all precession induced in the first field region is reversed in the second, if the neutron velocity does not change in the instrument, ie.

$$\gamma B_1 \frac{L_1}{v_1} = -\gamma B_2 \frac{L_2}{v_2} \quad (5.32)$$

with B the magnetic field strength, L the length of the precession region and v the neutron velocity. The index refers to the first or second precession region. It follows that such a spin echo instrument is sensitive to small changes of the neutrons kinetic

energy. In SESANS the field regions are inclined (see figure 5.8), so that the instrument becomes sensitive to small changes in the neutrons transverse wavevector component, q (small angle scattering). If the velocity of the neutron is unchanged the net phase accumulated by the neutron after a small angle scattering event is simply

$$\chi = \gamma B_2 \frac{\Delta L_2}{v} \quad (5.33)$$

where ΔL_2 is the difference between the scattered and non-scattered neutron flight path length in the second arm, given by

$$\Delta L_2 = L_2 \cot(\theta_0) \alpha = L_2 \cot(\theta_0) \frac{q}{k} \quad (5.34)$$

with α the scattering angle. It follows that the phase is given by

$$\chi = \frac{\gamma m B_2 L_2 \cot(\theta_0) \lambda^2}{4\pi^2 \hbar} q = \delta_{SE} q \quad (5.35)$$

with the spin-echo length δ_{SE} equal to the induced transverse separation between the up and down spin state. When the SESANS instrument utilizes a resonant spin echo technique, such as the instrument described later in this manuscript, the spin-echo length is twice as large

$$\delta_{SE} = \frac{\gamma m B_2 L_2 \cot(\theta_0) \lambda^2}{2\pi^2 \hbar} \quad (5.36)$$

since the RF flippers used in these techniques induce zero field precession at an effective rate equal to two times the applied magnetic field.

Note that figure 5.8, also indicates a longitudinal separation between the spin states referred to as the spin-echo time, τ_{SE} , which is relevant for inelastic scattering, but in the case of the work presented here, the spin echo time is simply an undesired artifact, which we will later learn how to compensate. Returning to the analysis at hand: given the form of the phase χ , the polarisation can be written a cosine transform of the scattering function $S(q)$

$$P = \int dq \cos(\delta_{SE} q) S(q) = G(\delta_{SE}) \quad (5.37)$$

with $G(\delta_{SE})$ the real space correlation function. Since δ_{SE} is proportional to λ , a broadband/white beam instrument, measures many different correlation lengths simultaneously. Then the polarization can be written as

$$P = \frac{\int d\lambda G(\delta_{SE}) I(\lambda)}{\int d\lambda I(\lambda)} \quad (5.38)$$

with $I(\lambda)$ the intensity distribution of the sampled beam. To extract the wavelength information an additional precession coil can be inserted into the beam. This precession coil adds a phase which is field and wavelength dependent

$$\varphi = \frac{\gamma B m \lambda d}{2\pi \hbar} = \kappa \lambda \quad (5.39)$$

with d the length of the precession coil. Hence by simply adding a precession coil the final polarisation becomes the cosine transform of the correlation function times the intensity distribution

$$P(\kappa) = \frac{\int d\lambda G(\delta_{SE}) I(\lambda) \cos(\kappa\lambda)}{\int d\lambda I(\lambda)} \quad (5.40)$$

with κ proportional to the field and therefore current in the precession coil. It follows that the cosine transform of the polarization of the spin echo group, $P(\kappa)$ yields the correlation function weighted by the normalized intensity distribution. The correlation function of a specific sample can be extracted by normalizing the cosine transform of the spin echo group with sample, $P_1(\kappa)$ by a cosine transform of the spin echo group without the sample, $P_0(\kappa)$.

$$G(\delta_{SE}) = \frac{\int d\kappa P_1(\kappa) \cos(\kappa\lambda)}{\int d\kappa P_0(\kappa) \cos(\kappa\lambda)} \quad (5.41)$$

Since the correlation function of a vacuum is constant, the cosine transform of the spin echo group without a sample should simply be equal to the normalized spectrum.

SESANS may also be used to produce simple structured waves. In the quantum mechanical view magnetic refraction splits the two spin states transversely (see figure 5.8), hence such an instrument can be used for coherent averaging with two partial wavefunctions. As stated earlier the longitudinal separation induced by a SESANS instrument is an undesired artifact for coherent averaging. This can be compensated by using a different tilt angle in the second arm compared to the first arm, since this retains the length of both arms (i.e. $\gamma B_1 L_1 = \gamma B_2 L_2$) and therefore brings the two wavepackets back in phase longitudinally. Due to the different angle of the interface, however the refraction angle changes and the second arm fails to focus the spin states transversely and we are left with a residual transverse separation between the wavefunctions. The concept is illustrated in figure 5.9. This residual transverse separation is given by

$$\delta_{res} = \frac{\gamma m B L \lambda^2}{4\pi^2 \hbar} (\cot(\theta_1) - \cot(\theta_2)) \quad (5.42)$$

where we have assumed that $B = B_1 = B_2$ and $L = L_1 = L_2$. So for a Gaussian input wavefunction

$$\psi_0 = A e^{-x^2/\sigma^2} e^{ik_y y} \quad (5.43)$$

Then the output wavefunction after spin selection would be equal to

$$\psi_1 = A' [e^{-(x - \frac{\delta_{res}}{2})^2/\sigma^2} + e^{i\eta} e^{-(x + \frac{\delta_{res}}{2})^2/\sigma^2}] e^{ik_y y} \quad (5.44)$$

with η a longitudinal phase between the two partial wavefunctions. Note that we have already analyzed the longitudinal OAM of this type of wavefunction in section 2.5. The OAM distribution function is shown in figure 2.7 and can also be deduced from the work done in the previous section. In this figure we show that for small transverse separations compared to the coherence length we can produce linear OAM states that exist in an equal superposition of $\ell = -1$ and $\ell = 1$. As we will see this may be useful for detecting changes in scattering and absorption cross sections, due to OAM.

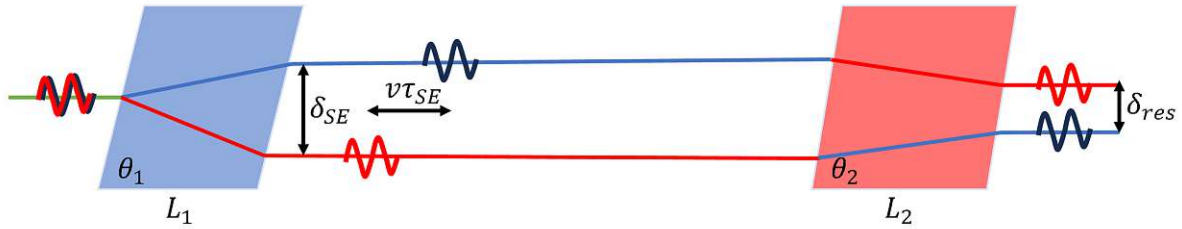


Figure 5.9: Schematic representation of the coherent averaging mode of a SESANS instrument. This mode is almost equivalent to regular SESANS, the only difference being the different angles between the two field regions. This leads to an incomplete focusing of the two spin states, which is indicated by the residual distance δ_{res} between the states at the end of the instrument.

5.2.2 CANISIUS the Austrian Spin Echo Interferometer

In this subsection we report on the new broad band spin-echo interferometer, CANISIUS (Coherent Averaging Neutron Instrument for Spin-echo Interferometry and fUNDamental Science), designed to investigate the properties of vortex neutrons carrying non-zero OAM. CANISIUS follows similar design doctrines as the Offspec [122] and Larmor [123, 124] instruments at the ISIS neutron source. That is to say, CANISIUS uses adiabatic RF flippers [125] to generate the magnetic field regions by the zero field precession technique [126] and to ensure broad band efficiency. The instrument is built in a modular way so that it can be applied to a variety of different modes (SESANS, SEMSANS [112], NRSE and MIEZE). In addition CANISIUS can quickly change between a continuous white beam and a pulsed beam for time of flight. Here we will report on the design and efficiency of the adiabatic RF-flippers and the instrument, the interferograms produced by the instrument in broad-band and time of flight (ToF) and the calibration of the spin echo length in SESANS mode.

Instrument Overview

A three dimensional render of the CANISIUS instrument in a SESANS configuration is shown in figure 5.10. CANISIUS is situated at the white beamline of the Atominstut (TU Wien) 250 kW reactor. The instrument can be operated in either a continuous broad-band or two distinct ToF modes. A standard mechanical chopper is used for the regular ToF mode. The second mode is enabled by a spin chopping system, which is made possible since the beam is initially polarized by double reflection from a pair of $m=4$ single flat substrate supermirrors, this allows the beam to be chopped by inserting a broad-band spin flipper between the two mirrors which can be pulsed [127, 128]. Due to the cut-off of the supermirrors the available wavelength range is $2\text{\AA} - 6\text{\AA}$, with a peak at 2.5\AA . After the double reflection polarizer the beam is passed through a v-coil which adiabatically rotates the neutron spin around the propagation axis from vertical

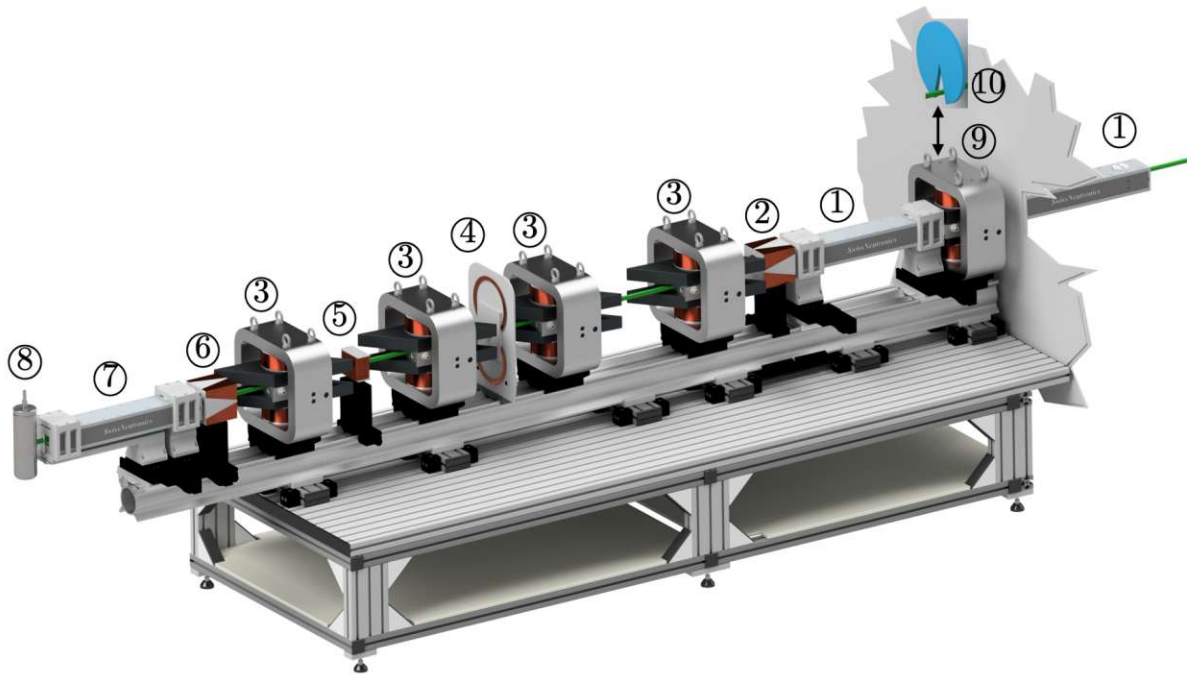


Figure 5.10: Render of the CANISIUS instrument configured for white beam SESANS. The beam propagates from right to left. First the beam is polarised by double reflection from two single substrate $m=4$ polarising supermirrors (1). Next the polarisation is adiabatically rotated by 90 degrees by a v-coil (2). The beam then passes through a pair (arm 1) of adiabatic RF flippers with parallelogram shaped poleshoes, which act as the first beam splitter and mirror (3). A field stepper is positioned between the first and second pair (arm 2) of RF flippers, to facilitate a fast non-adiabatic field transition from arm 1 to arm 2 (4). Samples of various types may be inserted right before the field stepper. The second arm of RF flippers serve effectively as a mirror and beam splitter to recombine the split beams. Between the last two RF flippers the beam is passed through a precession coil (5). Finally before the spin is selected by the last polarising supermirror (7) the neutrons pass through a final v-coil facilitating another adiabatic 90 degree rotation (6). Neutrons passing the polarising supermirror are detected by a high-efficiency ^3He counting tube. In addition to the usual continuous mode of operation the CANISIUS instrument can also be operated in ToF mode. For this purpose two chopper device are available: a conventional mechanical chopper (10) as well as a spin-chopper system (9), consisting of an RF flipper in combination with the pre-polarizer, that is the very first supermirrors (1). The length of the instrument, given by the distance between chopper (9,10) and detector (8) is 3 meters.

to horizontal. Quantum mechanically this implies that the neutron spin can be seen as being in a superposition of the up and down spin state. In the first arm of the instrument which consists of a pair of adiabatic RF flippers [129], the two spin states are separated longitudinally (standard NRSE) and if parallelogram shaped poleshoes are employed also transversely (SESANS). The second arm with equal but opposite field of the first arm recombines the spin states. Spatial overlap between the two spin states is ultimately measured by a spin projective measurement, which in practice is enabled by a v-coil and a supermirror. An additional closed coil in arm 2, allows variation of the phase between the two spin states. Finally a series of wedges can be inserted to change and calibrate the angle of the poleshoes by up to ± 5 degrees. This gives some more flexibility to tune the transverse spin state separation, however its primary purpose is to enable the new coherent averaging mode, to produce structured neutron waves. If both arms of the interferometer are operated at a different poleshoe angle the instrument fails to focus the spin states transversely. As a result some residual separation is left between the spin states. As shown previously, this residual separation induces a structured wave with OAM. The residual separation may also be scanned, thus allowing one to measure the correlation between the spin up and down wavefunctions, similar to what is described in [118]. In Chapter 6 we will explore measuring wavefunction correlations with this technique to determine the structure of said wavefunction. On average over the entire wavelength band the polarization of the instrument in the non-echo mode (RF system and v-coils turned off), in which there should be no spin precession, is 0.904. The RF coils are matched to the output impedance of the amplifiers for operation at 1.4 MHz, however the coils may also be operated in resonant mode (ToF or monochromatic), in which case they can be operated at any frequency between 10 kHz and 5 MHz, since the power requirements are low (1-2 W) and the amplifiers are equipped to handle up to 400 W of reflected power. We will now turn to the details of the instrument starting with the design of the RF flippers and then moving on to the Time of Flight operations and then finally we turn to the measurements conducted in SESANS mode.

Adiabatic Radio Frequency Flippers

An RF flipper, used by the CANISIUS setup, is depicted in figure 5.11, for 3 different poleshoe configurations, square for NRSE and MIEZE, parallelogram for SESANS and SEMSANS and tilted parallelogram for coherent averaging. The poleshoes in addition to the magnetic cores were machined from soft iron and subsequently heat treated. The yokes were machined from construction steel. Coils of 400 windings each are situated around each magnetic core. The gap between the poleshoes is 30 mm, in which the RF system is situated (figure 5.11 (d)). This RF system consists of an aluminium housing containing an 80 mm long RF coil with a diameter of 20 mm and a gradient coil which has minimal winding density in the center and increases towards in the ends of the coil. The RF coil consists of 2 mm copper tubing (inner diameter 1.5 mm) wound on a PEEK bobbin and encased in kapton foil to prevent arcing. 250 ml/min of G12 coolant is pumped through the tubing, to facilitate heat transport, the coolant

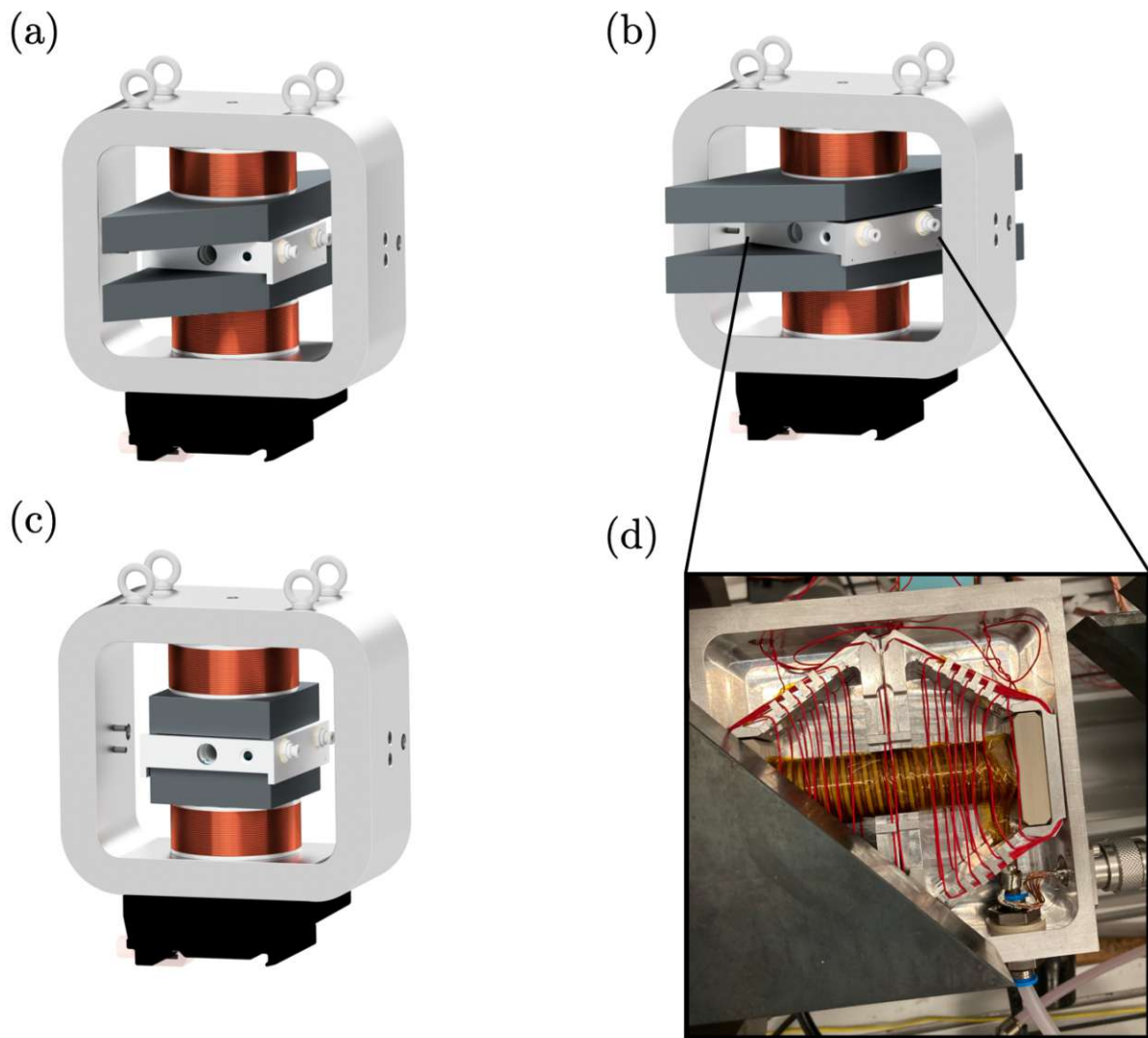


Figure 5.11: Render of the adiabatic RF spin flippers with parallelogram shaped poleshoes at 45 deg (a), 45 ± 5 deg (b), and 90 deg in (c). The photo in (d) shows a top-view of one RF coil partly taken out of the parallelogram shaped poleshoes for demonstration purposes to see water the cooled RF coil, the gradient field coil, as well as the inlet of the coolant and the electrical conducting.

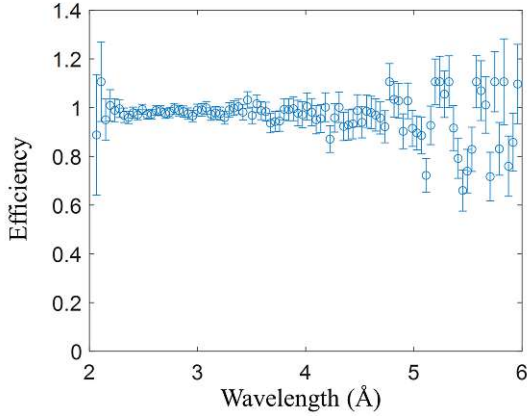


Figure 5.12: Flipping efficiency of one adiabatic RF flipper against wavelength measured using the ToF technique. This is calculated using ToF spectrums with the flipper on and off, the result is finally normalised by the instrument efficiency of 0.904. The weighted average of the flipping efficiency over the entire spectrum is 0.977.

is cooled to 3 degrees by a secondary loop connected to a chiller. Matching of the RF coils to the amplifier output is done capacitively for a single frequency, 1.4 MHz. Mica capacitors were used for their high stability and low loss at typical NRSE frequencies. In adiabatic flipping mode, roughly 60 W are dissipated in each coil, in addition to 40 W in each gradient coil. In resonant flipping mode only 1-2 W are required depending on the frequency, hence in this mode matching between load and amplifier is not necessary. The efficiency of a single adiabatic RF flipper is shown in figure 5.12, which is determined first by measuring the polarization in a non precessing mode (v-coil turned off) and then normalizing said polarization by the the instrument spin transport efficiency, which as mentioned earlier is 0.904. The polarization is calculated using the well known formula

$$P = \frac{I_+ - I_-}{I_+ + I_-} \quad (5.45)$$

with I_+ the intensity of the spin state aligned to the analyzing direction (i.e. when the flipper is turned on) and I_- the opposite spin state. Figure 5.12 demonstrates that our RF flippers have a constant flip efficiency over the entire wavelength band indicating a good adiabaticity of the flippers. A weighted average efficiency of 0.977 can be extracted from the data shown in figure 5.12. This is comparable to some other adiabatic RF flipper designs [130]. Though we note that flipping efficiency of 99% are possible with similar design [131]. In some other designs efficiencies of up to 99.9% have been reported [132].

5 Coherent Averaging

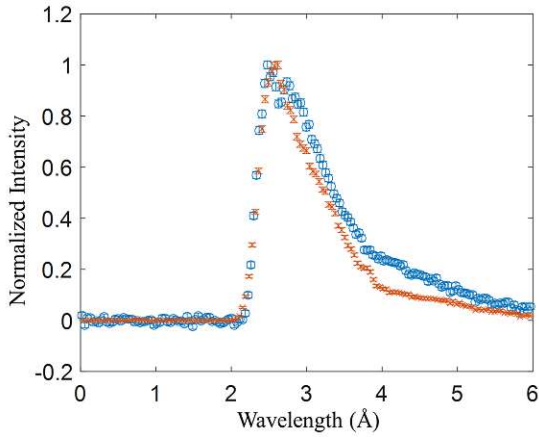


Figure 5.13: Normalized Time of Flight spectra produced using the RF spin chopping device (blue circular data points) and the mechanical chopper (red cross shaped data points).

Time of Flight Options

CANISIUS has two options available for producing a pulsed beam. The first is a fermi like chopper which consists of stacked, short, straight, cadmium lined channels, which is spun at 50 Hz, resulting in an effective pulse frequency of 100 Hz. The second method, uses an RF flipper positioned between the two polarizing supermirrors. In this case the the two mirrors are oriented to select opposite spins, so that when the flipper is off no beam is transmitted into the instrument. In resonant mode the phase accumulated by a neutron in the flipper is given by

$$\alpha = \gamma B_{RF} t \quad (5.46)$$

with γ the gyromagnetic moment of the neutron B_{RF} the field strength and t the time for which the particle is exposed to the field. Hence if the RF pulse time is much shorter than the flight time through the device of the fastest neutron then this phase is wavelength independent. Therefore to produce a pulsed beam the RF flipper is simply shortly pulsed in resonant mode, which flips all neutrons that are in the RF coil at the time of the pulse. These neutrons can then be transmitted through the instrument and to the detector. This RF flipper is designed equivalently to the others described in the previous section, with the exception of the gradient coil, since this is not required. The RF field pulse length is $5 \mu s$, ten times shorter than the flight time of 2.5 \AA neutrons through the RF coil. This corresponds to 7 cycles of the RF field at 1.4 MHz. In figure 5.13 a comparison between the ToF spectra of the mechanical and spin chopper can be seen. It can be seen that for short wavelengths the chopper systems perform with equal relative efficiency, however at longer wavelengths the spin chopper has a higher transmission compared to the mechanical chopper. This is due to the wavelength dependent transmission of the mechanical fermi chopper [133] which we may approximate at long wavelengths by 1 minus the ratio between the channel width seen by a neutron of wavelength λ and the

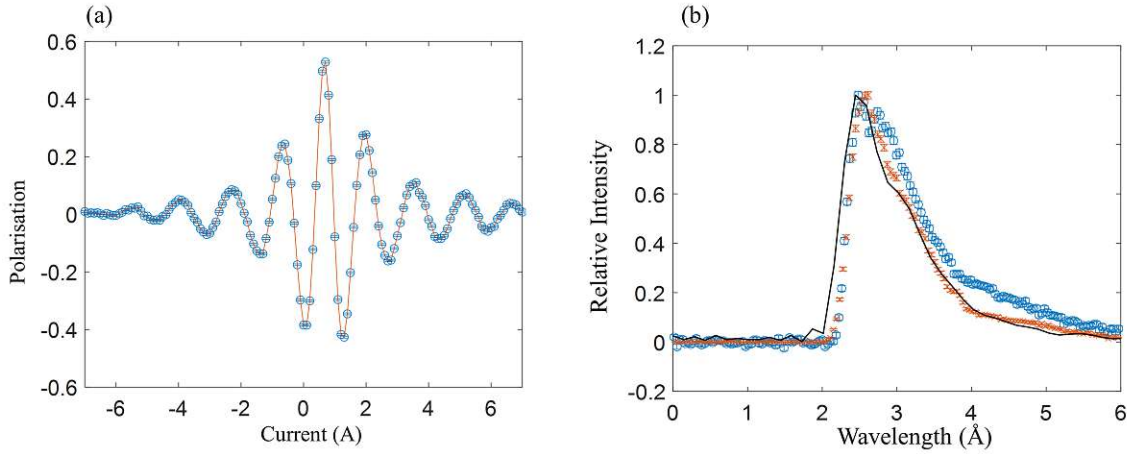


Figure 5.14: (a) Polarisation of the spin echo group measured against current in the precession coil. The individual data points with errorbars are shown in blue and in interpolation of the data is shown in red. (b) The Fourier transform of the spin echo group is shown in black, while the spectra measured using both chopping techniques also shown in figure 5.13 is superposed.

channel width when the chopper is at rest:

$$T = 1 - \frac{\omega m \lambda D^2}{4\pi d \hbar} \quad (5.47)$$

with ω the rotation frequency of the device, D the length and d the width of the channels. The transmission of the spin chopper on the other hand is independent of wavelength when the RF pulse time is much shorter than the flight time of the neutron through the RF coil. In this case, much like the double disk chopper [134], the wavelength resolution is also wavelength independent, depending only on the distance between the chopper and the detector, L and the length of the RF coil D

$$\frac{\Delta\lambda}{\lambda} = \frac{D}{L} \quad (5.48)$$

In addition the RF pulse frequency can be optimized for a given detector distance to maximize intensity.

Interferograms and Calibration of SESANS mode

Figure 5.14 (a) shows an interferogram measured by scanning the precession coil (nr. 5 in figure 5.10). Recall that we previously showed that this so called spin-echo group is the Fourier transform of the wavelength spectrum (i.e. equation 5.40), hence figure 5.14 (b) shows the Fourier transform of the measured spin echo group superposed on the spectra measured using time of flight methods. The spin echo length of CANISIUS was calibrated using two different kinds of nanoporous alumina membranes from

smartmembranes [135], similar to the method described in [136]. The first sample has pores with a diameter of 25nm and a pitch of 65nm, while the second sample has pores with a diameter of 40nm and a pitch of 125nm. Both samples have a thickness of 50 microns. The pore diameter and the pitch were both confirmed by SEM imaging (see figure 5.15). Since both samples display some long range ordering, we expect the correlation function $G(\delta_{SE})$ to be sinusoidal for δ_{SE} equal to small multiples of the pitch. And since sample two has twice the pitch of sample 1 we expect the period of the oscillations in the correlation function of sample 2 to be twice as large as those in the correlation function of sample 1. Hence these samples are ideal for calibrating the spin echo length of the instrument. The raw correlation functions of both samples measured by CANISIUS are shown in figure 5.16. The correlation function of the sample with the shorter pitch, shows clearly multiple oscillations with a period of approximately 58.5nm, while the correlation function of the longer pitch sample shows only one full oscillation where we estimate the period to be equal to 112.6nm. This is confirmed by taking the Fourier transform of the data and determining the location of the peak in the Fourier transform. To reduce $1/f$ noise we use the transmitted corrected data for the Fourier transform which is defined as [136]

$$G_{TC} = \log(G(\delta_{SE}))/\lambda^2 \quad (5.49)$$

These Fourier transforms show that the periods of the correlation functions do indeed differ by a factor of two within the sampling width, indicating that CANISIUS does indeed split a neutron wavefunction into two equal parts separated transversely by 100 – 600 nm. Our calibration measurements show that the expected spin echo length, calculated using equation 5.35, is within 10% of the actual spin echo length produced by the instrument.

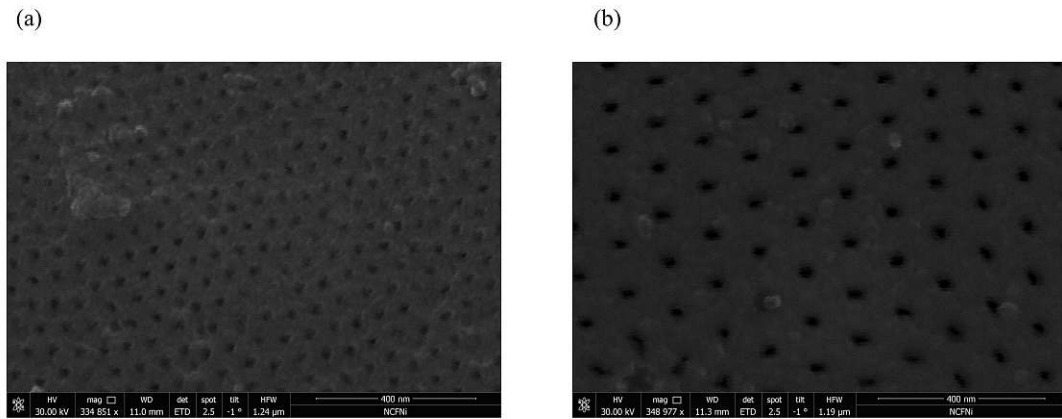


Figure 5.15: SEM images recorded of the (a) 65nm and (b) 125nm period smartpore alumina membranes. The scale indicated at the bottom right is the same for both images and is equal to 400nm

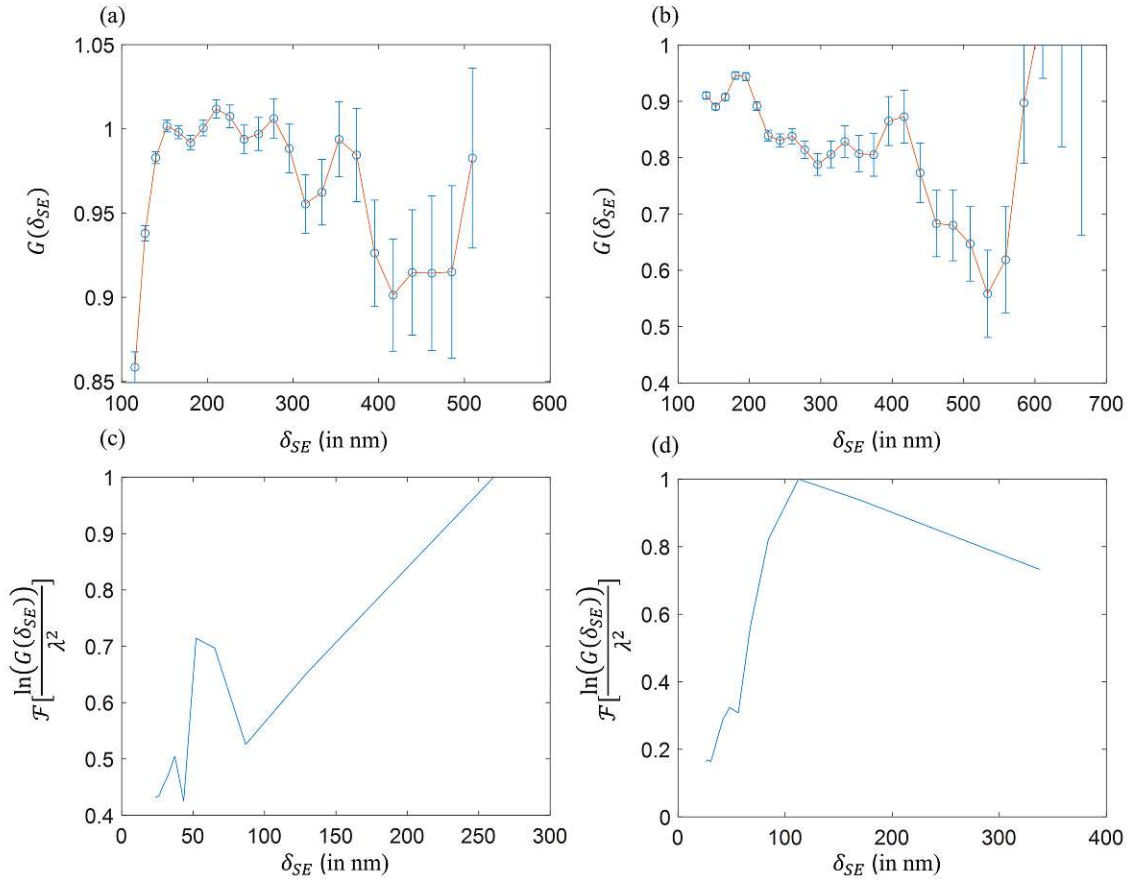


Figure 5.16: Correlation functions of the (a) 65nm and (b) 125nm pitch smartmembrane alumina membranes measured using CANISIUS. The insets (c) and (d) show the Fourier transforms of the transmission corrected versions of the correlation functions shown in insets (a) and (b) respectively. Each inset shows the spin echo length in nm on the x-axis. In the case of the Fourier transforms this axis corresponds to the period as opposed to the frequency. The spin echo lengths shown are calculated based on equation 5.35

5.2.3 Two Dimensional SESANS as a Generator of OAM

In the previous subsection we showed that a regular SESANS instrument produces two partial wavefunctions which can be used for coherent averaging. This is sufficient to produce linear OAM states, which have an average OAM of zero. As we will see later this can be quite useful and has a few unique applications, however in some cases it is necessary to produce an OAM state with a non-zero OAM expectation value. As we saw in section 5.1.4, we need at least 3 partial wavefunctions to produce an $\ell = 1$ or $\ell = -1$ state, ideally more. In this subsection we will see that a SESANS instrument where the fields of arm 1 and arm 2 are orthogonal to each other, produces four partial wavefunctions. In principle the work described in [33] and [114] describes such a two

dimensional spin echo device, though they considered a SEMSANS instrument which uses reciprocal space coherent averaging. Here we will look at the SESANS equivalent using real space coherent averaging. The former setups, but also the one we are about to describe uses magnetic Wollaston prisms [112], which have the added advantage of not introducing a spin-echo time, as was the case in the previous setups. A schematic representation of a Wollaston prism can be seen in figure 5.17. The square prism is divided into two right sided triangular field regions with a field of equal magnitude but opposite direction. As a result at the interface between the two field regions the neutron spin states are split apart transversely according to the Zeeman interaction. Since both field regions are equal in length the net field integral and therefore the result spin-echo time are zero. That is to say the Wollaston prism induces transverse separation but no longitudinal displacement. A pair of Wollaston prisms with opposite fields can be used for real space coherent averaging, as the second prism stops the divergence of the two partial wavefunctions and thereby fixes the transverse displacement between the two partial waves. An additional precession coil can be used to influence the phase between the partial wavefunctions. A regular SESANS instrument would have a second arm consisting of two more Wollaston prisms with opposite field direction. This arm would spatially recombine the spin states. However if we rotate the second arm of the device 90 degrees with respect to the first beam around the beam, the second arm induces transverse splitting in the direction orthogonal to the splitting produced in the first arm. Each partial wavefunction produced by the first SESANS arm is split transversely into two new partial wavefunctions. Hence the second arm produces a total of four partial wavefunctions. As we know from our work in section 5.1.4 this is a sufficient number of waves to produce an $\ell = 1$ or $\ell = -1$ state. The instrument we just described is shown schematically in figure 5.18. The state of the total wavefunction is written explicitly in the figure to show how it evolves as it traverses the instrument.

We have already shown generally how to create and $|\ell| = 1$ vortex state with four partial wavefunctions in 5.1.4. In particular we must choose $\Delta\theta_1 = \Delta\theta_2 = \frac{\pi}{2}$ to produce the desired vortex state. In addition the displacement parameter d must be chosen such that $d < \sigma$. Since ideally we would like the vortex state to be pure (i.e. the distribution function should be zero for all ℓ except the desired vortex mode), we will calculate equation 5.29 for the special case where $N = 4$ and $\ell = 1$ for various δ/σ . The results are shown in figure 5.19. We find that full suppression of side-bands occurs for $\delta/\sigma < 0.5$, though as figure 5.3 shows for small displacement parameters the phase parameter, must be very precisely set or else no vortex states are produced at all. For this reason it can be advantageous to accept small side-bands and use a higher displacement as this produces (a) more intensity and (b) requires less precision in terms of calibration.

Since this type of setup, produces relatively pure vortex states it is ideal for investigating the properties of single vortex modes, in particular scattering and absorption characteristics. Hence we will use this type of setup in chapter 7 where we look at the dependence of absorption cross sections on the OAM of the incident beam.

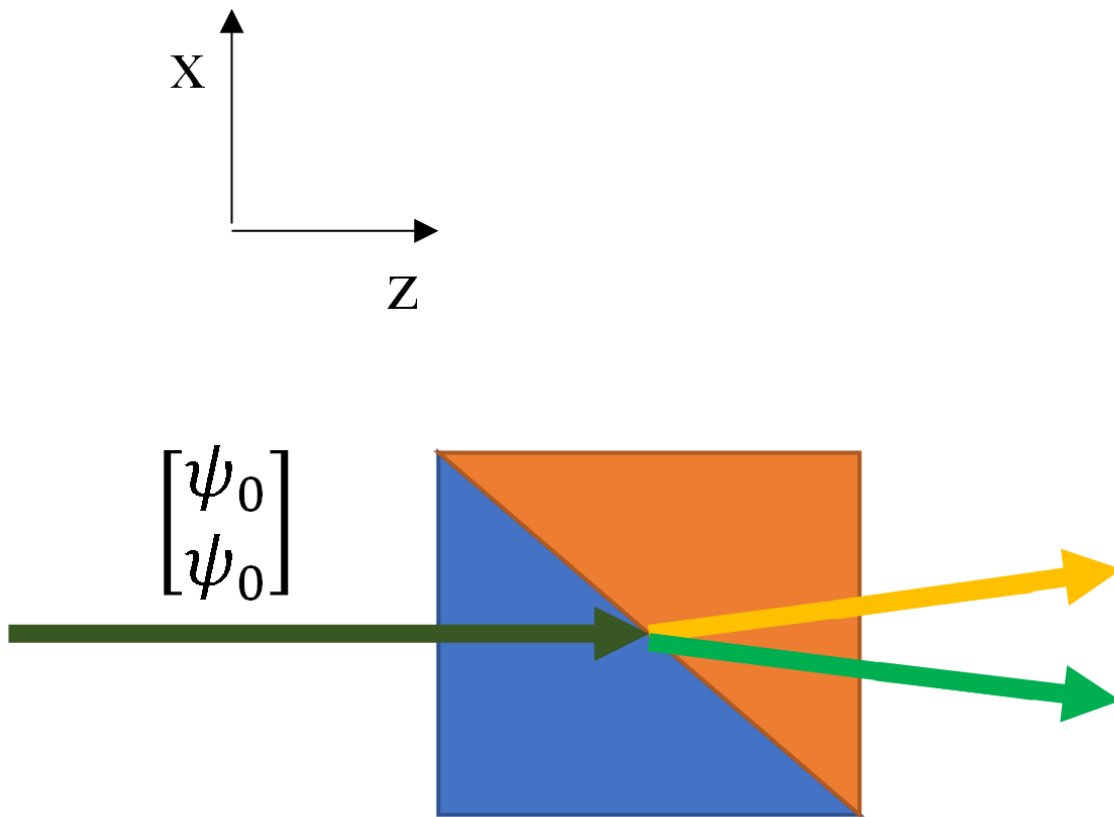


Figure 5.17: Schematic of a magnetic Wollaston prism. The square prism is divided into two right sided triangles. The two colors, orange and blue, represent a magnetic field of equal magnitude but opposite direction. A neutron which is initially in a superposition of the up and down spin state, splits spatially in its two separate spin states ones it reaches the field boundary, causing the two states to diverge transversely from each other.

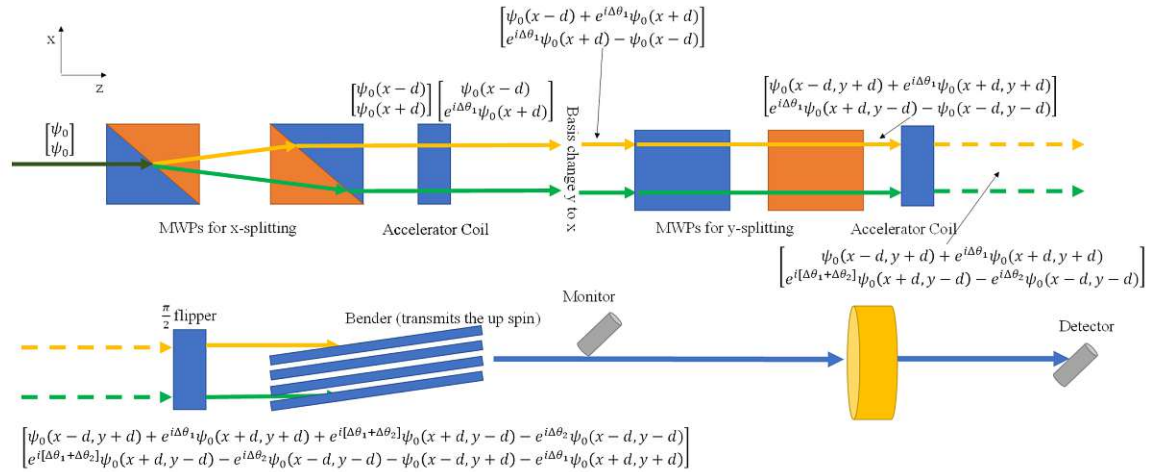


Figure 5.18: Schematic of a setup showing a neutron being separated in the x-direction by a pair of Wollaston prisms. Next a longitudinal phase difference is induced using a magnetic coil (here called accelerator coil). Afterwards a second pair of Wollaston prisms split the neutron in the y-direction (into the page not visible). A second precession coil induces another phase shift. Finally a $\pi/2$ flipper and a polarizing bender select the L=-1 composite state. The composite state is passed through a sample which is being investigated after which the intensity normalized by the monitor value is measured.

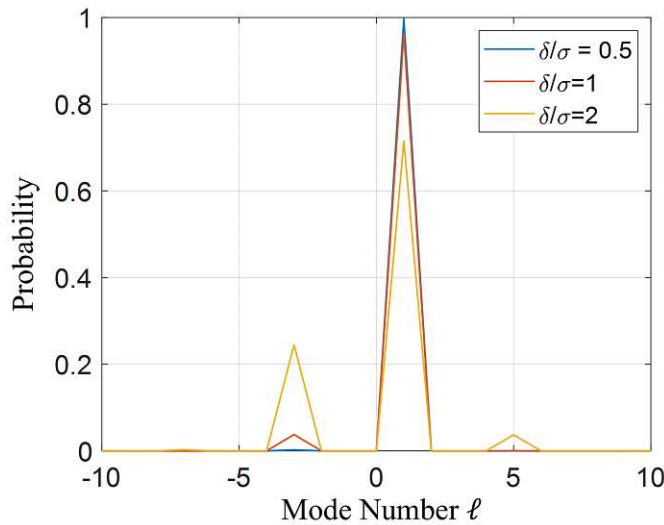


Figure 5.19: OAM distribution function for $N = 4$ and $\ell = 1$ (i.e. the state produced in the instrument shown in figure 5.18) for various displacement parameters. In blue we see a displacement parameter that is 50% of the coherence length, in red 100% and yellow 200%. We see that full suppression of sidebands already occurs for a displacement parameter that is 0.5σ or smaller.

5.3 Conclusion

We have explored the coherent averaging method and its application to producing vortex states. We saw that this method was first explored in spin echo methodologies in [32] and [33] and later generalized to interferometry in [34]. The latter experiment and its potential applications were also explored in this chapter. The former methods all utilized reciprocal space coherent averaging, however in this chapter we found that real space coherent averaging would be a better fit to neutron optics, as it is more efficient, produces larger amplitudes in the vortex state and existing neutron optics are more suited to this particular method. With this knowledge we generalized the real space coherent averaging method and calculated OAM distribution functions of composite wavefunctions which are made up of N partial Gaussian wavefunctions. We found that one requires at least $N = 2\ell + 1$ partial waves to produce a composite wave with an OAM equal to ℓ . With this knowledge we moved on to applying real space coherent averaging to spin echo interferometry. We found that a regular SESANS instrument can produce linear OAM states which consist of an equal superposition of $\ell = 1$ and $\ell = -1$. In addition when the second arm is rotated around the beam by 90 degrees with respect to the first arm, the instrument can produce high purity $\ell = 1$ or $\ell = -1$ states. Finally we looked at the CANISIUS spin echo interferometer built at the Atominstitut with the explicit purpose of exploring linear OAM states, finding that both the wavelength and spin echo length calibrations were quite precise, with theory and measurement differing only by 10%.

6 OAM Detection in Interferometry

Up until now we have look at the general theory behind neutron OAM and various methods of producing vortex states in OAM, while giving very little attention to the detection of neutron OAM. In these last chapters we will turn our attention to the problem of OAM detection. This first chapter on detection focuses on the use of interferometry to determine the OAM of a test wavefunction. However you may have noticed, in the previous chapters on generation of OAM we did claim to demonstrate some wave or beam OAM. So how did that OAM detection scheme work? There we used the simplest interferometric technique, which attempts to resolve the interference pattern between a reference wavefunction and the wavefunction under investigation. For this reason in all these chapters we either used a detector with position resolution, or angular (i.e. momentum) resolution. This method becomes technically impossible once we decide to produce vortices on the length scale of the neutron coherence length (i.e. by real space coherent averaging), since there are no detectors with this type of resolution and in addition the neutron flux would be insufficient to provide sufficient statistics to get a meaningful result.

In this chapter we will look at a modified interferometric technique which can be used to resolve azimuthal structure of a test wavefunction relative to a reference wavefunction on the length scale of the neutron coherence. The chapter is subdivided into two sections, a theoretical overview and an experimental demonstration, where we measure the autocorrelation of a typical neutron wavefunction. These techniques are derived from previous work done with perfect crystal neutron interferometers [118]. We will focus in particular on applying this method to spin-echo interferometry, since the perfect crystal analog has been covered extensively in previous literature.

6.1 Theoretical Overview

Our methodology for resolving the wavefunction is based strongly on our work done on coherent averaging, in particular coherent averaging using a regular one dimensional SESANS instrument. Our method relies on using a SESANS in which the tilt angle of the second arm (θ_2) differs from that of the first arm (θ_1). As a result the two spin states fail to fully recombine (figure 5.9). The output wavefunction shown schematically

in figure 5.9 can be written as

$$\psi = \begin{pmatrix} \psi_{\uparrow}(x, y, z) \\ \psi_{\downarrow}(x + \delta_{res}, y, z) \end{pmatrix} \quad (6.1)$$

where the basis (z) is chosen parallel to the direction of the magnetic fields. Without position sensitivity the transverse polarization components are then

$$\langle \sigma_x \rangle (\delta_{res}) = \int d\mathbf{r} \psi_{\uparrow}^{\dagger}(x, y, z) \psi_{\downarrow}(x + \delta_{res}, y, z) + \psi_{\uparrow}(x, y, z) \psi_{\downarrow}^{\dagger}(x + \delta_{res}, y, z) \quad (6.2)$$

and

$$\langle \sigma_y \rangle (\delta_{res}) = i \int d\mathbf{r} \psi_{\uparrow}^{\dagger}(x, y, z) \psi_{\downarrow}(x + \delta_{res}, y, z) - \psi_{\uparrow}(x, y, z) \psi_{\downarrow}^{\dagger}(x + \delta_{res}, y, z) \quad (6.3)$$

which appear to be the transverse cross correlations between the up and down state wavefunctions, also known as coherence functions [137, 138]. If the two wavefunctions are the same we obtain the autocorrelation. Thus we can obtain information about the wavefunction structure by measuring $\langle \sigma_x \rangle$ and/or $\langle \sigma_y \rangle$ as a function of the tilt angle of the second arm of a SESANS interferometer. Similar principles have been used to measure the longitudinal coherence in neutron spin echo. In fact the spin echo group is nothing other than the longitudinal autocorrelation function [124, 41, 74, 137]. However in this chapter we will continue to focus on the transverse cross correlations, since longitudinal OAM is a transverse structure.

While autocorrelations are useful to determine the coherence of a wavefunction, it cannot resolve the phase structure of the underlying function. For this reason we require a reference function that carries a known amount of OAM to resolve the azimuthal structure of an unknown vortex state. That is to say, one of the spin states would be occupied by the reference wavefunction, while the other spin state would be equal to the wavefunction under investigation. Ideally this reference wavefunction would be a delta function as in that case the cross correlation is equal to the test wavefunction. To be more precise $\langle \sigma_x \rangle$ would reveal the real part while $\langle \sigma_y \rangle$ the imaginary part of the wavefunction. In reality we have to settle for Gaussian or Sinc type reference functions. The sinc reference function is motivated by the fact that the transverse momentum distribution in a neutron instrument is usually determined by a pair of slits, which results in a square momentum distribution (see figure 3.1). The Fourier transform therefore dictates that the real space wavefunction must be a sinc.

Since a vortex state manifests as a two dimensional phase structure a one dimensional coherence function is insufficient to determine whether or not a wavefunction carries OAM. A two dimensional coherence function must be measured. This can be done by either rotating the SESANS instrument around the beam, or by rotating the OAM generator around the beam, which effectively rotates the generated vortex. We have seen that we require $2|\ell| + 1$ coherent sources to generate a vortex of mode ℓ . A similar argument can be made for detection: we require the coherence function for $2|\ell| + 1$ different angles to be able to resolve vortices of mode $|\ell|$ or smaller. This is because

the OAM of the sum of the two polarization components $\langle \sigma_x \rangle + i \langle \sigma_y \rangle$ (the two dimensional coherence function) carries the same OAM as the test wavefunction assuming the reference wavefunction carries no OAM. For visualization we show a pair of two dimensional coherence functions in figure 6.1, for a test wavefunction with $\ell = 1$ and $\ell = 2$ OAM under the assumption that the reference is a sinc wave. It is quit clear

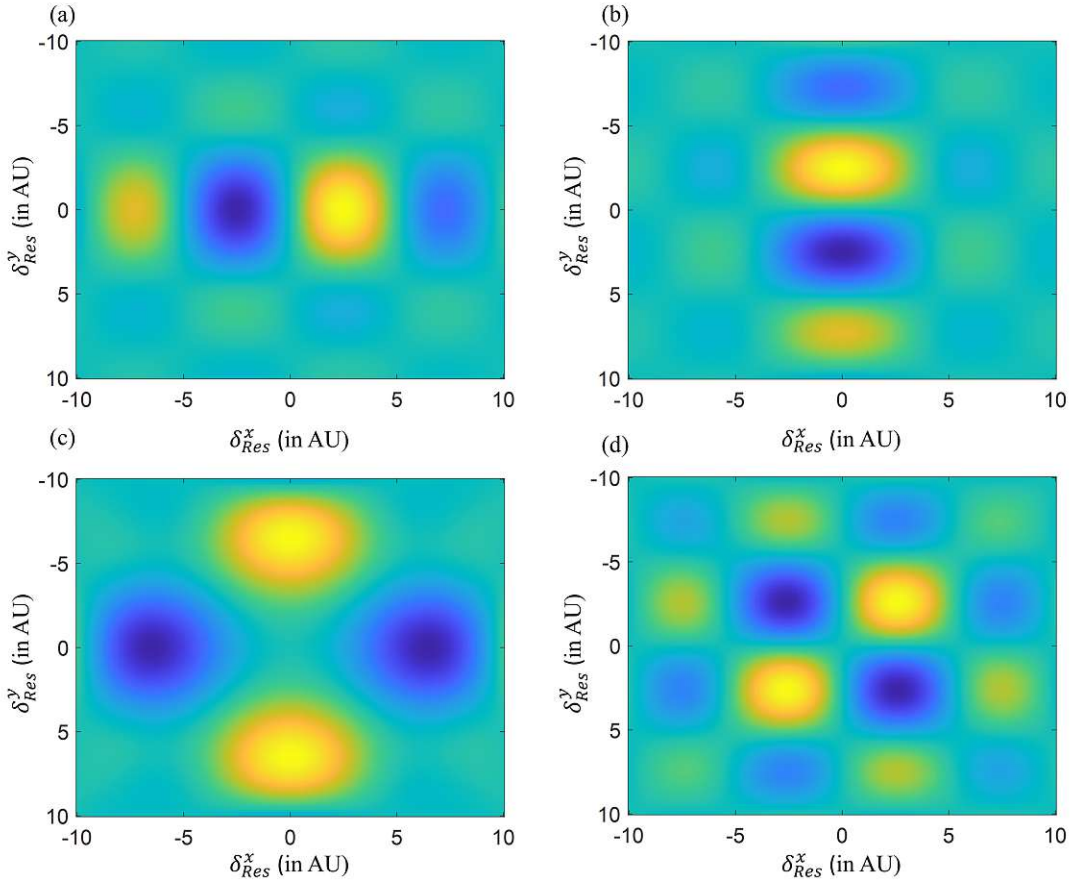


Figure 6.1: Plots of the two dimensional coherence functions eq. 6.2 (left) and 6.3 (right) for an $\ell = 1$ vortex (top) and an $\ell = 2$ vortex (bottom). The reference wavefunction is assumed to be a sinc function with no azimuthal structure. The color axis is arbitrary and therefore not labeled

that the sum of the imaginary and real two dimensional coherence functions have the same azimuthal structure as the test wavefunction. As a result we can conclude that this is a fitting method for measuring the OAM of an unknown vortex state. A danger exists in undersampling. A vortex state with a higher mode number may appear to have a lower mode number using this method if insufficient samples are chosen along the azimuthal direction.

6.2 Measurement of the Autocorrelation of a Neutron Wavefunction on a Spin Echo Interferometer

The method described above has not yet been applied to vortex states, since the thermal neutron vortex generators as well as the interferometers required to resolve them are quite large, such that they haven't both been accommodated by a single beamline yet. Though the methodology has been applied plenty of times to measuring the coherence length and autocorrelation of the neutron wavefunction [118, 74]. Here we report on such an experiment where the one dimensional transverse coherence function of a neutron was determined using a SESANS interferometer. The interferometer used for this investigation is the versatile Offspec spin echo and reflectometry instrument [122, 139], which combines a multitude of spin echo techniques (SESANS, SEMSANS, NRSE) with reflectometry (SERGIS) [140]. Just like CANISIUS, Offspec produces the magnetic field regions necessary for SESANS using adiabatic RF spin flippers with shaped poleshoes. The poleshoes are rotatable making the instrument ideal for coherent averaging methods and the technique described in the previous section.

As we argued above when the beam is collimated by a single slit the transverse wavefunction can be described by a sinc function:

$$\psi_{\perp}(x, y) = \text{sinc}(k_x x) \text{sinc}(k_y y) \quad (6.4)$$

with the transverse wavevectors equal to the magnitude of the total wavevector times the beam divergence $k_{x,y} = |k| \theta_{x,y}$. At a distance D from a slit with diameter d the maximal divergence angle is given by $\theta = \frac{d}{2D}$. The intensity is distributed uniformly over all angles small than θ . When we pair two slits together with diameters d_1 and d_2 and a distance D between them, we must convolve the two uniform momentum distributions provided by each slit to obtain the total momentum distribution [141]. In real space this is the same as multiplying the sinc wavefunction that would be generated by slit 1 by the sinc wave generated by slit 2. So for 2 slits/collimators we can write the total wavefunction as

$$\psi_{\perp}(x, y) = \prod_{i=1}^2 \text{sinc}\left(\frac{\pi d_i^x}{D\lambda} x\right) \text{sinc}\left(\frac{\pi d_i^y}{D\lambda} y\right) \quad (6.5)$$

with d_i the diameter of the i^{th} slit in x or y direction. We can define a coherence for each individual term in the wavefunction by $\sigma_{\perp} = 1/k_{\perp}$

$$\sigma_{x,y} = \frac{D\lambda}{\pi d_{x,y}} \quad (6.6)$$

which interestingly is proportional to the wavelength. The residual transverse separation/spin echo length on the other hand is proportional to λ^2 (eq. 5.42). Hence in SESANS we scan through the entire transverse coherence by fixing the tilt angles of the two field regions and scanning only the wavelength.

We will now begin estimate $\langle \sigma_x \rangle$ by filling in our guessed wavefunction (eq. 6.5) into equation 6.2 (note since our measurement is one dimensional we will neglect the y-coordinate)

$$\langle \sigma_x \rangle (\delta_{res}) = A \int dx \prod_{i=1}^2 \text{sinc}\left(\frac{\pi d_i^x}{D\lambda} x\right) \text{sinc}\left(\frac{\pi d_i^x}{D\lambda} (x + c\lambda^2)\right) \quad (6.7)$$

with A a normalization constant and $c = \frac{\gamma m B L}{4\pi^2 \hbar} [\cot(\theta_1) - \cot(\theta_2)]$ (justified by eq. 5.42).

Our measurement carried out at Offspec used a wavelength band of $2\text{\AA} - 12\text{\AA}$, an effective magnetic field of $B = 68.6\text{mT}$, a field region length of 1m , the tilt angle of the first field region (see for example figure 5.9) was effectively 55.72 degrees, while the tilt angle of the second field region was scanned. Both slits were set to a diameter of 5mm with a distance of 5.84m between them. Results of our measurements superposed on the expected polarization (based on eq. 6.7) are shown in figure 6.2 Since our theoretical

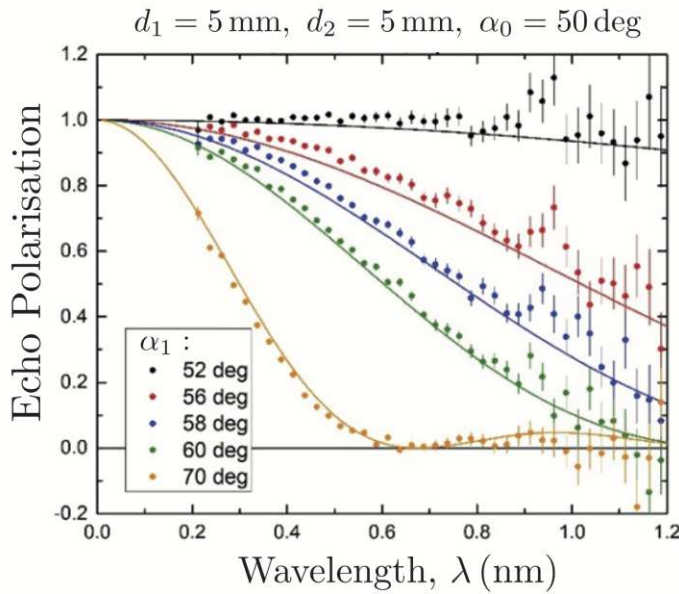


Figure 6.2: Experimental data (points with errorbars) superposed on theoretical calculations (solid lines based on eq. 6.7) for the coherence measurements conducted on the Offspec instrument. The tilt angles α_0 and α_1 are the angles of the first and second arm respectively (see figure 5.9).

prediction is in good agreement with the experimental data we may carefully conclude that our estimated wavefunction correctly describes the average neutron wavefunction on Offspec. Carefully since the cross correlation is not an invertible operation, so in principle other wavefunctions could explain our result. Nonetheless the combined data from theory and experiment give a strong argument for our wavefunction. As a result we can conclude the coherence length of neutrons in this experiment ranged from $75\text{nm} - 450\text{nm}$.

6 OAM Detection in Interferometry

Our experiment serves as a proof of principle, demonstrating that wavefunction structure can be resolved using this interferometric technique and therefore could be applied to measuring OAM states in the future when more compact OAM generators such as those described in [21] become available for thermal neutrons.

7 OAM Dependent Cross Sections

Neutron scattering and absorption depend strongly on the state of the nucleus and the neutron. For example for thermal and cold neutrons all absorption cross sections are directly proportional to the inverse of the neutrons kinetic energy. In addition many nuclei display a strong spin asymmetry in their scattering and or absorption cross sections. One of the most notable examples is nuclearly polarized Helium-3, which due to the Pauli exclusion principle only absorbs neutrons with the opposite spin polarization of the nucleus into the singlet state [142]. In principle neutrons with parallel spin could be absorbed into the triplet state, but this is energetically unfavorable and hence a non-zero cross section has not been determined experimentally to date [143]. In fact due to this strong asymmetry polarized Helium-3 has been employed very successfully as a neutron spin filter [94].

Since such strong spin asymmetries have been observed one may begin to wonder whether or not other forms of neutron angular momentum may contribute to the scattering and or absorption cross section. Absorption of optical OAM has been observed in trapped ions [144]. Furthermore twisted x-rays are being investigated as a means to excite giant resonances [27]. Since neutrons interact directly with the nucleus, it follows that twisted neutrons could be an even better candidate for exciting these resonances. Either way, if scattering and/or absorption are OAM dependent, these methods could provide a good way of detecting the OAM of a neutron beam.

Scattering [22, 23, 51] and absorption [145, 24] of twisted neutrons by matter has been studied extensively in theory. The general consensus is that OAM does change scattering/absorption behavior, however in the case of macroscopic targets, the modification of the scattering function is prohibitively small to measure using current techniques. There is one exception however, the only analysis conducted on absorption of twisted neutrons in Helium-3 so far [24] concluded that large OAM dependent asymmetries in the absorption cross section are possible. The paper reports on a theoretical estimate of a 60% difference between the $\ell = 1$ and $\ell = -1$ absorption cross sections. While their analysis appears to be correct, it seems to be missing important considerations, such as the coherence length of the neutron and the so called impact parameter, which is the distance between the target nucleus and the vortex center at the moment of absorption. The authors also neglect Doppler shifting, arising from the fact that the thermal Helium gas is in motion and therefore sees a different effective OAM in its own frame of reference, though this may be negligible since this is an extrinsic contribution to the neutrons OAM, while the vortex states investigated in [24] are intrinsic.

Despite these objections the authors make a compelling case to set up an experiment to attempt to measure the change in Helium-3 absorption cross section that occurs due to neutron OAM, while at the same time a more detailed theoretical analysis should be conducted. In this chapter I report on the theoretical analysis conducted so far, covered in [24] and report on an experiment carried out at the High Flux Isotope Reactor (HFIR) at Oak Ridge National Laboratory (ORNL), which attempted to measure the OAM asymmetry in the Helium-3 cross section. Finally we will conclude with an outlook on future searches for OAM dependent cross sections.

7.1 Theory and Motivation

This section serves primarily as the motivation for the experiment detailed in the next section. we heavily rely on the work provided by the authors of [24], who extend the calculations conducted in [146] on spin dependence in absorption of a neutron into a polarized Helium-3 nucleus to consider the total angular momentum of the neutron. Though their calculations only allow for $\ell = 1$ and $\ell = -1$ neutrons. This is quite important since it means that the most likely state, $\ell = 0$, is excluded.

Just like in [24] we will begin by considering absorption of neutrons without OAM in Helium-3. Since both systems are spin 1/2 the total angular momentum of the composite state can be either $j = 1$ (triplet case) or $j = 0$ (singlet). The triplet capture cross sections is given by

$$\sigma_{j=1} = \frac{K(j=1)}{4} [3 + P_N p] \quad (7.1)$$

while the singlet cross section is given by

$$\sigma_{j=0} = \frac{K(j=0)}{4} [1 - P_N p] \quad (7.2)$$

here K is a parameter that must be determined experimentally and p and P_N are defined as the neutron and nuclear polarization respectively. Interestingly we see that in the singlet state when neutron and nuclear polarization are aligned the cross section drops to zero. Only when they are anti-aligned is the cross section non-zero. This is the basis of the neutron spin filter. The triplet case has not yet been observed since $K(j=1)$ is prohibitively small. The authors then define an OAM polarization, where the neutron can be either in the $\ell = 1$ or $\ell = -1$ state

$$P_L = \frac{p_{\ell,+} - p_{\ell,-}}{p_{\ell,+} + p_{\ell,-}} \quad (7.3)$$

with $p_{\ell,\pm}$ the probability of finding the neutron in the $\ell = 1$ or $\ell = -1$ state. With the additional OAM degree of freedom the total angular momentum of the composite state can be $j = 0$, $j = 1$ or $j = 2$. When we extend the arithmetic discussed in [146, 24] to include OAM authors find

$$\sigma_{j=2} = \frac{K'(j=2)}{24} [24 - 5(1 - pP_L) - 4(1 - pP_N) - 5(1 - P_L P_N)] \quad (7.4)$$

$$\sigma_{j=1} = \frac{K'(j=1)}{24} [3(1 - pP_L) + (6 - 4\sqrt{2})(1 - pP_N) + (3 + 4\sqrt{2}(1 - P_LP_N))] \quad (7.5)$$

and

$$\sigma_{j=0} = \frac{K'(j=0)}{12} [1 - pP_L + pP_N - P_LP_N] \quad (7.6)$$

Note that when $P_L = 0$ the cross sections do not reduce to the case we discussed previously where OAM is neglected. This is because in this analysis $P_L = 0$ corresponds to a linear OAM state (an equal superposition of $\ell = 1$ and $\ell = -1$), which is qualitatively different than a non-vortex state ($\ell = 0$). Furthermore since this analysis rejects the $\ell = 0$ possibility it follows $K'(j)$ is not necessarily equal to $K(j)$. Nonetheless the authors of [24] make compelling energetic arguments as to why $K'(j=1) = 0$ and $K'(j=0) = K'(j=2) = K(j=0)$, energetically speaking the composite state $n + ^3\text{He}$ is for thermal neutrons only slightly above the absorption resonances leading to the $j=0$ and $j=2$ states, while this total energy is below the energy level of the $j=1$ state. The total estimated absorption cross section according to [24] can then be written as

$$\sigma = \frac{K(j=0)}{12} [1 - pP_L + pP_N - P_LP_N + 12 - \frac{5}{2}(1 - pP_L) - 2(1 - pP_N) - \frac{5}{2}(1 - P_LP_N)] \quad (7.7)$$

Assuming a Helium polarization of +50% the maximal change can be observed if the OAM polarization is parallel to the Helium polarization $P_L = 1$ and the neutron spin is flipped. In this case the cross section changes by a factor of 2.6. A more interesting experiment however is to keep the neutron polarization constant and flip the OAM polarization. To this end it is best to keep the neutron polarization parallel to the Helium polarization. In this case the cross section changes by a factor of 1.86 upon flipping the OAM. Note that when we neglect OAM and have 100% Helium polarization there is no absorption when the neutron polarization is parallel, once we introduce OAM this changes. Also, interestingly $P_L = 0$ implies a linear OAM state, which is different from an $\ell = 0$ neutron. Helium-3 is therefore expected to exhibit a different absorption cross section in this case. It follows that a SESANS instrument like CANISIUS could in principle be used to investigate the interaction between polarized Helium-3 and polarized neutrons. For the time being however we will focus on a device that can generate pure vortex states of $\ell = 1$ or $\ell = -1$. In the next section we will look at an attempt to measure this cross section using a polarized Helium-3 target and an OAM generator which exploits coherent averaging.

7.2 Measurement of the Helium-3 Capture Cross Section with $|\ell| = 1$ Neutrons

Here we report on an experiment conducted in July and August 2023 on the HB1D beamline at the High Flux Isotope Reactor (HFIR) at Oak Ridge National Laboratory (ORNL) aiming to determine the change of the Helium-3 cross section that occurs due to flipping the OAM of the incident neutron. Our setup is identical to that shown in

figure 5.18. The figure is copied here for ease of access for the reader (see figure 7.1). As

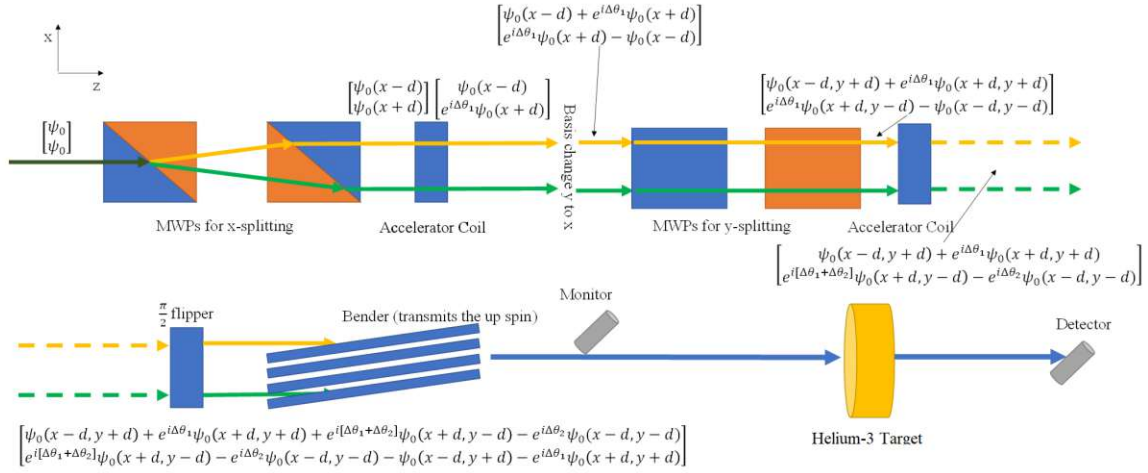


Figure 7.1: Schematic of a setup showing a neutron being separated in the x-direction by a pair of Wollaston prisms. Next a longitudinal phase difference is induced using a magnetic coil (here called accelerator coil). Afterwards a second pair of Wollaston prisms split the neutron in the y-direction (into the page not visible). A second precession coil induces another phase shift. Finally a $\pi/2$ flipper and a polarizing bender select the $\ell = 1$ or $\ell = -1$ composite state (depending on the settings of the accelerator coils). The composite state is passed through the polarized Helium-3 target after which the intensity normalized by the monitor value is measured. The length of the Helium-3 cell was 9cm, with a filling pressure of 1.5bar. The average Helium polarization obtained was 67%

demonstrated in chapter 5 at numerous instances this type of setup is ideal for producing pure vortex states with mode number $\ell = 1$ or $\ell = -1$. Our measurements consisted of setting the displacement parameter δ_{SE} equal to 0.7 coherence lengths and then scanning the current on both precession coils shown in figure 7.1. As a result of these scans we would see the effect of each phase combination on the absorption cross section of the Helium-3. Our measurements consisted of simple transmission measurements, where we measured the beam intensity with and without the Helium-3 sample for various phase shift combinations. The displacement parameter was set to 0.7 transverse coherence length², by using the assumption that the transverse wavefunction could be described as Gaussian. Then by using the fact that the transverse polarization can be described as the cross correlation between the up and down spin wavefunctions (Chapter 6) we can calculate the expected loss in polarization that results from setting δ_{SE} to 0.7 transverse coherence lengths. Finally we scan the current in the wollaston prisms of the first arm until the expected degree of polarization loss is reached. We repeat this procedure on the second arm. By then scanning through all combinations of $\Delta\theta_1$ and $\Delta\theta_2$ (see fig. 7.1), we can scan through the $\ell = 1$, $\ell = -1$ and $\ell = 0$ state. The calculated interferogram, OAM

expectation value and transmission are shown as a function of both phase shifts, $\Delta\theta_1$ and $\Delta\theta_2$ in figure 7.2. The interferogram shows the intensity before the Helium-3 sample, hence it does not contain the transmission. As a starting point for our calculations we

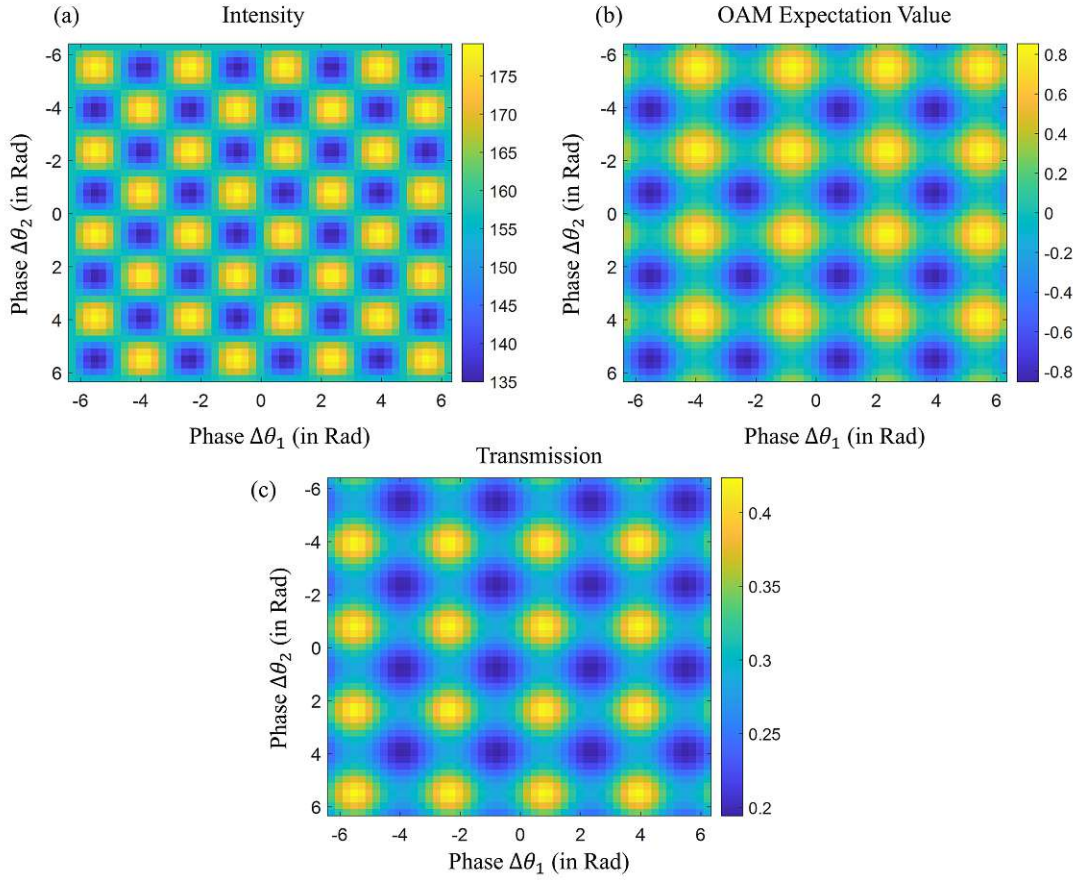


Figure 7.2: Calculated interferogram/intensity (a), OAM expectation value (b) and Helium-3 transmission (c) as a function of both phase shift parameters $\Delta\theta_1$ and $\Delta\theta_2$ (allowing us to choose between $\ell = 1$ and $\ell = -1$). The interferogram is calculated before the Helium sample and does therefore not contain the transmission. As a starting point for these calculations we used the experimentally determined, Helium polarization (67%), cell length (9cm), cell filling pressure (1.5bar) and neutron polarization (95%). In addition for calculating the absorption cross section and resulting transmission we used the values given in [24].

used the experimentally determined, Helium polarization (67%), cell length (9cm), cell filling pressure (1.5bar) and neutron polarization (95%). In addition for calculating the absorption cross section and resulting transmission we used the values given in [24]. We can see that the expected change in transmission that occurs due to flipping the OAM is significant (100% change). An additional telltale metric that can be used is the period of the oscillations in the transmission compared to that in the intensity. Notice that the

7 OAM Dependent Cross Sections

period of the transmission oscillations is larger compared to those in the intensity (by a factor $\sqrt{2}$). Finally the direction along which the oscillations occur change as well. Hence we have a sufficient number of obvious variables to look out for making it easy enough to measure whether or not the Helium-3 transmission changes as a function of OAM.

Raw Measurement results are shown in the top insets of figure 7.3. Since the raw data

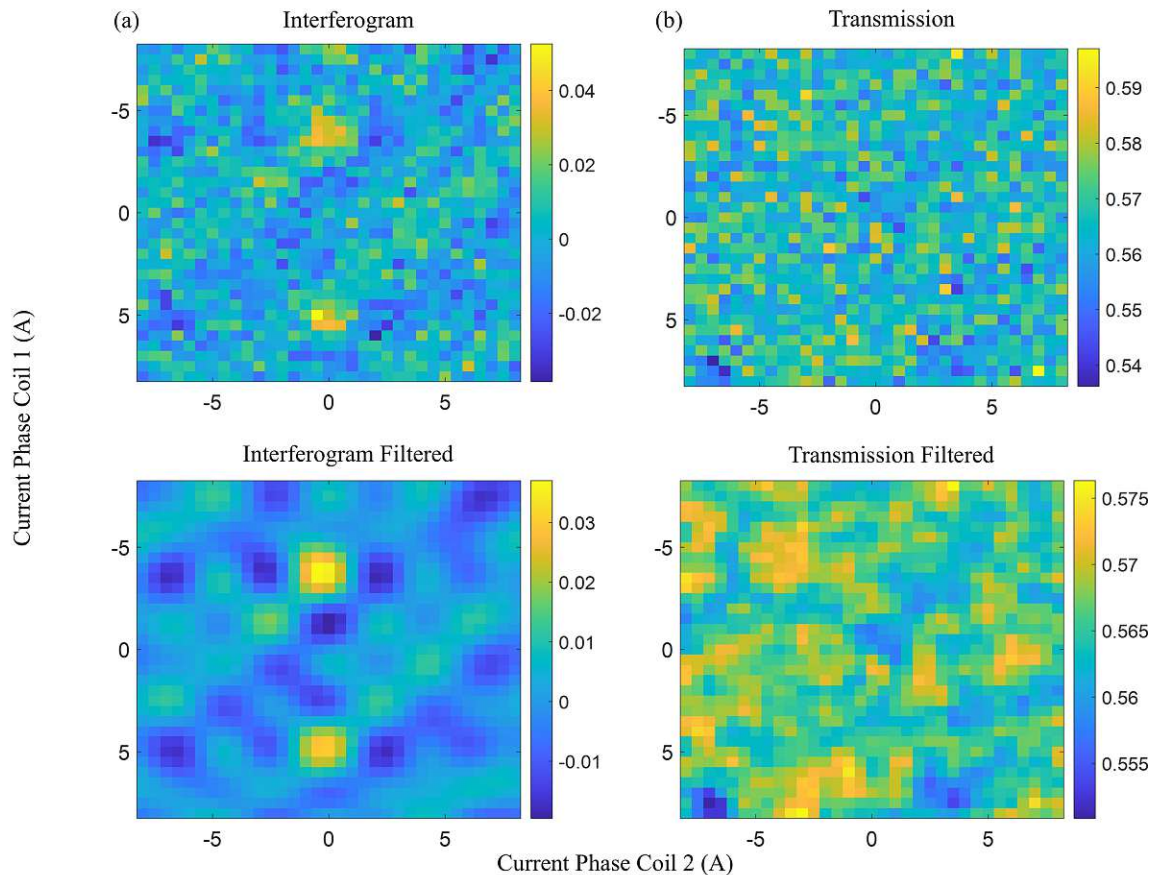


Figure 7.3: (a) Raw interferogram, (b) raw transmission data, (c) interferogram convolved with a Gaussian filter and (d) Transmission convolved with a Gaussian filter. All data is plotted against the current in the first and second accelerator coils.

is noisy we applied a Gaussian smoothing filter to the data. The filtered data is shown in the bottom insets of figure 7.3. Both the raw and filtered interferogram show clearly a periodic structure traveling diagonally from top left to the bottom right. This is confirmed by the Fourier Transform of the data shown in figure 7.4 The transform also reveals a problematic issue, the interferogram only contains one diagonal oscillation, while our calculations in figure 7.2 show that the interferogram should consist of a superposition of two perpendicular diagonal oscillations. This could be due to one of the SESANS arms not being sufficiently aligned with the optical axis of the beam which

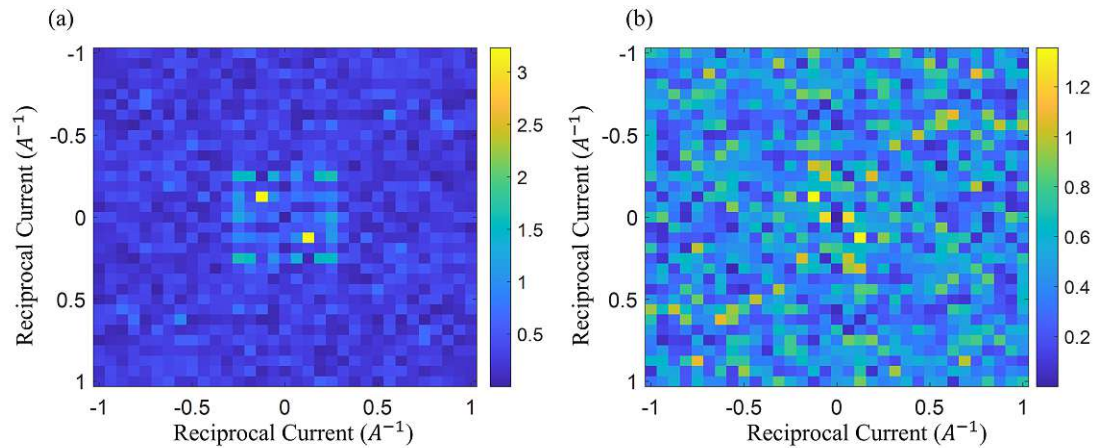


Figure 7.4: Fourier transform of the raw (a) interferogram and (b) the transmission. The FTs confirm that both signals have a diagonal oscillation with the same period.

causes dephasing. This is confirmed by the fact that when we measure interferograms in front of the polarized Helium setup, closer to the OAM generator, we do indeed see both oscillations. This is further evidenced by a different interferogram measured using the same setup, using a slightly different tune of the Wollaston prisms (see figure 7.5). The

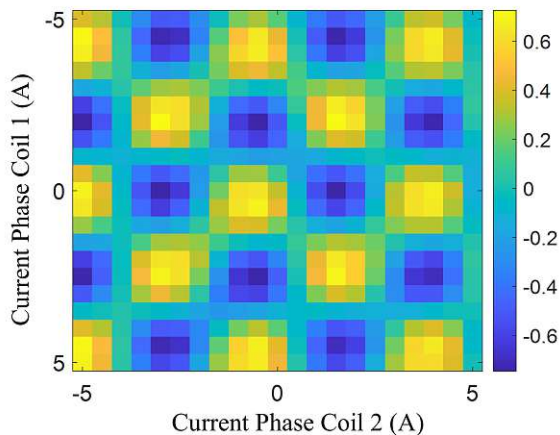


Figure 7.5: High contrast interferogram measured against both accelerator coil currents. The contrast here is better since the magnetic Wollaston prisms were tuned slightly differently. This measurement cannot be used to determine the Helium transmission since it cannot be properly normalized by a monitor measurement.

Fourier transform of the transmission reveals that this oscillation persists in the shape of the transmission, which is curious, but not consistent with our calculations. One may

also wonder why we did not use the higher contrast interferograms such as that shown in figure 7.5, to determine the transmission. This because for these measurements the monitor and detector were spatially separated, which results in a different phase and contrast of the oscillations, so the only correct way to measure the transmission was to conduct a measurement with the target in the beam and one without. The detector would have to remain at the same position for both measurements. One can perform phase corrections to this dataset, however in this case we also do not see any of the expected signs in the transmission (such as a rotation of the oscillations or a change in the period).

We conclude that none of our measurements contain any signs of a large asymmetry in the neutron absorption cross section of polarized Helium-3 connected to the neutrons OAM. While our experimental method contains flaws, leading to a lower contrast, which could be corrected in a follow up experiment, the theory is missing key considerations such as a discussion pertaining to the impact parameter and Doppler shifting due to the thermal motion of the Helium gas. These issues need to be clarified before a second measurement attempt is made.

7.3 Conclusion and Outlook

A strong OAM dependent asymmetry in the polarized Helium-3 cross section was not confirmed experimentally. In fact no discernible structure was found in the transmission profile within error. This however, does not imply that there is no asymmetry or even that there is no strong asymmetry. The latter can be understood from our work done in chapter 2, where we showed that an initially pure vortex state that is displaced from the origin must be described using a superposition of many different modes. It follows that if the Helium-3 nucleus is not located on the vortex center when absorption occurs, the composite nucleus cannot be described by the formalism covered in [24]. This has also been demonstrated in work conducted with twisted photons [147]. So it is possible that a Helium nucleus absorbing a vortex neutron on axis, would still display a large asymmetry as discussed in [24], however the probability of such an event is very low, as the Helium nucleus has a radius of \propto fm, while the thermal neutron transverse coherence length is at least 10nm, so the probability of a Helium-3 nucleus being on the vortex center is on the order of 10^{-15} . Since such an event is so unlikely to happen and it is difficult to envisage a way to either sufficiently shrink the transverse coherence of thermal neutrons or increase the target size, it is necessary to expand the theory of twisted neutron absorption to allow for arbitrary mode numbers, such that one can account for off-axis absorption. Should these calculations predict a measurable change in cross section follow up experiments should be conducted.

Should an updated theory also suggest that linear OAM states interact differently with a macroscopic Helium-3 target compared to the simple $\ell = 0$ state, one could conduct follow up measurements on a simple one dimensional SESANS like CANISIUS, as

these instruments are simpler to tune than the two dimensional variant used for this experiment.

Even if macroscopic targets have only a minute sensitivity to the vorticity of incident neutrons it can be of scientific and societal interest to continue research into the topic, as if OAM can be transferred from neutrons to nuclei it becomes possible to excite giant resonances [27], which can be of particular interest in the case of some super stable metastable nuclei such as ^{180}Ta . These isomers gain their immense stability from the fact that the transition from the excited to the ground state is forbidden, due to angular momentum considerations [148]. Should it be possible to deplete these isomers on demand, by adding or subtracting angular momentum with vortex particles, one would have an incredibly dense energy source. These nuclear batteries would have a much higher energy density than that found in chemical batteries. As a result further exploration in the topic of nuclear scattering with twisted particles is warranted.

8 Rotation Angular Momentum Coupling

The final OAM measurement technique explored in this manuscript exploits a coupling between rotation and (orbital) angular momentum arising from (Galilean) relativity. In particular we will look at the Fizeau and Sagnac effects [18, 149, 56], applied to the problem of quantum mechanical OAM. Both of these effects arise from the rotational Doppler shift experienced in a rotating frame of reference. Assuming the frame rotates around the z-axis with a rate Ω we can describe the shifted azimuthal coordinate as

$$\phi' = \phi + \Omega t \quad (8.1)$$

with t the time and ϕ the azimuthal coordinate in the non-rotating frame. It follows that the OAM Eigenstates, $e^{i\ell\phi}$ become Doppler shifted, such that their total energy becomes

$$E' = E_0 + \hbar\ell\Omega \quad (8.2)$$

with E_0 the particles energy in a non-rotating frame. As a result OAM states become dispersive in a rotating frame of reference and the change in energy is directly proportional to the OAM quantum number ℓ . This dispersion is the origin of both the Sagnac and Fizeau effects. The former simply describes the phase shift acquired by OAM states in a rotating frame of reference, while the latter describes the additional phase shift that is acquired if the OAM state is propagating through some medium. This latter additional phase shift has its origin in the fact that the index of refraction presented by a medium is dependent on the energy of the incident particle. Especially in the vicinity of absorption resonances this effect can be strongly amplified leading to observable phase shifts even in neutrons.

This chapter will cover the Sagnac effect through the lens of neutron OAM. A neutron optical experiment will be presented which uses the rotation of the earth to measure the transverse OAM of neutrons. Then we will shortly look at the "quantum" version of the Sagnac effect. Finally the Fizeau effect will be discussed in this context and we will look at a class of previous neutron interferometric experiments that observed this effect.

8.1 The Sagnac Effect

This section covers the most immediate angular momentum rotation coupling known as the Sagnac effect [149]. Here we will closely follow the work we presented in [14]. The effect was first observed with photons in 1913 by Georges Sagnac. In an attempt to prove the existence of an ether, Sagnac observed a phase shift in his interferometer which depended on the direction in which the interferometer was rotated [18]. In addition the famous 1925 experiment by Michelson, Gale and Pearson, was also able to observe this coupling in a very large optical interferometer due to the Earth's rotation [150]. Since then this coupling has been observed in various types of matter waves, including superconducting electrons [151], free electrons [152], atoms [153, 154] and, indeed, neutrons [13, 14]. The 1979 neutron experiment conducted by Werner, Staudenmann, and Colella was the first to demonstrate that free matter waves are also subject to the Sagnac effect. Specifically neutrons traversing a rotating interferometer also experience a phase shift proportional to the inner product between the rotation frequency, Ω and the Orbital Angular Momentum (OAM), \hat{L} spanned by the neutron's motion in the interferometer ($\Omega \cdot \hat{L}$) [13]. The rotation of the interferometer was realized by the natural rotation of the earth, as was the case in the 1925 Michelson/Gale/Pearson experiment.

In 1988 Mashhoon realized that this rotation coupling applies to the total angular momentum

$$\hat{\mathbf{J}} = \hat{\mathbf{L}} + \hat{\mathbf{S}} \quad (8.3)$$

therefore extending the effect to the spin angular momentum $\hat{\mathbf{S}}$ of particles as well as their orbital angular momentum [155]. Recently the Mashhoon effect has been observed in neutron polarimetry [156] and in neutron interferometry [157]. In these cases the rotating frame was realized by creating a rotating magnetic field in the laboratory frame of the interferometer which, for the projective measurement of the neutron spin employed in the apparatus, can be shown to be equivalent to observing the neutron spin in a rotating frame of reference.

In this section we present a theoretical framework and an experiment designed to measure OAM using the Sagnac effect. To this end a neutron interferometer with a precisely calibrated path separation was used. Since, this spatial separation and the neutron momentum are precisely known, it follows that the extrinsic transverse OAM carried by the neutrons is also precisely known. By measuring the resulting Sagnac phase we are able to determine the sensitivity of the setup to any transverse OAM, whether extrinsic or intrinsic. Compared to the previous neutron Sagnac effect measurement [13], the experiment described here improves the angular momentum sensitivity by 5 orders of magnitude. This improvement in sensitivity marks an important step towards observation of the quantized Sagnac effect, the final subject of this section. In optics this quantized Sagnac effect has been observed using spinning Dove prisms [15]. The observation of a quantized energy shift from the Sagnac effect is an attractive method to resolve quantized OAM states in neutrons. We will report on an experimental observation of the Sagnac effect in a neutron interferometer which uses microscopic path separation on

the order of the transverse coherence of the neutron ($0.001\mu\text{m} - 100\mu\text{m}$) [118, 158, 119]. In addition we demonstrate that the Sagnac effect provides a good method for a basis to definitively detect the OAM of a particle. Our experiment was carried out on the Larmor instrument at the ISIS pulsed neutron source. Larmor is a neutron spin echo type interferometer [41], which employs shaped RF spin flippers to induce horizontal spin and energy dependent path separation [111, 123].

This section is subdivided into three subsections, we will first cover the theoretical frameworks necessary to understand the Sagnac effect and the setup used in the next subsection describing the experiment and the results. Finally we will provide an outlook, looking at applications and the quantum Sagnac effect.

8.1.1 Theoretical Framework

In a rotating frame of reference, particles experience a pseudo potential proportional to the rotation rate of the frame and the OAM possessed by the particle around the axis of rotation. Equation 8.2, strongly implies the form of the "Sagnac potential"

$$\hat{V} = \Omega \cdot \hat{\mathbf{L}} \quad (8.4)$$

Intuitively, such a potential allows us to measure the OAM component of a wavefunction parallel to the axis of rotation. As discussed extensively in sections 2.5 and 5.1.4 wavefunctions traversing an interferometer carry OAM transverse to the propagation direction (parallel to the normal of the plane of splitting) and longitudinally, parallel to the propagation direction. Our setup, shown in figure 8.1, consists of a SESANS type interferometer. As we have motivated in previous chapters the spin polarized

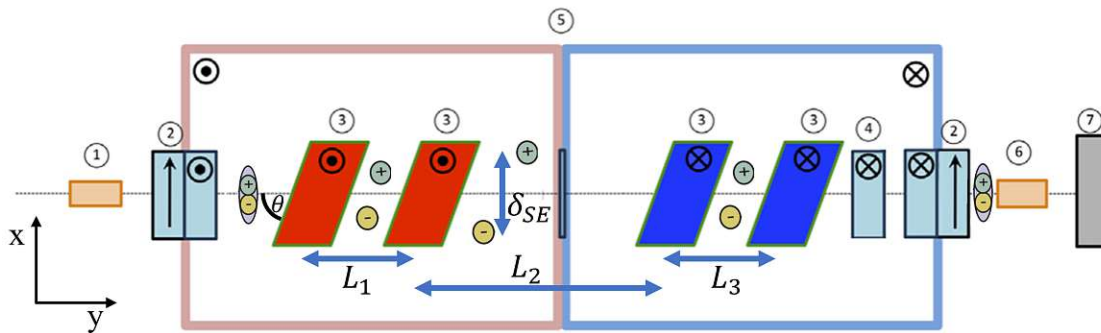


Figure 8.1: Schematic of the Larmor neutron spin echo interferometer, the propagation of the + and - spin through the device and the neutron optical components: (1) polarizer (2) adiabatic $\pi/2$ rotator (v-coil), (3) RF spin flipper with tilted field region, (4) ramped $\pi/2$ rotator (5) guide field, (6) spin analyzer and (7) detector.

wavefunction can be described mathematically as

$$\psi_{\pm} = \frac{A}{\sqrt{2}} e^{\pm i\beta/2} e^{-\frac{(x \pm \delta_{SE}/2)^2 - y^2 - z^2}{\sigma^2}} e^{ik_y y} \quad (8.5)$$

The \pm refers to the spin state either being aligned with the z -axis $+$ or anti-aligned $-$. β is an arbitrary phase between the up and down spin state. As shown previously (for example figure 2.6 and eq. 2.73) the average OAM mode transverse to the propagation direction of such a wavefunction is given by

$$\ell_{\pm} = \pm \frac{\delta_{SE} |k|}{2} \quad (8.6)$$

Usually the state in the interferometer is expressed as a spin-path entangled state. The path states are often characterized by the spin echo length δ_{SE} . As we have seen this degree of freedom also characterizes the transverse OAM of the wavefunction. It follows that the two path states, defined by the spin echo length, can also be described by two OAM states. Thus, for the purposes of this experiment, we describe our state not as spin-path entangled, but as spin-orbit entangled, such that the state in the interferometer can be described as

$$|\psi\rangle = e^{i\beta/2} |\ell_+\rangle |+\rangle + e^{-i\beta/2} |\ell_-\rangle |-\rangle \quad (8.7)$$

We note that state preparation and measurement are not instantaneous. Between the first and second RF flipper spin echo length and therefore transverse OAM is linearly increased, while between the third and fourth RF flipper, the spin echo length and transverse OAM are reduced back to zero. The Sagnac effect will obviously also act on these intermediate states. This is taken into account by allowing for an OAM which depends on the y -coordinate. The precession frequency between the two states due to the Sagnac effect follows from eq. 8.4 and 8.6 and is given by

$$\delta\omega_s = [\ell_+ - \ell_-] \Omega \sin(\Lambda) \quad (8.8)$$

with Λ the latitude of the interferometer. This expression demonstrates one of the advantages of using the Sagnac effect to measure OAM: the precession frequency depends only on the OAM difference between the two states. This difference is invariant under spatial translations of the frame of reference, hence intrinsicality/extrinsicality becomes an irrelevant detail. Integrating this precession frequency over the length of the instrument leads to the Sagnac phase shift

$$\delta\phi_s = \int dt \delta\omega_s = \frac{m\Omega\Delta\ell}{\hbar|k|} \sin(\Lambda) [L_1 + L_3 + 2L_2], \quad (8.9)$$

which can be reduced to the result shown in [13, 121], for a horizontal interferometer

$$\delta\phi_s = \frac{2mA\Omega}{\hbar} \sin(\Lambda) \quad (8.10)$$

with A the area spanned by the two paths of the interferometer. The area, illustrated in figure 8.1, is given by

$$A = \delta_{SE} \left[\frac{L_1 + L_3}{2} + L_2 \right]. \quad (8.11)$$

As we have shown for spin echo interferometers the spin echo length, δ_{SE} is proportional to wavelength squared. Hence to vary the area of the interferometer and therefore strength of the Sagnac effect, we may simply vary the wavelength of incident neutrons, whereas the 1979 perfect crystal experiment required physical rotation of the interferometer, which may induce systematic errors.

We have calculated the OAM along the z-axis and the resulting phase shift that occurs as a result of this angular momentum. The longitudinal OAM of our wavefunction eq. 8.5 has been described in section 2.5, specifically equation 2.83. This OAM also couples to rotation, but the coupling is orders of magnitude weaker, since the amount of OAM along this axis is orders of magnitude lower, compared to the transverse OAM. Hence our experiment will only "see" the transverse OAM of neutrons in the instrument.

In equation 8.9 we put the acquired Sagnac phase in a form that shows that one can extract the difference between the quantum numbers for two OAM states, assuming instrument parameters and the rotation rate of the instrument are well known. Hence, using the Sagnac effect can be a good relative measure to determine the OAM of a beam.

8.1.2 Experimental Setup and Results

Measurements were carried out on the Larmor instrument at the ISIS pulsed neutron source [159]. Larmor is a SANS instrument with a versatile neutron resonant spin echo toolbox, based on four gradient radio frequency spin flippers with shaped poleshoes, capable of performing inelastic techniques such as Modulated Intensity Emerging from Zero Effort (MIEZE) [123] and Spin Echo (Modulated) Small Angle Neutron Scattering (SE(M)SANS) [40, 112, 10, 11]. Our experiment makes use of the SESANS mode of the instrument.

Since Larmor uses spin dependent refraction to realise the interferometer, the path and spin states of the neutron are coupled (i.e. mode entangled). Hence any path dependent phase shift is projected onto the spin and vice-versa. As pointed out previously the path and OAM degree of freedom are related, hence the path state and also path phases, may also be described as orbit states/phases. In SESANS the spin is usually prepared, along the x-axis, orthogonal to the beam propagation and B_0 direction. The expectation value of the spin, also called polarization, is usually also measured along the x-direction, leading to a polarization of

$$P_x = P_0 \cos(\Delta\phi(\lambda)) \quad (8.12)$$

with $P_0 = \sqrt{P_x^2 + P_y^2 + P_z^2}$ and $\Delta\phi(\lambda)$ a polynomial in λ

$$\Delta\phi(\lambda) = a_0 + a_1\lambda + a_2\lambda^2 + O(\lambda^3). \quad (8.13)$$

One may independently control the a_0 term by means of a ramped precession field, with $B(t) \propto 1/t$, which ensures that the spin of each wavelength on a ToF source is rotated by the same angle [160, 161]. By setting a_0 equal to $\pi/2$ we effectively change the measurement direction to along the y-axis, the propagation direction. Hence the measured polarization becomes

$$P_y = P_0 \sin(\Delta\phi'(\lambda)), \quad (8.14)$$

which for small $\Delta\phi'$ may be linearized. For more details on the pre- and post-selection in SESANS type interferometers we direct the reader to [162]. To remove the scaling factor P_0 , we may normalise P_y by P_x . This normalized polarization still has a simple and accurate linearization for small $\Delta\phi$

$$\frac{P_y}{P_x} \approx \epsilon + a_1\lambda + a_2\lambda^2 \quad (8.15)$$

with ϵ any imprecision in the quality of the $\pi/2$ rotation provided by the ramped precession field. We can estimate the second order parameter, due to the Sagnac effect using equations 8.10 and 5.36

$$a_2 = c_{SE} \frac{m\Omega}{\hbar} \sin(\Lambda)[L_1 + L_3 + 2L_2]. \quad (8.16)$$

with the spin echo constant $c_{SE} = \frac{\gamma m B_2 L_2 \cot(\theta_0)}{2\pi^2 \hbar}$, such that $\delta_{SE} = c_{SE} \lambda^2$. Additional perturbations arising from imperfections in the instrument can occur which can affect the magnitude of the second order term. Most notably a slight change in the precession plane can occur if an imperfect spin optical component introduces an unintended low probability spin flip. Components that may be suspected to introduce such an effect are primarily those which use adiabatic field changes to effect a spin rotation, for example v-coils (item 2 in figure 8.1) and adiabatic RF flippers (item 3 in figure 8.1), since adiabatic spin flip probabilities in both of these components can be described as

$$\rho \approx A_i \lambda^2 \cos^2(k_i \lambda + \alpha) \quad (8.17)$$

assuming only slight imperfection [129, 163] (i.e. low spin flip probability). As a result the precession plane will appear to oscillate with an amplitude proportional to λ^2 and in addition this effect will produce an aberration on a_2 , since the \cos^2 component in equation 8.17 produces a constant offset ($A \cos^2(x) = A/2(1 + \cos(2x))$). This offset can of course be isolated and subtracted from a_2 , by measuring the amplitude of the precession plane oscillation. Since this effect is small it has not been relevant to measurements conducted with Larmor before, however our experiment has sufficient sensitivity to uncover this systematic.

Measurements of the Sagnac phase were conducted using a poleshoe angle of $\theta = 40$ degrees and at an RF frequency of 2 MHz corresponding to an effective magnetic field strength of 68.6 mT. These consisted of polarization measurements with the ramped $\pi/2$ rotator turned off and on with both polarities (corresponding to a $\pi/2$ or $-\pi/2$

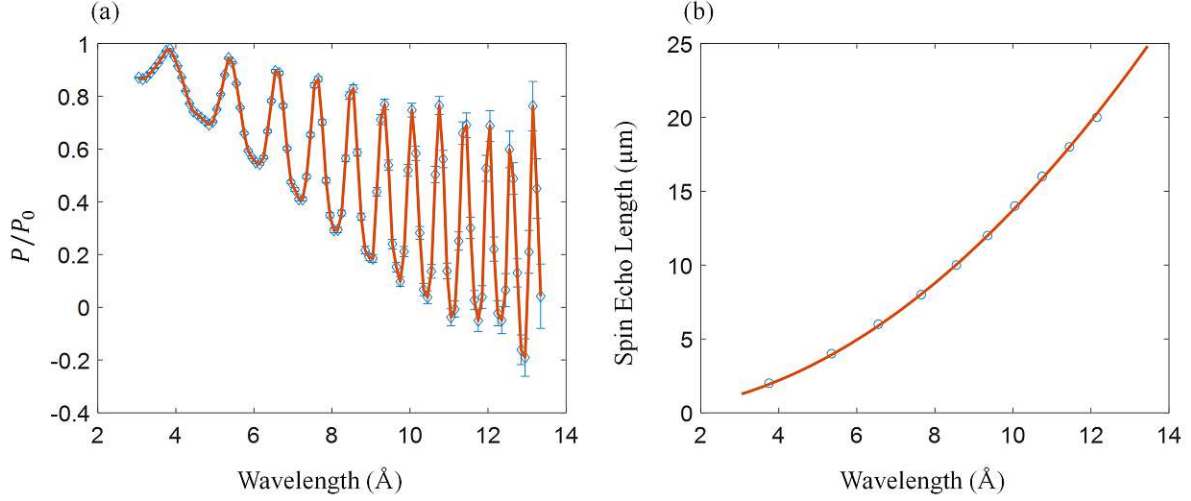


Figure 8.2: Calibration curves of the instrument produced using a 2 μm period silicon grating. (a) Plot of the normalized spin-echo polarization against wavelength. The n^{th} peak corresponds to a spin echo length equal to n times the grating period. The wavelength and corresponding spin echo length is extracted and plotted in the next panel (b). The quadratic fit is drawn in red.

rotation). In addition with the ramped $\pi/2$ rotator turned off a calibration measurement was carried out, in which a 2 micron silicon grating was inserted into the sample position of the instrument. The resulting correlation function, shown in figure 8.2 (a), allows us to experimentally determine the proportionality constant between the spin echo length and the wavelength squared, which is essential to estimate a_2 . Since the n^{th} peak in figure 8.2 (a) corresponds to a spin echo length of n times the grating period, one can extract the relationship between spin echo length and wavelength, shown in figure 8.2 (b). By applying a quadratic fit one finds the spin echo constant, c_{SE} , to be equal to $0.137\mu\text{m}\text{\AA}^{-2}$. Using this and equation 8.16 it follows that for the instrument settings used in this experiment the Sagnac constant a_2 , should be equal to $-1.15 \times 10^{-3}\text{\AA}^{-2}$. Equations 8.6 or 8.9, show that the difference between OAM states scales linearly with λ (i.e. $\delta\ell = c_{OAM}\lambda$). Using equation 8.9 we can express c_{OAM} in terms of a_2

$$c_{OAM} = \frac{2\pi\hbar a_2}{m\Omega \sin(\Lambda)[L_1 + L_3 + 2L_2]} \quad (8.18)$$

which for our estimated value of a_2 is equal to $-8.62 \times 10^3\text{\AA}^{-1}$. Since according to equation 8.6 ℓ_+ and ℓ_- are equal in magnitude it follows that the OAM of each state scales with $\ell_{\pm} = \pm \frac{1}{2}c_{OAM}\lambda$.

Measurement Results

The normalized polarization, for the positive $\pi/2$ rotator polarity, is shown in figure 8.3 (a). This represents a typical spin-echo curve obtained from this experiment. It is clear that the raw data contains oscillations which increase in amplitude with wavelength squared, analogous to the precession plane oscillation described in the previous section (see eq. 8.17). By subtracting a quadratic fit from the data and dividing the result by λ^2 , the oscillations can be isolated (see figure 8.3 (b)). It can be shown that the aberration

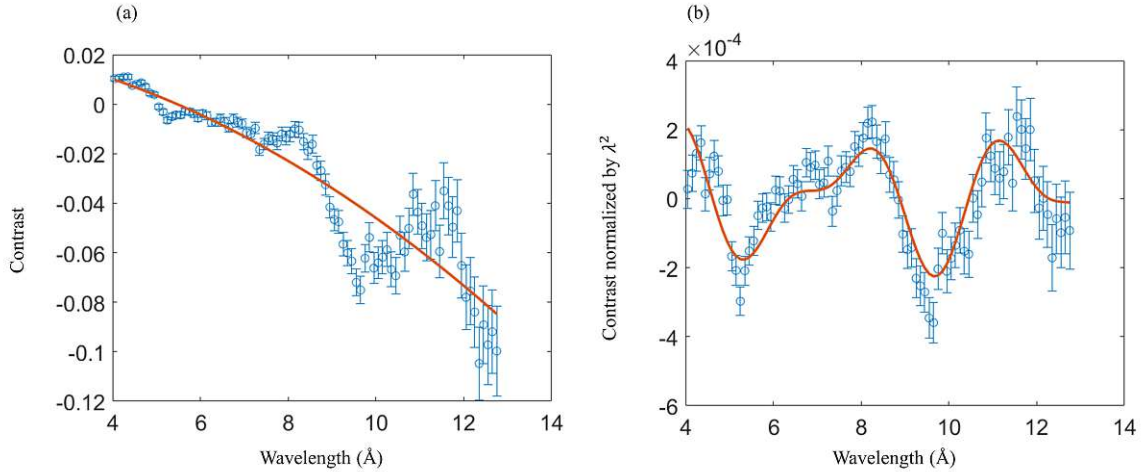


Figure 8.3: (a) Typical normalized polarization for the 40 degree poleshoe setting, in which the Sagnac phase shift is expected (blue). A quadratic fit is shown in red. The quadratic fit can be subtracted from the data to isolate the oscillations (b) Since the amplitude of the oscillations scale with wavelength squared, we divide these by λ^2 . A fit consisting of two sines is shown in red.

consists of two oscillations with frequencies $k_2 \approx 2k_1$. As pointed out previously it is important to correct for these oscillations, since in addition to improving the overall fit quality, the amplitude information is necessary to correct for a systematic error coming from imperfections of the instrument, hence both amplitudes are listed in table 8.1. The data is corrected by fitting two sine waves to the oscillations and subtracting said fit multiplied by λ^2 from the data. The corrected data for both $\pi/2$ coil settings is shown in figure 8.4. Quadratic fits using a weighted least squares method are applied to the corrected data. The weights are given by the inverted variance. The second order fit parameters are illustrated in table 8.1. The first estimate for the second order parameter a_2^S , due to the Sagnac effect is obtained using the following

$$a_2^S = \frac{a_2^+ - a_2^-}{2} \quad (8.19)$$

Alternatively the corrected data may be aggregated according to a similar formula

$$P_S = \frac{P_+ - P_-}{2} \quad (8.20)$$

	$a_2 (\text{\AA}^{-2}) \times 10^3$	$ A_1 (\text{\AA}^{-2}) \times 10^5$	$ A_2 (\text{\AA}^{-2}) \times 10^5$
P_+	-0.891 ± 0.0853	14.4 ± 2.31	8.22 ± 2.24
P_-	0.898 ± 0.0739	8.88 ± 1.85	6.23 ± 1.83
$a_2^S = (-0.894 \pm 0.0564) \times 10^{-3} \text{\AA}^{-2} \quad c_{OAM} = -6767 \pm 427 \text{\AA}^{-1}$			

Table 8.1: Table containing the second order fit parameters, a_2 and their respective standard deviations, for both coil polarities and the amplitudes of the oscillations found in the data with their respective errors. The final estimate for the second order parameter due to the Sagnac effect, a_2^S , which is calculated using equation 8.19, is shown at the bottom, in addition to the OAM proportionality constant (see equation 8.18).

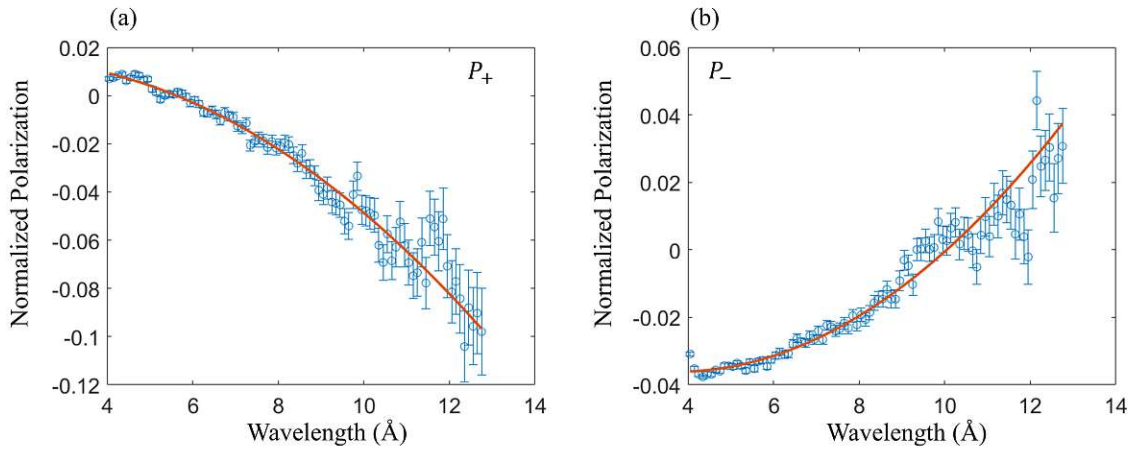


Figure 8.4: Plots of the normalized and corrected polarization in blue for (a) positive polarity and (b) negative $\pi/2$ rotator polarity. The quadratic fits are plotted in red. The errorbar introduced by subtracting the sinusoidal fit is negligible.

and a weighted least squares quadratic fit is applied to this result. P_S is shown in figure 8.5. The resulting second order fit parameter is $(-0.899 \pm 0.0631) \times 10^{-3}$, which is in good agreement with the value a_2^S shown in table 8.1. For comparison figure 8.5 contains a fit in green which uses the theoretically exact value for the second order parameter, while the zeroth and first order coefficients are determined via least squares regression.

Discussion

Figure 8.5 indicates a good agreement between our calculated Sagnac parameter of $-1.15 \times 10^{-3} \text{\AA}^{-2}$ and the measured parameter, however the exact fit parameters shown in table 8.1, indicate that for a single $\pi/2$ rotator polarity, the measured value differs from our calculation by roughly 3σ . Furthermore the averaged fit parameter a_2^S , differs from theory by 4.3σ , indicating a high likelihood of a systematic perturbation. In this section we correct this perturbation to the second order fit parameter, assuming it is caused by

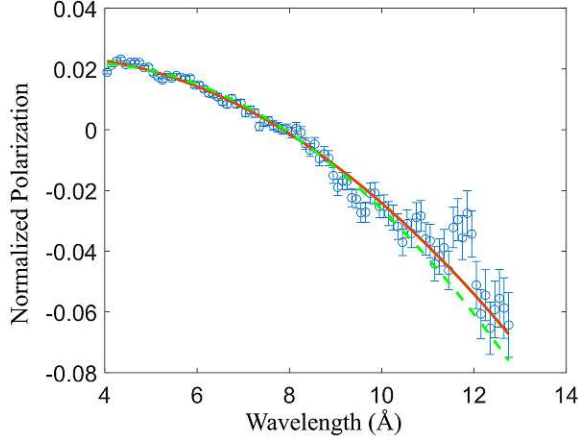


Figure 8.5: Averaged normalized polarization of all data, according to equation 8.20, shown in blue. The quadratic fit is shown as a red solid line. While a fit containing the exact theoretical expectation value for the second order term due to the Sagnac effect is shown as a green dashed line.

imperfections in the adiabatic spin optical components. Both the oscillations shown in figure 8.3 and the large $\propto 4\sigma$ deviation between data indicate that such imperfections are likely. As indicated earlier at low efficiencies adiabatic spin flip probabilities scale with λ^2 , consistent with our observation. Therefore we postulate that the oscillations shown in figure 8.3 (b) arise due to an oscillation of the precession plane of the form

$$P = 2\lambda^2[|A_1| \cos^2(k_1\lambda + \phi_1) + |A_2| \cos^2(k_2\lambda + \phi_2)] \quad (8.21)$$

similar to equation 8.17, which introduces a systematic to the second order fit parameter of $\pm[|A_1| + |A_2|]$. Where the sign is determined by the polarity of the $\pi/2$ rotator. The corrected second order parameters, \bar{a}_2 , using the amplitudes shown in table 8.1 are shown in the table 8.2. After applying this correction the average estimated second order parameter due to the Sagnac effect is $(-1.083 \pm 0.078) \times 10^{-3}$, which is within 1σ of the expected theoretical value. This corresponds to an OAM proportionality constant of -8197 ± 590 units of $\hbar/\text{\AA}$ according to equation 8.18. From this the average OAM Eigenvalues ℓ_{\pm} of the two path states can be extracted: $\ell_{\pm} = \pm 4098 \pm 295\hbar/\text{\AA} \cdot \lambda$. This

	\bar{P}_+	\bar{P}_-	$\frac{P_+ - P_-}{2}$
$\bar{a}_2(\text{\AA}^{-2}) \times 10^3$	-1.117 ± 0.121	1.049 ± 0.098	-1.083 ± 0.078
$\bar{c}_{OAM}(\text{\AA}^{-1})$	-8454 ± 916	7940 ± 742	-8197 ± 590

Table 8.2: Corrected estimates for the second order parameter due to the Sagnac effect, \bar{a}_2 , and their respective errors for both $\pi/2$ coil polarities and their average, in addition to the OAM proportionality constant, \bar{c}_{OAM} for each setting. For comparison our theoretical estimate for a_2 is $-1.15 \times 10^{-3} \text{\AA}^{-2}$ and for c_{OAM} is $-8.62 \times 10^3 \text{\AA}^{-1}$

can be compared to the results of our calibration measurement (figure 8.2), which, based on equation 8.6, allows us to estimate the average OAM Eigenvalue $\ell_{\pm} = \pm 4310$, which is within 1σ of the estimate achieved using the Sagnac effect. In 2022 the first definitive observation of intrinsic longitudinal OAM was reported [21]. We now conclude that the Sagnac effect represents the first definitive detection of transverse neutron OAM, since it depends only on the projection of the OAM on the axis of rotation (equation 8.4), meaning that OAM must be present to explain a non-zero result.

8.1.3 Conclusion and Outlook

Before concluding the subject of the Sagnac effect we first look forward to potential applications and realizations of our OAM detection scheme. We posit that our measurement can be an answer to criticism raised in [29], against the first experiments with neutron beam OAM [28]. We propose to use OAM-rotation coupling to definitively detect longitudinal OAM. To accomplish this two technical difficulties need to be overcome (1) the sensitivity of the technique needs to be increased and (2) the rotation axis should be more closely aligned with the beam axis to measure the longitudinal OAM component. The sensitivity of this method, using the earth's rotation, is sufficient for detecting large quanta of OAM $|\ell| > 10^3$, however it can be significantly improved by increasing the rotation frequency. A higher effective rotation frequency can be achieved by inserting a rotating Dove mirror (see figure 8.6 and [15, 16, 35]) in the center of the instrument. Such devices are ubiquitous in photo-optics when it comes to measuring and sorting

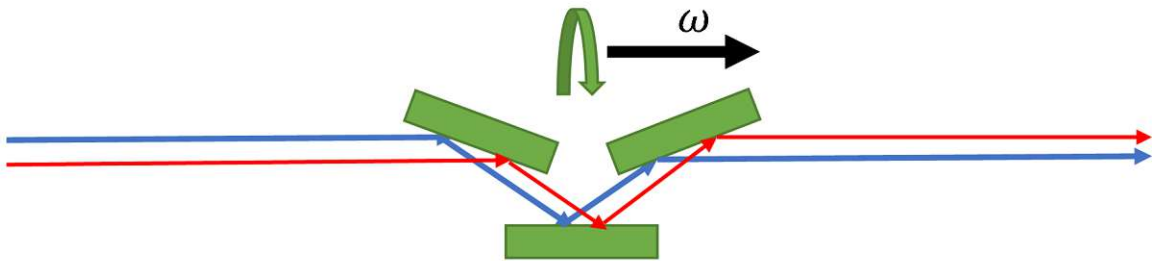


Figure 8.6: Schematic representation of a dove mirror assembly. It can be seen that the dove mirror inverts an image with respect to the axis of reflection. As a result, the image is also rotated around the optical axis. Spinning the device around the optical axis results in a spinning image, as if one were observing the image in a rotating frame of reference, necessary for observing the Sagnac effect. The two arrows are shown in different colors, for ease of visibility of the function of a dove mirror, but also can indicate the two perpendicular spin states that are separated transversely in a SESANS interferometer

spin-orbit states [164, 165], hence we expect them to be equally useful in neutron optics, should they be implemented. A pair of dove mirrors effectively rotate the image around

the optical axis of the devices. A low rotation frequency of 1 Hz, would increase sensitivity by 10^5 , compared to earths rotation. This method would increase a_2 and c_{OAM} , such that the systematic induced by the slight oscillations of the precession plane, becomes insignificant, since both parameters are proportional to the rotation frequency Ω . In addition the dove prism would address the second difficulty as well, since the axis of rotation for such a device can be chosen arbitrarily, including parallel to the propagation direction. The Dove mirror could be made compact, albeit monochromatic, if mosaic crystals are used to produce reflections. Intuitively one may come to the conclusion that the dove mirror technique would only work if the cross section of the dove mirror is of a similar size as the neutron coherence length, owing to the fact that a neutron propagating off-axis but parallel to optical axis of the dove mirror, in its own frame of reference is not only rotated around its propagation axis, but also translated on a circle around the optical axis of the dove mirror. However intrinsic longitudinal OAM is translation invariant. In addition we have shown that the Sagnac method measures the OAM difference between two states which is translation invariant. As a result we conclude that the ratio between the cross section of the mirror and the neutron coherence length is irrelevant to the success of this technique. Instead in SESANS interferometers it is important that the optical axis of the dove mirrors is precisely aligned with the optical axis of the interferometer. SESANS is designed to measure ultra small angle scattering, hence the alignment precision must exceed the instrument resolution. Luckily the resolution is proportional to the spin-echo length $q_{min} \propto \frac{1}{\delta_{SE}}$ and figure 2.7, demonstrates that a low spin echo length produces an optimal superposition of $\ell = \pm 1$. Thus for a typical thermal neutron beam the alignment of the dove prism must be to within $0.1 - 1$ degree of the optical axis of the interferometer, so as to not introduce artifacts. We postulate that dove mirrors will play an important role in neutron OAM optics for OAM manipulation and detection, since as opposed to the scattering methods reported on in [22, 23, 24] and chapter 7 of this manuscript, which depend on still unknown matrix elements, the efficiency of a Sagnac based method is independent of other attributes of the neutron wavepacket such as transverse momentum and coherence length. In addition the Sagnac method ought to provide a faster method than the interferometric methods used in for example [21, 34], since these approaches require detectors with spatial resolution to resolve the OAM phase structure. Due to the low flux of neutron beams this requirement of spatial or angular resolution results in a larger integration time compared to the Sagnac method. Since the matrix elements, which determine the scattering amplitudes of twisted neutrons from nuclei are still unknown, the Sagnac method may be used to calibrate twisted scattering techniques. (Dove) mirrors may also be used to increase the sensitivity of our measurement to extrinsic transverse OAM. A mirror at the center of our instrument rotating around the vertical of the instrument effectively acts as a rotation of the instrument. As a result one can simulate faster rotating frequencies than that provided by the earth.

As pointed out in previously our technique uses spin-orbit entanglement to imprint OAM dependent phases on the spin (see for example eq. 8.7) and to characterize these phases by measuring the spin projection. This is somewhat analogous to the entangled optical

interferometer reported on in [166], which makes use of inter-particle entanglement, while we report on intra-particle or mode entanglement. The 1σ precision achieved in our experiment corresponds to a rotational sensitivity of $5.1\mu\text{rad} \cdot \text{s}^{-1}$, similar to what is reported in [166], which to our knowledge is the most sensitive measurement of the Sagnac effect using entanglement.

In this section we have reported on the Sagnac effect and its application to OAM detection. We have seen that the efficiency of the technique is directly proportional to the amount of OAM carried by the beam. Hence this technique nicely augments the interferometric method reported on in chapter 6, which is useful primarily for detecting lower mode numbers. Though once the neutron optical dove prism is developed, the quantum Sagnac effect will likely displace interferometric techniques for detecting OAM, given that no position or angular resolution is needed to measure the OAM of a beam using this technique.

8.2 Rotary Drag: The Fizeau Effect

The second type of OAM rotation coupling discussed in the introduction to this chapter is the Fizeau effect, sometimes also called the rotary drag effect. We described the Fizeau effect as a phase shift that occurs due to a change in the refractive index of a rotating material, owing to a rotational Doppler shift. The refractive index is given by

$$n = \sqrt{1 - \frac{V}{E}} = \sqrt{1 - \frac{\lambda^2 N b_c}{\pi}} \quad (8.22)$$

with N the number density of the particles in the medium and b_c the coherent scattering length of said medium. Given that the potential $V(E)$ is flat for many materials in the thermal energy range, that V/E is exceedingly small and $\ell\hbar\Omega$ is usually much smaller than E , it is not possible to measure the Fizeau effect in most materials with neutrons [167]. However some materials exhibit an absorption resonances which causes the materials potential to vary rapidly with energy. One of the first non-zero measurements of the neutron Fizeau effect was carried out in a perfect crystal neutron interferometer with a rotating disk of Samarium-149, which exhibits an absorption resonance at 97.3meV. Here the disk was rotated at a frequency of roughly 300Hz resulting in a phase shift of 3 degrees [168]. Since in perfect crystal interferometry we are dealing with particles carrying 10^9 units of OAM it should be obvious that this method will not suffice for detecting single quanta of neutron OAM. The Fizeau phase shift can be written as the difference between the wavevector in the non-rotating and rotating medium times the path length of the medium

$$\delta\phi = (k - k')D \approx k_0 D \left(1 - \frac{V}{2E} - 1 + \frac{V}{2(E + \ell\hbar\Omega)}\right) = k_0 D V \frac{\ell\hbar\Omega}{E^2} \quad (8.23)$$

which for single units of angular momentum and thermal neutrons is about 10^{-14} radians if the medium rotates at a frequency of 100 Hz.

However a second Fizeau type phase shift arises if the boundaries of the medium are in motion with respect to the particle. This situation is described in detail in [169]. This phase shift basically arises from the fact that the material is either moving towards or away from the particle, which results in the particle staying in the potential for a shorter or longer time respectively. This effect is much stronger than the first Fizeau effect we discussed here. In 1981, authors measured a 90 degree phase shift by passing neutrons through a double slit interferometer and a quartz rod which was rotating at 100 Hz [170]. Though contrary to what one may think we cannot look at the work done in [169] and [170] through the lens of OAM, as for realistic rotational velocities the phase shift is independent of the neutron momentum and hence also independent of neutron OAM. Hence we conclude that neutron OAM detection using rotary drag is only an intellectual curiosity, except in the case of very fast moving matter and ultra cold neutrons.

8.3 Conclusion

In this chapter we have presented two types of coupling between rotation and angular momentum, the Fizeau effect and the Sagnac effect. While the former turned out to be unfeasible in practice for detecting any kind of OAM except very large quanta of transverse and extrinsic OAM, the Sagnac effect was shown to be incredibly effective at determining the OAM of a neutron beam. This is confirmed by our experiment on Larmor where we precisely detect the transverse OAM of the beam using the Sagnac phase shift to within statistical error, despite the relatively slow rotation rate of the interferometer, given by Earth's rotation. Furthermore we argued that by employing the neutron optical equivalent of dove mirrors we may be able to increase sensitivity by five orders of magnitude thereby paving the way for detecting single quanta of longitudinal neutron OAM. If single quanta of OAM become accessible it follows that the Mashhoon effect (half integer angular momentum) would also become visible in these kinds of setups, thereby opening an avenue to measuring the total angular momentum, spin angular momentum and OAM in a single measurement.

Finally it should be emphasized that the Sagnac method is the most direct method presented in this manuscript of determining OAM and according to the author the most direct technique to determine neutron OAM to date. This due to the fact that the Sagnac effect is a direct linear coupling to the neutrons OAM, without any pollution from other parameters and the technique reduces the measurement of OAM to one observable, a phase, directly proportional to the neutrons OAM. Hence it is important that neutron dove mirrors are developed to facilitate easy and fast detection of neutron OAM.

9 Conclusion

This thesis has introduced and explored the topic of neutron orbital angular momentum from a theoretical and applied perspective. On the theoretical side first an introduction to the mathematical formalism was provided. This included a derivation of the OAM Eigenfunctions and a proof that quantum mechanical OAM does not require a restoring source, contrary to popular intuition, since twisted vortex states are not associated with an azimuthal velocity. As a result we found that vortex states are solutions to the free space cylindrical Schrödinger equation. Next in the context of integral transforms we derived the OAM distribution function, which is an indispensable tool in the field and especially for the work shown throughout this thesis.

After this general theoretical introduction we looked at two special theoretical topics, first the intrinsic and extrinsic natures of quantum mechanical OAM and second we looked at the distinction between longitudinal and transverse OAM states. While exploring the formed topic we found that the OAM expectation value of pure vortex states is translation invariant and hence we can consider this type of OAM to have an intrinsic character. Hence, we refer to all OAM states which exhibit a translation invariant expectation value as intrinsic, while other OAM states are regarded as extrinsic. However we disputed the idea that intrinsic states are "quantum" while extrinsic states are classical, by showing that superpositions of two pure vortex states with neighboring mode numbers exhibit extrinsic OAM and since we consider pure states to be "quantum" we must consider this superposition and therefore the extrinsic OAM state to also have quantum properties. Furthermore we demonstrated that despite the expectation value being invariant, the OAM distribution function is not invariant under translation, thus upon translation a pure vortex state loses its purity. On the topic of longitudinal and transverse states, we found that besides the extrinsic transverse OAM states which mimic classical non-accelerating angular momentum, in that it arises from the choice of reference frame, there exist also intrinsic transverse OAM states. Using an example wavefunction we derived the (transverse and longitudinal) OAM distribution function of a displaced Gaussian and a split Gaussian wavefunction. These findings were used in almost every following chapter. Finally we introduced the concept of a linear OAM state which consists of a superposition of two vortex modes, equal in magnitude but opposite in sign. A concept that was also used in many of the following chapters.

After this theoretical chapter we moved on to a series of chapters that cover the novel methods of neutron OAM production, explored during the time of this thesis. Starting with the Schwinger interaction, where an electric field acts as a mediator, coupling neu-

tron spin to neutron momentum. This allows for angular momentum exchange between the neutron spin and the momentum (and therefore orbital angular momentum). We showed that the total angular momentum in this interaction is conserved, hence when the spin is flipped by an electric field we gain some OAM which compensates the change in total angular momentum. Since the required fields to produce longitudinal OAM states is incredibly large ($10^{10} \text{ V} \cdot \text{m}^{-1}$), we looked into exploiting intra-atomic electric fields (i.e. the field between nuclei and electron shells), as here we find fields of the required magnitude. For this reason we introduced the theory of dynamical diffraction, which describes the propagation of neutrons through perfect crystals. Naturally we included the Schwinger spin-orbit term so that we would be able to calculate the amount of OAM generate in neutrons diffracted from crystals in Laue and Bragg geometry. All calculations were focused on quartz, since this crystal is well explored for the purpose of neutron diffraction, can be produced to a very high degree of perfection and produces a large spin-orbit contribution due to its non-centrosymmetry. We found that OAM is produced in all geometries, however clean textbook vortex states are only produced in a Bragg backscattering geometry, though only with a very small amplitude. In Laue geometry we found that OAM is also produced, however the state is not pure, judging by the OAM distribution function. In all backscattering cases, the OAM of the spin flipped wavefunction is raised/lowered by one unit of \hbar compared to the incident wave. Finally we presented an experiment looking at polarized dynamical diffraction from quartz and found that in Bragg geometry likely linear OAM states were produced.

By analogy we showed that the neutron nucleus weak interaction produces OAM in a similar way as the Schwinger interaction. This theoretical demonstration was followed by an experimental proof of angular momentum conservation in the weak interaction. This experiment made use of a Lanthanum-139 target the strongest known amplifier of the neutron nucleus weak interaction, due to a relatively broad and low energy resonance.

After this we moved on to coherent averaging methods, for producing OAM. We started by presenting the status quo and our neutron interferometric experiment on OAM generation using reciprocal space coherent averaging. Our experiment generalized the existing coherent averaging method, allowing us to exploit the much stronger strong nuclear interaction. We demonstrated that it is possible to generate a tight lattice of beam vortices. After this we moved on to a theoretical section, motivating why real space coherent averaging is a more efficient approach and producing a generalized theoretical approach to coherent averaging. Here we derived the number of partial waves necessary to produce a vortex with mode number ℓ . After this we showed that certain types of spin echo interferometers are particularly suited for real space coherent averaging and we presented the Austrian SESANS instrument designed specifically for generating linear OAM states and investigating the properties of OAM. Finally we presented a two dimensional SESANS type scheme which can be used to generate pure $\ell = 1$ or $\ell = -1$ vortex states, by coherently averaging four partial waves in real space. This approach was later used to investigate unique scattering properties of twisted states.

Next we moved on to three different OAM detection methods, the first, interferometry

relies on using a neutron interferometer to measure the transverse cross correlation function between the test wavefunction, which presumably carries some OAM and a reference wavefunction which ideally does not carry any OAM. While this technique allows us to resolve vortices, it becomes increasingly difficult as the vortex number is increased. To demonstrate the method we presented an experiment where we used a spin echo type interferometer to measure the one dimensional transverse auto-correlation of a neutron wavefunction.

Following this chapter we looked into OAM dependence of neutron cross sections, specifically the absorption cross section of Helium-3, given that this cross section already shows a strong angular momentum dependence, at least when it comes to spin. However we demonstrated experimentally that if any effect exists it is more subtle than that which was predicted in the theoretical literature. We then provided a few qualitative arguments explaining this discrepancy, the most important of which is likely the difference between the size of the neutron vortex versus the helium nucleus, as the nucleus needs to be captured in the center of the vortex for any meaningful OAM dependent effect to be measured. We argue that this topic requires more theoretical investigation before any follow up experiment is conducted.

Finally in the penultimate chapter of this manuscript different kinds of rotation OAM couplings were explored (1) the Sagnac effect and (2) the Fizeau effect. It was determined that only the Sagnac effect is strong enough to produce an observable effect with quantum OAM, when the wavefunction carries only a few \hbar of longitudinal OAM. This was demonstrated by our experiment which was sufficiently sensitive to observe a coupling between the very slow rotation rate of the earth and a few thousand \hbar worth of transverse neutron OAM. Hence we argued that a neutron optical dove mirror spinning at only 1 Hz would produce a strong enough signal to measure the OAM of neutrons carrying only a few quanta of OAM. The Sagnac effect is a particularly elegant method, since the coupling depends only on the OAM of the test particle and the rotation rate of the system, hence the result is not polluted by other parameters such as transverse momentum.

Looking forward the author posits that the quartz diffraction and real space coherent averaging methods should be developed further as these have yielded the most promising results and theory indicates that these methods produce the purest vortex states at very high yields. On the measurement side, it is important to develop the neutron optical dove mirror, as this provides the most direct measure of neutron OAM and such a device can be relatively compact, especially compared to devices based on any other detection method discussed in this thesis. Once dedicated instruments are produced, which can generate and characterize vortex states accurately one can revisit explorations into OAM dependent interactions. These investigations could be of societal importance especially in the realm of energy storage, since they could help reveal methods for depleting super stable metastable nuclei, thereby paving the way towards nuclear batteries with very high energy densities.

Bibliography

- [1] L. Allen, M. Beijersbergen, R. Spreeuw, and J. Woerdman, “Orbital angular momentum of light and the transformation of laguerre-gaussian laser modes,” *Phys. Rev. A*, vol. 45, p. 8185, 1992.
- [2] S. J. van Enk and G. Nienhuis, “Spin and orbital angular momentum of photons,” *EPL*, vol. 25, p. 497, 1994.
- [3] R. Beth, “Mechanical detection and measurement of the angular momentum of light,” *Physical Review*, vol. 50, pp. 115–125, 1936.
- [4] H. He, M. E. J. Friese, N. R. Heckenberg, and H. Rubinsztein-Dunlop, “Direct observation of transfer of angular momentum to absorptive particles from a laser beam with a phase singularity,” *Phys. Rev. Lett.*, vol. 75, p. 826, 1995.
- [5] A. Anhaeuser, R. Wunenburger, and E. Brasselet, “Acoustic rotational manipulation using orbital angular momentum transfer,” *Phys. Rev. Lett.*, vol. 109, p. 034301, 2012.
- [6] G. Gibson, J. Courtial, M. Padgett, M. Vasnetsov, V. Pas’ko, S. Barnett, and S. Franke-Arnold, “Free-space information transfer using light beams carrying orbital angular momentum,” *Optics Express*, vol. 12, p. 5448–5456, 2004.
- [7] G. Vallone, V. D’Ambrosio, A. Sponselli, S. Slussarenko, L. Marrucci, F. Sciarrino, and P. Villoresi, “Free-space quantum key distribution by rotation-invariant twisted photons,” *Phys. Rev. Lett.*, vol. 113, p. 060503, 2014.
- [8] R. Fickler, R. Lapkiewicz, M. Huber, M. Lavery, M. Padgett, and A. Zeilinger, “Interface between path and orbital angular momentum entanglement for high-dimensional photonic quantum information,” *Nat. Commun.*, vol. 5, p. 4502, 2014.
- [9] Y. Hasegawa, R. Loidl, G. Badurek, K. Durstberger-Rennhofer, S. Sponar, and H. Rauch, “Engineering of triply entangled states in a single-neutron system,” *Phys. Rev. A*, vol. 81, p. 032121, 2010.
- [10] J. Shen, S. Kuhn, R. Dalgliesh, V. de Haan, N. Geerits, A. Irfan, F. Li, S. Lu, S. Parnell, J. Plomp, A. van Well, A. Washington, D. Baxter, G. Ortiz, W. Snow, and R. Pynn, “Unveiling contextual realities by microscopically entangling a neutron,” *Nat. Commun.*, vol. 11, p. 930, 2020.
- [11] S. J. Kuhn, S. McKay, J. Shen, N. Geerits, R. M. Dalgliesh, E. Dees, A. A. M.

- Irfan, F. Li, S. Lu, V. Vangelista, D. V. Baxter, G. Ortiz, S. R. Parnell, W. M. Snow, and R. Pynn, “Neutron-state entanglement with overlapping paths,” *Phys. Rev. Research*, vol. 3, p. 023227, 2021.
- [12] Y. Aharonov, S. Popescu, D. Rohrlich, and P. Skrzypczyk, “Quantum cheshire cats,” *New Journal of Physics*, vol. 15, p. 113015, 2013.
- [13] S. A. Werner, J. L. Staudenmann, and R. Colella, “Effect of earth’s rotation on the quantum mechanical phase of the neutron,” *Phys. Rev. Lett.*, vol. 42, pp. 1103–1106, 1979.
- [14] N. Geerits, S. Sponar, K. E. Steffen, W. M. Snow, S. R. Parnell, G. Mauri, G. N. Smith, R. M. Dalgliesh, and V. O. de Haan., “Measuring the angular momentum of a neutron using earth’s rotation,” *Physical Review Research*, vol. 7, p. 013046, 2025.
- [15] J. Courtial, K. Dholakia, D. A. Robertson, L. Allen, and M. J. Padgett, “Measurement of the rotational frequency shift imparted to a rotating light beam possessing orbital angular momentum,” *Phys. Rev. Lett.*, vol. 80, pp. 3217–3219, 1998.
- [16] J. Leach, M. Padgett, S. Barnett, S. Franke-Arnold, and J. Courtial, “Measuring the orbital angular momentum of a single photon,” *Phys. Rev. Lett.*, vol. 88, p. 257901, 2002.
- [17] N. Bohr, “On the constitution of atoms and molecules, part i,” *The London, Edinburgh, and Dublin Philosophical Magazine and Journal of Science*, vol. 26, pp. 1–25, 1913.
- [18] M. G. Sagnac, “The demonstration of the luminiferous aether by an interferometer in uniform rotation,” *Comptes Rendus*, vol. 157, pp. 708,1410, 1913.
- [19] B. J. McMorran, A. Agrawal, I. M. Anderson, A. A. Herzing, H. J. Lezec, J. J. McClelland, and J. Unguris, “Electron vortex beams with high quanta of orbital angular momentum,” *Science*, vol. 331, pp. 192–195, 2011.
- [20] A. Luski, Y. Segev, R. David, O. Bitton, H. Nadler, A. Barnea, A. Gorlach, O. Cheshnovsky, I. Kaminer, and E. Narevicius, “Vortex beams of atoms and molecules,” *Science*, vol. 373, p. 1105, 2021.
- [21] D. Sarenac, M. E. Henderson, H. Ekinici, C. W. Clark, D. G. Cory, L. DeBeer-Schmitt, M. G. Huber, C. Kapahi, and D. A. Pushin, “Experimental realization of neutron helical waves,” *Sci. Adv.*, vol. 8, p. eadd2002, 2022.
- [22] A. Afanasev, D. Karlovets, and V. Serbo, “Schwinger scattering of twisted neutrons by nuclei,” *Phys. Rev. C*, vol. 100, p. 051601, 2019.
- [23] A. Afanasev, D. Karlovets, and V. Serbo, “Elastic scattering of twisted neutrons by nuclei,” *Phys. Rev. C*, vol. 103, p. 054612, 2021.

- [24] T. Jach and J. Vinson, “Method for the definitive detection of orbital angular momentum states in neutrons by spin-polarized ^3He ,” *Phys. Rev. C*, vol. 105, p. L061601, 2022.
- [25] M. E. Henderson, B. Heacock, M. Bleuel, D. G. Cory, C. Heikes, M. G. Huber, J. Krzywon, O. Nahman-Levesqué, G. M. Luke, M. Pula, D. Sarenac, K. Zhernenkov, and D. A. Pushin, “Three-dimensional neutron far-field tomography of a bulk skyrmion lattice,” *Nat. Phys.*, vol. 19, p. 1617–1623, 2023.
- [26] M. E. Henderson, D. G. Cory, D. Sarenac, and D. A. Pushin, “Quantum advancements in neutron scattering reshape spintronic devices,” *Arxiv*, p. 2407.10822, 2024.
- [27] Z.-W. Lu, L. Guo, Z.-Z. Li, M. Ababekri, F.-Q. Chen, C. Fu, C. Lv, R. Xu, X. Kong, Y.-F. Niu, and J.-X. Li, “Manipulation of giant multipole resonances via vortex gamma photons,” *Phys. Rev. Lett.*, vol. 131, p. 202502, 2023.
- [28] C. W. Clark, R. Barankov, M. G. Huber, M. Arif, D. G. Cory, and D. A. Pushin, “Controlling neutron orbital angular momentum,” *Nature*, vol. 525, pp. 504–506, 2015.
- [29] R. Cappelletti, T. Jach, and J. Vinson, “Intrinsic orbital angular momentum states of neutrons,” *Phys. Rev. Lett.*, vol. 120, p. 090402, 2018.
- [30] J. Nsofini, D. Sarenac, C. J. Wood, D. G. Cory, M. Arif, C. W. Clark, M. G. Huber, and D. A. Pushin, “Spin-orbit states of neutron wave packets,” *Phys. Rev. A*, vol. 94, p. 013605, 2016.
- [31] D. Sarenac, J. Nsofini, I. Hincks, M. Arif, C. W. Clark, D. G. Cory, M. G. Huber, and D. A. Pushin, “Methods for preparation and detection of neutron spin-orbit states,” *New J. Phys*, vol. 20, p. 103012, 2018.
- [32] D. Sarenac, D. G. Cory, J. Nsofini, I. Hincks, P. Miguel, M. Arif, C. W. Clark, M. G. Huber, and D. A. Pushin, “Generation of a lattice of spin-orbit beams via coherent averaging,” *PRL*, vol. 121, p. 183602, 2018.
- [33] D. Sarenac, C. Kapahi, W. Chen, C. W. Clark, D. G. Cory, M. G. Huber, I. Taminiou, K. Zhernenkov, and D. A. Pushin, “Generation and detection of spin-orbit coupled neutron beams,” *PNAS*, vol. 116, pp. 20328–20332, 2019.
- [34] N. Geerits, H. Lemmel, A. Berger, and S. Sponar, “Phase vortex lattices in neutron interferometry,” *Nat. Comm. Phys*, vol. 6, p. 209, 2023.
- [35] N. Geerits and S. Sponar, “Twisting neutral particles with electric fields,” *Phys. Rev. A*, vol. 103, p. 022205, 2021.
- [36] V. V. Voronin, E. G. Lapin, S. Y. Semenikhin, and V. V. Fedorov, “Depolarization of a neutron beam in laue diffraction by a noncentrosymmetric crystal,” *J. Exp. Theor. Phys.*, vol. 72, p. 308, 2000.

Bibliography

- [37] B. Heckel, M. Forte, O. Schaerpf, K. Green, G. L. Greene, N. F. Ramsey, J. Byrne, and J. M. Pendlebury, “Measurement of parity nonconserving neutron spin rotation in lanthanum,” *Phys. Rev. C*, vol. 29, pp. 2389–2391, 1984.
- [38] N. Geerits, S. Hack, A. van Well, S. R. Parnell, H. Abele, and S. Sponar, “Canisius the austrian neutron spin echo interferometer,” *Arxiv*, vol. 2408.06216, 2024.
- [39] R. Pynn, “Neutron spin-echo and three-axis spectrometers,” *Journal of Physics E: Scientific Instruments*, vol. 11, p. 1133, 1978.
- [40] M. Rekveldt, “Novel sans instrument using neutron spin echo,” *Nucl. Inst. and Meth. in Phys. Res. B*, vol. 114, pp. 366–370, 1996.
- [41] R. Gaehler, R. Golub, K. Habicht, T. Keller, and J. Felber, “Space-time description of neutron spin echo spectrometry,” *Physica B*, vol. 229, pp. 1–17, 1996.
- [42] H. Bateman, *Tables of Integral Transforms*, vol. 2. McGRAW-HILL BOOK COMPANY, INC., 1954.
- [43] K. Y. Bliokh and F. Nori, “Transverse and longitudinal angular momenta of light,” *Physics Reports*, vol. 592, pp. 1–38, 2015.
- [44] J. Durnin, “Exact solutions for nondiffracting beams. i. the scalar theory,” *J. Opt. Soc. Am. A*, vol. 4, pp. 651–654, 1986.
- [45] V. Grillo, E. Karimi, G. Gazzadi, S. Frabboni, M. Dennis, and R. Boyd, “Generation of nondiffracting electron bessel beams,” *Phys. Rev. X*, vol. 4, p. 011013, 2014.
- [46] N. Baddour, “Chapter 1 - two-dimensional fourier transforms in polar coordinates,” *Advances in Imaging and Electron Physics*, vol. 165, pp. 1–45, 2011.
- [47] M. Abramowitz and I. Stegun, *Handbook of Mathematical Functions with Formulas, Graphs, and Mathematical Tables*. Cambridge University Press, 1964.
- [48] P. MacAulay-Owen, “Parseval’s theorem for hankel transforms,” *Proceedings of the London Mathematical Society*, vol. s2-45, pp. 458–474, 1939.
- [49] M. V. Berry, “Paraxial beams of spinning light,” *Proc. SPIE*, vol. 3487, pp. 6–11, 1998.
- [50] A. T. O’Neil, I. MacVicar, L. Allen, and M. J. Padgett, “Intrinsic and extrinsic nature of the orbital angular momentum of a light beam,” *Physical Review Letters*, vol. 88, p. 053601, 2002.
- [51] J. Sherwin, “Scattering of slow twisted neutrons by ortho- and parahydrogen,” *Physics Letters A*, vol. 437, p. 128102, 2022.
- [52] K. Y. Bliokh and F. Nori, “Spatiotemporal vortex beams and angular momentum,” *Phys. Rev. A*, vol. 86, p. 033824, 2012.

- [53] V. Y. Bazhenov, M. Soskin, and M. Vasnetsov, “Screw dislocations in light wavefronts,” *Journal of Modern Optics*, vol. 39, pp. 985–990, 1992.
- [54] Y. Li, J. Kim, and M. J. Escuti, “Controlling orbital angular momentum using forked polarization gratings,” *Proc. SPIE*, vol. 7789, p. 77890F, 2010.
- [55] G. Watson, *A Treatise on the Theory of Bessel Functions*. Cambridge, UK: Cambridge University Press, 1944.
- [56] S. Franke-Arnold, G. Gibson, R. W. Boyd, and M. J. Padgett, “Rotary photon drag enhanced by a slow-light medium,” *Science*, vol. 333, pp. 65–67, 2011.
- [57] J. Schwinger, “On the polarization of fast neutrons,” *Phys. Rev.*, vol. 73, pp. 407–409, 1948.
- [58] S. Bruce and J. Diaz-Valdes, “Neutron interaction with electromagnetic fields: a didactic approach,” *Eur. J. Phys.*, vol. 41, p. 045402, 2020.
- [59] B. W. Batterman and H. Cole, “Dynamical diffraction of x rays by perfect crystals,” *Reviews of Modern Physics*, vol. 36, pp. 681–717, 1964.
- [60] V. F. Sears, “Dynamical theory of neutron diffraction,” *Canadian Journal of Physics*, vol. 56, pp. 1261–1288, 1978.
- [61] C. Stassis and J. A. Oberteuffer, “Neutron diffraction by perfect crystals,” *Phys. Rev. B*, vol. 10, pp. 5192–5202, 1974.
- [62] M. Blume, “Polarization effects in slow neutron scattering ii spin-orbit scattering and interference,” *Phys. Rev.*, vol. 133, pp. 1366–1369, 1964.
- [63] M. Forte, “Neutron-optical effects sensitive to p and t symmetry violation,” *J. Phys. G: Nucl. Phys.*, vol. 9, pp. 745–754, 1983.
- [64] V. Alexeev, V. Fedorov, E. Lapin, E. Leushkin, V. Rumiantsev, O. Sumbaev, and V. Voronin, “Observation of a strong interplanar electric field in a dynamical diffraction of polarized neutrons,” *Nuclear Instruments and Methods in Physics Research A*, vol. 284, pp. 181–183, 1989.
- [65] V. Fedorov, V. Voronin, and E. Lapin, “On the search for neutron edm using laue diffraction by a crystal without a centre of symmetry,” *J. Phys. G: Nucl. Part. Phys.*, vol. 18, pp. 1133–1148, 1992.
- [66] M. Forte and C. Zeyen, “Neutron optical spin-orbit rotation in dynamical diffraction,” *Nuclear Instruments and Methods in Physics Research A*, vol. 284, pp. 147–150, 1989.
- [67] A. Zangwill, *Modern Electrodynamics*. New York, USA: Cambridge University Press, 2013.
- [68] K. Bliokh, I. Ivanov, G. Guzzinati, L. Clark, R. V. Boxem, A. Béch e, R. Juchtmans,

Bibliography

- M. Alonso, P. Schattschneider, F. Nori, and J. Verbeeck, “Theory and applications of free-electron vortex states,” *Physics Reports*, vol. 690, pp. 1–70, 2017.
- [69] F. Mezei, “The principles of neutron spin echo,” in *Neutron Spin Echo* (F. Mezei, ed.), (Berlin, Heidelberg), pp. 1–26, Springer Berlin Heidelberg, 1980.
- [70] M. Toney, J. Howard, J. Richer, G. Borges, J. Gordon, O. Melroy, D. Wiesler, D. Yee, and L. Sorensen, “Distribution of water molecules at $ag(1\ 1\ 1)$ /electrolyte interface as studied with surface x-ray scattering,” *Surf. Sci.*, vol. 355, pp. 326–332, 1995.
- [71] I. Danielewicz-Ferchmin and A. Ferchmin, “A phase transition in H_2O due to a high electric field close to an electrode,” *Chem. Phys. Lett.*, vol. 351, pp. 397–402, 2002.
- [72] H. Rauch and D. Petrascheck, “Grundlagen fuer ein laue-neutroneninterferometer - teil 1,” *AIAU 74405b, Atominstytut der Osterreichischen Universitaten*, 1976.
- [73] H. Rauch and D. Petrascheck, “Grundlagen fuer ein laue-neutroneninterferometer - teil 2,” *AIAU 74405b, Atominstytut der Osterreichischen Universitaten*, 1976.
- [74] H. Rauch and S. Werner, *Neutron Interferometry*. Oxford, UK: Clarendon Press, 2000.
- [75] V. Voronin, E. Lapin, S. S. Yu, and V. Fedorov, “Direct measurement of the delay time for a neutron in a crystal in the case of the laue diffraction,” *Journal of Experimental and Theoretical Physics Letters*, vol. 71, pp. 76–79, 2000.
- [76] W. Bragg and W. Bragg, “The reflection of x-rays by crystals,” *Proceedings of the Royal Society of London. Series A, Containing Papers of a Mathematical and Physical Character*, vol. 88, no. 605, pp. 428–438, 1913.
- [77] J. Knowles, “Anomalous absorption of slow neutrons and x-rays in nearly perfect single crystals,” *Acta Crystallographica*, vol. 9, no. 1, pp. 61–69, 1956.
- [78] S. Peterson and H. Smith, “Anomalous neutron diffraction in α cadmium sulfide,” *Physical Review Letters*, vol. 6, no. 1, p. 7, 1961.
- [79] E. Fermi, “Sul moto dei neutroni nelle sostanze idrogenate,” *Ricerca scientifica*, vol. 7, no. 2, pp. 13–52, 1936.
- [80] Oxford Cryosystems Ltd, “Crystallographica v1.60d,” 2007.
- [81] F. Bloch, “Über die quantenmechanik der elektronen in kristallgittern,” *Zeitschrift für physik*, vol. 52, no. 7, pp. 555–600, 1929.
- [82] M. Agamalian, J. Carpenter, and W. Treimer, “Remarkable precision of the 90-year-old dynamic diffraction theories of darwin and ewald,” *Journal of Applied Crystallography*, vol. 43, no. 4, pp. 900–906, 2010.

- [83] V. Fedorov and V. Voronin, “Neutron diffraction and optics in noncentrosymmetric crystals: New feasibility of a search for neutron edm,” *Nuclear Instruments and Methods in Physics Research Section B: Beam Interactions with Materials and Atoms*, vol. 201, no. 1, pp. 230–242, 2003.
- [84] G. Friedel, “Sur les symétries cristallines que peut révéler la diffraction des rayons röntgen,” *CR Acad. Sci. Paris*, vol. 157, pp. 1533–1536, 1913.
- [85] M. Nespolo and G. Ferraris, “Applied geminography symmetry analysis of twinned crystals and definition of twinning by reticular polyholohedry,” *Acta Crystallographica Section A: Foundations of Crystallography*, vol. 60, no. 1, pp. 89–95, 2004.
- [86] V. Fedorov, M. Jentschel, I. Kuznetsov, E. Lapin, E. Lelievre-Berna, V. Nesvizhevsky, A. Petoukhov, S. Semeníkhin, T. Soldner, F. Tasset, V. Voronin, and Y. Braginetz, “Measurement of the neutron electric dipole moment by crystal diffraction,” *Nuclear Instruments and Methods in Physics Research Section A: Accelerators, Spectrometers, Detectors and Associated Equipment*, vol. 611, no. 2, pp. 124–128, 2009.
- [87] F. Michel, “Parity nonconservation in nuclei,” *Physical Review*, vol. 133, pp. 329–349, 1964.
- [88] G. Karl and D. Tadić, “Model for scattering with parity violation,” *Physical Review C*, vol. 16, no. 5, pp. 1726–1734, 1977.
- [89] M. Forte, B. Heckel, N. Ramsey, K. Green, G. Greene, J. Byrne, and J. Pendlebury, “First measurement of parity-nonconserving neutron-spin rotation: The tin isotopes,” *Physical Review Letters*, vol. 45, no. 26, pp. 2088–2091, 1980.
- [90] V. Skoy, E. Sharapov, N. Gundorin, Y. P. Popov, Y. V. Prokofichev, N. Roberson, and G. Mitchell, “Isotopic identification of the parity-violating neutron p-wave resonance at energy $e_0 = 3.2$ eV in Xe,” *Physical Review C*, vol. 53, no. 6, p. R2573, 1996.
- [91] V. Alfimenkov, S. Borzakov, V. Van Thuan, Y. Mareev, L. Pikelner, A. Khrykin, and E. Sharapov, “Parity nonconservation in neutron resonances,” *Nuclear Physics A*, vol. 398, no. 1, pp. 93–106, 1983.
- [92] F. Tasset, “Towards helium-3 neutron polarizers,” *Physica B: Condensed Matter*, vol. 213–214, pp. 935–938, 1995.
- [93] H. Humblot, W. Heil, E. Lelievre-Berna, and F. Tasset, “The ^3He neutron spin filter at ill,” *Neutron News*, vol. 8, no. 4, pp. 27–32, 1997.
- [94] W. Heil, H. Humblot, D. Hofmann, I. Krasnoschekova, E. Lelièvre-Berna, A. Petoukhov, G. Petrov, A. Serebrov, F. Tasset, and G. Valsky, “Neutron optics p-violation effects near p-wave resonance,” *Physica B: Condensed Matter*, vol. 267,

pp. 289–293, 1999.

- [95] T. Haseyama, K. Asahi, J. Bowman, P. Delheij, H. Funahashi, S. Ishimoto, G. Jones, A. Masaike, Y. Masuda, Y. Matsuda, K. Morimoto, S. Muto, S. Penttilä, V. Pomeroy, K. Sakai, E. Sharapov, D. Smith, and V. Yuan, “Measurement of parity-nonconserving rotation of neutron spin in the 0.734-eV p-wave resonance of ^{139}La ,” *Physics Letters B*, vol. 534, no. 1, pp. 39–44, 2002.
- [96] V. Bodnarchuk, W. Kraan, M. Rekveldt, and A. Ioffe, “Neutron spin turners with a rotating magnetic field: first experiments,” *Measurement science and technology*, vol. 19, no. 3, p. 034012, 2008.
- [97] Demé and Guérard *ILL News*, vol. 38, pp. 9–10, 2002.
- [98] J. Clergeau, M. Ferraton, B. Guérard, A. Khaplanov, F. Piscitelli, M. Platz, J. Rigal, P. V. Esch, and T. Daullé, “An information-theoretical approach to image resolution applied to neutron imaging detectors based upon individual discriminator signals,” *IEEE Transactions on Nuclear Science*, vol. 64, no. 1, pp. 735–742, 2016.
- [99] D. Braun and S. Popescu, “Coherently enhanced measurements in classical mechanics,” *Quantum Measurements and Quantum Metrology*, vol. 2, no. 1, p. 000010247820140003, 2014.
- [100] J. Fraïsse and D. Braun, “Coherent averaging,” *Annalen der Physik*, vol. 527, no. 9-10, pp. 701–712, 2015.
- [101] H. Wang and A. Afanasev, “Topology and polarization of optical vortex fields from atomic phased arrays,” *Applied Sciences*, vol. 13, no. 9, p. 5672, 2023.
- [102] F. Mezei, “Neutron spin-echo - new concept in polarized thermal-neutron techniques,” *Zeitschrift Fur Physik*, vol. 255, no. 2, p. 146, 1972.
- [103] M. Heinrich, D. Petrascheck, and H. Rauch, “Test of a four plate neutron interferometer,” *Zeitschrift für Physik B Condensed Matter*, vol. 72, pp. 357–363, Sep 1988.
- [104] Y. Hasegawa, M. Zawisky, H. Rauch, and A. I. Ioffe, “Geometric phase in coupled neutron interference loops,” *Phys. Rev. A*, vol. 53, pp. 2486–2492, Apr 1996.
- [105] N. Geerits, A. Berger, and H. Lemmel, “Generation of neutron spin-orbit states,” 2021. doi:10.5291/ILL-DATA.CRG-2883.
- [106] S. Filipp, Y. Hasegawa, R. Loidl, and H. Rauch, “Noncyclic geometric phase due to spatial evolution in a neutron interferometer,” *Phys. Rev. A*, vol. 72, p. 021602, Aug 2005.
- [107] H. Geppert-Kleinrath, T. Denkmayr, S. Sponar, H. Lemmel, T. Jenke, and Y. Hasegawa, “Multifold paths of neutrons in the three-beam interferometer de-

- tected by a tiny energy kick,” *Phys. Rev. A*, vol. 97, p. 052111, May 2018.
- [108] M. Strobl, C. Gruenzweig, A. Hilger, I. Manke, N. Kardjilov, C. David, and F. Pfeiffer, “Neutron dark-field tomography,” *Phys. Rev. Lett.*, vol. 101, p. 123902, 2008.
- [109] M. Strobl, B. Betz, R. P. Harti, A. Hilger, N. Kardjilov, I. Manked, and C. Gruenzweig, “Wavelength-dispersive dark-field contrast: micrometre structure resolution in neutron imaging with gratings,” *J. Appl. Cryst.*, vol. 49, p. 569–573, 2016.
- [110] W. G. Bouwman, C. P. Duif, and R. Gahler, “Spatial modulation of a neutron beam by larmor precession,” *Physica B*, vol. 404, pp. 2585–2589, 2009.
- [111] W. G. Bouwman, C. P. Duif, J. Plomp, A. Wiedenmann, and R. Gahler, “Combined SANS-SESANS, from 1 nm to 0.1 mm in one instrument,” *Physica B*, vol. 406, pp. 2357–2360, 2011.
- [112] F. Li, S. R. Parnell, H. Bai, W. Yang, W. A. Hamilton, B. B. Maranville, R. Ashkar, D. V. Baxter, J. T. Cremer, and R. Pynn, “Spin echo modulated small-angle neutron scattering using superconducting magnetic wollaston prisms,” *Journal of Applied Crystallography*, vol. 49, pp. 55–63, 2016.
- [113] J. Valsecchi, M. Strobl, R. P. Harti, C. Carminati, P. Trtik, A. Kaestner, C. Grünzweig, Z. Wang, K. Jefimovs, and M. Kagias, “Characterization of oriented microstructures through anisotropic small-angle scattering by 2d neutron dark-field imaging,” *Commun. Phys.*, vol. 3, p. 42, 2020.
- [114] Q. L. Thien, S. McKay, R. Pynn, and G. Ortiz, “Spin-textured neutron beams with orbital angular momentum,” *Phys. Rev. B*, vol. 107, p. 134403, 2023.
- [115] T. Adachi, T. Oku, S. Morita, H. Ohmori, Y. Takizawa, H. Shimizu, J. Suzuki, C. Loong, K. Littrell, and R. Goyette, “Development of neutron compound refractive optics: a progress report,” *Applied Physics A*, vol. 74, pp. S180–S182, 2002.
- [116] C. Kapahi, D. Sarenac, M. Bleuel, D. Cory, B. Heacock, M. Henderson, M. Huber, I. Taminiau, and D. A. Pushin, “Next-generation high transmission neutron optical devices utilizing micro-machined structures,” *arXiv:2112.13176*, 2021.
- [117] H. Lemmel, M. Jentschel, H. Abele, F. Lafont, B. Guerard, C. P. Sasso, G. Mana, and E. Massa, “Neutron interference from a split-crystal interferometer,” *J. Appl. Cryst.*, vol. 55, pp. 870–875, 2022.
- [118] H. Rauch, H. Wolwitsch, H. Kaiser, R. Clothier, and S. A. Werner, “Measurement and characterization of the three-dimensional coherence function in neutron interferometry,” *Phys. Rev. A*, vol. 53, pp. 902–908, 1996.
- [119] S. McKay, A. A. M. Irfan, Q. L. Thien, N. Geerits, S. R. Parnell, R. M. Dalgliesh, N. V. Lavrik, I. I. Kravchenko, G. Ortiz, and R. Pynn, “Experimental evidence for

- the two-path description of neutron spin echo,” *Phys. Rev. A*, vol. 109, p. 042420, 2024.
- [120] S. R. Parnell, A. A. van Well, J. Plomp, R. M. Dalgliesh, N.-J. Steinke, J. F. K. Cooper, K. E. S. N. Geerits, W. M. Snow, and V. O. de Haan, “Search for exotic spin-dependent couplings of the neutron with matter using spin-echo based neutron interferometry,” *Phys. Rev. D*, vol. 101, p. 122002, 2020.
- [121] V.-O. de Haan, J. Plomp, A. A. van Well, M. T. Rekveldt, Y. H. Hasegawa, R. M. Dalgliesh, and N.-J. Steinke, “Measurement of gravitation-induced quantum interference for neutrons in a spin-echo spectrometer,” *Phys. Rev. A*, vol. 89, p. 063611, 2014.
- [122] R. Dalgliesh, S. Langridge, J. Plomp, V. de Haan, and A. van Well, “Offspec, the isis spin-echo reflectometer,” *Physica B: Condensed Matter*, vol. 406, pp. 2346–2349, 2011.
- [123] N. Geerits, S. R. Parnell, M. A. Thijs, A. A. van Well, C. Franz, A. L. Washington, D. Raspon, R. M. Dalgliesh, and J. Plomp, “Time of flight modulation of intensity by zero effort,” *Review of Scientific Instruments*, vol. 90, p. 125101, 2019.
- [124] N. Geerits, S. Parnell, M. Thijs, W. Bouwman, and J. Plomp, “Applying resonant spin flippers with poleshoes and longitudinal radio frequency fields to time of flight MIEZE,” *Journal of Physics: Conference Series*, vol. 1316, p. 012011, 2019.
- [125] A. Bazhenov, V. Lobashev, A. Pirozhkov, and V. Slusar *Nucl. Instr. and Meth. in Phys. Res. A*, vol. 332, pp. 534–536, 1993.
- [126] R. Gähler, R. Golub, and T. Keller, “Neutron resonance spin echo—a new tool for high resolution spectroscopy,” *Physica B: Condensed Matter*, vol. 180-181, pp. 899 – 902, 1992.
- [127] H. Rauch, J. Harms, and H. Moldaschl, “A neutron spin-flip chopper for time-of-flight measurements,” Sep 1968.
- [128] H. Freisleben and H. Rauch, “Neutron spin-flip-chopper with high repetition rates,” *Nuclear Instruments and Methods*, vol. 98, pp. 61–67, 1972.
- [129] S. V. Grigoriev, R. Kreuger, W. H. Kraan, F. M. Mulder, and M. T. Rekveldt, “Neutron wave-interference experiments with adiabatic passage of neutron spin through resonant coils,” *Phys. Rev. A*, vol. 64, p. 013614, 2001.
- [130] F. Li, R. Dadisman, and D. C. Wasilko, “Optimization of a superconducting adiabatic radio frequency neutron resonant spin flipper,” *Nuclear Inst. and Methods in Physics Research, A*, vol. 955, p. 163300, 2020.
- [131] J. Plomp, *Spin-echo development for a time-of-flight neutron reflectometer*. Universal Press, 2009.

- [132] W. C. Chen, R. Erwin, P. Tsai, M. T. Hassan, N. Hadad, and C. F. Majkrzak, “A large beam high efficiency radio frequency neutron spin flipper,” *Review of Scientific Instruments*, vol. 92, p. 063906, 2021.
- [133] E. Fermi, J. Marshall, and I. Marshall, “A thermal neutron velocity selector and its application to the measurement of the cross section of boron,” *Physical Review*, vol. 72, pp. 193–196, 1947.
- [134] A. van Well and H. Fredrikze, “On the resolution and intensity of a time-of-flight neutron reflectometer,” *Physica B: Condensed Matter*, vol. 357, pp. 204–207, 2005.
- [135] “Smartmembranes,” 2024. <http://www.smartmembranes.de/en/products/nanoporous-alumina/> [Accessed: 2024].
- [136] F. Funama, C. M. Wolf, K. Weigandt, J. Shen, S. R. Parnell, and F. Li, “Spin echo small-angle neutron scattering using superconducting magnetic wollaston prisms,” *Review of Scientific Instruments*, vol. 95, p. 073709, 2024.
- [137] T. Keller, W. Besenböck, J. Feller, R. Gähler, R. Golub, P. Hank, and M. Köppe, “A comparison of spin echo and conventional neutron instruments by the coherence properties of the neutrons,” *Physica B: Condensed Matter*, vol. 234, pp. 1120–1125, 1997.
- [138] V. de Haan, J. Plomp, M. Rekveldt, A. van Well, R. Dalgliesh, S. Langridge, A. Böttger, and R. Hendrikx, “Coherence approach in neutron, x-ray, and neutron spin-echo reflectometry,” *Phys. Rev. B*, vol. 81, p. 094112, 2010.
- [139] J. Plomp, V. D. Haan, R. Dalgliesh, S. Langridge, and A. van Well, “Neutron spin-echo labelling at offspec, an isis second target station project,” *Thin Solid Films*, vol. 515, no. 14, pp. 5732–5735, 2007.
- [140] S. Parnell, R. Dalgliesh, N. Steinke, J. Plomp, and A. V. Well, “Rf neutron spin flippers in time of flight spin-echo resolved grazing incidence scattering (sergis),” in *Journal of Physics: Conference Series*, vol. 1021, p. 012040, 2018.
- [141] R. Gähler, J. Felber, F. Mezei, and R. Golub, “Space-time approach to scattering from many-body systems,” *Physical Review A*, vol. 58, p. 280, 1998.
- [142] L. Passell and R. Schermer, “Measurement of the spin dependence of the $^3\text{He}(n, p)t$ reaction and of the nuclear susceptibility of adsorbed ^3He ,” *Physical Review*, vol. 150, p. 146, 1966.
- [143] S. Borzakov, H. Malecki, L. Pikel’ner, M. Stempinski, and E. Sharapov, “Features of the departure from the $1/v$ law of the cross section for the reaction $^3\text{He}(n, p)t$. excited level of the ^4He nucleus,” *Soviet Journal of Nuclear Physics*, vol. 35, pp. 307–312, 1982.
- [144] C. Schmiegelow, J. Schulz, H. Kaufmann, T. Ruster, U. Poschinger, and F. Schmidt-Kaler, “Transfer of optical orbital angular momentum to a bound

- electron,” *Nature communications*, vol. 7, p. 12998, 2016.
- [145] A. Afanasev, V. Serbo, and M. Solyanik, “Radiative capture of cold neutrons by protons and deuteron photodisintegration with twisted beams,” *Journal of Physics G: Nuclear and Particle Physics*, vol. 45, p. 055102, 2018.
- [146] M. Rose, *Elementary Theory of Angular Momentum*. Wiley, New York, 1957.
- [147] A. Picón, A. Benseny, J. Mompart, V. D. Aldana, L. Plaja, G. Calvo, and L. Roso, “Transferring orbital and spin angular momenta of light to atoms,” *New Journal of Physics*, vol. 12, p. 083053, 2010.
- [148] J. Carroll, “Nuclear structure and the search for induced energy release from isomers,” *Nuclear Instruments and Methods in Physics Research Section B: Beam Interactions with Materials and Atoms*, vol. 261, pp. 960–964, 2007.
- [149] E. J. Post, “Sagnac effect,” *Reviews of Modern Physics*, vol. 39, pp. 475–493, 1967.
- [150] A. A. Michelson, H. G. Gale, and F. Pearson, “The effect of the earth’s rotation on the velocity of light, ii,” *AstroPhysical Journal*, vol. 61, p. 140, 1925.
- [151] J. E. Zimmerman and J. E. Mercereau, “Compton wavelength of superconducting electrons,” *Phys. Rev. Lett.*, vol. 14, pp. 887–888, 1965.
- [152] F. Hasselbach and M. Nicklaus, “Sagnac experiment with electrons: Observation of the rotational phase shift of electron waves in vacuum,” *Phys. Rev. A*, vol. 48, pp. 143–151, 1993.
- [153] F. Riehle, T. Kisters, A. Witte, J. Helmcke, and C. J. Bordé, “Optical ramsey spectroscopy in a rotating frame: Sagnac effect in a matter-wave interferometer,” *Phys. Rev. Lett.*, vol. 67, p. 117, 1991.
- [154] R. Gautier, M. Guessoum, L. A. Sidorenkov, Q. Bouton, A. Landragin, and R. Geiger, “Accurate measurement of the sagnac effect for matter waves,” *Science Advances*, vol. 8, p. eabn8009, 2022.
- [155] B. Mashhoon, “Neutron interferometry in a rotating frame of reference,” *Physical Review Letters*, vol. 61, pp. 2639–2642, 1988.
- [156] B. Demirel, S. Sponar, and Y. Hasegawa, “Measurement of the spin–rotation coupling in neutron polarimetry,” *New Journal of Physics*, vol. 17, p. 023065, 2015.
- [157] A. Danner, B. Demirel, W. Kersten, H. Lemmel, R. Wagner, S. Sponar, and Y. Hasegawa, “Spin-rotation coupling observed in neutron interferometry,” *npj Quantum Information*, vol. 6, no. 23, 2020.
- [158] A. G. Wagh, S. Abbas, and W. Treimer, “The plain truth about forming a plane wave of neutrons,” *Nuclear Instruments and Methods in Physics Research Section A: Accelerators, Spectrometers, Detectors and Associated Equipment*, vol. 634, pp. S41–S45, 2011.

- [159] R. Dalglish, M. Snow, V. de Haan, K. Steffen, and N. Geerits, “Detection of the sagnac effect in SESANS,” 2024. <https://doi.org/10.5286/ISIS.E.RB2410116>.
- [160] G. J. Nilsen, J. Kosata, M. Devonport, P. Galsworthy, R. I. Bewley, D. J. Voneshen, R. Dalglish, and J. R. Stewart, “Polarisation analysis on the let time-of-flight spectrometer,” *Journal of Physics: Conference Series*, vol. 862, p. 012019, 2017.
- [161] G. Cassella, J. R. Stewart, G. M. Patern, V. G. Sakai, M. Devonport, P. J. Galsworthy, R. I. Bewley, D. J. Voneshen, D. Raspino, and G. J. Nilsen, “Polarization analysis on the LET cold neutron spectrometer using a ^3He spin-filter: first results,” *Journal of Physics: Conference Series*, vol. 1316, p. 012007, 2019.
- [162] S. Lu, A. A. M. Irfan, J. Shen, S. J. Kuhn, W. M. Snow, D. V. Baxter, R. Pynn, and G. Ortiz, “Operator analysis of contextuality-witness measurements for multimode-entangled single-neutron interferometry,” *Physical Review A*, vol. 101, p. 042318, 2020.
- [163] W. Kraan, S. Grigoriev, M. Rekveldt, H. Fredrikze, C. de Vroege, and J. Plomp, “Test of adiabatic spin flippers for application at pulsed neutron sources,” *Nuclear Instruments and Methods in Physics Research A*, vol. 510, p. 334–345, 2003.
- [164] S. Slussarenko, V. D’Ambrosio, B. Piccirillo, L. Marrucci, and E. Santamato, “The polarizing sagnac interferometer: a tool for light orbital angular momentum sorting and spin-orbit photon processing,” *Optics Express*, vol. 18, pp. 27205–27216, 2010.
- [165] F. Wang, W. Chen, Y. Li, G. Zhang, Z. Yin, S. Wang, G. Guo, and Z. Han, “Single-path sagnac interferometer with dove prism for orbital-angular-momentum photon manipulation,” *Optics Express*, vol. 25, pp. 24946–24959, 2017.
- [166] R. Silvestri, H. Yu, T. Strömberg, C. Hilweg, R. W. Peterson, and P. Walther, “Experimental observation of earth’s rotation with quantum entanglement,” *Science Advances*, vol. 10, p. eado0215, 2024.
- [167] M. Arif, H. Kaiser, S. Werner, A. Cimmino, W. Hamilton, A. Klein, and G. Opat, “Null fizeau effect for thermal neutrons in moving matter,” *Physical Review A*, vol. 31, p. 1203, 1985.
- [168] M. Arif, H. Kaiser, R. Clothier, S. Werner, R. Berliner, W. Hamilton, A. Cimmino, and A. Klein, “Fizeau effect for neutrons passing through matter at a nuclear resonance,” *Physica B+ C*, vol. 151, pp. 63–67, 1988.
- [169] M. Horne, A. Zeilinger, A. Klein, and G. Opat, “Neutron phase shift in moving matter,” *Physical Review A*, vol. 28, p. 1, 1983.
- [170] A. Klein, G. Opat, A. Cimmino, A. Zeilinger, W. Treimer, and R. Gähler, “Neutron propagation in moving matter: the fizeau experiment with massive particles,” *Physical Review Letters*, vol. 46, p. 1551, 1981.

A Appendix 1

A.1 Note 1: Calculation of the Moments of $\langle \hat{L} \rangle$ for Section 5.1.2

In this note the step by step calculations of $\langle L_z \rangle$ (for isotropic and anisotropic momentum distributions) and $\langle L_z^2 \rangle$ of the test wavefunction 5.4 are shown. Starting with the calculation of $\langle L_z \rangle$ in cylindrical coordinates

$$\langle L_z \rangle = -i \frac{\int d\mathbf{r} \psi_t^*(\mathbf{r}) \frac{\partial}{\partial \phi} \psi_t(\mathbf{r})}{\int d\mathbf{r} |\psi_t(\mathbf{r})|^2}$$

with

$$\int d\mathbf{r} |\psi_t(\mathbf{r})|^2 = 1 + \cos(\Delta\alpha) e^{-\frac{\sigma^2 k_\perp^2}{4}} = N$$

and

$$-i \frac{\partial}{\partial \phi} \psi_t(\mathbf{r}) = \frac{1}{\sqrt{2}} \psi_0 [k_\perp \rho \cos(\phi) e^{ik_\perp \rho \sin(\phi)} - e^{i\Delta\alpha} k_\perp \rho \sin(\phi) e^{ik_\perp \rho \cos(\phi)}]$$

hence it follows

$$\langle L_z \rangle = \frac{1}{2N} \int d\mathbf{r} |\psi_0|^2 [k_\perp \rho \cos(\phi) - k_\perp \rho \sin(\phi) + k_\perp \rho \cos(\phi) e^{-i\Delta\alpha} e^{ik_\perp \rho (\sin(\phi) - \cos(\phi))} - k_\perp \rho \sin(\phi) e^{i\Delta\alpha} e^{ik_\perp \rho (\cos(\phi) - \sin(\phi))}]$$

which, using $\int_0^{2\pi} d\phi \cos(\phi) = \int_0^{2\pi} d\phi \sin(\phi) = 0$, simplifies to

$$\langle L_z \rangle = \frac{1}{2N} \int d\mathbf{r} k_\perp \rho |\psi_0|^2 [\cos(\phi) e^{-i\Delta\alpha} e^{ik_\perp \rho (\sin(\phi) - \cos(\phi))} - \sin(\phi) e^{i\Delta\alpha} e^{ik_\perp \rho (\cos(\phi) - \sin(\phi))}]$$

$$\langle L_z \rangle = \frac{1}{2N} \int d\mathbf{r} k_\perp \rho |\psi_0|^2 [\cos(\phi) e^{-i\Delta\alpha} e^{i\sqrt{2} k_\perp \rho \sin(\phi - \pi/4)} - \sin(\phi) e^{i\Delta\alpha} e^{-i\sqrt{2} k_\perp \rho \sin(\phi - \pi/4)}]$$

Then we apply the Jacobi-Anger expansion, $e^{iz \sin(\phi)} = \sum_\ell J_\ell(z) e^{i\ell\phi}$, and use that $\int_0^{2\pi} d\phi e^{i\ell\phi} = 0$ for $\ell \neq 0$. This allows us to easily solve the azimuthal integral.

$$\langle L_z \rangle = \frac{\pi}{2N} \int d\rho k_\perp \rho^2 |\psi_0|^2 [J_{-1}(\sqrt{2} k_\perp \rho) e^{-i\Delta\alpha} e^{i\frac{\pi}{4}} + J_1(\sqrt{2} k_\perp \rho) e^{-i\Delta\alpha} e^{-i\frac{\pi}{4}}]$$

A Appendix 1

$$-iJ_{-1}(\sqrt{2}k_{\perp}\rho)e^{i\Delta\alpha}e^{i\frac{\pi}{4}} + iJ_1(\sqrt{2}k_{\perp}\rho)e^{i\Delta\alpha}e^{-i\frac{\pi}{4}}$$

Next we use the anti-symmetry of the Bessel function of first order $J_{-1}(z) = -J_1(z)$ and begin grouping the exponential/trigonometric terms.

$$\langle L_z \rangle = -i\frac{\pi}{N} \int d\rho k_{\perp} \rho^2 |\psi_0|^2 J_1(\sqrt{2}k_{\perp}\rho) [e^{-i\Delta\alpha} \sin(\frac{\pi}{4}) - e^{i\Delta\alpha} \cos(\frac{\pi}{4})]$$

$$\langle L_z \rangle = 2\pi \frac{\sin \Delta\alpha}{\sqrt{2}N} \int d\rho k_{\perp} \rho^2 |\psi_0|^2 J_1(\sqrt{2}k_{\perp}\rho)$$

Which can be rewritten into the form of a standard Hankel transform of first order with known result. This brings us to the equation (8) seen in the main text

$$\langle L_z \rangle = \sin(\Delta\alpha) \frac{k_{\perp}^2 \sigma^2}{4N} e^{-\frac{\sigma^2 k_{\perp}^2}{4}}$$

Next we examine the generalized case where the momentum distribution is anisotropic (see equation (13) in the main text). This is best done in Cartesian coordinates:

$$L_z \psi_t = -i(x \frac{\partial}{\partial y} - y \frac{\partial}{\partial x}) \psi_t$$

$$= -\frac{i}{\sqrt{\pi\sigma_x\sigma_y}} e^{-\frac{x^2}{\sigma_x^2} - \frac{y^2}{\sigma_y^2}} (2xy(e^{ik_{\perp}y} + e^{i\Delta\alpha}e^{ik_{\perp}x})) [\frac{1}{\sigma_x^2} - \frac{1}{\sigma_y^2}] + ik_{\perp}x e^{ik_{\perp}y} - ik_{\perp}y e^{i\Delta\alpha}e^{ik_{\perp}x})$$

Hence it follows

$$\langle L_z \rangle = \frac{k_{\perp}}{\pi\sigma_x\sigma_y N} \int dx dy e^{-2\frac{x^2}{\sigma_x^2} - 2\frac{y^2}{\sigma_y^2}} [x e^{-ik_{\perp}(x-y) - i\Delta\alpha} - y e^{ik_{\perp}(x-y) + i\Delta\alpha}]$$

Where all odd terms have been dropped since their integral is zero. To proceed we use $i\frac{\partial}{\partial k} e^{-ik(a+b)} = (a+b)e^{-ik(a+b)}$ to get

$$\langle L_z \rangle = \frac{k_{\perp}}{\pi\sigma_x\sigma_y N} \int dx dy e^{-2\frac{x^2}{\sigma_x^2} - 2\frac{y^2}{\sigma_y^2}} [i\frac{\partial}{\partial k_{\perp}} e^{-ik_{\perp}(x-y) - i\Delta\alpha} - i\frac{\partial}{\partial k} e^{ik_{\perp}(x-y) + i\Delta\alpha} + y e^{-ik_{\perp}(x-y) - i\Delta\alpha} - x e^{ik_{\perp}(x-y) + i\Delta\alpha}]$$

Note the final term is minus the complex conjugate of our previous expression for $\langle L_z \rangle$ hence it follows

$$\langle L_z \rangle = \frac{k_{\perp}}{\pi\sigma_x\sigma_y N} \int dx dy e^{-2\frac{x^2}{\sigma_x^2} - 2\frac{y^2}{\sigma_y^2}} [i\frac{\partial}{\partial k_{\perp}} e^{-ik_{\perp}(x-y) - i\Delta\alpha} - i\frac{\partial}{\partial k} e^{ik_{\perp}(x-y) + i\Delta\alpha}] - \langle L_z \rangle^*$$

and since expectation values must be real we can conclude

$$\langle L_z \rangle = \frac{ik_{\perp}}{2\pi\sigma_x\sigma_y N} \int dx dy e^{-2\frac{x^2}{\sigma_x^2} - 2\frac{y^2}{\sigma_y^2}} \frac{\partial}{\partial k_{\perp}} [e^{-ik_{\perp}(x-y) - i\Delta\alpha} - e^{ik_{\perp}(x-y) + i\Delta\alpha}]$$

We may now swap integration and differentiation and realize that we are left with a standard Fourier transform

$$\langle L_z \rangle = \frac{ik_{\perp}}{2\pi\sigma_x\sigma_y N} \frac{\partial}{\partial k_{\perp}} \int dx dy e^{-2\frac{x^2}{\sigma_x^2} - 2\frac{y^2}{\sigma_y^2}} [e^{-ik_{\perp}(x-y) - i\Delta\alpha} - e^{ik_{\perp}(x-y) + i\Delta\alpha}]$$

Conducting the transform and grouping the exponential/trigonometric terms leads to

$$\langle L_z \rangle = \frac{k_{\perp}}{2N} \frac{\partial}{\partial k_{\perp}} e^{-\frac{(\sigma_x^2 + \sigma_y^2)k^2}{8}} \sin(\Delta\alpha)$$

Finally carrying out the differentiation leads to the result shown in equation (14) of the main text

$$\langle L_z \rangle = \sin(\Delta\alpha) \frac{k_{\perp}^2 (\sigma_x^2 + \sigma_y^2)}{8N} e^{-\frac{k_{\perp}^2 (\sigma_x^2 + \sigma_y^2)}{8}}$$

Finally we calculate the second moment of the OAM distribution, $\langle L_z^2 \rangle$

$$\langle L_z^2 \rangle = - \frac{\int d\mathbf{r} \psi_t^*(\mathbf{r}) \frac{\partial^2}{\partial \phi^2} \psi_t(\mathbf{r})}{N}$$

$$\frac{\partial^2}{\partial \phi^2} \psi(\mathbf{r}) = -\frac{1}{\sqrt{2}} \psi_0 [(k_{\perp}^2 \rho^2 \sin^2(\phi) + ik_{\perp} \rho \cos(\phi)) e^{i\Delta\alpha} e^{ik_{\perp} \rho \cos(\phi)} + (k_{\perp}^2 \rho^2 \cos^2(\phi) + ik_{\perp} \rho \sin(\phi)) e^{ik_{\perp} \rho \sin(\phi)}]$$

Therefore

$$\langle L_z^2 \rangle = \frac{1}{2N} \int d\mathbf{r} |\psi_0|^2 [(k_{\perp}^2 \rho^2 \sin^2(\phi) + ik_{\perp} \rho \cos(\phi)) + (k_{\perp}^2 \rho^2 \cos^2(\phi) + ik_{\perp} \rho \sin(\phi)) + (k_{\perp}^2 \rho^2 \sin^2(\phi) + ik_{\perp} \rho \cos(\phi)) e^{i\Delta\alpha} e^{ik_{\perp} \rho [\cos(\phi) - \sin(\phi)]} + (k_{\perp}^2 \rho^2 \cos^2(\phi) + ik_{\perp} \rho \sin(\phi)) e^{-i\Delta\alpha} e^{ik_{\perp} \rho [\sin(\phi) - \cos(\phi)]}]$$

First we use $\cos(\phi) - \sin(\phi) = -\sqrt{2} \sin(\phi - \frac{\pi}{4})$

$$\langle L_z^2 \rangle = \frac{1}{2N} \int d\mathbf{r} |\psi_0|^2 [k_{\perp}^2 \rho^2 \sin^2(\phi) + k_{\perp}^2 \rho^2 \cos^2(\phi) + (k_{\perp}^2 \rho^2 \sin^2(\phi) + ik_{\perp} \rho \cos(\phi)) e^{i\Delta\alpha} e^{-i\sqrt{2} k_{\perp} \rho \sin(\phi - \frac{\pi}{4})} + (k_{\perp}^2 \rho^2 \cos^2(\phi) + ik_{\perp} \rho \sin(\phi)) e^{-i\Delta\alpha} e^{i\sqrt{2} k_{\perp} \rho \sin(\phi - \frac{\pi}{4})}]$$

We simplify the expression by using the identity $\cos^2(\phi) + \sin^2(\phi) = 1$

$$\langle L_z^2 \rangle = \frac{1}{2N} \int d\mathbf{r} |\psi_0|^2 [k_{\perp}^2 \rho^2 + (k_{\perp}^2 \rho^2 \sin^2(\phi) + ik_{\perp} \rho \cos(\phi)) e^{i\Delta\alpha} e^{-i\sqrt{2} k_{\perp} \rho \sin(\phi - \frac{\pi}{4})} +$$

$$(k_{\perp}^2 \rho^2 \cos^2(\phi) + ik_{\perp} \rho \sin(\phi)) e^{-i\Delta\alpha} e^{i\sqrt{2}k_{\perp} \rho \sin(\phi - \frac{\pi}{4})}$$

We solve the azimuthal integral by using the Jacobi-Anger expansion again, $e^{iz \sin(\phi)} = \sum_{\ell} J_{\ell}(z) e^{i\ell\phi}$, and again use that $\int_0^{2\pi} d\phi e^{i\ell\phi} = 0$ for $\ell \neq 0$. Note that the latter identity paired with the trigonometric terms in the previous line filter out all but the $\ell = 0$ and $\ell = \pm 1$ terms of the Jacobi-Anger expansion.

$$\langle L_z^2 \rangle = \frac{1}{2N} \int d\rho \rho |\psi_0|^2 [2\pi k_{\perp}^2 \rho^2 + (\pi k_{\perp}^2 \rho^2 J_0(\sqrt{2}k_{\perp} \rho) - \sqrt{2}\pi k_{\perp} \rho J_1(\sqrt{2}k_{\perp} \rho)) e^{i\Delta\alpha} + (\pi k_{\perp}^2 \rho^2 J_0(\sqrt{2}k_{\perp} \rho) - \sqrt{2}\pi k_{\perp} \rho J_1(\sqrt{2}k_{\perp} \rho)) e^{-i\Delta\alpha}]$$

Here we have once again used the asymmetry of the first order Bessel function. Next we group together the trigonometric terms

$$\langle L_z^2 \rangle = \frac{1}{2N} \int d\rho \rho |\psi_0|^2 [2\pi k_{\perp}^2 \rho^2 + \cos(\Delta\alpha) (2\pi k_{\perp}^2 \rho^2 J_0(\sqrt{2}k_{\perp} \rho) - \sqrt{8}\pi k_{\perp} \rho J_1(\sqrt{2}k_{\perp} \rho))]$$

Now we attempt to solve the radial integrals

$$\langle L_z^2 \rangle = \frac{1}{\pi\sigma^2 N} \int d\rho \rho e^{-2\frac{\rho^2}{\sigma^2}} [2\pi k_{\perp}^2 \rho^2 + \cos(\Delta\alpha) (2\pi k_{\perp}^2 \rho^2 J_0(\sqrt{2}k_{\perp} \rho) - \sqrt{8}\pi k_{\perp} \rho J_1(\sqrt{2}k_{\perp} \rho))]$$

The first integral seen above:

$$\int_0^{\infty} d\rho 2\pi k_{\perp}^2 \rho^3 e^{-2\frac{\rho^2}{\sigma^2}}$$

can be solved using integration by parts and substitution ($u = \rho^2$ and $du = \rho d\rho$)

$$\int_0^{\infty} du \pi k_{\perp}^2 u e^{-2\frac{u}{\sigma^2}} = [-\pi k_{\perp}^2 \frac{u\sigma^2}{2} e^{-\frac{2u}{\sigma^2}}]_0^{\infty} + \int_0^{\infty} du \pi k_{\perp}^2 \frac{\sigma^2}{2} e^{-2\frac{u}{\sigma^2}} = \frac{\pi k_{\perp}^2 \sigma^4}{4}$$

The next radial integral in $\langle L_z^2 \rangle$ is a Hankel transform with a known result:

$$2\pi \cos(\Delta\alpha) \int_0^{\infty} d\rho k_{\perp}^2 \rho^3 e^{-2\frac{\rho^2}{\sigma^2}} J_0(\sqrt{2}k_{\perp} \rho) = \frac{\pi k_{\perp}^2 \sigma^4}{4} \cos(\Delta\alpha) e^{-\frac{\sigma^2 k_{\perp}^2}{4}} (1 - \frac{k_{\perp}^2 \sigma^2}{4})$$

The final integral is the same Hankel transform as for the first moment

$$-\sqrt{8}\pi \cos(\Delta\alpha) \int d\rho e^{-2\frac{\rho^2}{\sigma^2}} k_{\perp} \rho^2 J_1(\sqrt{2}k_{\perp} \rho) = -\cos(\Delta\alpha) \frac{\pi k_{\perp}^2 \sigma^4}{4} e^{-\frac{k_{\perp}^2 \sigma^2}{4}}$$

Hence we find

$$\langle L_z^2 \rangle = \frac{k_{\perp}^2 \sigma^2}{4N} + \cos(\alpha) \frac{k_{\perp}^2 \sigma^2}{4N} e^{-\frac{\sigma^2 k_{\perp}^2}{4}} (1 - \frac{k_{\perp}^2 \sigma^2}{4}) - \cos(\alpha) \frac{k_{\perp}^2 \sigma^2}{4N} e^{-\frac{k_{\perp}^2 \sigma^2}{4}}$$

$$\langle L_z^2 \rangle = \frac{k_{\perp}^2 \sigma^2}{4N} - \cos(\alpha) \frac{k_{\perp}^4 \sigma^4}{16N} e^{-\frac{\sigma^2 k_{\perp}^2}{4}}$$

A.2 Note 2: Image Processing and Data Reduction of Phase Vortices Produced in Interferometry

Here the processing and fitting techniques are shown which were used to reconstruct the test wavefunction and obtain the images shown in section 5.1.

A.2.1 Data Processing

The images shown in section 5.1 were generated using two recorded datasets, the first with prisms inserted in the interferometer and the second without prisms. Each dataset consists of 14 recordings 30 minutes a piece. The raw images shown in figure A.1 show the summed averages over all 14 images. To obtain the image shown in figure 5.4 both raw images (figure A.1) are binned by a factor of 10×10 squared pixels to increase statistics. Next the binned "prisms-in" image is divided by the binned "prisms-out" image to remove artifacts induced by uneven illumination of the detector and spatial phase drifts inherent to the interferometer. After this initial normalization the resulting image still has a slight intensity drift over the vertical (y) direction. This is removed by fitting a quadratic polynomial to the average intensity along the vertical direction and dividing the image by this polynomial. After this step the image is normalized by dividing it by the mean intensity and subtracting one $I_{norm} = \frac{I}{\langle I \rangle} - 1$. Finally a noise reduction scheme is applied to improve the overall signal quality. This is achieved by Fourier transforming the image, removing all content from the FT below a certain noise floor and transforming the modified FT back to real space. Figure A.2 shows the image at each point of the data reduction.

A.2.2 Fitting Procedure

The fit shown in figure 5.4 is based on equation (5.17), with a few modifications to take into account perturbations not considered in our simplified theory. By normalizing the data as described above we forfeit the need for a constant offset in the fit function. In addition to account for the dephasing which reduces the contrast towards the edges of the image since the neutrons have to pass through more material, we multiply (5.17) by a Gaussian envelope. Finally we note that the interference pattern in the images indicate that the prisms were not totally orthogonal, as a result the fit function takes on the form

$$f = e^{\frac{(\vec{x}-\vec{\mu})^2}{s^2}} [a_1 \cos(\vec{\eta}_1 \cdot \vec{x} + \alpha'_1) + a_2 \cos(\vec{\eta}_2 \cdot \vec{x} + \alpha'_2) + a_3 \cos((\vec{\eta}_1 - \vec{\eta}_2) \cdot \vec{x} + \alpha'_1 - \alpha'_2)] \quad (\text{A.1})$$

Here initial guesses for $\vec{\eta}_1$, $\vec{\eta}_2$, α'_1 , α'_2 , a_1 , a_2 and a_3 are extracted from the Fourier transform of the processed data. An initial guess for $\vec{\mu}$ is found by determining the expectation value of the squared processed data $\langle \vec{x} \rangle = \frac{\int dx dy \vec{x} I^2}{\int dx dy I^2}$. Finally the parameter

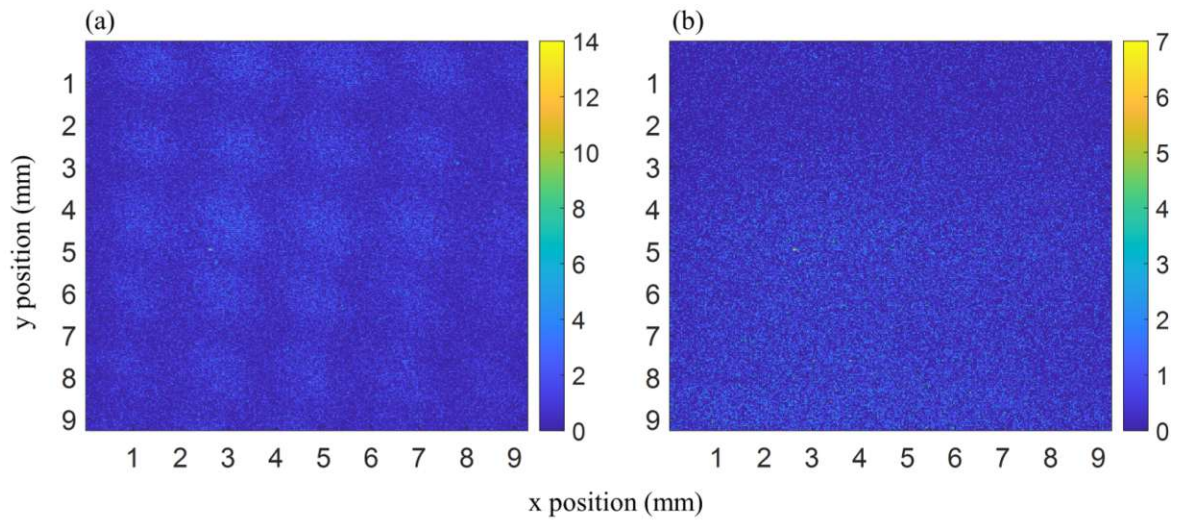


Figure A.1: Sum over the raw datasets used to generate the figures shown in this paper. (a) Image with the prisms inserted. (b) Image of the intensity distribution without prisms in the interferometer.

s^2 is guessed by calculating the variance of the squared processed data $\frac{\int dx dy |\bar{x}|^2 I^2}{\int dx dy I^2} - \langle \bar{x} \rangle^2$

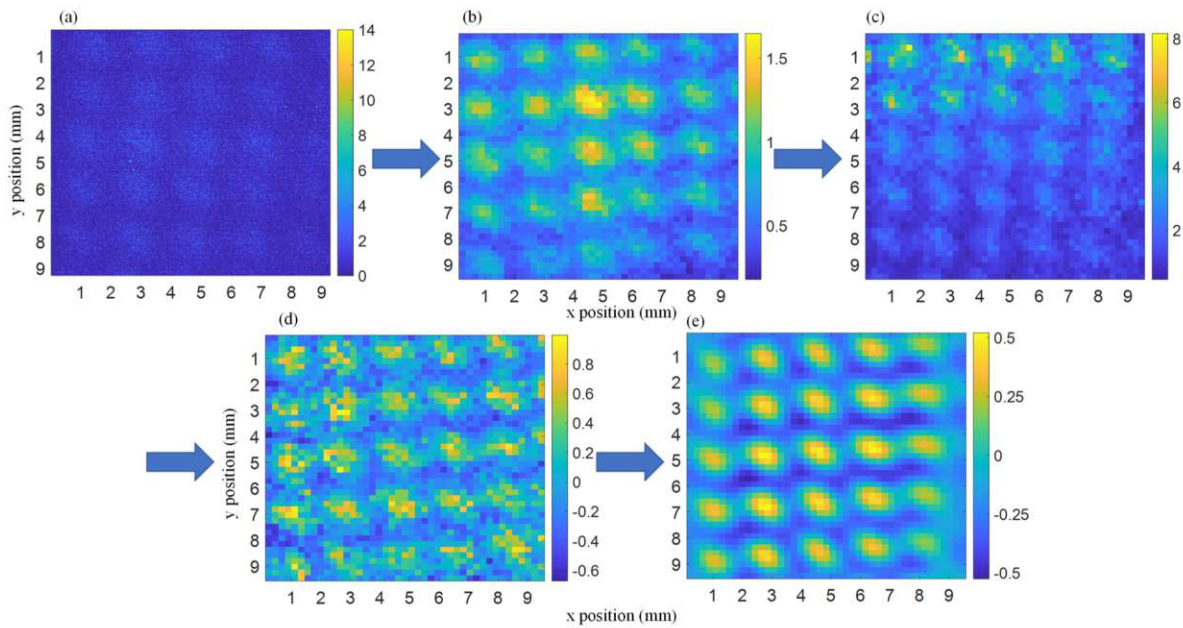


Figure A.2: Step by step illustration of the image processing technique. The raw image (a) is binned (b) by a factor of 10×10 squared pixels. The first normalization is shown in (c), followed by the next normalization steps (d) by dividing by a quadratic polynomial and subsequently dividing by the mean intensity and subtracting one. Finally the Fourier filter is applied resulting in the last image (e)

B Curriculum Vitae

Personal data



Name: Niels Geerits MSc., BSc.
Address: Rennweg 64/1/11, 1030 Vienna, Austria
Email: niels.geerits@tuwien.ac.at, niels_geerits@hotmail.com
Place/Date of birth: Voorburg, The Netherlands, 28.04.1995
Nationality: Netherlands

Education

- Feb 2019 - Now PhD Applied Physics, TU Wien (Vienna, Austria)
Topic of Disseration: *Generation and Detection of Neutron Orbital Angular Momentum*
(Supervisor: Stephan Sponar)
- Apr 2017 - Feb 2019 Master's Degree Applied Physics, TU Delft (Delft, The Netherlands)
Thesis: *Development of Time of Flight Modulation of Intensity by Zero Effort for Larmor*
(Supervisors: Jeroen Plomp, Wim Bouwman, Stephan Eijt, Niels van Dijk)
- Sep 2013 - Apr 2017 Bachelor's Degree Applied Physics, TU Delft (Delft, The Netherlands)
Thesis: *Spin Echo Modulated Small Angle Neutron Scattering Using Radio Frequency Flippers*
(Supervisors: Ad van Well, Jeroen Plomp, Lambert van Eijck)
- Sep 2006 - Jun 2013 Hermann Billung Gymnasium Celle., 29225 Celle, Germany (Abitur 2013)

Work Experience

July 2023 - now	Scientific stays as Oak Ridge National Laboratory (ORNL) Oak Ridge, USA
Feb 2019 - now	Projekt Assistent, TU-Wien (Vienna, Austria) Atominstitut, Neutron and Quantum Physics Group Development of neutron optics for OAM
July 2019 - now	Scientific stays at Institute Laue Langevin (ILL) Grenoble, France
November 2018 - February 2019	Intern at TNO, Delft (Delft, The Netherlands) Electron impact induced plasma research project
October 2018 - now	Scientific stays at ISIS Neutron and Muon Source Didcot, England
May 2017 - July 2017	Teaching Assistant at TU Delft (Delft, The Netherlands)
March 2015 - June 2015	Teaching Assistant at TU Delft (Delft, The Netherlands)

Language skills:

Dutch, English, German

Publications

Publications

- Niels Geerits, Steven R. Parnell, Michel A. Thijs, Ad A. van Well, Christian Franz, Adam L. Washington, Davide Raspino, Rob M. Dalgliesh and Jeroen Plomp *Time of Flight Modulation of Intensity by Zero Effort on Larmor*, Review of Scientific Instruments **90**, 125101 (2019).
- N. Geerits, S.R. Parnell, M.A. Thijs, W.G. Bouwman and J. Plomp *Time of Flight MIEZE Spectrometer*, Journal of Physics: Conference Series **1316** 012011 (2019)
- J. Shen, S.J. Kuhn, R.M. Dalgliesh, V.O. de Haan, N. Geerits, A.A.M. Irfan, F. Li, S. Lu, S.R. Parnell, J. Plomp, A.A. van Well, A.L. Washington, D.V. Baxter, G. Ortiz, W.M. Snow and R. Pynn *Unveiling Contextual Realities by Microscopically Entangling a Neutron*, Nature Communications **11**, 930 (2020).
- S.R. Parnell, A.A. van Well, J. Plomp, R.M. Dalgliesh, N. Juliane-Steinke, J. Cooper, N. Geerits, K.E. Steffe, W.M. Snow, V.O. de Haan *Search for exotic spin-dependent couplings of the neutron with matter using spin-echo based neutron interferometry*, Physical Review D **101**, 122002 (2020).
- N. Geerits and S. Sponar *Twisting Neutral Particles with Electric Fields* Physical Review A **103** 022205 (2021)
- S. J. Kuhn, S. McKay, J. Shen, N. Geerits, R. M. Dalgliesh, E. Dees, A. A. M. Irfan, F. Li, S. Lu, V. Vangelista, D. V. Baxter, G. Ortiz, S. R. Parnell, W. M. Snow and R. Pynn, *Neutron State Entanglement with Overlapping Paths* Physical Review Research **3** 023227 (2021)
- S.J. Kuhn, N. Geerits, C. Franz, J. Plomp, R.M. Dalgliesh, S.R. Parnell *Time-of-flight modulated intensity small-angle neutron scattering measurement of the self-diffusion constant of water* Journal of Applied Crystallography **54** (3), 751-758 (2021)
- Jacqueline van Veldhoven, Aneta S Stodólna, Arnold Storm, Jeroen van den Brink, Niels Geerits, Jasper Vlaar, Michael Dekker, Andrey Ushakov, *Low-Energy Plasma Source for Clean Vacuum Environments: EUV Lithography and Optical Mirrors Cleaning* IEEE Transactions on Plasma Science **49** 3132-3141 (2021)
- H. Lemmel, N. Geerits, A. Danner, H.F. Hofmann, S. Sponar *Quantifying the*

presence of a neutron in the paths of an interferometer Physical Review Research **4** 023075 (2022)

- Niels Geerits, Hartmut Lemmel, Anna-Sophie Berger, Stephan Sponar *Phase Vortex Lattices in Neutron Interferometry* Communications Physics **6** 209 (2023)
- B. Schillinger, N. Geerits, T. Jünger, J. Matoušková, T. Neuwirth, F. Oppermann, S. Sebold, S. Sponar *Flexible camera detector box design using 3D printers* Journal of Physics: Conference Series **2605** 012008 (2023)
- Armin Danner, Niels Geerits, Hartmut Lemmel, Richard Wagner, Stephan Sponar, Yuji Hasegawa *Three-Path Quantum Cheshire Cat Observed in Neutron Interferometry* Communications Physics **7** 14 (2024)
- S. McKay, A.A.M. Irfan, Q. Le Thien, N. Geerits, S.R. Parnell, R.M. Dalgliesh, Nickolay V. Lavrik, Ivan I. Kravchenko, G. Ortiz, R. Pynn *Experimental evidence for the two-path description of neutron spin echo* Physical Review A **109** 042420 (2024)
- J.C. Leiner, S.J. Kuhn, S. McKay, J.K. Jochum, F. Li, A.A.M. Irfan, F. Funama, D. Mettus, L. Beddrich, C. Franz, J. Shen, S.R. Parnell, R.M. Dalgliesh, M. Loyd, N. Geerits, G. Ortiz, C. Pfeiderer, and R. Pynn *Spin-energy entanglement of a time-focused neutron* Phys. Rev. Appl **22** L031005 (2024)
- Elisabeth Kreuzgruber, Richard Wagner, Niels Geerits, Hartmut Lemmel, Stephan Sponar *Violation of a Leggett-Garg inequality using ideal negative measurements in neutron interferometry* Physical Review Letters **132** 260201 (2024).
- Niels Geerits, Stephan Sponar, Kyle E. Steffen, William M. Snow, Steven R. Parnell, Giacomo Mauri, Gregory N. Smith, Robert M. Dalgliesh, Victor de Haan *Measuring the angular momentum of a neutron using Earth's rotation* Physical Review Research **7** 013046 (2025).

Preprints

- Niels Geerits, Simon Hack, Ad van Well, Steven R Parnell, Hartmut Abele, Stephan Sponar *CANISIUS The Austrian Neutron Spin Echo Interferometer* arXiv:2408.06216 (2024)

Invited Talks

- N. Geerits Generation and Detection of Neutron Orbital Angular Momentum at the Atominstitut. Twisted Light in Quantum and Sub-Atomic Systems 2023, Mainz, Germany.
- N. Geerits Engineering Designer Neutrons for Fundamental Physics Experiments. Workshop on Scientific Benefits and Applications of Resonant Spin Echo 2024, Oak Ridge, USA.
- N. Geerits Production of Neutron with Orbital Angular Momentum for Fundamental Physics Experiments. Vortex states in nuclear and particle physics 2024, Zhuhai, China.
- N. Geerits Measuring the Angular Momentum of a Neutron with Earths Rotation. Polarized Neutrons for Condensed Matter Investigations 2025, Dongguan, China. (Planned)

Grants & Funding

- Stephan Sponar and Niels Geerits, FWF, Spin - Orbital Angular Momentum Entanglement with Neutrons. P – 34239.
- William Michael Snow and Niels Geerits et al., US Department of Energy, Development of Mode-Entangled Neutron Beams with Orbital Angular Momentum for Quantum Sensing. DE-SC0023695.

C Related Publications

- [N. Geerits](#) and S. Sponar *Twisting Neutral Particles with Electric Fields* Physical Review A **103** 022205 (2021)
- [Niels Geerits](#), Hartmut Lemmel, Anna-Sophie Berger, Stephan Sponar *Phase Vortex Lattices in Neutron Interferometry* Communications Physics **6** 209 (2023)
- [Niels Geerits](#), Simon Hack, Ad van Well, Steven R Parnell, Hartmut Abele, Stephan Sponar *CANISIUS The Austrian Neutron Spin Echo Interferometer* arXiv:2408.06216 (2024)
- [Niels Geerits](#), Stephan Sponar, Kyle E. Steffen, William M. Snow, Steven R. Parnell, Giacomo Mauri, Gregory N. Smith, Robert M. Dalgliesh, Victor de Haan *Measuring the angular momentum of a neutron using Earth's rotation* Physical Review Research **7** 013046 (2025).